

UNIVERSITY OF OKLAHOMA

GRADUATE COLLEGE

OBSERVATIONAL AND MODEL ANALYSES OF
THE OKLAHOMA CITY URBAN HEAT ISLAND

A DISSERTATION

SUBMITTED TO THE GRADUATE FACULTY

in partial fulfillment of the requirements for the

Degree of

DOCTOR OF PHILOSOPHY

By

KODI LYNN NEMUNAITIS

Norman, Oklahoma

2014

OBSERVATIONAL AND MODEL ANALYSES OF
THE OKLAHOMA CITY URBAN HEAT ISLAND

A DISSERTATION APPROVED FOR THE
SCHOOL OF METEOROLOGY

BY

Dr. Petra Klein, Chair

Dr. Jeffrey B. Basara, Co-Chair

Dr. Kelvin K. Droegemeier

Dr. Evgeni Fedorovich

Dr. Aondover Tarhule

ACKNOWLEDGEMENTS

Over the past ten years, I received support and encouragement from a number of people. I thank Dr. Jeff Basara, my committee co-chair, for encouraging me to pursue a doctorate, helping me develop my writing skills, and being a friend during stressful times. I thank Dr. Petra Klein, my committee chair, for showing me an alternate path to the finish line of my dissertation. Without her assurance and a much needed push in a new direction, this study would have stagnated. I thank Dr. Evgeni Fedorovich for instilling a little bit of fear in me, which motivated me to prove him wrong and exceed his expectations. I thank Drs. Kelvin Droegemeier and Aondover Tarhule for their continuous encouragement and support.

Without support from the Oklahoma Climatological Survey and the Oklahoma Mesonet, this study would not have been successful. Peter Hall and Dr. Chris Fiebrich provided invaluable guidance on the quality assurance of surface energy balance data, as well as diagnosing problematic data collected by others. Dr. Ken Crawford provided encouragement and support, as well as his rules of writing, which I still try to follow. Dr. Renee McPherson provided opportunities to work on external projects and proposals that gave me invaluable experience and boosted my confidence.

I thank Dr. Christa Peters-Lidard and others with the Hydrological Sciences Laboratory at NASA's Goddard Space Flight Center for teaching me the importance of land surface spin-up during my summer fellowship. I thank the OU Supercomputing Center for Education and Research (OSCER) for providing the computing resources for this project, as well as technical expertise. I thank Kent Knopfmeier and Jeremy Gibbs

for providing diagnostic expertise when WRF would either crash or produce “features of WRF.” I thank Kevin Kelleher and Dr. Suzanne Van Cooten for recognizing my potential when I could not see it myself, and pushing me to live up to that potential.

I thank my family and friends for their encouragement and unwavering support, and abiding by my visitation ban during the final months of my degree. They were always confident in my ability to complete my dissertation, even when I wasn't. I thank Justin Monroe for his stubbornness and passion for computers and programming. Without his help, one of the most interesting components of this study would not have been included. Finally, I thank my daughter, Camryn, for always putting a smile on my face when I felt overwhelmed. “Itsy Bitsy Spider” could not have been better timed.

TABLE OF CONTENTS

	<u>Page</u>
ACKNOWLEDGEMENTS	iv
LIST OF TABLES	viii
LIST OF FIGURES	x
ABSTRACT	xv
1. INTRODUCTION	1
2. SCIENTIFIC BACKGROUND	7
2.1. THE URBAN CANOPY	7
2.2. STRUCTURE OF THE URBAN BOUNDARY LAYER	12
2.2.1. Urban Heat Island	14
2.2.2. Surface Energy Balance	22
2.2.3. Aerodynamic Structure	35
2.3. OBSERVATIONS OF THE URBAN ENVIRONMENT	41
2.3.1. Urban Field Campaigns	41
2.3.2. Long-Term Observation Networks	44
2.4. REPRESENTATION OF URBAN AREAS IN MESOSCALE MODELS	46
2.4.1. Thermal and Dynamical Parameterizations	47
2.4.2. Urban Canopy Models	51
3. OBSERVATIONAL DATA	54
3.1. JOINT URBAN 2003 (JU2003)	54
3.1.1. Air Temperature Data	56
3.1.2. Surface Energy Balance Data	57
3.1.3. Data Quality Assurance	61
3.2. THE OKLAHOMA MESONET	62
3.2.1. The OASIS Project	63
3.2.2. Instrumentation	63
3.2.3. Quality Assurance of Super Site Data	66
3.3. OKLAHOMA CITY MORPHOLOGY	75
4. MODELING SYSTEMS	77
4.1. HIGH-RESOLUTION LAND DATA ASSIMILATION SYSTEM (HRLDAS)	77
4.2. THE WEATHER RESEARCH AND FORECASTING MODEL VERSION 3	78
4.2.1. Microphysics Schemes in the ARW Model	79
4.2.2. Cumulus Convection Schemes in the ARW Model	79
4.2.3. Atmospheric Radiation Schemes in the ARW Model	80
4.2.4. Surface Layer Schemes in the ARW Model	80
4.2.5. Land Surface Schemes in the ARW Model	82
4.2.6. Planetary Boundary Layer Schemes in the ARW Model	82
4.2.7. Single-Layer Urban Canopy Model	84

4.3.	ATMOSPHERIC DATA	91
5.	URBAN-RURAL COMPARISON OF OBSERVATIONS	93
5.1.	AIR TEMPERATURE	93
5.2.	COMPONENTS OF THE SURFACE ENERGY BALANCE	95
5.3.	PARTITIONING OF AVAILABLE ENERGY	106
6.	MODEL EXPERIMENTS	109
6.1.	EXPERIMENT DESIGN	109
6.1.1.	Model Domain Specifications	109
6.1.2.	Urban Canopy Parameters	110
6.1.3.	Land Surface Initialization	114
6.2.	LAND SURFACE SPIN-UP	116
6.2.1.	Spin-Up Results	117
6.3.	CASE STUDY: 14-15 JULY 2003	121
6.3.1.	Air Temperature	121
6.3.2.	Components of the Surface Energy Balance	127
6.3.3.	Skin Temperature	142
6.4.	SUMMARY	146
7.	SUMMARY AND CONCLUSIONS	148
7.1.	FINAL REMARKS	148
7.2.	FUTURE WORK	150
	REFERENCES	153
A.	APPENDIX: PROGNOSTIC EQUATIONS FOR THE NOAH LSM	180
B.	APPENDIX: SURFACE ENERGY BALANCE COMPONENTS	191
C.	APPENDIX: URBPARAM.TBL	198
D.	APPENDIX: ENERGY FLUXES WITH MYJ PBL SCHEME	204

LIST OF TABLES

- Table 2-1.** Urban canopy parameters commonly used to describe the urban morphology of an area. Unless otherwise noted, parameter descriptions and relevance are from Burian et al. (2005).
- Table 2-2.** Large field campaigns to study the urban climate (Adapted from Grimmond (2006)).
- Table 2-3.** Long-term observation networks to study the urban climate.
- Table 2-4.** Examples of thermal parameterizations for urban land use in mesoscale models.
- Table 2-5.** Examples of dynamical parameterizations for urban land use in mesoscale models.
- Table 2-6.** Examples of urban canopy models developed for use in mesoscale models.
- Table 3-1.** The U.S. organizations that participated in Joint Urban 2003 (Allwine and Flaherty 2006).
- Table 3-2.** Instruments mounted on the Indiana University towers during Joint Urban 2003. At the TM site two dataloggers (A and B) were installed. Manufacturer/Model (M/M) abbreviations: CSI CSAT (CSAT), R.M. Young 81000 (RMY), CSI KH20 (KH20), Radiation and Energy Balance Systems, Inc. Q*6.7.1 (REBS), Licor Li-200SZ (200SZ), CSI CS500 (CS500), Cole-Palmer CP39670-10 K-Type (CP-K), height in meters [Ht (m)] (Grimmond et al. 2004b).
- Table 3-3.** Urban morphological parameters calculated by Burian et al. (2005) for a 27-km² area of Oklahoma City, Oklahoma.
- Table 5-1.** The coefficients of determination (R^2) and slopes of the best-fit lines for the components of the surface energy balance at the ASU, ATDD, and IU sites relative to NRMN from 10 days with solar insolation near theoretical values during July 2003.
- Table 5-2.** Mean daily values of net radiation (Q^* ; $W\ m^{-2}\ d^{-1}$), sensible heat flux (Q_H ; $W\ m^{-2}\ d^{-1}$), latent heat flux (Q_E ; $W\ m^{-2}\ d^{-1}$), ground heat flux (Q_G ; $W\ m^{-2}\ d^{-1}$), normalized sensible heat flux (Q_H/Q^*), normalized latent heat flux (Q_E/Q^*), normalized ground heat flux (Q_G/Q^*), and Bowen ratio ($\beta = Q_H/Q_E$) calculated over daytime observations from 10 days with solar insolation near theoretical values during July 2003.

Table 6-1. Urban canopy parameter values selected for Oklahoma City sensitivity analysis for low-intensity residential (LIR), high-intensity residential (HIR), and industrial/commercial (I/C) land use categories. Bold numbers indicate values used in the control model prediction.

Table 6-2. Descriptions of the parameter variations for each HRLDAS and WRF model predictions.

Table 6-3. Mean peak daytime (nighttime) differences in heat fluxes (W m^{-2}) between model runs varying urban parameters and the control run.

LIST OF FIGURES

- Figure 2.1.** Illustrations of various definitions of the urban surface: (a) complete, (b) ground level, (c) rooftop equivalent (“black box”), (d) bird’s-eye view, (e) “surface” (screen level) observed, and (f) zero-plane displacement (Voogt and Oke 1997).
- Figure 2.2.** The four attractors of urban form (Osmond 2004).
- Figure 2.3.** Simplified classification of the urban climate zones arranged in decreasing order of impact to local climate.
- Figure 2.4.** Definitions for local climate zones (Stewart and Oke 2012). Local climate zones 1-9 correspond to urban climate zones (Oke 2004).
- Figure 2.5.** Illustration of boundary layer structures over a city (Oke 1988).
- Figure 2.6.** Vertical cross-section of a typical urban heat island (Oke 1987).
- Figure 2.7.** Profiles of potential temperature illustrating the thermal structure of the UBL in a large city during the (a) day and (b) at night (Oke 1987).
- Figure 2.8.** Illustration of the urban heat island circulation during calm winds (Brown 2000).
- Figure 2.9.** Flow patterns around a sharp-edged building. Vertical cross-section of (a) streamlines (solid lines) and flow zones (dashed lines and letters). Plan view of streamlines around a building (b) normal and (c) diagonal to the flow (Oke 1987).
- Figure 2.10.** Flow patterns associated with different building density (Oke 1987).
- Figure 3.1.** Locations of the HOBO temperature data loggers deployed by Pacific Northwest National Laboratory (PNNL) during Joint Urban 2003.
- Figure 3.2.** Locations of the energy flux towers deployed by Arizona State University (ASU), Atmospheric Turbulence and Diffusion Division (ATDD), and Indiana University (IU) during Joint Urban 2003.
- Figure 3.3.** Location of energy tower deployed by Arizona State University (ASU) during Joint Urban 2003. Source of imagery: Google Imagery.
- Figure 3.4.** Locations of the (a) Gravel, (b) Grass, and (c) Concrete energy flux towers deployed by Atmospheric Turbulence and Diffusion Division (ATDD) during Joint Urban 2003. Source of imagery: Google Imagery.
- Figure 3.5.** Locations of energy flux towers deployed by Indiana University (IU) during Joint Urban 2003. Source of imagery: Google Imagery.

- Figure 3.6.** Current locations of the Oklahoma Mesonet sites. Mesonet sites are indicated by solid black circles. Urban areas are shaded in red.
- Figure 3.7.** Locations of the OASIS Super Sites in July 2003. Super Sites are indicated by solid black diamonds. Urban areas are shaded in red.
- Figure 3.8.** Average Krypton voltage (mV; black) and precipitation (mm; blue) at WASH from (a) 17 September 2002 through 5 July 2005, and (b) 1-31 July 2003.
- Figure 3.9.** Average Krypton voltage (mV; black) and precipitation (mm; blue) at NRMN from (a) 1 August 2002 through 26 April 2005, and (b) 1-31 July 2003.
- Figure 3.10.** Average Krypton voltage (mV; black) and precipitation (mm; blue) at MARE from (a) 1 June 1999 through 31 May 2005, and (b) 1-31 July 2003.
- Figure 3.11.** Times series of net radiation (W m^{-2} ; black), density-corrected sensible heat flux (W m^{-2} ; red), and precipitation (mm; blue) at MARE on (a) 17 October 2002 and (b) 13 May 2002.
- Figure 3.12.** Time series plots of net radiation (W m^{-2} ; black), logger-derived sensible heat flux (W m^{-2} ; light blue), density-corrected sensible heat flux (W m^{-2} ; red), precipitation (mm; blue), and relative humidity (%; green) at (a) the Idabel Super Site on 10 June 2003 and (b) Burneyville Super Site on 30 January 2003.
- Figure 4.1.** Schematic of the two-dimensional canyon used in the SLUCM (Loridan et al. 2010).
- Figure 5.1.** Locations of the HOBO temperature data loggers deployed by Pacific Northwest National Laboratory (PNNL) and the surrounding Oklahoma Mesonet sites during Joint Urban 2003.
- Figure 5.2.** The mean diurnal cycles of (a) urban air temperatures (red) and rural air temperatures (black) and (b) temperature differences between urban and rural locations from 10 days with solar insolation near theoretical values during July 2003.
- Figure 5.3.** Time series of fractional water index at 25 cm at NRMN (light blue), 60 cm at NRMN (dark blue), 25 cm at MARE (red), and 60 cm at MARE (dark red) for 1-30 July 2003.
- Figure 5.4.** The mean diurnal cycles of (a) downwelling shortwave radiation and (b) upwelling shortwave radiation at the NRMN, MARE, ASU, IU BH, IU

GR, IU TMA, IU TMB, IU WH, ATDD Gravel, and ATDD Concrete sites from 10 days with solar insolation near theoretical values during July 2003. The respective differences between urban (ASU, ATDD, IU) and rural (NRMN) mean diurnal cycles of (c) downwelling shortwave radiation and (d) upwelling shortwave radiation.

Figure 5.5. The mean diurnal cycles of (a) downwelling longwave radiation and (b) upwelling longwave radiation at the NRMN, MARE, and ASU sites from 10 days with solar insolation near theoretical values during July 2003. (c) The respective differences between urban (ASU) and rural (NRMN) mean diurnal cycles of upwelling longwave radiation.

Figure 5.6. (a) The mean diurnal cycles of net radiation at the NRMN, MARE, ASU, IU BH, IU GR, IU TMA, IU TMB, IU WH, ATDD Gravel, and ATDD Concrete sites from 10 days with solar insolation near theoretical values during July 2003. (b) The respective differences between urban (ASU, ATDD, IU) and rural (NRMN) mean diurnal cycles of net radiation.

Figure 5.7. The mean diurnal cycles of (a) sensible heat flux and (b) latent heat flux at the NRMN, MARE, ASU, IU BH, IU GR, IU TMA, IU TMB, IU WH, ATDD Gravel, and ATDD Concrete sites from 10 days with solar insolation near theoretical values during July 2003. The respective differences between urban (ASU, ATDD, IU) and rural (NRMN) mean diurnal cycles of (c) sensible heat flux and (d) latent heat flux.

Figure 5.8. (a) The mean diurnal cycles of ground heat flux at the NRMN, MARE, ASU, IU BH, IU GR, IU TMA, IU TMB, IU WH, ATDD Gravel, and ATDD Concrete sites from 10 days with solar insolation near theoretical values during July 2003. (b) The respective differences between urban (ASU, ATDD, IU) and rural (NRMN) mean diurnal cycles of storage heat flux.

Figure 5.9. The diurnal cycles of (a) the conductive heat flux at a fixed depth ($W m^{-2}$; green), energy stored in the layer above the heat flux plates ($W m^{-2}$; grey), and the surface storage heat flux ($W m^{-2}$; black); and (b) soil temperatures (K) under sod at 5 cm (black) and 10 cm (grey) at the NRMN site from 14 July 2003.

Figure 6.1. Locations of domains employed in the WRF and HRLDAS models.

Figure 6.2. Percent difference values of soil temperature (a) 0-10 cm, (b) 10-40 cm, (c) 40-100 cm, and (d) 100-200 cm soil temperature after no land surface spin-up relative to the control run.

Figure 6.3. Percent difference values of soil temperature for 0-10 cm (column 1), 10-40 cm (column 2), 40-100 cm (column 3), and 100-200 cm (column

4) after a cold start (row 1), 1-year spin-up (row 2), and 2-year spin-up (row 3) relative to the control run.

- Figure 6.4.** Diurnal cycles of net radiation, latent heat fluxes, sensible heat fluxes, and ground heat fluxes predicted by the WRF model using the YSU PBL scheme for 14-15 July 2003. Observational data from the ATDD Concrete site are shown for comparison.
- Figure 6.5.** Diurnal cycles of mean urban and rural air temperatures at 2 m predicted by the WRF model using the MYJ PBL scheme for 14-15 July 2003. Observational data from the PNNL HOBO and Mesonet sites are shown for comparison.
- Figure 6.6.** Diurnal cycles of mean urban and rural air temperatures at 2 m predicted by the WRF model using the YSU PBL scheme for 14-15 July 2003. Observational data from the PNNL HOBO and Mesonet sites are shown for comparison.
- Figure 6.7.** Diurnal cycles of mean UHI intensity at 2 m predicted by the WRF model using the MYJ and YSU PBL schemes for 14-15 July 2003. Observational data from the PNNL HOBO and Mesonet sites are shown for comparison.
- Figure 6.8.** Diurnal cycles of net radiation, latent heat fluxes, sensible heat fluxes, and ground heat fluxes predicted by the WRF model using the MYJ PBL scheme for 14-15 July 2003. Observational data from the ATDD Concrete site are shown for comparison.
- Figure 6.9.** Diurnal cycles of net radiation, latent heat fluxes, sensible heat fluxes, and ground heat fluxes predicted by the WRF model using the YSU PBL scheme for 14-15 July 2003. Observational data from the ATDD Concrete site are shown for comparison.
- Figure 6.10.** Diurnal cycles of net radiation, latent heat fluxes, sensible heat fluxes, and ground heat fluxes predicted by the WRF model using the YSU PBL scheme for 14-15 July 2003. Observational data from the ATDD Gravel site are shown for comparison.
- Figure 6.11.** Diurnal cycles of net radiation, latent heat fluxes, sensible heat fluxes, and ground heat fluxes predicted by the WRF model using the YSU PBL scheme for 14-15 July 2003. Observational data from the ASU site are shown for comparison.
- Figure 6.12.** Diurnal cycles of net radiation, latent heat fluxes, sensible heat fluxes, and ground heat fluxes predicted by the WRF model using the YSU PBL

scheme for 14-15 July 2003. Observational data from the IU GR, TMA, TMB, and WH sites are shown for comparison.

- Figure 6.13.** Diurnal cycles of net radiation, latent heat fluxes, sensible heat fluxes, and ground heat fluxes predicted by the WRF model using the YSU PBL scheme for 14-15 July 2003. Observational data from the NRMN site are shown for comparison.
- Figure 6.14.** Diurnal cycles of latent heat fluxes, sensible heat fluxes, and ground heat fluxes predicted by the HRLDAS model for 14-15 July 2003. Observational data from the ATDD Concrete site are shown for comparison.
- Figure 6.15.** Diurnal cycles of latent heat fluxes, sensible heat fluxes, and ground heat fluxes predicted by the HRLDAS model for 14-15 July 2003. Observational data from the ATDD Gravel site are shown for comparison.
- Figure 6.16.** Diurnal cycles of latent heat fluxes, sensible heat fluxes, and ground heat fluxes predicted by the HRLDAS model for 14-15 July 2003. Observational data from the IU GR, TMA, TMB, and WH sites are shown for comparison.
- Figure 6.17.** Diurnal cycles of latent heat fluxes, sensible heat fluxes, and ground heat fluxes predicted by the HRLDAS model for 14-15 July 2003. Observational data from the NRMN site are shown for comparison.
- Figure 6.18.** Diurnal cycles of mean urban skin temperatures predicted by the WRF model using the MYJ and YSU PBL schemes for 14-15 July 2003.
- Figure 6.19.** Diurnals cycle of mean urban skin temperatures and air temperatures at 2 m predicted by the WRF model using the YSU PBL scheme for 14-15 July 2003. Observational data from the PNNL HOBO and Mesonet sites are shown for comparison.

ABSTRACT

To date, much of the current understanding of the impacts of urban areas on atmospheric processes results from a number of field programs. Between 28 June and 31 July 2003, a vast array of instrument systems collected high-resolution observations of meteorological variables in and around Oklahoma City during Joint Urban 2003, the largest urban dispersion field experiment to date. The data collected from the field measurements, combined with data collected from existing atmospheric observing systems in central Oklahoma presented a unique opportunity to investigate the urban heat island of Oklahoma City.

As numerical weather prediction models continue to evolve toward finer grid spacing, it becomes increasingly important to properly represent urban effects in land surface, surface layer, and PBL schemes. Recent efforts have been undertaken to “urbanize” numerical weather prediction and climate models. One common approach is to couple an urban canopy model with a land surface model.

For this study, the single-layer urban canopy model in the High-Resolution Land Data Assimilation System (HRLDAS) and Advanced Research Weather Research and Forecasting (ARW-WRF) modeling systems were used to investigate the sensitivity of near-surface air temperatures and energy fluxes to urban canopy parameters in uncoupled (land) and coupled (land-atmosphere) predictions. The model results were compared with observations collected by the Oklahoma Mesonet and Joint Urban 2003 collaborators.

While the components of the surface energy balance were sensitive to albedo and thermal conductivity of the urban roof surface, and to the fraction of the grid cell that was impervious, near-surface air temperatures, particularly during the daytime, did not show significant variations with urban parameters. The sensitivity of near-surface temperatures to urban canopy parameters depended on the method used to calculate the skin temperature of the impervious surface.

1. INTRODUCTION

A recent study by the United Nations (2010) found that half of the world's population lives in cities and by 2050, that proportion is expected to increase to 69%. The land-use differences between the rural and urban areas, as well as increased atmospheric pollution, considerably impact the climate from local to regional scales. Further, urban-induced weather phenomena directly impact society through more intense heat waves, increased flooding, and reduced visibility, which in turn lead to more direct and indirect weather-related accidents and deaths as well as significant economic loss (Changnon 1992). Thus, weather and climate within urban environments significantly affect the majority of people worldwide through various mechanisms.

To date, much of the current understanding of the impacts of urban areas on atmospheric processes results from a number of field programs including those conducted in a number of North American cities: St. Louis (Changnon et al. 1971, 1976; Lowry 1974), Chicago (Changnon and Semonin 1978; Grimmond and Oke 1995), Los Angeles (Grimmond and Oke 1995), Vancouver (Steyn et al. 1997), Montreal (Mailhot et al. 1998), Mexico City (Doran et al. 1998), Tucson (Grimmond and Oke 1995), Salt Lake City (Allwine et al. 2002; Doran et al. 2002), and Phoenix (Grimmond and Oke 1995; Fast et al. 2000). Because of the complex atmospheric processes involved in urban areas, field experiments of this nature are critical to scientific advancements in this field of research.

During June and July 2003, the largest urban dispersion field experiment of its kind, Joint Urban 2003 (JU2003), was conducted in Oklahoma City (OKC). Between 28

June and 31 July 2003, a vast array of instrument systems installed specifically for JU2003 collected high-resolution observations of meteorological variables in and around OKC. The data collected from the field instrumentation, combined with data collected from existing atmospheric observing systems in central Oklahoma represent perhaps the largest conglomeration of instruments ever assembled to quantify the impact of urban areas on atmospheric process within the planetary boundary layer.

While observational studies have long shown that urban areas significantly impact local weather and climate, the prediction of urban effects is a major weakness of current land surface models (Sailor and Fan 2002; Best 2005; Jin et al. 2007). Most land surface schemes were developed for coarse-resolution global models in which urban effects were once thought to be negligible (Jin et al. 2007; Oleson et al. 2008). As a result, recent efforts have been made to “urbanize” numerical weather prediction and climate models (Masson 2006; Martilli 2007; National Research Council 2012). One common approach is to couple an urban canopy model with a land surface model (Masson 2000; Kusaka et al. 2001; Martilli et al. 2002; Wang et al. 2011a; Grimmond et al. 2010, 2011). The inclusion of urban meteorological processes and anthropogenic heat release within the land surface schemes of numerical weather prediction and regional climate models is vital for assessing potential impacts of extreme weather events and climate change in heavily populated areas (Betts and Best 2004).

The most documented urban-induced weather phenomenon is the urban heat island (UHI) effect whereby air temperature in the urban canopy is warmer compared to the rural surroundings (Landsberg 1981; Oke 1987; Arnfield 2003). The changes in the

surface energy balance combine to impact the development of the UHI, with some factors being more important according to the time of day. The validation of land surface schemes that predict the urban surface energy balance is often neglected or insufficient (Masson 2006). Urban surface schemes validated against in situ data are commonly compared to observations of air temperature, surface temperature, wind speed, wind direction, boundary layer height, and turbulence statistics (Taha 1999; Martilli et al. 2002; Dupont et al. 2004; Otte et al. 2004; Best 2005; Chin et al. 2005; Fan and Sailor 2005; Grossman-Clarke et al. 2005; Kondo et al. 2005; Holt and Pullen 2007; Lin et al. 2008; Miao et al. 2009; Salamanca et al. 2011; Zhang et al. 2011) as opposed to observations of the components of the surface energy balance (Masson et al. 2002; Lemonsu et al. 2004; Best et al. 2006; Dupont et al. 2006; Grimmond et al. 2010, 2011; Loridan et al. 2010). Validation with observations of surface variables, such as air temperature and humidity, does not demonstrate whether the energetic processes represented in the urban scheme are physically realistic (Masson et al. 2002; Samuelsson et al. 2003). In addition, validation activities for urban surface schemes typically occur after coupling with an atmospheric model (Martilli et al. 2002; Dupont et al. 2004; Otte et al. 2004; Best 2005; Chin et al. 2005; Fan and Sailor 2005; Grossman-Clarke et al. 2005; Kondo et al. 2005; Liu et al. 2006; Jin et al. 2007; Holt and Pullen 2007; Lin et al. 2008; Lemonsu et al. 2009; Miao et al. 2009; Salamanca et al. 2011; Zhang et al. 2011), which makes it difficult to distinguish the biases of the surface scheme from those of the atmospheric model. Further, model performance depends on whether it is executed in coupled or uncoupled mode due to feedback

mechanisms in coupled systems (Margulis and Entekhabi 2001; Samuelsson et al. 2003; Best et al. 2006). As a result, thorough validation of an urban surface scheme must include both uncoupled and coupled model predictions (Best et al. 2006), as well as observations of the components of the surface energy balance and surface variables.

This study seeks to answer the following scientific questions:

1. How does the partitioning of available energy into heat fluxes vary with land use and land cover types within and surrounding OKC?
2. What are the quantitative differences in the components of the surface energy balance and surface variables between the uncoupled and coupled model predictions using a single-layer urban canopy model over several land use and land cover types within and surrounding OKC?
3. What are the critical urban canopy parameters in a single-layer urban canopy model that define the urban surface for OKC?

Based on the research questions above, it is hypothesized that (1) the partitioning of available energy into heat fluxes, observed and modeled, throughout OKC is significantly different from that of rural Oklahoma, and (2) those differences and sensitivity to parameter values are less for coupled land-atmosphere model predictions than for uncoupled predictions. Observations of surface variables and the components of the surface energy balance are used to evaluate the performance of land surface processes in the numerical model predictions.

The first objective of this study is to quantify the spatial and temporal variability of the partitioning of available energy into heat fluxes over several land use and land cover types within and surrounding OKC. This objective is achieved by analyzing observations of 2-meter air temperature, net radiation, downwelling shortwave radiation, and latent, sensible, and ground heat fluxes collected throughout OKC during

the JU2003 field experiment and at the Norman and Marena Mesonet sites. This analysis serves as the foundation for the two subsequent objectives of the study.

The second objective of this study is to quantify the differences in the components of the surface energy balance between uncoupled (land) and coupled (land-atmosphere) predictions. This objective is achieved by using the High Resolution Land Data Assimilation System to execute predictions using the Noah land surface model coupled with a single-layer urban canopy model (Noah-SLUCM) with prescribed atmospheric conditions and no feedback processes between the land surface and the atmosphere. In addition, the Weather Research and Forecasting model is used to execute coupled predictions of the Noah-SLUCM with feedback processes between the land surface and the atmosphere.

The final objective of this study assesses the sensitivity of uncoupled and coupled predictions to determine the critical urban canopy parameters in the Noah-SLUCM that define the urban surface for OKC. This objective is accomplished by executing coupled and uncoupled predictions of the Noah-SLUCM using default parameter values, values more representative of the morphology of OKC, and some extreme parameter values.

To provide scientific background for this research, Chapter 2 summarizes how the impacts of the urban canopy on surface variables and the surface energy balance have been observed and modeled. Chapter 3 describes the data utilized in this study collected during JU2003 and from the Oklahoma Mesonet, while Chapter 4 describes the offline, online, and urban modeling systems. Chapter 5 describes the methodology

and results of the variability of the partitioning of available energy within and surrounding OKC. Chapter 6 describes the methodology and results of the validation of uncoupled and coupled model sensitivity tests to determine the importance of urban surface parameters in defining surface variables and the surface energy balance. A summary of important results and concluding remarks are presented in Chapter 7.

2. SCIENTIFIC BACKGROUND

2.1. THE URBAN CANOPY

Due to the patchy and heterogeneous nature of the urban environment, no single representative urban surface exists. However, several urban approximations are used to study the urban boundary layer (UBL) (Nunez and Oke 1977). One such urban unit is the urban street canyon, which consists of the walls, street, and other elements between two adjacent buildings (Nunez and Oke 1977). While the urban street canyon is an important and fundamental unit of urban meteorology, it is difficult to incorporate as a representation for an entire city.

Voogt and Oke (1997) presented six additional urban surface units: complete, ground level, rooftop equivalent, bird's-eye view, "surface" (screen level) observed, and zero-plane displacement (Fig. 2.1). Most of the urban surfaces defined by Voogt and Oke (1997) refer to the surface seen by particular meteorological sensors. For example, the "surface" (screen level) observed coincides with the measurement level of air temperature. Bird's-eye view corresponds to the surface seen by aircraft-based measurements from above the urban canopy. On the other hand, zero-plane displacement is a concept typically used for numerical simulations.

Oke (1987, 1988) suggested that the concept of a massless urban surface be replaced with an active near-surface volume with a top at or above roof-level. The use of the building-air volume simplified the surface radiation, energy, and water budgets and neglected the complex spatial arrangement of energy sources and sinks (Oke 1988).

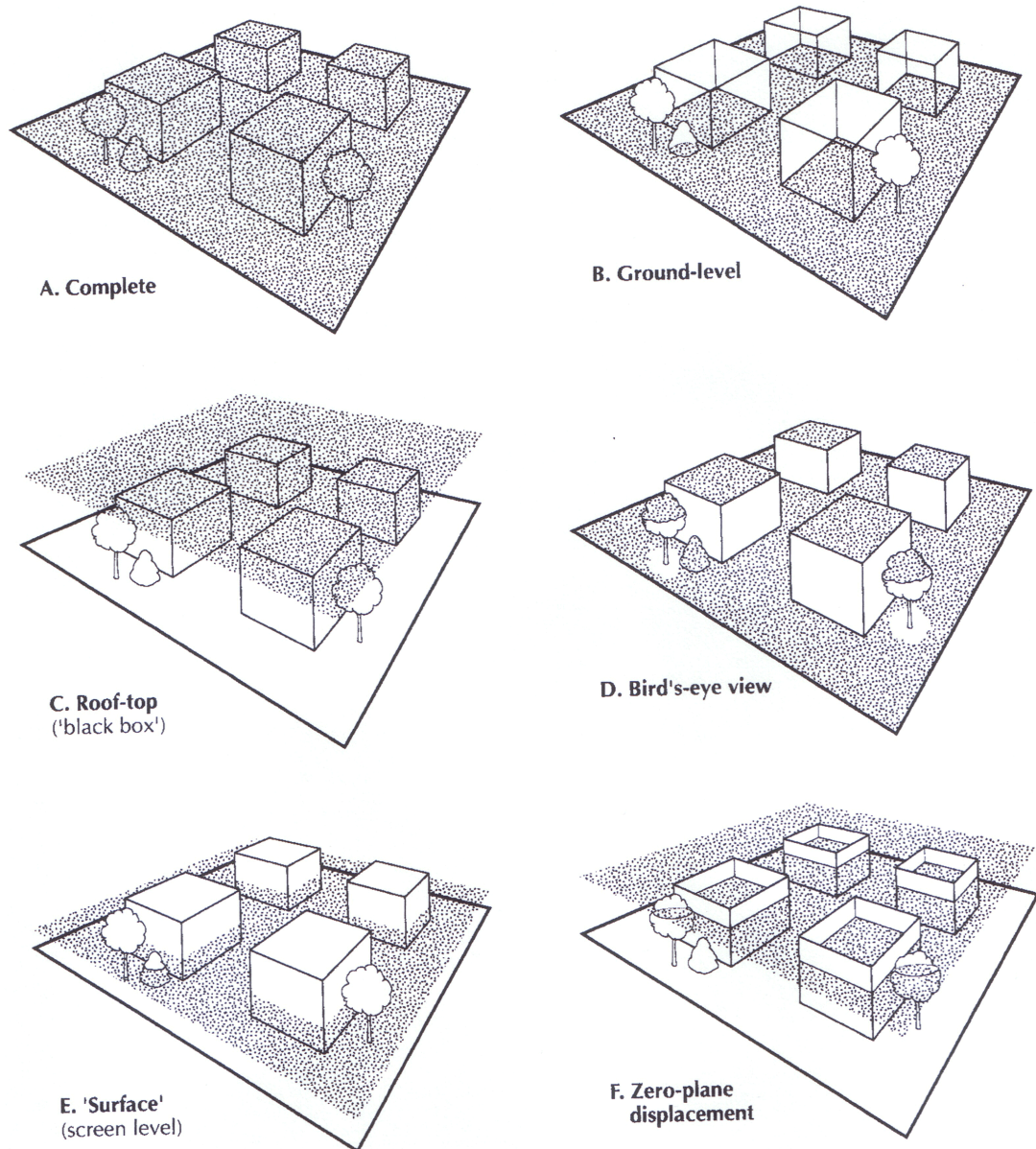


Figure 2.1. Illustrations of various definitions of the urban surface: (a) complete, (b) ground level, (c) rooftop equivalent (“black box”), (d) bird’s-eye view, (e) “surface” (screen level) observed, and (f) zero-plane displacement (Voogt and Oke 1997).

In addition, energy fluxes are restricted to those through the top of the building-air volume.

Urbanization radically changes the surface and atmospheric properties of a region (Oke 1987). Thermal, radiative, moisture, and aerodynamic characteristics of a

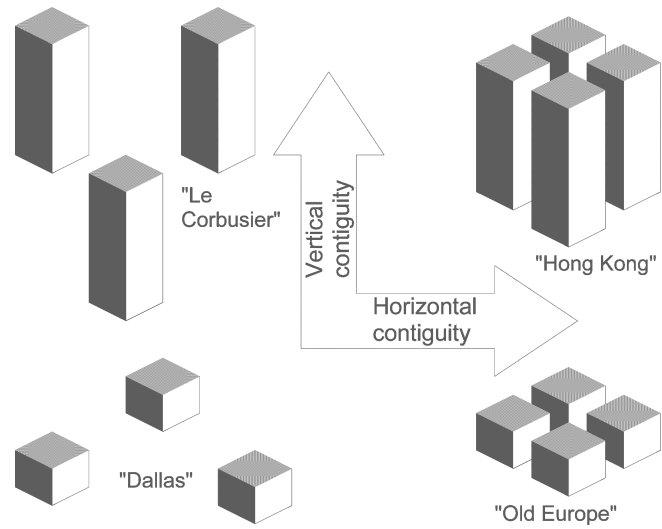


Figure 2.2. The four attractors of urban form (Osmond 2004).

region are modified by the urban landscape, which further impact the radiative, energy, momentum, and water balances. The overall magnitude of the impact urbanization on the boundary layer depends on building height and density, or urban form. Osmond (2004) identified four attractors of urban form: high density, high-rise (“Hong Kong”); low density, high-rise (“Le Corbusier”); high density, low-rise (“Old Europe”); and low density, low-rise (“Dallas”). These four urban forms are illustrated in Figure 2.2.

Oke (2004) developed districts of urban forms, called Urban Climate Zones (UCZs), based on their ability to modify the local climate (Fig. 2.3). Through use of aerial photographs, detailed maps, and satellite imagery, an urban area can be divided into several climate zones. This classification is particularly useful for siting instruments throughout an urban area and assessing the impact on the mesoscale environment. Stewart and Oke (2012) expanded the concept of the UCZ and introduced the local climate zone (LCZ) classification system to standardize urban heat island studies worldwide. The LCZs represent a composition of surface structure (tall, mid-,

Urban Climate Zone, UCZ ¹	Image	Roughness class ²	Aspect ratio ³	% Built (impermeable) ⁴
1. Intensely developed urban with detached close-set high-rise buildings with cladding, e.g. downtown towers		8	> 2	> 90
2. Intensely developed high density urban with 2 – 5 storey, attached or very close-set buildings often of brick or stone, e.g. old city core		7	1.0 – 2.5	> 85
3. Highly developed, medium density urban with row or detached but close-set houses, stores & apartments e.g. urban housing		7	0.5 – 1.5	70 - 85
4. Highly developed, low or medium density urban with large low buildings & paved parking, e.g. shopping mall, warehouses		5	0.05 – 0.2	70 - 95
5. Medium development, low density suburban with 1 or 2 storey houses, e.g. suburban housing		6	0.2 – 0.6, up to >1 with trees	35 - 65
6. Mixed use with large buildings in open landscape, e.g. institutions such as hospital, university, airport		5	0.1 – 0.5, depends on trees	< 40
7. Semi-rural development, scattered houses in natural or agricultural area, e.g. farms, estates		4	> 0.05, depends on trees	< 10

Key to image symbols: buildings; vegetation; impervious ground; pervious ground

Figure 2.3. Simplified classification of the urban climate zones arranged in decreasing order of impact to local climate. ¹A simplified set of classes plus physical measures relating to wind, thermal, and moisture controls. ²Effective terrain roughness. ³Aspect ratio ($\overline{z_H}/W$) is average height of the main roughness elements divided by average spacing. ⁴Average proportion of ground plan covered by built features (Oke 2004).

and low-rise buildings of varying densities) and land cover (trees, bushes, plants, paved, bare soil, and water) in varying amounts into 17 patterns (Stewart and Oke 2012; Fig. 2.4).

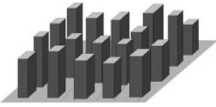
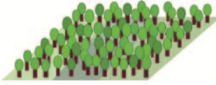



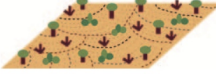



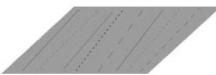


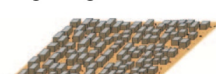




Built types	Definition	Land cover types	Definition
 <p>1. Compact high-rise</p>	Dense mix of tall buildings to tens of stories. Few or no trees. Land cover mostly paved. Concrete, steel, stone, and glass construction materials.	 <p>A. Dense trees</p>	Heavily wooded landscape of deciduous and/or evergreen trees. Land cover mostly pervious (low plants). Zone function is natural forest, tree cultivation, or urban park.
 <p>2. Compact midrise</p>	Dense mix of midrise buildings (3–9 stories). Few or no trees. Land cover mostly paved. Stone, brick, tile, and concrete construction materials.	 <p>B. Scattered trees</p>	Lightly wooded landscape of deciduous and/or evergreen trees. Land cover mostly pervious (low plants). Zone function is natural forest, tree cultivation, or urban park.
 <p>3. Compact low-rise</p>	Dense mix of low-rise buildings (1–3 stories). Few or no trees. Land cover mostly paved. Stone, brick, tile, and concrete construction materials.	 <p>C. Bush, scrub</p>	Open arrangement of bushes, shrubs, and short, woody trees. Land cover mostly pervious (bare soil or sand). Zone function is natural scrubland or agriculture.
 <p>4. Open high-rise</p>	Open arrangement of tall buildings to tens of stories. Abundance of pervious land cover (low plants, scattered trees). Concrete, steel, stone, and glass construction materials.	 <p>D. Low plants</p>	Featureless landscape of grass or herbaceous plants/crops. Few or no trees. Zone function is natural grassland, agriculture, or urban park.
 <p>5. Open midrise</p>	Open arrangement of midrise buildings (3–9 stories). Abundance of pervious land cover (low plants, scattered trees). Concrete, steel, stone, and glass construction materials.	 <p>E. Bare rock or paved</p>	Featureless landscape of rock or paved cover. Few or no trees or plants. Zone function is natural desert (rock) or urban transportation.
 <p>6. Open low-rise</p>	Open arrangement of low-rise buildings (1–3 stories). Abundance of pervious land cover (low plants, scattered trees). Wood, brick, stone, tile, and concrete construction materials.	 <p>F. Bare soil or sand</p>	Featureless landscape of soil or sand cover. Few or no trees or plants. Zone function is natural desert or agriculture.
 <p>7. Lightweight low-rise</p>	Dense mix of single-story buildings. Few or no trees. Land cover mostly hard-packed. Lightweight construction materials (e.g., wood, thatch, corrugated metal).	 <p>G. Water</p>	Large, open water bodies such as seas and lakes, or small bodies such as rivers, reservoirs, and lagoons.
 <p>8. Large low-rise</p>	Open arrangement of large low-rise buildings (1–3 stories). Few or no trees. Land cover mostly paved. Steel, concrete, metal, and stone construction materials.	VARIABLE LAND COVER PROPERTIES	
 <p>9. Sparsely built</p>	Sparse arrangement of small or medium-sized buildings in a natural setting. Abundance of pervious land cover (low plants, scattered trees).	<p><i>b. bare trees</i></p>	Leafless deciduous trees (e.g., winter). Increased sky view factor. Reduced albedo.
 <p>10. Heavy industry</p>	Low-rise and midrise industrial structures (towers, tanks, stacks). Few or no trees. Land cover mostly paved or hard-packed. Metal, steel, and concrete construction materials.	<p><i>s. snow cover</i></p>	Snow cover >10 cm in depth. Low admittance. High albedo.
		<p><i>d. dry ground</i></p>	Parched soil. Low admittance. Large Bowen ratio. Increased albedo.
		<p><i>w. wet ground</i></p>	Waterlogged soil. High admittance. Small Bowen ratio. Reduced albedo.

Figure 2.4. Definitions for local climate zones (Stewart and Oke 2012). Local climate zones 1-9 correspond to urban climate zones (Oke 2004).

Loridan and Grimmond (2012) proposed a method to classify urban environments that uses “active surface indices.” This approach derives active surface indices as ratios of the active (built and vegetated) surface covers to the total three-dimensional surface cover. Active surface ratios characterize the portion of the total surface actively involved in energy exchange with the atmosphere (Loridan and Grimmond 2012).

Additionally, several parameters are used to quantitatively describe the urban morphology of a city. The National Urban Database with Access Portal Tool (NUDAPT) is a database and decision support system that hosts high-resolution building data (e.g., size, shape, orientation, and relative location) and urban canopy parameter data (Table 2-1) for 33 cities in the United States, with varying degrees of coverage and completeness (Ching et al. 2009).

Some urban canopy parameters can include trees as roughness elements, depending on their relative aerodynamic importance. The inclusion of trees significantly decreases the spacing between roughness elements, thus impacting parameters based on element spacing. For example, Grimmond and Oke (1999a) found that the inclusion of trees can increase the height-to-width ratio and frontal area index.

2.2. STRUCTURE OF THE URBAN BOUNDARY LAYER

“Urban climate effects are ultimately due to differences of the budgets of energy, mass, and momentum between the city and its surrounding landscape” (Oke and McCaughey 1983). Thus, as the landscape transitions from rural to urban, the urban boundary layer (UBL), defined as the part of the planetary boundary layer (PBL) whose

Table 2-1. Urban canopy parameters commonly used to describe the urban morphology of an area. Unless otherwise noted, parameter descriptions and relevance are from Burian et al. (2005).

Parameter	Description	Relevance
Mean building height	The ratio of the sum of the building heights to the total number of buildings in the area	Depth through which the urban canopy directly impacts the atmosphere
Building plan area fraction	The ratio of the plan area of buildings to the total surface area of the study region	Related to the surface roughness, accounts for enhanced mixing and drag effects
Building plan area density	The average building plan area within a height increment divided by the volume of the height increment	How much of the air volume is occupied by buildings
Roof area density	The rooftop plan area per height increment divided by the volume of the height increment	Describes thermodynamics of the urban canopy
Building frontal area index	The ratio of the surface area of the roughness elements exposed to the mean wind to the plan area of the study site	Related to the surface roughness, accounts for enhanced mixing and drag effects
Frontal area density	The ratio of the surface area of the roughness elements exposed to the mean wind to the total land surface area (Raupach 1994)	Helps quantify the drag force as a function of height
Building surface-to-plan area ratio	The sum of building surface area divided by the total plan area	Important when evaluating the urban canopy energy budget in a city
Complete aspect ratio	The summed surface area of roughness elements and exposed ground divided by the total plan area (Voogt and Oke 1997)	Interpreting surface temperatures derived from remote sensing instruments; relative increase in the potential momentum sink (Grimmond and Oke 1999a)
Height-to-width ratio	The ratio of the height of buildings to the horizontal distance (or street width) between the buildings	Influences flow regime
Sky view factor	The solar radiation received by a planar surface divided by the radiation received from the entire hemispheric radiating environment (Watson and Johnson 1987)	Related to the trapping of longwave radiation

characteristics are impacted by the presence of the urban surface below (Arnfield 2003), develops (Fig. 2.5). The UBL extends from roof level to a height where the impacts of

the urban surface are no longer apparent (Oke 1988) and if the size of the urban area is sufficiently large, the UBL may include the entire depth of the PBL (Schmid et al. 1991).

The UBL includes the roughness layer, surface layer, and mixed layer (Fig. 2.5). The urban canopy layer is the layer from the ground to roof level where airflow and energy exchanges are dominated by microscale characteristics and processes (Oke 1988). The flow within the roughness layer is complex and strongly dependent on the individual trees and buildings. As such, the nature of the urban surface results in a roughness layer with a depth several times the average building height (Roth 2000). Monin-Obukhov Similarity Theory (MOST; Monin and Obukhov 1954) is not valid within the roughness layer and the turbulent fluxes are height-dependent. The surface layer, often referred to as the constant flux layer (Oke 1987), is the part of the PBL immediately above the surface where the vertical variation of turbulent fluxes is less than 10%. The mixed layer, which is driven by convection, is characterized by uniform mixing of heat, moisture, and momentum in the vertical profile (Stull 1988).

2.2.1. Urban Heat Island

The most notable impact of urbanization is the urban heat island (UHI) effect whereby air temperature in the urban canopy is warmer compared to the rural surroundings. The UHI refers to closed isotherms that separate the urban air temperature from the larger scale temperature field (Manley 1958) and the magnitude of the UHI varies in time, in space, and according to the synoptic conditions (Kim and Baik 2005; Fast et al. 2005). Further, the intensity of the UHI (i.e., the urban-rural difference in air

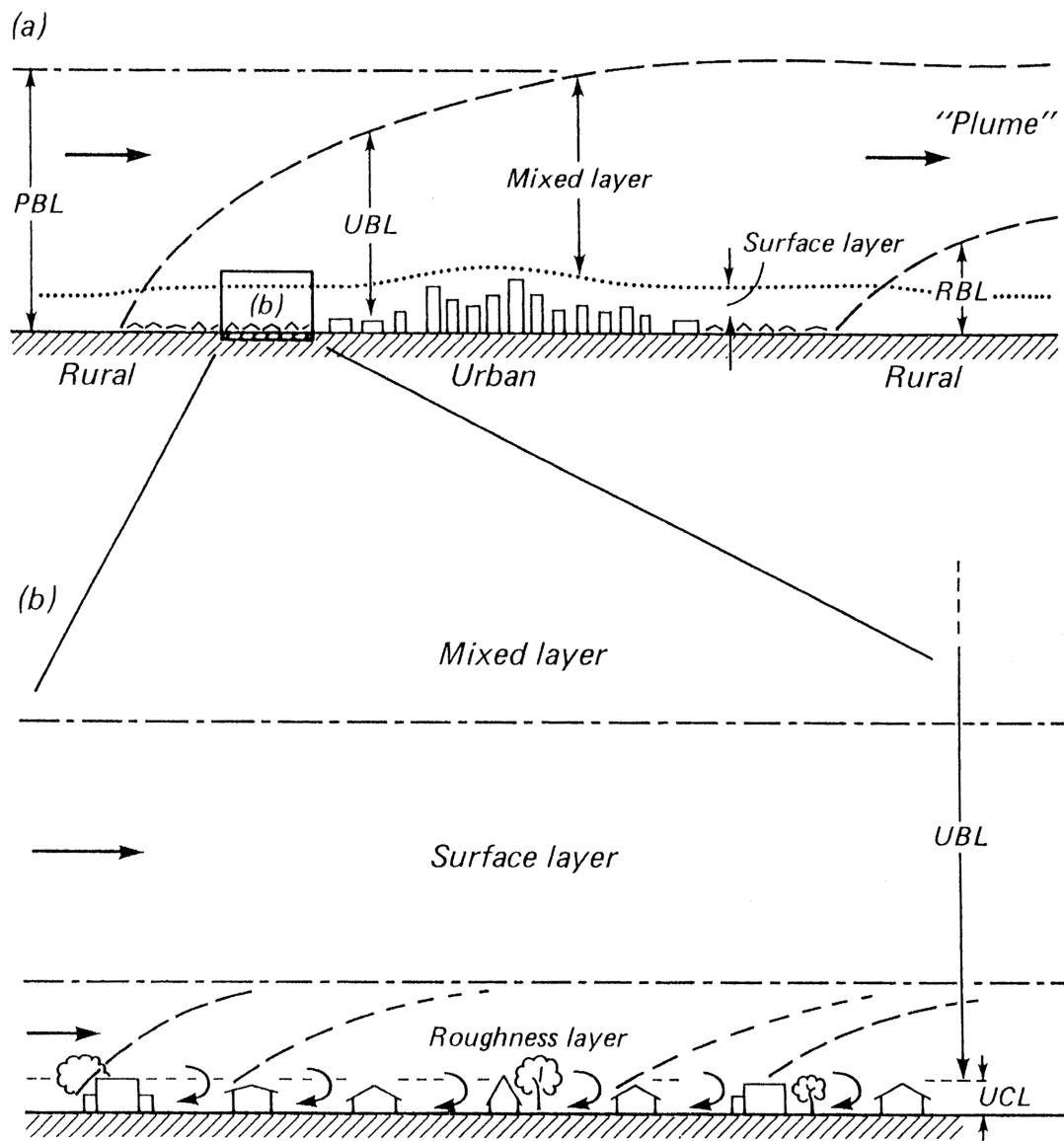


Figure 2.5. Illustration of boundary layer structures over a city (Oke 1988).

temperature) is largest during clear, calm conditions with horizontal gradients as large as $4^{\circ}\text{C km}^{-1}$ (Ackerman 1985; Oke 1987; Kim and Baik 2005). Conversely, the urban-rural differences are smallest during cloudy, windy conditions (Vukovich et al. 1976; Fast et al. 2005).

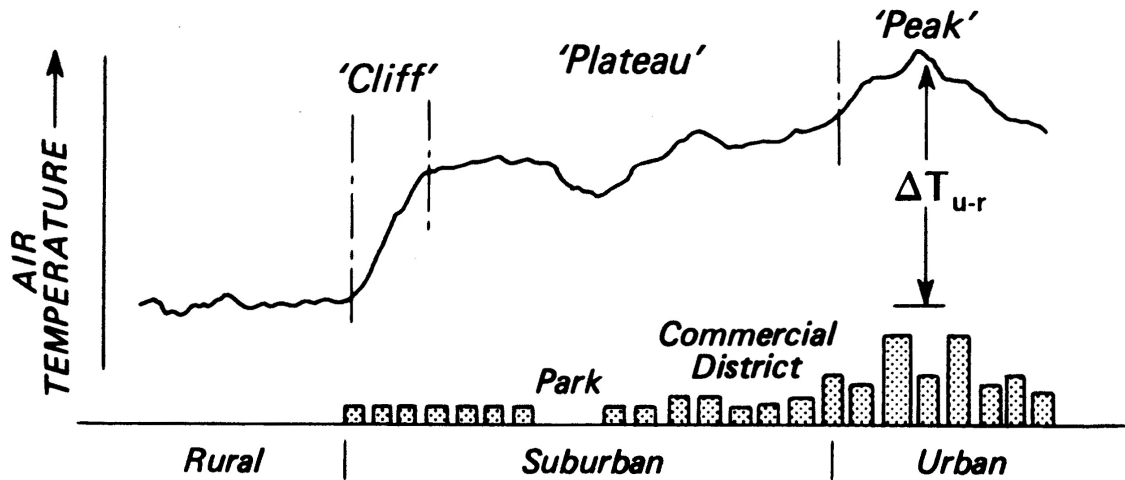


Figure 2.6. Vertical cross-section of a typical urban heat island (Oke 1987).

Figure 2.6 depicts a vertical cross-section of a typical urban heat island. The rural-urban boundary is characterized by a steep temperature gradient at the urban-rural interface and a weaker gradient towards the urban core (Oke 1987). Often, the urban temperature maximum is co-located with or slightly downwind of the urban core due to thermal advection.

The UHI intensity is often defined according to the availability of observations. For example, when a limited number of observation sites are present, the UHI intensity (ΔT_{u-r}) is often calculated as the difference between the background rural and maximum urban temperatures (Oke 1973). However, when numerous observation sites are available, UHI intensity can be calculated as the difference between mean urban and rural temperatures. Although the UHI is defined according to air temperature, recent studies have investigated the UHI based on remotely sensed land surface temperatures (Roth et al. 1989a; Epperson et al. 1995; Jin et al. 2005).

The values of ΔT_{u-r} vary across several time scales. After sunset, ΔT_{u-r} grows rapidly and reaches a maximum approximately three to five hours later (Ackerman 1985; Vukovich et al. 1979; Wanner and Hertig 1984; Kim and Baik 2005; Fast et al. 2005). Once at peak intensity, ΔT_{u-r} decreases slowly throughout the night, but may still be detectable at sunrise in large cities (Landsberg 1981). As a result, minimum temperature values in urban areas may be warmer than rural minimum temperatures (Cayan and Douglas 1984; Comrie 2000; Baker et al. 2002). After sunrise, ΔT_{u-r} rapidly decreases due to the slower warm-up of the urban area relative to rural areas as a result of the high heat capacity of urban materials, and ΔT_{u-r} may be negative at midday whereby the rural landscape is warmer than the urban core (Unwin 1980; Ackerman 1985; Wanner and Hertig 1984; Peterson 2003; Kim and Baik 2005).

On a weekly time scale, Kim and Baik (2005) detected a stronger UHI on weekdays than weekends due to heavy traffic and/or high commercial activities. UHI also varies with season, with the largest values of ΔT_{u-r} occurring during the summer (Wanner and Hertig 1984; Ackerman 1985). In addition, a second maximum in ΔT_{u-r} can be found during the winter as a result of the increased impacts of anthropogenic heating.

The magnitude of ΔT_{u-r} is primarily related to urban geometry, construction material, and the amount of anthropogenic heat flux released (Oke 1987). Urban geometry, in the form of building height and density, plays a significant role in (a) the trapping of radiation and (b) reducing wind speeds within the urban canopy layer. Further, building and traffic heat serve as anthropogenic heat sources while pollution

increases downward longwave radiation. Additionally, the construction materials of the urban canopy result in increased heat storage and decreased latent heat fluxes. The changes in the surface energy balance combine to impact the development of the UHI, with some factors being more important according to the time of day. Atkinson (2003) found differences in the causes of daytime and nighttime UHIs whereby, during the daytime, surface resistance to evaporation and roughness length were the most important factors in modeling ΔT_{u-r} (Atkinson 2003). Conversely, during the nighttime, Q_F was the greatest factor on the magnitude of ΔT_{u-r} . Furthermore, Atkinson (2003) determined that the size of the urban area had a minimal impact on the magnitude of ΔT_{u-r} .

The temporal and spatial variations of urban-rural humidity differences are smaller and more complex than those of temperature. For mid-latitude cities, the consensus is that urban canopy air is drier during the day and more humid during the night (Hage 1975; Changnon 1981; Hildebrand and Ackerman 1984; Oke 1987; Ackerman 1987). During the warm season, daytime humidity values are higher in rural areas due to evapotranspiration from the surface, with maximum mixing ratio values occurring at sunset (Hilberg 1978). The impermeable surfaces within the city convert precipitation into run-off rapidly via sewer systems, thus reducing surface evaporation. Further, urban areas have limited vegetation surfaces and larger roughness elements, which limit transpiration and enhance vertical mixing, respectively (Sisterson and Dirks 1978). While combustion, open water (pools, canals), and irrigation provide moisture to the atmosphere, the impacts are not enough to counteract the reduced evapotranspiration

due to vegetated surfaces being replaced with impervious surfaces (Brazel and Balling 1986). As a result of expanding impervious surfaces and rapid run-off, the UHI can be accompanied by a dry “island” (Hilberg 1978), even in arid climates (Brazel and Balling 1986).

Rural humidity decreases during the night due to depletion by dewfall and reaches a minimum at sunrise (Hilberg 1978). In the urban canopy at night, anthropogenic moisture, reduced dewfall, and stagnant airflow combine to maintain a more humid atmosphere and produce a moisture “island” similar to that of temperature (Oke 1987), with maximum humidity values occurring after midnight (Hilberg 1978). During the cold season, daytime humidity values can be higher in the city than in rural areas, especially when the ground is covered with snow or ice, vegetation is dormant, and anthropogenic fluxes of moisture are significant (Hage 1975; Oke 1987). If a daytime UHI is present, a portion of the urban-rural humidity difference is attributed to the increased air temperature (Landsberg and Maisel 1972). Spatial analyses of urban-rural humidity and temperature differences revealed that dry regions correlate well with the intensity of the UHI, with the driest areas characterized by little vegetation cover (Sisterson and Dirks 1978).

Figure 2.7 illustrates the overall thermal structure of the UBL during the day and night. During the day, the vertical influence of the urban canopy can extend up to 0.6 to 1.5 km as a result of mechanical and thermal convection from the rougher warmer city (Oke 1987). Conversely, the nocturnal UBL contracts to 0.1 to 0.3 km because an elevated nocturnal inversion suppresses vertical motion (Oke and East 1971; Tapper

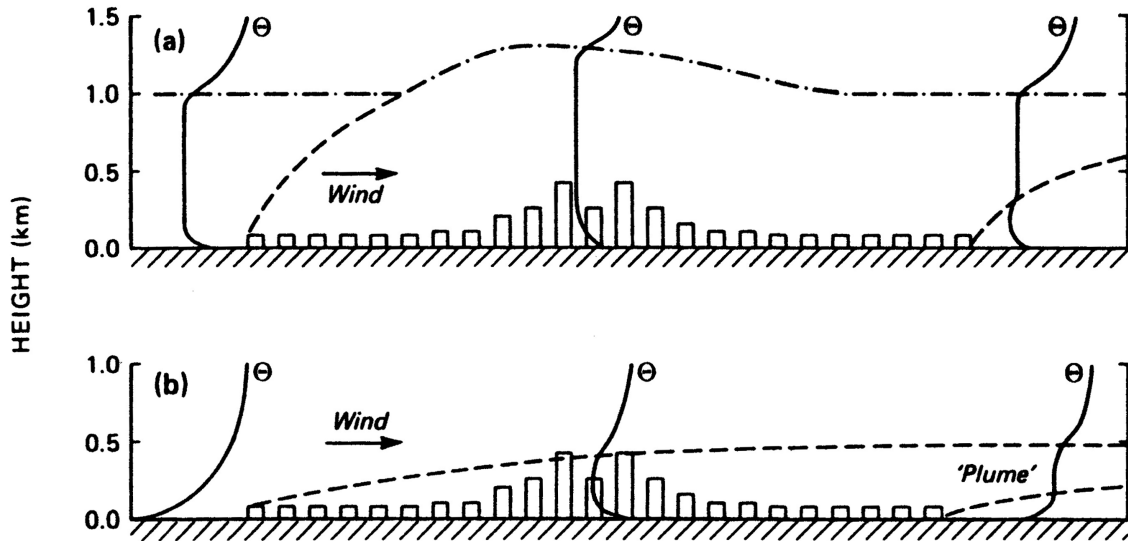


Figure 2.7. Profiles of potential temperature illustrating the thermal structure of the UBL in a large city during the (a) day and (b) at night (Oke 1987).

1990) while upwind of the city a ground-based inversion extends to a depth of approximately 600 m. At the urban-rural boundary, (a) the lowest layers are unstable, (b) the layers above are neutral or weakly stable up to approximately 300 m, and (c) above 300 m the profile resembles that of the rural atmosphere (Oke and East 1971). At the urban core, the UHI increases the depth of the UBL to approximately 300 m, which is isothermal and capped by the stable rural air above via an elevated nocturnal inversion (Bornstein 1968; Oke and East 1971; Shahgedanova et al. 1997). On some occasions, the air above the rural surface inversion is warmer than over the urban zone at the same height and is referred to as the crossover effect (Duckworth and Sandberg 1954; Bornstein 1968; Landsberg 1981). The depth of the UBL increases with height with downwind distance over the city (Clarke 1969). However, downwind of the urban core, a stable layer reforms at the surface due to radiational cooling. Subsequently, the warm urban air is advected over the rural stable layer and is often referred to as the

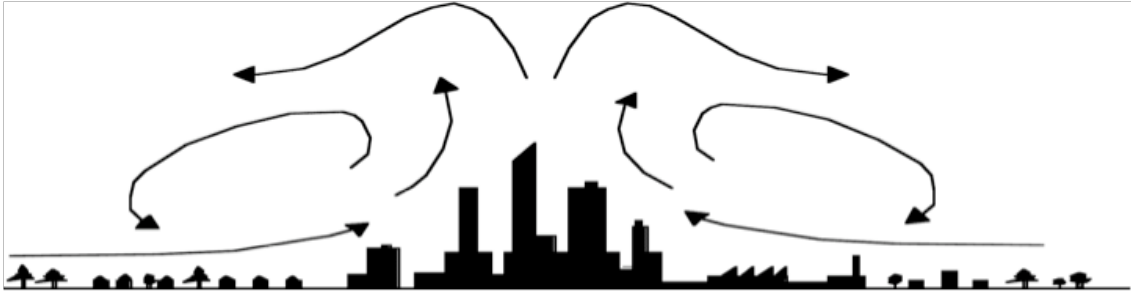


Figure 2.8. Illustration of the urban heat island circulation during calm winds (Brown 2000).

urban plume (Oke 1987). Because the UBL is well mixed during the day and night, strong diurnal variation in stability does not typically occur.

Limited information is available regarding the vertical profile of humidity in the UBL. Results from prior studies suggest that urban-rural differences may be detected up to 1 km over the city and in the downwind urban plume (Oke 1987).

In combination with the UHI, an urban-rural circulation pattern develops in which low-level air converges into the urban area from all directions (Fig. 2.8; Changnon et al. 1971; Shreffler 1979a, b; Landsberg 1981; Oke 1987; Eliasson and Holmer 1990). It was originally hypothesized that the strength of the UHI circulation was directly related to the strength of the UHI (Chandler 1965). However, Shreffler (1979a, b) demonstrated that stronger convergence occurs with weak UHIs during the daytime than with strong UHIs during the nighttime. Studies have also shown that atmospheric stability plays a key role in determining the strength of the UHI circulation (Vukovich and Dunn 1978; Draxler 1986). During the daytime, heating in the boundary layer is distributed through a much deeper layer than the nocturnal boundary layer, and as a result, a larger pressure perturbation and greater horizontal and vertical accelerations at the surface contribute to a more intense UHI circulation (Vukovich and

Dunn 1978). Thus, the UHI circulation is strongest in the early afternoon and weakens near sunset as the UHI strengthens (Shreffler 1979b; Landsberg 1981). Additionally, the rising motion due to the UHI and frictional effects can cause the UBL to “dome” over the city by approximately 250 m in the daytime (Oke 1987) while downwind of the city the airflow subsides over the rural land surface.

2.2.2. Surface Energy Balance

The surface energy balance (SEB) is a critical component of boundary layer meteorology and climatology because it provides the driving forces for the vertical fluxes of heat, mass, and momentum (Oke 1988). Several studies have demonstrated that urbanization drastically modifies the SEB of a city compared to that of rural areas (Yap and Oke 1974; White et al. 1978; Kalanda et al. 1980), which in turn impacts stability conditions within the boundary layer, thermodynamic properties, and mixing layer height.

To numerically simulate atmospheric processes in the UBL, it is critical to quantify how the SEB of an urban area is modified by the presence of the urban fabric. The energy balance of a building-air volume can be expressed as

$$Q^* + Q_F = Q_H + Q_E + \Delta Q_S + \Delta Q_A \quad (2.1)$$

where Q^* is net all-wave radiation flux; Q_F is the anthropogenic heat flux or heat flux due to combustion; Q_H is the sensible heat flux; Q_E is the latent heat flux; ΔQ_S are the heat storage changes in the ground, buildings, and air within the volume; and ΔQ_A is the advection of sensible and latent heat through the sides of the building-air volume (Oke 1987). Each component of the urban SEB is discussed in the following sections.

Shortwave Radiation

Net all-wave radiation (Q^*) is the most important energy exchange because it represents the limit to the available energy source or sink (Oke 1987). The Q^* can be expressed as

$$Q^* = K \downarrow - K \uparrow + L \downarrow - L \uparrow = K^* + L^* \quad (2.2)$$

where $K \downarrow$ is downwelling shortwave radiation flux, $K \uparrow$ is upwelling shortwave radiation flux, $L \downarrow$ is downwelling longwave radiation flux, $L \uparrow$ is upwelling longwave radiation flux, K^* is net shortwave radiation flux, and L^* is net longwave radiation flux. As defined, Q^* is positive when the surface gains energy and negative when the surface loses energy.

In 1970, the consensus was that the average city received 15 to 20% less $K \downarrow$ than unpolluted rural areas (Landsberg 1970; Oke 1988). This estimate remains consistent for industrial cities where coal-burning or industrial processing is prevalent (Oke 1988). However, legislation such as the Clean Air Act has resulted in decreased pollution levels over many U.S. cities (Peterson and Stoffel 1980). As a result, more recent studies estimated that urban sites received 2-10% less $K \downarrow$ than rural sites (Bergstrom and Peterson 1977; White et al. 1978; Oke and McCaughey 1983; Oke 1988; Christen and Vogt 2004). When analyzed by season, radiative depletion by aerosols was greater during the winter than summer due in part to a greater solar path length in winter, which causes an effective increase in optical depth (Changnon et al. 1971; Peterson and Stoffel 1980).

When K_{\downarrow} was dissected into its direct and diffuse components, studies showed that direct K_{\downarrow} was less at urban sites (Estournel et al. 1983) but may be recovered at the surface as diffuse K_{\downarrow} (Sprigg and Reifsnyder 1972; Wesely and Lipschutz 1976). Furthermore, when wind direction was taken into account, Peterson and Stoffel (1980) found that suburban and rural sites experienced decreased values of K_{\downarrow} due to the advection of pollutants from the urban center.

Urban areas also decrease the surface albedo, which decreases K_{\uparrow} . Several aspects of the urban canopy contribute to a decreased albedo for urban areas. For example, as building height and density increases, urban street canyons capture more solar radiation due to multiple reflections from the canyon walls (Aida 1982; Aida and Gotoh 1982; Brest 1987; Oke 1988; Arnfield 1988; Christen and Vogt 2004). As such, albedo decreases. Additionally materials such as asphalt for roads and tar on roofs have lower values of albedo than rural surfaces (Oke 1988). Albedo is also impacted by the presence or absence of vegetation. White et al. (1978) and Brest (1987) found that suburban land use had an albedo similar to that of rural land use due to the amount of plant cover. The presence of snow during winter months can result in large differences between urban and rural values of albedo. The urban albedo is significantly lower in the presence of snow than rural areas due to several factors: snow removal, soiling of snow by cars and pollution, snow-free vertical walls, and faster snow melt within the city (Brest 1987; Oke 1987, 1988; Christen and Vogt 2004).

Suggested values of albedo for urban and suburban land use are 0.14 and 0.15 respectively (Oke 1988). However, observed values of mean albedo for urban centers

are as low as 0.08 to 0.10 compared to values of approximately 0.20 for rural areas (Offerle et al. 2003; Christen and Vogt 2004; Lemonsu et al. 2004). Further, albedo of the urban canopy does display a diurnal variation whereby values reach a minimum at solar noon and increase with increasing solar zenith angle. As a result, a diurnal variation of albedo of 3 to 4% (Aida 1982) is possible.

Because aerosols decrease K_{\downarrow} and albedo differences decrease K_{\uparrow} , the urban-rural differences in K^* are not large. However, the balance or imbalance of these effects varies with urban geometry and construction material. Thus, some urban-rural differences in K^* are significant and dependent upon location (Christen and Vogt 2004).

Longwave Radiation

Urbanization alters the infrared radiative properties of the surface and the atmosphere (Oke 1988). For example, observations demonstrate that urban pollution enhances L_{\downarrow} at the surface, with urban-rural differences peaking between 2 and 25% on clear nights (Oke and Fuggle 1972; Aida and Yaji 1979; Estournel et al. 1983; Nunez et al. 2000). At the same time, Christen and Vogt (2004) found that urban values of L_{\downarrow} were lower than rural values during the day due to drier air within the UBL. Thus, because L_{\downarrow} is affected by UBL temperature, humidity, and aerosol composition and concentration, daytime trends in the urban-rural differences of L_{\downarrow} can vary.

The infrared radiative properties of the land surface are altered by large differences between urban-rural surface characteristics. As such, the surface temperature of urban areas tends to be greater than rural zones (Christen and Vogt 2004). For example, satellite and in situ measurements have shown that urban surface temperatures

are 1 to 5°C higher than those over croplands (White et al. 1978; Jin et al. 2005). In addition, peak surface heating within urban areas occurs approximately one hour after solar noon, with residential land use having lower surface temperatures than industrial or commercial land use (White et al. 1978). As a result of the increased thermal capacity of urban areas, more $L\uparrow$ is emitted from urban surfaces than rural. Urban-rural differences in $L\downarrow$ are strongest in the evening and decrease throughout the night due to radiation trapping within urban street canyons.

Net Radiation

Overall, the attenuation of $K\downarrow$ by aerosols in urban areas tends to be offset by the enhancement of $L\downarrow$. Similarly, the reduction in $K\uparrow$ due to decreased albedo is generally offset by the increase in $L\uparrow$. The net outcome results in only slight differences in Q^* received over urban, suburban, and rural surfaces (Peterson and Stoffel 1980; Oke and Fuggle 1972; White et al. 1978; Kalanda et al. 1980; Oke and McCaughey 1983; Cleugh and Oke 1986; Oke 1988; Christen and Vogt 2004).

Anthropogenic heat flux

Anthropogenic heat flux (Q_F) is defined as the release of heat due to the combustion of fuels and electric heating (Oke 1988). The average Q_F depends on the average energy use by individuals as well as the population density of a city. As a result, the largest values of Q_F are often found in the urban core of cities with cold climates (Klyzik 1996). Due to the dependence on human activity, Q_F often exhibits diurnal, weekly, and annual patterns, with peak periods in the morning and evening of weekdays and during winter.

Because Q_F is difficult to measure, it is often omitted from the observed SEB with the assumption that it is embedded within the other energy fluxes (Oke and Cleugh 1987; Grimmond and Oke 2002). However, in energy balance studies, it is important to assess the spatial and temporal variability of Q_F to determine the significance of its role in boundary layer processes. For example, heat added to the atmosphere from traffic and subway vents primarily impacts the UCL, whereas heat injected from smoke stacks and chimneys impacts the UBL (Oke 1988). Thus, Q_F must be simulated using models or inventory methods based on traffic and energy consumption (Grimmond 1988; Schmid et al. 1991; Sailor and Lu 2004) or measurements of the components of the SEB (Pigeon et al. 2003; Offerle et al. 2005).

Storage heat flux

Storage heat flux (ΔQ_S) is defined as the total heat uptake or release from the urban system and includes sensible and latent heat changes in the air, buildings, vegetation, and ground extending from above roof-level to a depth in the ground where net heat exchange over the period of study is negligible (Oke and Cleugh 1987). Because the thermal conductivity of most building materials is higher and the heat capacity is lower than those of rural soils (Landsberg 1981; Oke and Cleugh 1987; Oke 1988), ΔQ_S of urban areas is large in comparison with the ground heat flux at the surface (Q_G) measured in rural areas. As such, ΔQ_S is considered to be a key factor in the formation of the urban heat island (UHI).

Measurements of Q_G obtained with soil heat flux plates are calculated by two components: 1) the measured flux at a fixed depth (Q_{Gfixed}) and 2) the energy stored in the layer above the heat flux plates:

$$Q_G = Q_{Gfixed} + \frac{\Delta T_{soil} C_{soil} d}{t} \quad (2.3)$$

where ΔT_{soil} is the change in soil temperature over the observation interval (t), C_{soil} is the specific heat of the soil, and d is the fixed depth at which Q_{Gfixed} is measured. The specific heat of the soil is given by

$$C_{soil} = \rho_b (C_d + \Theta_m C_w) = \rho_b C_d + \Theta_v \rho_w C_w \quad (2.4)$$

$$\Theta_m = \frac{\rho_w}{\rho_b} \Theta_v$$

where ρ_b is the bulk density, ρ_w is the density of water, C_d is the heat capacity of the dry soil, Θ_m is soil water content by mass, Θ_v is soil water content by volume, and C_w is the specific heat of water. This calculation requires site-specific values of bulk density, soil water content by mass, soil water content by volume, and specific heat of dry soil. The volumetric soil water content is typically measured with a collocated water content reflectometer. Bulk density and soil water content by mass are commonly determined by sampling.

In contrast to rural surfaces, ΔQ_S in the urban environment cannot be measured directly due to the large number of surface types, orientations, and interactions within the urban canopy (Oke and McCaughey 1983; Oke 1988; Christen and Vogt 2004). Doll et al. (1985) illustrated the limitations of measuring ΔQ_S in the urban canopy. Thermistors were embedded in soil, concrete, and blacktop at various depths. Results demonstrated that diurnal variation of soil was very different from that of concrete and

blacktop. In addition, the diurnal amplitude and peak values for soil were significantly less than that of concrete and blacktop (Doll et al. 1985). Further, the peak in ΔQ_S for the urban surfaces occurred two hours earlier than the peak for soil. Even so, these measurements were for flat horizontal surfaces and do not include many of construction materials within the urban canopy.

As a result of measurement limitations, ΔQ_S is commonly estimated as the residual of the SEB from direct observations of Q^* , Q_H , and Q_E (Ching et al. 1983; Oke and Cleugh 1987; Grimmond and Oke 1995; Christen and Vogt 2004; Moriwaki and Kanda 2004; Pearlmutter et al. 2005). The main disadvantage to estimating ΔQ_S as the residual of the SEB is the accumulation of measurement errors of each component in ΔQ_S . Errors in the SEB components include standard measurement error in addition to the spatial variability of the SEB in the urban environment. Given that ΔQ_S during the daytime is small relative to the other components of the SEB, the uncertainty is large as a result of the systematic underestimation of the turbulent fluxes by eddy correlation systems or lack of closure of the SEB (Brotzge 2000; Wilson et al. 2002).

One alternative to estimating ΔQ_S as the SEB residual is to use a parameterization. Offerle et al. (2005) proposed a method to parameterize ΔQ_S in terms of element surface temperature observations. However, the most common method is to parameterize ΔQ_S in terms of Q^* (Oke et al. 1981; Camuffo and Bernardi 1982; Doll et al. 1985; Oke and Cleugh 1987; Grimmond et al. 1991). Oke and Cleugh (1987) compared ΔQ_S estimated as the residual of the SEB with parameterized values using the methods of Oke et al. (1981) and Doll et al. (1985) and found the residual values to be

reasonable and consistent. However, the hourly variation of ΔQ_S as the SEB residual, displayed a hysteresis effect whereby the peak value occurred one to two hours before the peak value of Q^* . Such a phase difference in peak values was not found in the parameterized values (Oke and Cleugh 1987). As such, if a parameterization is used to estimate ΔQ_S the hysteresis must be accounted for (Oke and Cleugh 1987; Grimmond et al. 1991; Roth and Oke 1994). For example, Grimmond and Oke (1999b) proposed:

$$\Delta Q_S = a_1 Q^* + a_2 \frac{\partial Q^*}{\partial t} + a_3 \quad (2.5)$$

where t is time, a_1 indicates the strength of the dependence of ΔQ_S on Q^* , a_2 describes the degree and direction of the phase difference between ΔQ_S and Q^* , and a_3 indicates the relative timing when ΔQ_S and Q^* become negative. Moriwaki and Kanda (2004) discovered a potential downside of a hysteresis-type parameterization. Upon analysis of ΔQ_S estimated as the residual of the SEB, they found that ΔQ_S in the daytime was approximately the same for summer as winter; the result contrasts with models that assume ΔQ_S is a function of Q^* . Generally, the ratio $\Delta Q_S/Q^*$ is larger in winter than in summer. Moriwaki and Kanda (2004) determined that the three-dimensional orientations of the urban surfaces readily absorbed radiation even when the sun was at a lower angle. Thus, the vertical walls in the urban canopy can efficiently absorb the radiative energy in the winter even though the solar azimuth angle is relatively low.

Urban-rural comparisons have revealed that ΔQ_S values at urban sites were significantly higher than at rural sites (Christen and Vogt 2004; Offerle et al. 2006a). Because, the urban canopy represents a much larger three-dimensional surface than rural areas, the urban environment can store more heat than the rural surface. For

example, as the day progresses, building surfaces that were previously shaded become illuminated as the sun angle decreases. Thus, the vertical structures become an efficient heat sink when horizontal surfaces are already in equilibrium (Christen and Vogt 2004). As a result, the daytime ΔQ_S into buildings is counterbalanced by nocturnal release of ΔQ_S in the form of $L\uparrow$, Q_H , and Q_E . This nocturnal release reaches a maximum one to two hours after sunset and decreases throughout the night. Schmid et al. (1991) showed little spatial variation in ΔQ_S within the urban zone. On the other hand, Pearlmutter et al. (2005) found that during the summer as building density increases, so does the amount of heat stored in the urban fabric.

Turbulent heat fluxes

The general focus of the urban SEB is on the magnitude, sign, temporal variability, and spatial variability of turbulent latent (Q_E) and sensible (Q_H) heat fluxes (Kalanda et al. 1980). Often it is assumed that Q_E is significantly lower in urban areas than in rural areas due to the abundance of impervious construction materials and sparse vegetation (Peterson 1969; Christen and Vogt 2004). However, SEB studies have illustrated that urban and suburban areas can have significant Q_E (Oke 1979; Suckling 1980; Kalanda et al. 1980; Oke and McCaughey 1983; Cleugh and Oke 1986; Oke 1988; Grimmond and Oke 1995; Spronken-Smith et al. 2000; Moriwaki and Kanda 2004; Grimmond et al. 2004a; Offerle et al. 2006a).

Due to reduced water availability, Q_H is the most significant heat flux in the urban environment (Nunez and Oke 1977; Cleugh and Oke 1986; Grimmond and Oke 1995; Christen and Vogt 2004; Pearlmutter et al. 2005). Urban-rural comparisons

revealed that urban daytime values of Q_H are typically twice as large as rural values (Hildebrand and Ackerman 1984; Christen and Vogt 2004). Relative to Q^* , Q_H accounts for approximately 50 to 95% of available energy in the urban core, 35 to 50% in suburban neighborhoods, and 30% or less in rural areas during the summer (Grimmond et al. 2004a; Christen and Vogt 2004; Offerle et al. 2006a). However, during the winter these values can approach 130 to 140% due to the contribution by Q_F (Offerle et al. 2006b).

Overall, the diurnal cycle of Q_H resembles Q^* early in the day but typically peaks one to two hours later than Q^* ; this trend varies with each city (Grimmond and Oke 1995). Further, Q_H retains a tail of relatively high values into the late afternoon and remains positive after Q^* becomes negative in the evening due to the heat storage (ΔQ_S) which is similar to desert-like environments (Yap and Oke 1974; Kalanda et al. 1980; Oke 1988; Grimmond and Oke 1995; Grimmond et al. 2004a; Offerle et al. 2006b). Unlike rural and suburban surfaces, often Q_H remains positive, or directed away from the surface, throughout the night. As a result, the UBL is often near neutral or unstable (Yap and Oke 1974; Kalanda et al. 1980; Oke 1988; Christen and Vogt 2004; Grimmond et al. 2004a) and the positive Q_H values are considered a significant contributor to the development of the UHI (Yap and Oke 1974).

The lack of vegetation in urban areas can result in seasonal changes in Q_H that are minimal when compared to rural seasonal trends (Offerle et al. 2006b). However, due to the impact of Q_F , observations of Q_H in winter can be greater than other periods of the year (Offerle et al. 2006b).

Recent work has revealed that urban-rural trends in Q_E are more complicated than once thought. Typically, the Q_E values measured in urban areas are relatively small due to small fractions of vegetation cover, limited open water in the upstream fetch of the instruments, and enhanced run-off reducing the availability of surface water (Christen and Vogt 2004; Grimmond et al. 2004a). However, Q_E is not negligible. Sources of Q_E in urban and suburban areas include dewfall, irrigation (lawns, gardens, golf courses, and cemeteries), open water (lakes, swimming pools, and ponds), street cleaning, and leakage from water mains and sewers tapped by deep-rooting trees (Kalanda et al. 1980; Oke and McCaughey 1983; Grimmond et al. 2004a). In addition, Moriwaki and Kanda (2004) found that urban construction materials, such as concrete and asphalt, can absorb water and serve as a significant source of Q_E .

During daytime, Q_E is approximately 20% of Q^* in the urban core, 30% in suburban neighborhoods, and 60% in rural areas (Christen and Vogt 2004). However, practices such as irrigation in suburban neighborhoods, have a significant impact on Q_E . Kalanda et al. (1980) found that even under mild drought conditions, much of the available energy in the suburban area was partitioned into Q_E due to lawn irrigation. Furthermore, a downward flux or horizontal advection of Q_H can enhance evaporation and result in an oasis effect whereby the hourly and daily values of Q_E exceed Q^* (Oke 1979; Suckling 1980; Oke and McCaughey 1983; Cleugh and Oke 1986). The oasis effect occurs when warm dry air, likely heated by pavement and buildings, is advected across an irrigated lawn or garden. A large moisture gradient develops and creates a high potential for evaporation. In addition to suburban neighborhoods, the oasis effect

can be observed in urban parks. Spronken-Smith et al. (2000) observed that a wet park evaporated three times more water than the surrounding residential neighborhood, and 1.3 to 1.4 times more than an irrigated rural sod farm.

Sparse or patchy urban vegetation can impact Q_E because it transpires at a higher rate than a completely vegetated surface. For example, the radiation and turbulence around an isolated tree increases Q_E at the leaf surface over most of the tree versus a tree where radiation and turbulence affect evaporation mainly at the upper part of the tree within a homogeneous forest (i.e., increased surface area available for Q_E ; Moriwaki and Kanda 2004). Unfortunately, numerical models assume that all vegetation has the same evaporation rate as that of a homogeneous forest. As a result, evaporation rates for vegetated fractions in urban areas may be significantly underestimated (Moriwaki and Kanda 2004; Offerle et al. 2006a).

Q_E is also an important energy sink during the morning hours as water from irrigation and dewfall are evaporated. Once the water sources are exhausted, Q_H becomes dominant and remains so throughout the day (Oke and Cleugh 1986). However, a secondary peak in Q_E may occur in the evening due to lawn irrigation (Grimmond and Oke 1995). Further, the amount of vegetation cover exerts some control over the diurnal cycle of Q_E . At heavily built sites, Q_H and Q_E increase simultaneously, whereas at vegetated sites, Q_H lags Q_E (Offerle et al. 2006a). During the nighttime, Q_E is often away from the surface (Kalanda et al. 1980; Christen and Vogt 2004; Offerle et al. 2006a). Despite the day-to-day variability of fluxes, many cities display similarities in the timing of peaks and changes in sign of the fluxes (Grimmond and Oke 1995).

Advection of turbulent fluxes

Direct measurement of the advection of latent and sensible heat through the sides of the building-air volume (ΔQ_A) is very difficult over a complex surface such as the urban canopy. However, past studies at the street canyon-scale demonstrated that ΔQ_A depends on the wind speed and amount of energy available to the canyon system (Nunez and Oke 1977). Because of the difficulty associated with obtaining measurements of ΔQ_A , most measurement programs assume advective influences are negligible (Oke 1988). However, horizontal variations in Q_H and Q_E in the presence of a mean flow induce advection (Schmid et al. 1999). As such, ΔQ_A can be estimated from the spatial analysis of the variability of Q_H and Q_E .

Ching et al. (1983) determined that the magnitude and impact of thermal advection is important and can dominate the variability in Q_H and Q_E observed in an urban area. Because land use exerts significant control on Q_H and Q_E , large differences in the heat fluxes were found over different land use types for different seasons (Ching et al. 1983).

2.2.3. Aerodynamic Structure

Buildings obstruct the wind and induce significant changes in airflow. If an isolated building is oriented normal to the wind, air is deflected over the top, down the front, or around the sides of the building and produces lee eddies (Fig. 2.9). The bulk of the flow is displaced over the building, which results in increased wind speeds in the displacement zone, labeled B in Figure 2.9a. After passing over the building, the air decelerates and cannot immediately fill the increased volume downwind of the building,

thus the flow separates and becomes more turbulent in the wake zone (D, Fig. 2.9a). The cavity zone (C, Fig. 2.9a), immediately behind the building, is characterized by low pressure which produces lee eddies or vortices. The isolated building impacts the flow at least three times the building height vertically, three times the building height upstream of the building, and 5 to 10 times the building height in the horizontal distance downstream of the building (Oke 1987).

The flow pattern of an urban area can be thought of as the combined effects of many individual buildings, which depends significantly on the building density. If the distance between buildings is relatively large, the flow patterns are similar to those of isolated buildings (Fig. 2.10a). When more closely spaced, the lee vortex of each

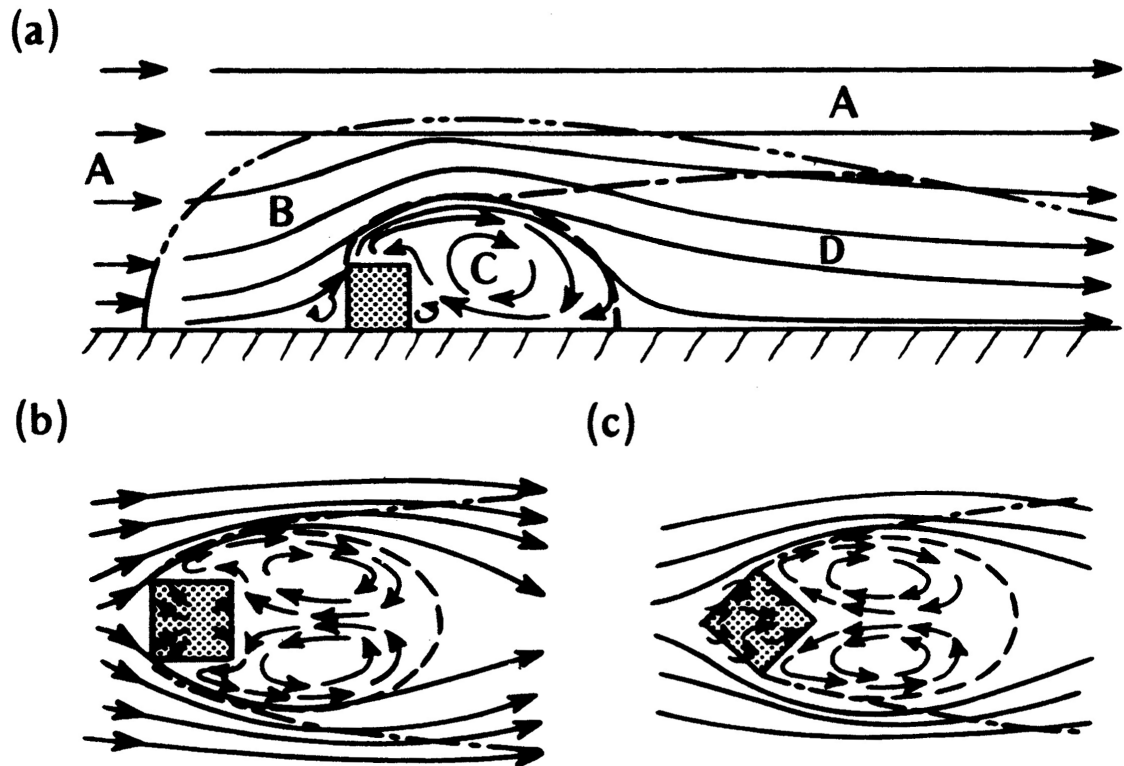
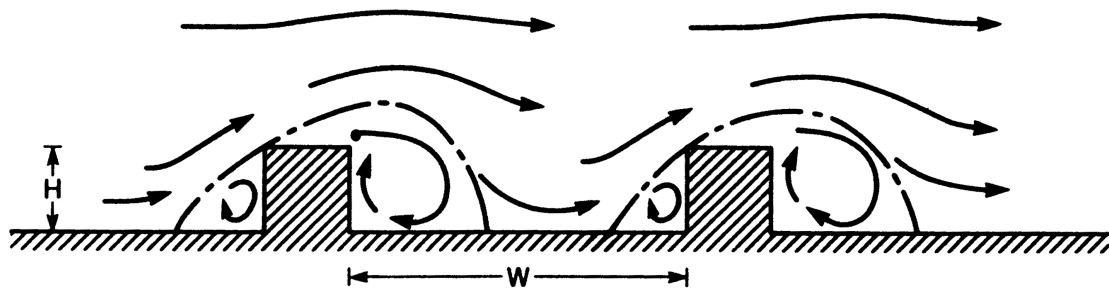


Figure 2.9. Flow patterns around a sharp-edged building. Vertical cross-section of (a) streamlines (solid lines) and flow zones (dashed lines and letters). Plan view of streamlines around a building (b) normal and (c) diagonal to the flow (Oke 1987).

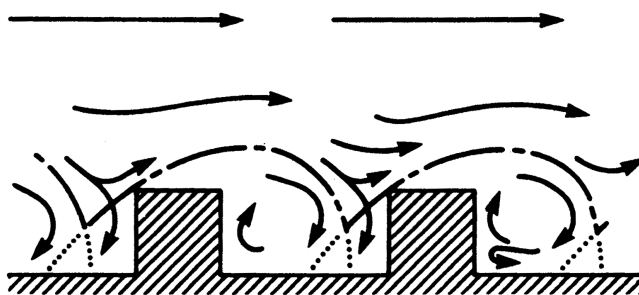
building interacts with those downwind and results in a complicated airflow pattern (Fig 2.10b). When buildings are even closer, the airflow skims over the top of the buildings and creates a vortex in the street canyon (Fig. 2.10c). However, if the airflow is parallel to the street, winds are channeled through the street canyon at speeds faster than those over a flat surface area.

The lee vortices that develop in urban areas are commonly characterized by increased vertical velocities and reverse flow at the surface (Kastner-Klein et al. 2004). However, when pitched roofs are used in wind tunnel studies, the canyon vortex does not develop (Rafailidis 1997; Kastner-Klein et al. 2004). As a result, wind speed values within the canyon are dramatically reduced.

(a) Isolated roughness flow



(b) Wake interference flow



(c) Skimming flow

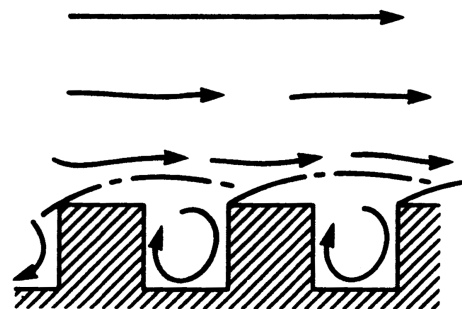


Figure 2.10. Flow patterns associated with different building density (Oke 1987).

Overall, wind speeds in the urban canopy are less than those in rural environments at the same height (Changnon et al. 1971; Landsberg 1981; Oke 1987). However, studies have shown that when wind speed values drop below a threshold of 2.5 to 5.0 m s⁻¹, referred to as the critical wind speed, winds are stronger in the city than in rural areas (Chandler 1965; Bornstein and Johnson 1977; Wong and Dirks 1978; Shreffler 1979a; Landsberg 1981; Hildebrand and Ackerman 1984). Below the critical wind speed, increased vertical mixing in the urban atmosphere and pressure gradients induced by the UHI produce stronger winds within the city, whereas above the critical wind speed, frictional forces reduce wind speed values within the city (Chandler 1965; Wong and Dirks 1978).

While wind speed is reduced within the urban canopy, wind profile data reveal that maximum wind speeds occur at roof top level. As such, strong momentum transfer occurs at the roof top level (Graham 1968; Castro et al. 2006) and the resultant shear layer produced may shelter the canopy flow from that above (Coceal et al. 2006). At the same time, eddies larger than the thickness of the shear layer aid in the transport of heat, moisture, and pollutants from within the UCL to the roughness layer (Castro et al. 2006). From roof top level to two to five times the building height, the flow is complex and depends strongly on the individual roughness elements while the mean wind profile well above the roof top level is described by the logarithmic wind law.

The increased surface roughness in cities results in the increased importance of the mechanical production of turbulence as opposed to buoyant production (Shea and Auer 1978; Hildebrand and Ackerman 1984; Roth and Oke 1995). The increased drag

and turbulence due to the roughness elements produces a deep layer of frictional influence whereby wind speed values are reduced compared with those at the same height in the surrounding rural areas. As wind speed values decrease in urban areas, the airflow converges over the city and results in rising motion and divergence aloft (Hildebrand and Ackerman 1984). Wind tunnel studies have demonstrated that this effect is intensified in the presence of slanted roofs, as opposed to flat roofs. In case of slanted roofs, the retardation of the horizontal winds at roof level is accompanied by a simultaneous transfer of momentum to the vertical flow (Rafailidis 1997). The changes in speed across urban areas can also induce changes in wind direction due to changes in the strength of the Coriolis force. In the Northern Hemisphere, as air enters the urban area it slows and backs. Upon exiting the urban area, the winds veer and increase in speed.

To understand the exchanges of momentum, heat, moisture, and pollutants between the urban surface and the atmosphere, the turbulent structure of the UBL must be quantified (Roth 2000). Roth and Oke (1995) and Roth (2000) identified four processes primarily responsible for modifying the turbulence structure of the UBL:

1. An intense shear layer near the top of the canopy, where mean kinetic energy of the flow is converted into turbulent kinetic energy (TKE) and results in high turbulence intensity.
2. Wake diffusion (Thom et al. 1975), or the efficient mixing of momentum, heat, and moisture generated by turbulent wakes behind individual roughness elements. The size of these turbulent wakes is related to the dimensions of the roughness elements.
3. Form drag due to bluff-bodies, or pressure differences across individual roughness elements, which impacts the transport of momentum to the surface and has no analog in the transport of heat or mass (Thom 1972).

4. Sources and sinks of momentum, heat, and water vapor organized in three-dimensional arrays and not necessarily collocated, which results in the development of a complex system of discrete and localized heat and mass plumes.

Comprehensive comparisons between different studies on UBL turbulence are complicated by several factors: (a) the variety of statistics and normalizations utilized, (b) the strong dependence of turbulence on urban morphology and fetch conditions, (c) the focus on the height variation of turbulence based on a single profile, (d) the lack of data on air flows around buildings, and (e) the lack of knowledge of the upstream conditions (Roth 2000; Eliasson et al. 2006). Common turbulence statistics analyzed in UBL studies include Reynolds stress (Bowne and Ball 1970; Hildebrand and Ackerman 1984; Uno et al. 1988; Rotach 1993a, b; Oikawa and Meng 1995; Rafailidis 1997; Kastner-Klein and Rotach 2004; Castro et al. 2006), standard deviations of velocity (Bowne and Ball 1970; Jackson 1978; Steyn 1982; Högstrom et al. 1982; Ching 1985; Yersel and Goble 1986; Uno et al. 1988; Rotach 1993b; Roth and Oke 1995; Oikawa and Meng 1995; Eliasson et al. 2006), turbulence intensity (Graham 1968; Bowne and Ball 1970; Brook 1972; Jackson 1978; Högstrom et al. 1982; Yersel and Goble 1986; Uno et al. 1988; Rafailidis 1997; Kastner-Klein et al. 2004), TKE (Hildebrand and Ackerman 1984; Uno et al. 1988; Kastner-Klein and Rotach 2004; Kastner-Klein et al. 2004; Castro et al. 2006; Eliasson et al. 2006), and turbulent velocity spectra and cospectra (Bowne and Ball 1970; Brook 1972; Jackson 1978; Steyn 1982; Högstrom et al. 1982; Roth et al. 1989b; Oikawa and Meng 1995).

2.3. OBSERVATIONS OF THE URBAN ENVIRONMENT

Ideally, the impact of urbanization should be quantified as the temporal differences between urban and pre-urban observations stratified by weather type (Lowry 1977). Time trends would be analyzed and mean air temperature would increase with urbanization and population. Because most cities were built before the technology to observe the impact of the urban environment on atmospheric processes was developed, the most common method used to approximate the impact of urbanization is the comparison of synchronous observations at two sites which represent urban and surrounding rural environments (Oke and McCaughey 1983). Urban-rural comparisons must be interpreted carefully because terrain and local weather conditions can obscure or exaggerate the urban-rural signal (Lowry 1977, Hawkins et al. 2004). In addition to stratification by weather type, day of the week has been used to stratify observational data to identify human effects on the local climate (Forster and Solomon 2003).

The measurements used in urban-rural comparisons are commonly recorded by instrumentation deployed during short-term field experiments or long-term observation networks. Other methods to measure urban impacts include the use of wind tunnels (MacDonald 2000; Barlow and Belcher 2002; Cheng and Castro 2002; Uehara et al. 2003; Barlow et al. 2004) and open-air scale models (Pearlmutter et al. 2005; Kawai and Kanda 2010).

2.3.1. Urban Field Campaigns

Much of the current understanding of the impacts of urban areas on atmospheric processes results from a number of large field experiments conducted by groups of

scientists in cities worldwide, several of which were in North America (Table 2-2). These large short-term measurement campaigns provided data from vast arrays of instrumentation for a limited range of environmental conditions and addressed a wide range of research questions (National Research Council 2012; Grimmond 2006).

The goals of large-scale urban campaigns included improved knowledge of the impacts of urban areas on the formation of precipitation and severe weather (Changnon et al. 1971, 1976; Lowry 1974; Changnon and Semonin 1978), development of the nocturnal and convective boundary layers (Mailhot et al. 1998; Dupont et al. 1999; Fast et al. 2000; Menut et al. 2000; Doran et al. 2002; Masson et al. 2004; Rotach et al. 2005; Allwine and Flaherty 2006), formation and dispersion of pollutants (Changnon and Semonin 1978; Cowling et al. 1998; Doran et al. 1998; Fast et al. 2000; Menut et al. 2000; Doran et al. 2002; Allwine et al. 2002; Cowling and Furness 2004; Cros et al. 2004; Masson et al. 2004; Mestayer et al. 2005; Rotach et al. 2005; Allwine and Flaherty 2006; Watson et al. 2006), and evolution of urban aerosols (Doran et al. 1998; Menut et al. 2000; Masson et al. 2004). In addition, several campaigns aimed to improve the representation of urban processes in models (Mailhot et al. 1998; Dupont et al. 1999; Menut et al. 2000; Doran et al. 2002; Allwine et al. 2002; Cros et al. 2004; Rotach et al. 2005; Watson et al. 2006). To accomplish these goals, multi-institution collaborations deployed surface meteorological stations, surface energy balance stations, temperature data loggers, infrared temperature sensors, thermal scanners, radiosondes, tethered balloons, sodars, lidars, radar wind profiler/RASS systems, FM-CW radars, ceilometers, sonic anemometers, radiometers, aerosol and air chemistry

Table 2-2. Large field campaigns to study the urban climate [Adapted from Grimmond (2006)].

Location	Year	Experiment
St. Louis, MO, USA	1971-1973	METROPolitan Meteorological EXperiment (METROMEX)
Chicago, IL, USA	1976-1978	Chicago Area Program (CAP)
Atlanta, GA, USA	1990-1992, 1999	Southern Oxidants Study (SOS)
Vancouver, BC, Canada	1993	Pacific '93
Paris, France	1994-1995	Etude de la Couche Limite en Agglomération Parisienne (ECLAP)
Montreal, QC, Canada	1996	Montreal-96 Experiment on Regional Mixing and OZone (MERMOZ)
Nashville, TN, USA	1990-2000	Southern Oxidants Study (SOS)
Mexico City, Mexico	1997	Investigacion sobre MAteria particulada y Deterioro Atmosferico-Aerosol and Visibility Evaluation Research (IMADA-AVER)
Phoenix, AZ, USA	1998	1998 Ozone Field Study
Berlin, Germany	1998	BERLin OZone (BERLIOZ)
Paris, France	1998-1999	Étude et Simulation de la QUalité de l'air en Ile de France (ESQUIF)
Salt Lake City, UT, USA	2000	Vertical Transport and MiXing (VTMX), URBAN 2000
Houston, TX, USA	2000	Southern Oxidants Study (SOS)
Phoenix, AZ, USA	2001	2001 Phoenix Sunrise Experiment
Marseille, France	2001	Expérience sur Site pour CONtraindre les Modèles de Pollution atmosphérique et de Transport d'Emissions (ESCOMPTE)
Basel, Switzerland	2001-2002	Basel UrBan Boundary Layer Experiment (BUBBLE)
Beijing, China	2001, 2003	Beijing City Air Pollution EXperiment
London, England, UK	2002-2011	Dispersion of Air Pollution & Penetration into the Local Environment (DAPPLE)
Oklahoma City, OK, USA	2003	Joint Urban 2003 (JU2003)
New York City, NY, USA	2004-2007	New York City Urban Dispersion Program
Toulouse, France	2004-2005	Canopy and Aerosol Particles in TOulouse Urban Layer (CAPITOUL)

instruments, and instrumented aircraft and automobiles. Further, atmospheric tracer and wind tunnel experiments were conducted.

2.3.2. Long-Term Observation Networks

The National Research Council (2010) emphasized the need for urban mesonets to provide weather and air quality observations at high spatial and temporal resolutions for multiple years in the urban core and surrounding areas. A limited number of urban networks in North America focus on the long-term measurement of weather in urban areas (Table 2-3). For example, the Long-Term Ecological Research (LTER) network was established by the National Science Foundation to investigate ecological issues over long periods of time (Greenland and Swift 1991). The Central Arizona – Phoenix LTER (CAP-LTER) and Baltimore Ecosystem Study LTER (BES-LTER) sites were designed to analyze changes in the urban ecosystem due to the spatial and temporal variations of urbanization and population growth (Brazel et al. 2000) by quantifying the effects of land use change on the temperature, humidity, wind speed, and fluxes of radiation, energy, and momentum.

The Phoenix Real-time InStrumentation for Meteorological Studies (PRISMS; Brazel et al. 1992) network consists of 17 weather stations located throughout the Phoenix metropolitan area. Each site measures air temperature, dew point temperature, wind speed, wind direction, and atmospheric pressure every five minutes. Many sites are representative of the suburban climate because they are located at electric substations.

Table 2-3. Long-term observation networks to study the urban climate.

Location	Network
Phoenix, AZ	Central Arizona – Phoenix Long-Term Ecological Research (CAP-LTER)
Baltimore, MD	Baltimore Ecosystem Study Long-Term Ecological Research (BES-LTER)
Phoenix, AZ	Phoenix Real-time InStrumentation for Meteorological Studies (PRISMS)
Maricopa County, AZ Yavapai County, AZ Mojave County, AS	Automated Local Evaluation in Real Time (ALERT)
Oklahoma City, OK	OKlahoma City MicroNET (OKCNET)
Montreal, QC, Canada Vancouver, BC, Canada	Environmental Prediction in Canadian Cities (EPiCC)

Starting in the early 1980s, Automated Local Evaluation in Real Time (ALERT; FCDMC 2007) networks were installed in the Flood Control Districts of Maricopa, Yavapai, and Mohave Counties to monitor flood conditions in Arizona. The network includes 304 rain gauges, 167 streamflow gauges and 33 weather stations encompassing cities such as Phoenix, Tempe, Glendale, Prescott, and Lake Havasu City.

The Oklahoma City MicroNET (OKCNET) was designed to improve the monitoring of atmospheric conditions (air temperature, relative humidity, pressure, wind speed, wind direction, and rainfall) across the OKC metropolitan area (Basara et al. 2011; Schroeder et al. 2010). OKCNET included three Oklahoma Mesonet sites within OKC and 36 sites mounted on traffic signals. The traffic signal sites were concentrated within the CBD of OKC and decreased in density toward the periphery of the metropolitan area. The OKCNET traffic signal sites were retired in 2013. However, the three Mesonet sites remain operational within the Oklahoma Mesonet.

The Environmental Prediction in Canadian Cities (EPiCC) is a research network that seeks to better understand the urban atmosphere in Canada through a program of observing, modeling, and remote sensing (Voogt et al. 2007). The observational component includes long-term continuous observations of the radiation and energy balances from urban and rural sites in and around Montreal and Vancouver, as well as seasonal intensive observation periods with the deployment of additional instrumentation. The overall objective is to provide Canadian urban residents with better weather and air quality forecasts.

While there are several examples of past and ongoing efforts to establish long-term observation networks in urban areas, it remains a challenge to design, deploy, and maintain a network that combines instruments with strong stakeholder involvement in the United States (National Research Council 2012).

2.4. REPRESENTATION OF URBAN AREAS IN MESOSCALE MODELS

The 10th Prospectus Development Team of the U.S. Weather Research Program (Dabberdt et al. 2000) concluded, “As mesoscale model resolution increases, it will be increasingly important to properly represent urban influences on the radiation budget, surface moisture, sensible heat exchange processes, and anthropogenic heat and moisture fluxes...”

Due to restrictions on model resolution, limits on available computing resources, and required timeliness of forecasts, cities are poorly resolved in operational numerical weather prediction (NWP) models (Best 2005). The complex interactions between the urban canopy and the atmosphere are not treated explicitly in mesoscale models.

Instead, because they are subgrid-scale processes, they are parameterized using bulk transfer relations, which represent the area-average effects of the urban canopy (Brown 2000). As such, urban areas are typically represented in a vegetation-atmosphere-transfer model as bare soil or concrete with modified parameters such as increased surface roughness (Grimmond et al. 1998), reduced soil moisture availability, and reduced albedo (Arnfield and Grimmond 1998). The bare soil formulation is sufficient for large temporal or spatial scale simulations if the soil properties are tuned to mimic radiative trapping. However, “the bare soil scheme cannot correctly forecast the air temperatures in the canyon, and thus UHI intensities. The limit of the bare soil substitution is reached when purely urban areas are resolved in the atmospheric model” (Masson 2000). In addition, the parameterizations are typically based on MOST, which may be not applicable within the urban canopy. As a result, the current approach regarding the simulation of urban impacts in operation numerical models fails to reproduce the vertical structure of turbulent fluxes and UHI effects due to the neglect of the impacts of building geometry (Martilli et al. 2002).

2.4.1. Thermal and Dynamical Parameterizations

Parameterizations designed to improve the representation of urban areas in mesoscale models can be classified in several ways (Grimmond et al. 2009, 2010). This study classifies urban parameterizations as either thermal or dynamical (Martilli et al. 2002). Thermal parameterizations refer to how the urban canopy impacts the radiative and surface energy balances. Key physical processes represented in thermal parameterizations include building shadows, multiple reflections of radiation off wall

and road surfaces, ΔQ_S , and Q_F from buildings, automobiles, and industry (Table 2-3). Empirical parameterizations, such as the Objective Hysteresis Model (OHM; Grimmond et al. 1991), were derived from observations of the SEB. A more complicated approach represented the urban canopy as a layer between the surface and the atmosphere (Best 1998, 2005). Recent developments in the parameterization of Q_F involved a vertically distributed Q_F via the thermodynamic equation in the boundary layer to account for industrial emissions, as opposed to adding the term solely to the SEB (Fan and Sailor 2005).

Dynamical parameterizations focus on impacts of the urban canopy on winds and the generation of TKE. Important physical processes in dynamical parameterizations are the UHI circulation, reduced wind speeds by surface roughness, and urban turbulence (Table 2-4). To simulate the drag induced by buildings, many models include the drag force. This approach utilizes a high vertical resolution with several layers within the UCL. As such, a sink term is added to the momentum equations for the vertical layers in which buildings were present (Uno et al. 1989; Brown and Williams 1998; Urano et al. 1999; Dupont et al. 2004; Otte et al. 2004; Lien et al. 2005). In the drag force approach, it is assumed that the buildings do not occupy any volume within the grid cell. However, the porous flow approach does account for the reduction of air volume to the urban canopy by including a building fractional volume term in the momentum equations (Ca et al. 1999; Maruyama 1999). To represent the conversion of mean kinetic energy into TKE, a source term is added to the

Table 2-3. Examples of thermal parameterizations for urban land use in mesoscale models.

Model Name and Description	Reference
2-D block canyon model to calculate effective albedo	Aida and Gotoh (1982)
2-D urban canyon model to predict radiation budget	Arnfield (1982)
Predicts amount of shortwave radiation received by vertical walls	Brühl and Zdunkowski (1983)
Surface Heat Island Model (SHIM); Calculates L^* as a function of the sky-view factor	Johnson et al. (1991); Oke et al. (1991)
Tulane Urban Radiation Model (TURM); Simulates urban radiation balance with 2-D urban geometry and 3-D representation of solar angle	Sailor and Fan (2002)
Net All-wave Radiation Parameterization (NARP); Predicts $K\uparrow$, $L\downarrow$, and $L\uparrow$ with the use of meteorological and surface inputs	Offerle et al. (2003)
Objective Hysteresis Model (OHM); Simulates with the use of Q^* measurements, building dimensions, and areal coverage of surface types	Grimmond et al. (1991)
Modified Colorado State University Mesoscale Model; Simulates SEB using OHM and weighted temperature tendency term	Taha (1999)
Local-scale Urban Meteorological Parameterization Scheme (LUMPS); Predicts Q_H and Q_E using Q^* and standard weather observations	Grimmond and Oke (2002)
Microscale variability approach; Estimates Q_H based on remotely sensed surface temperature	Voogt and Grimmond (2000)
PORTable Surface Temperature (POST) model; Predicts temperature of various surfaces using standard forecast variables	Best (1998)
Vertical profiles of Q_F implemented in PBL schemes	Sailor and Lu (2004); Fan and Sailor (2005)
Simulates the SEB using MODIS monthly-mean albedo, emissivity, and LAI	Jin et al. (2007)

TKE balance and, if present, to the TKE dissipation (ε) equation (Uno et al. 1989; Brown and Williams 1998; Maruyama 1999).

Table 2-4. Examples of dynamical parameterizations for urban land use in mesoscale models.

Model Name and Description	Reference
Simulates development of the UHI circulation	Delage and Taylor (1970)
URBan METeorology (URBMET); Simulates flow over idealized city	Bornstein (1975)
1st order turbulence closure model with modified eddy diffusivity	Sorbjan and Uliasz (1982)
2nd order turbulence closure model with drag force and vertical profile of Q_F	Uno et al. (1989)
k - ϵ turbulence closure model with porous flow	Maruyama (1999)
k - ϵ turbulence closure model with porous flow and building air conditioning model	Ca et al. (1999)
k - ϵ turbulence closure model with drag force and vertical profile of Q_F	Urano et al. (1999)
k - ϵ turbulence closure model with drag force	Lien et al. (2005); Lien and Yee (2005)
E - l turbulence closure model with drag force, OHM, and radiation extinction	Otte (2004)
E - l turbulence closure model with drag force, radiation extinction, and roof-top heat flux	Brown and Williams (1998)
1st order turbulence closure model with canopy-element drag	Coceal and Belcher (2004)
(DA-SM2-U); E - l turbulence closure model with drag force	Dupont et al. (2004)

Attempts to determine which parameterizations are critical have found that both thermal and dynamical are crucial for simulating the UBL; in the lower UBL, thermal factors are more important, while in the upper UBL, the mechanical factors are more important (Martilli et al. 2002). In addition, it was determined that thermal factors significantly impact the UBL height in the morning and daytime hours, whereas mechanical factors were most influential in the evening (Martilli et al. 2002). Similarly,

Otte et al. (2004) determined that the full urban parameterization was preferable to the energy-only and momentum-only cases.

2.4.2. Urban Canopy Models

To more accurately simulate the SEB within the urban canopy, urban canopy models (UCMs) have been developed (Table 2-5). UCMs utilize three-dimensional geometry of urban street canyons to explicitly model the effects of vertical surfaces. UCMs incorporated into land surface models are called single-layer models because the interactions between the surface and the atmosphere occur only at the top of the canyons and roofs. As such, the first level of the atmospheric model is above roof level (Masson 2006). Many single-layer UCMs assume an exponential law for wind below roof level, logarithmic law above roof level, and air temperature and humidity are uniform throughout the street canyon (Masson 2006). Single-layer UCMs are easier to incorporate into NWP models because they do not require modifications to the dynamic

Table 2-5. Examples of urban canopy models developed for use in mesoscale models.

Model Name	Model Type	References
Town Energy Budget (TEB)	Single-layer	Masson (2000); Masson et al. (2002); Lemonsu et al. (2004)
Noah/Single-layer Urban Canopy Model (SLUCM)	Single-layer	Kusaka et al. (2001); Kusaka and Kimura (2004a, b)
Simple Urban energy balance Model for Mesoscale simulations (SUMM)	Single-layer	Kanda et al. (2005a, b)
Building Effect Parameterization (BEP), BEP coupled with Building Energy Model (BEM)	Multi-layer	Martilli et al.(2002); Salamanca et al. (2010); Salamanca and Martilli (2010)
Multilayer Urban Canopy Model (MUCM)	Multi-layer	Kondo et al. (2005)

core (Kusaka and Kimura 2004a). Multi-layer UCMs have atmospheric layers within the UCL. As a result, the drag force and porous approaches are often implemented within multi-layer UCMs. Because they require more computation time and modification to the dynamic core, multi-layer UCMs are more difficult to incorporate into NWP models. However, relative to the run time of the atmospheric model, the additional run time of the multi-layer UCM is negligible (Masson 2006). Thus, if the research focus is on the influence of cities, from mesoscale to urban scales, single-layer UCMs are recommended. If the research focus is on processes within the UCL, multi-layer UCMs are more suitable (Masson 2006).

For UCMs, the effects of shadowing and radiation trapping in urban canyons are simulated for either (a) infinite two-dimensional street canyons (Masson 2000; Kusaka et al. 2001; Martilli et al. 2002) or (b) an infinitely-extended regular array of buildings (Kanda et al. 2005b; Kondo et al. 2005). Further, UCMs typically have separate SEBs for the roofs, roads, and building walls and thin bucket models to represent drainage by sewer systems. Building heat is commonly represented by a constant internal building temperature. However, some UCMs can be coupled to a building energy model (Salamanca et al. 2010). Snow removal and dirty snow due to traffic can even be accounted for in an UCM (Masson 2000).

Comparisons of both single- and multi-layer UCMs with slab models have demonstrated the inability of the slab model to correctly simulate radiative trapping, nocturnal trends in ΔQ_s , and the UHI circulation despite tuning efforts (Kusaka et al. 2001; Kusaka and Kimura 2004a). However, despite the advances in urban canopy

modeling, the UCMs still fail, in a quantitative sense, to accurately represent urban effects (Martilli 2007). When compared with observational data, the TEB scheme was not able to capture the rapid increase in sensible heat fluxes during the morning due to traffic and overestimated nighttime roof temperatures by as much as 8 K (Masson et al. 2002). The SLUCM underestimated the nocturnal UHI, Q_H , and surface temperatures (Kanda et al. 2005a; Holt and Pullen 2007). Further, results indicated that albedo was underestimated by the radiation scheme when the urban canopy is represented as an infinite street canyon and too much radiation was trapped within the canyon (Kanda et al. 2005b). Most recently, Grimmond et al. (2010) determined that of 33 urban energy balance models, no single model performed best or worst for all of the components of the SEB. Overall, model performance was best for Q^* , followed by ΔQ_S , Q_H , and Q_E (Grimmond et al. 2010). In addition, models that performed best during the daytime did not perform best at night.

3. OBSERVATIONAL DATA

3.1. JOINT URBAN 2003 (JU2003)

The Department of Energy, the Department of Defense, and the Department of Homeland Security sponsored an urban dispersion experiment in OKC from 28 June through 31 July 2003. The goal of JU2003 was to “collect meteorological tracer data resolving atmospheric dispersion at scales-of-motion ranging from flows in and around a single city block, in and around several blocks in the downtown Central Business District (CBD), and into the suburban OKC area several kilometers from the CBD” (Clawson et al. 2005). JU2003 brought together over 150 scientists, engineers, technicians, and students from over 20 U.S. and foreign organizations (Table 3-1; Allwine and Flaherty 2006).

OKC was selected for JU2003 for several reasons, which included a consolidated and well defined CBD of tall buildings, relatively flat terrain without large bodies of water bordering the city, predictable wind conditions for the study period, the gridded nature of the city streets, and the support of city officials for the project. In addition, an extensive weather-observing infrastructure was in place in central Oklahoma that included the Oklahoma Mesonet (Brock et al. 1995; Shafer et al. 2000; McPherson et al. 2007), the KOUN dual polarization radar, the OUN upper air station, and four NEXRAD Doppler radars.

Ten intensive observation periods (IOPs) that spanned 8 hours in duration were completed during the 34-day study period. During the IOPs detailed meteorological, turbulence, and tracer measurements were recorded. The instruments employed during

Table 3-1. The U.S. organizations that participated in Joint Urban 2003 (Allwine and Flaherty 2006).

Department of Defense	Universities
Defense Threat Reduction Agency Army Research Laboratory Army Research Office Edgewood Chemical Biological Center Dugway Proving Ground Defense Advanced Research Projects Agency	Arizona State University Central Florida University Texas Tech University Indiana University University of Houston University of Oklahoma University of Utah Washington State University
Departments of Homeland Security and Energy	National Oceanic and Atmospheric Administration
Argonne National Laboratory Los Alamos National Laboratory Lawrence Berkley National Laboratory Lawrence Livermore National Laboratory Pacific Northwest National Laboratory	Air Resources Laboratory - Field Research Division Air Resources Laboratory - Atmospheric Turbulence and Diffusion Division National Severe Storms Laboratory
Other Federal Organizations	Private Companies
Department of Transportation - Volpe Center Center for Disease Control/National Institute for Occupational Safety and Health	Northrup Grumman Information Technology ITT Industries, Advanced Engineering Sciences Maccini Construction Company Allied Steel Construction Company
State of Oklahoma	
Oklahoma Climatological Survey Department of Environmental Quality	

JU2003 include 194 tracer bag samplers, 25 fast-response tracer analyzers, one seven-level tracer profile system, 106 3-D sonic anemometers for surface-based and tower-based measurements, seven 2-D sonic anemometers, 29 surface meteorological stations, eight surface energy budget stations, two CTI wind tracer lidars, three radiosonde systems, two tethersondes, three wind profiler/RASS systems, one FM-CW radar, three

ceilometers, a NOAA Twin Otter aircraft, and nine sodars (Allwine and Flaherty 2006). The majority of the meteorological and tracer instruments were located within or near the CBD, but some extended up to six kilometers from the CBD. The following sections provide details of the data collected during JU2003 that are utilized in this study.

3.1.1. Air Temperature Data

During JU2003, PNNL deployed 32 HOBO temperature data loggers (Whiteman et al. 2000) throughout OKC to measure air temperature [2 m above ground level (AGL)]. HOBOS were deployed along a north-south transect and an east-west transect centered on the CBD (Fig. 3.1). Air temperature data were stored as 5-minute averages.

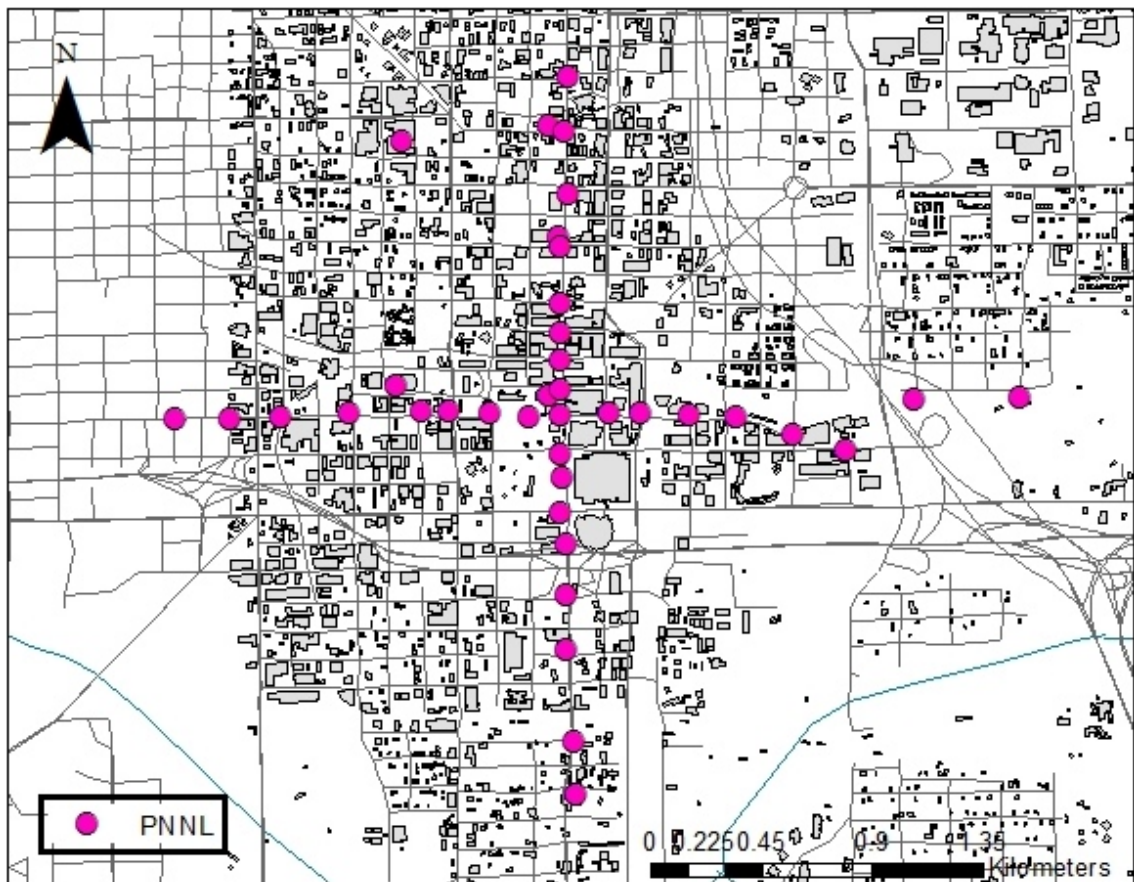


Figure 3.1. Locations of the HOBO temperature data loggers deployed by Pacific Northwest National Laboratory (PNNL) during Joint Urban 2003.

3.1.2. Surface Energy Balance Data

During JU2003, seven surface energy balance (SEB) sites were installed at a number of locations within the metropolitan area of OKC. The sites were installed over various land use classes across the city. For example, a number of sites were located on the periphery of the city near irrigated suburban lawns. Other sites were installed over gravel or concrete near the CBD of OKC. The SEB sites were deployed during JU2003 by three organizations: ASU, ATDD, and IU. The site locations for the energy balance measurements provided samples upwind, within, and downwind of the CBD of OKC (Fig. 3.2).

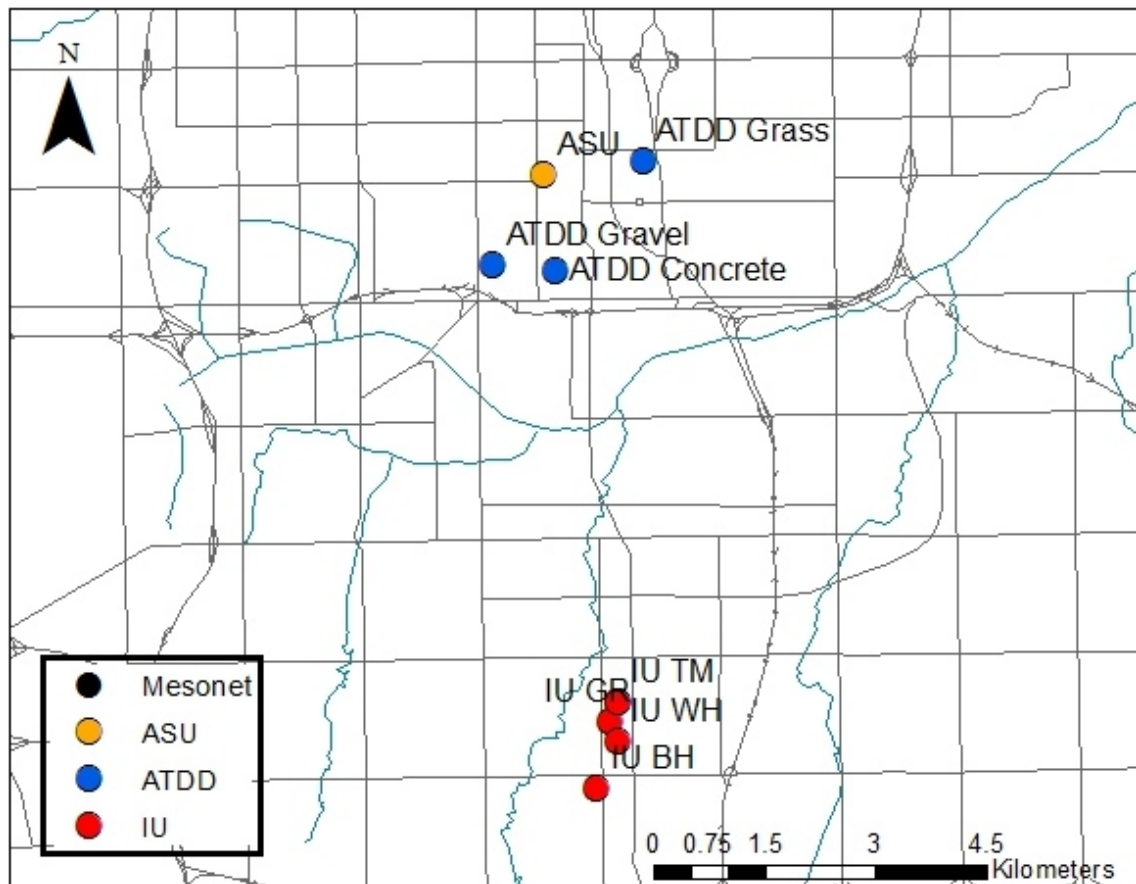


Figure 3.2. Locations of the energy flux towers deployed by Arizona State University (ASU), Atmospheric Turbulence and Diffusion Division (ATDD), and Indiana University (IU) during Joint Urban 2003.

The SEB site deployed by ASU was located on a grassy field northwest of the CBD near the intersection of N Walker Avenue and NW 11th Street (Fig. 3.3). The tower was instrumented with one net radiometer (Kipp and Zonen CNR1, 9.2 m AGL), two cup anemometers (Met-One Instruments 014A, 1.5 and 8.9 m AGL), two thermistors (1.1 and 8.3 m AGL), one infrared thermometer (Everest Interscience Inc. 4000.4 ZL, 3.5 m AGL), one upward facing pyranometer (Eppley Precision Spectral Pyranometer Model PSP, 3.5 m AGL), one downward facing pyrgeometer (Eppley Precision Infrared Radiometer Model PIR, 3.5 m AGL), one 3-D sonic anemometer [Campbell Scientific, Inc. (CSI) CSAT3, 2.5 m AGL], one krypton hygrometer (CSI KH20, 2.5 m AGL), one soil heat flux plate (Hukseflux HFP01SC, 6.5 cm BGL), six thermistors (2, 3, 4, 5, and 8 cm BGL), and one soil water content reflectometer (CSI CS616). Data from the net radiometer, cup anemometers, thermistors, pyranometer, pyrgeometer, and soil heat flux plate were stored as 5-minute averages. Data from the

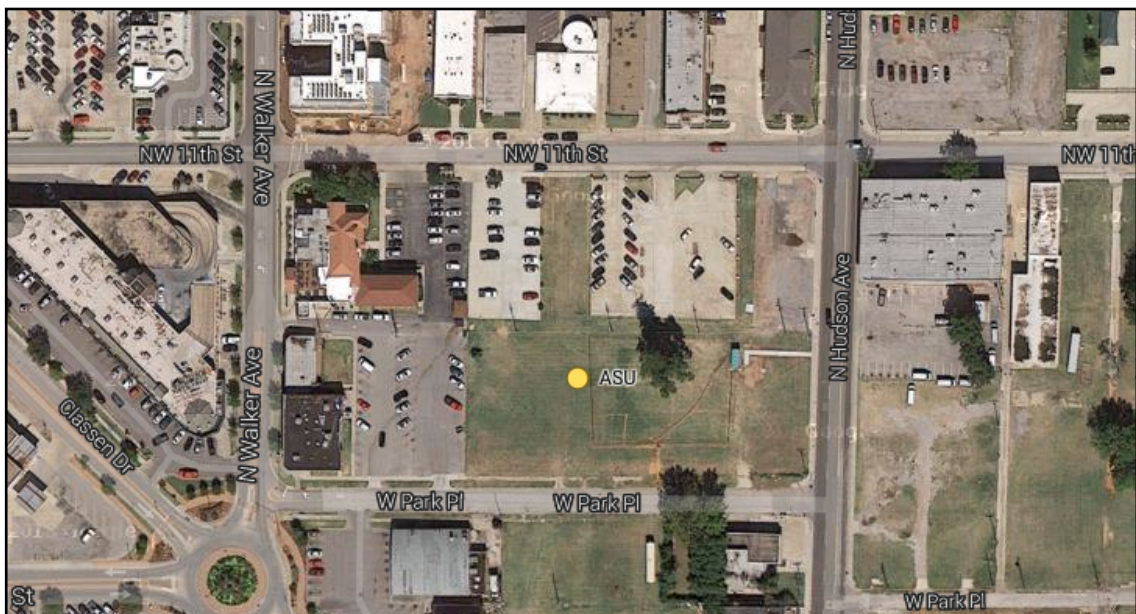


Figure 3.3. Location of energy tower deployed by Arizona State University (ASU) during Joint Urban 2003. Source of imagery: Google Imagery.

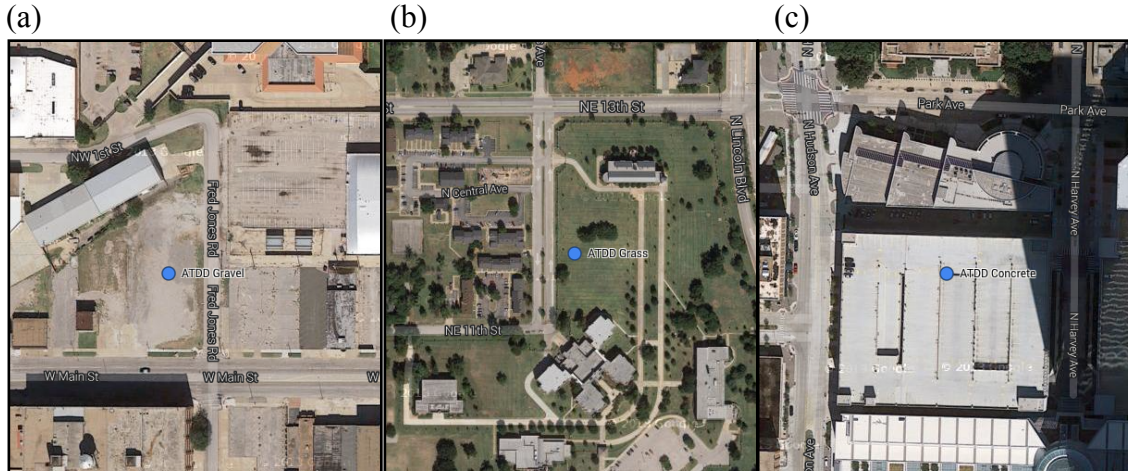


Figure 3.4. Locations of the (a) Gravel, (b) Grass, and (c) Concrete energy flux towers deployed by Atmospheric Turbulence and Diffusion Division (ATDD) during Joint Urban 2003. Source of imagery: Google Imagery.

infrared thermometer, sonic anemometer, krypton hygrometer, and soil water content reflectometer were stored as 1-minute averages.

ATDD deployed three energy balance towers over surfaces typical of the downtown commercial and industrial area of OKC (Fig. 3.4). Site A (ATDD Gravel; Fred Jones parking lot) was located in a dirt and gravel parking lot area just west of the OKC CBD. Site B (ATDD Grass; Oklahoma School for Science and Mathematics) was located in an irrigated grass area northeast of the CBD. Site C (ATDD Concrete; Galleria Parking Garage) was located on the top level of a large multi-level concrete parking garage at the southwest corner of the CBD. The Grass experienced occasional power outages and the effects of an automated sprinkler system, which operated every night. The ATDD data were stored as 30-minute averages.

IU deployed several energy balance towers in a suburban area approximately six kilometers south of the CBD and captured both local- and micro-scales (Fig. 3.5) SEB processes. The IU measurement sites of interest for this study are the Brick House (BH),



Figure 3.5. Locations of energy flux towers deployed by Indiana University (IU) during Joint Urban 2003. Source of imagery: Google Imagery.

Wood House (WH), Grass (GR), and Tyler Media sites (TM). The energy balance data from the BH, WH, GR, and TM sites were distributed as 1-hour averages.

The BH tower was located in an open field north of a residential neighborhood of one- to two-story brick homes while the WH tower was located in an open field north of a residential neighborhood of brick and wood homes. The GR site was deployed at the north end of the football practice field of Southeast High School. Instruments at the TM site were mounted on booms that extended from two radio/cell phone towers owned by the Tyler Media Group.

Instrumentation at each IU site is summarized in Table 3-2. Additional variables measured at the GR site were soil heat flux (CSI HFT3, 5 cm), soil temperature (CSI TCAV thermocouples, 1-4 cm), surface wetness (CSI 237), soil moisture (CSI TDR), atmospheric pressure (Vaisala PTA), and precipitation (Weathertronics 6011-B).

Table 3-2. Instruments mounted on the Indiana University towers during Joint Urban 2003. At the TM site two dataloggers (A and B) were installed. Manufacturer/Model (M/M) abbreviations: CSI CSAT (CSAT), R.M. Young 81000 (RMY), CSI KH20 (KH20), Radiation and Energy Balance Systems, Inc. Q*6.7.1 (REBS), Licor Li-200SZ (200SZ), CSI CS500 (CS500), Cole-Palmer CP39670-10 K-Type (CP-K), height in meters [Ht (m)] (Grimmond et al. 2004b).

Site	TMA		TMB		BH		WH)		GR	
	M/M	Ht (m)	M/M	Ht (m)	M/M	Ht (m)	M/M	Ht (m)	M/M	Ht (m)
Sonic Anemom.	CSAT	79.63	CSAT	37.26	RMY	28.87	RMY	17.51	RMY	3.69
Sonic Anemom.	RMY	54.56	RMY	19.35	RMY	18.27	—	—	—	—
Krypton Hygrom.	KH20	79.63	KH20	37.26	KH20	28.87	KH20	17.51	KH20	3.69
Net Radiom.	REBS	80.16	REBS	37.49	REBS	28.00	REBS	16.64	REBS	3.09
Pyranom.	200SZ	80.16	200SZ	37.49	200SZ	28.00	200SZ	16.64	200SZ	3.09
Temp/RH	CS500	76.73	CS500	37.26	CS500	28.30	CS500	16.64	CS500	3.19
Infrared Thermom.	CP-K	80.16	CP-K	37.49	CP-K	28.25	CP-K	16.64	CP-K	2.66

3.1.3. Data Quality Assurance

The quality assurance (QA) of JU2003 data was performed by the organization that collected the data. All erroneous data were assigned QA flags according to Dugway Proving Ground (2003). In addition to the QA performed by the data collecting organization, an independent QA contractor performs quarterly audits where random samples from 5% of the data are compared with the original data submitted to the database (Halvorson et al. 2006). Any discrepancies are reported to the JU2003 database/website staff. Despite QA efforts by each organization, the ATDD Grass site

data are excluded from this study due to erroneously large values of Q_E ($> 2000 \text{ W m}^{-2}$) that far surpass those documented in investigations of the suburban oasis effect (Oke 1979; Kalanda et al. 1980; Oke and McCaughey 1983; Cleugh and Oke 1986).

3.2. THE OKLAHOMA MESONET

The Oklahoma Mesonet is an automated network of over 100 remote, hydrometeorological stations across Oklahoma (Fig. 3.6; Brock et al. 1995; Shafer et al. 2000; McPherson et al. 2007). Each station measures 10 core variables which include: air temperature and relative humidity at 1.5 m, wind speed and direction at 10 m, barometric pressure, precipitation, incoming solar radiation, bare and vegetated soil temperatures (10 and 30 cm BGL), and soil moisture (5, 25, 60, and 75 cm). Observations from the Oklahoma Mesonet are collected every five minutes, with the exception of soil temperature (15 minutes) and soil moisture (30 minutes). The Mesonet was installed in 1993 and became operational on 1 January 1994.

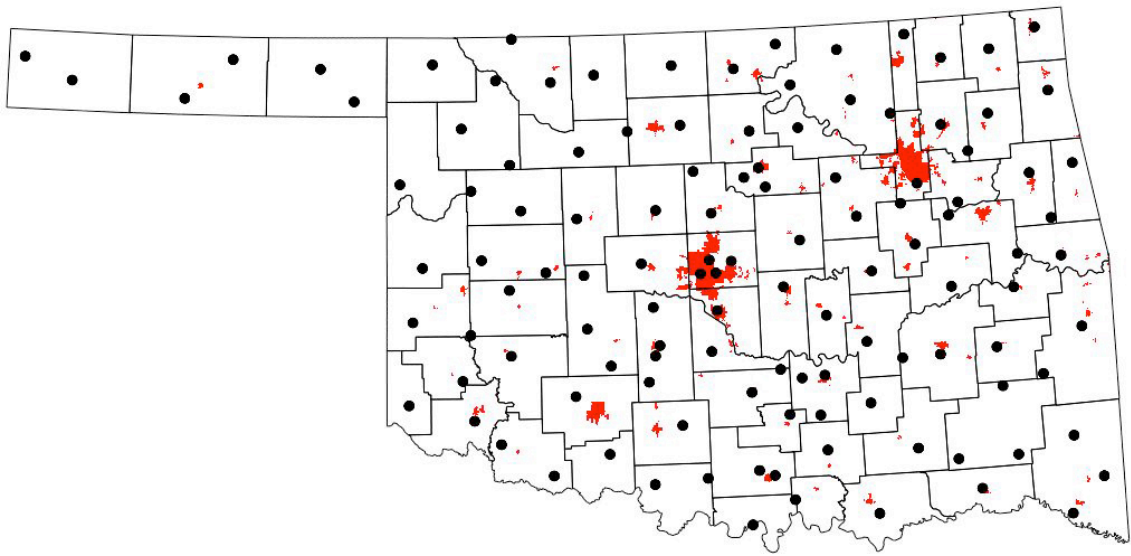


Figure 3.6. Current locations of the Oklahoma Mesonet sites. Mesonet sites are indicated by solid black circles. Urban areas are shaded in red.

An automated QA system checks each core measurement for possible errors. In addition, Mesonet staff and QA managers monitor the daily collection of data and perform extended QA on the data archive (Shafer et al. 2000; McPherson et al. 2007). Questionable observations are flagged and logged in the Mesonet's QA database. Due to occasional updates to sensor calibration equations by manufacturers, no data are removed or changed within the Mesonet archives.

3.2.1. The OASIS Project

In 1999, the Oklahoma Atmospheric Surface-layer Instrumentation System (OASIS) Project upgraded 89 Mesonet sites with a suite of instruments capable of estimating the surface energy balance (Brotzge et al. 1999; Brotzge 2000; Basara and Crawford 2002). In addition, OASIS Super Sites, a subset of 10 OASIS sites, were instrumented to measure the components of the surface energy balance with enhanced accuracy (Fig. 3.7). The 10 OASIS Super Sites measured latent and sensible heat fluxes using eddy covariance techniques, ground heat flux, the four components of net radiation, and skin temperature (Brotzge 2000). Each Super Site was located in a different climate region of Oklahoma and permitted the investigation of a wide range of atmospheric conditions over extended temporal periods. Due to their proximity to OKC, the OASIS Super Sites of interest in this study are WASH (far upwind), NRMN (upwind), and MARE (downwind).

3.2.2. Instrumentation

Air temperature was measured at the Mesonet sites at 1.5 m using the Vaisala HMP35C. Net radiation was measured at the Super Sites at 1.5 m using the Kipp and

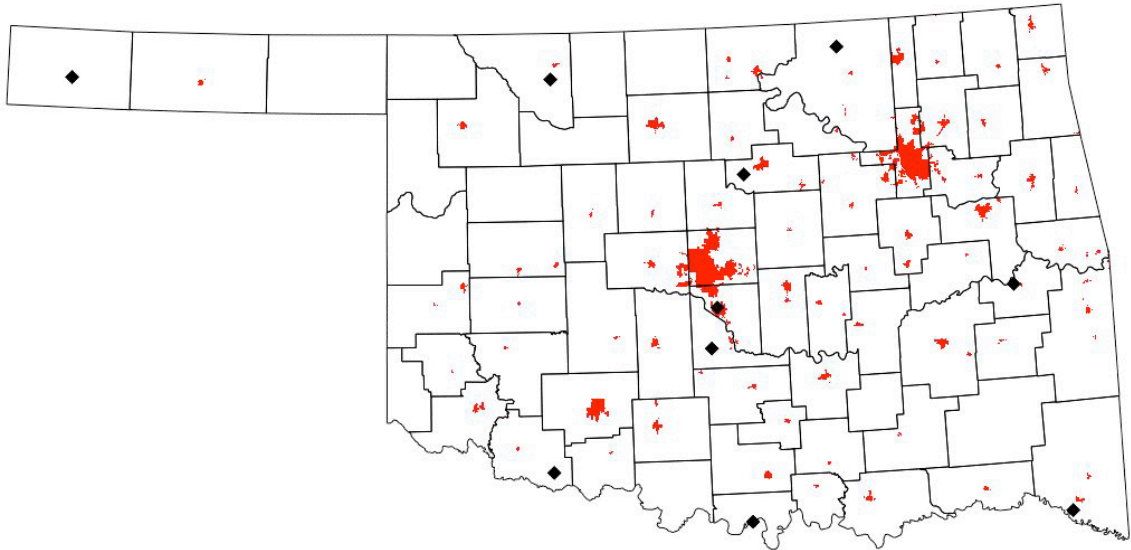


Figure 3.7. Locations of the OASIS Super Sites in July 2003. Super Sites are indicated by solid black diamonds. Urban areas are shaded in red.

Zonen 4-component CNR1 radiometers. The sensible and latent heat fluxes were measured directly via an eddy correlation approach using a CSI CSAT3 sonic anemometer and Krypton hygrometer installed at 4.5 m above ground (Brotzge 2000). During post-processing of the data, a number of algorithms were applied to ensure research quality: an adjustment to account for oxygen absorption by the krypton hygrometer (Tanner et al. 1993), a correction which accounts for density fluctuations caused by the fluxes of heat and moisture (Webb et al. 1980; Tanner et al. 1993), and the coordinate axis rotation (Brotzge 2000). Ground heat flux was estimated using a combination method (Tanner 1960) that uses measurements of soil heat flux using two REBS HFT3.1 heat flux plates. The soil heat storage was estimated using volumetric water content measured by the CSI 229-L heat dissipation probes installed at 5 cm and two REBS platinum resistance temperature detectors (Brotzge 2000; Basara 2001;

Brotzge and Richardson 2003). Surface skin temperature was measured at 2 m using an infrared thermocouple (IRT) sensor manufactured by Apogee (Fiebrich et al. 2003).

Most studies have documented that the eddy correlation technique fails to close the surface energy balance (McNeil and Shuttleworth 1975; Shuttleworth et al. 1984; Dugas et al. 1991; Fritschen et al. 1992; Stannard et al. 1994; Lloyd et al. 1997; Twine et al. 2000; Brotzge 2000; Brotzge and Crawford 2003). Numerous reasons exist for non-closure including surface heterogeneity, slope, and fetch. Brotzge (2000) and Brotzge and Crawford (2003) assessed closure of the surface energy balance at the OASIS Super Sites during 1999 and 2000. The results revealed that in general, the closure was approximately 85-90%, but varied according to location and time of year.

A key consideration for non-closure at OASIS sites includes the instrumentation. The sensible and latent heat fluxes computed via eddy correlation are not only subject to measurement errors, but also represent observations of conditions at and upstream of the site (i.e. fetch). Conversely, net radiation is an integrated measurement at the site spanning the field of view of the sensor. Further, ground heat flux is a point measurement collected in heterogeneous soil and vegetation conditions. All considered, the measured energy budget components represent slightly varying physical scales, which further impact closure. Even so, closure at OASIS sites compared very favorably with other experiments and measurement techniques.

The original OASIS Super Sites, installed in 1999, included 10 stations across Oklahoma, with one in each of Oklahoma's nine climate regions. During July 2002, the original Norman Super Site (NORM) was decommissioned and the new Norman Super

Site (NRMN) was installed approximately 3 km to the south. On 20 August 2002, the Bessie OASIS Super Site (BESS) was downgraded to a standard OASIS site and the Super Site instrumentation was installed at the Washington Mesonet site (WASH). WASH was commissioned as an OASIS Super Site on 20 September 2002.

In 2004, the Oklahoma Mesonet QA staff discovered that several of the KH20 Krypton hygrometers were not performing as desired. As such, the KH20s were removed from the network because the observations were no longer research quality. Although the KH20s were removed from the network in 2004, the sensors were not physically removed from the towers until 2005 (C. A. Fiebrich, personal communication). In 2006, all OASIS Super Sites, except NRMN and WASH, were downgraded. With the change of instrumentation across the network and the conclusion of the OASIS project several years before, “OASIS” was removed from the Mesonet site naming convention on 1 July 2006. NRMN and WASH are now called Oklahoma Mesonet Super Sites while the original 89 standard OASIS sites are designated Oklahoma Mesonet Enhanced Sites.

3.2.3. Quality Assurance of Super Site Data

Because the OASIS measurements were not core variables, they were not regularly QA'd. Initial QA procedures for the OASIS Super Site data collected at WASH, NRMN, and MARE consisted of visually inspecting the radiation and heat flux time-series plots for each site while scanning the data one observation at a time to assign QA flags. These QA procedures were tedious and time consuming. Reliable, automated procedures based on inspection of time series can reduce QA efforts and

provide a consistent product (Lee et al. 2004). Thus, to utilize any automated QA procedures, periods of bad or missing data were documented and entered into the Mesonet's operational QA database.

Latent Heat Fluxes

The KH20's long-term exposure to the elements resulted in a significant decline in data reliability. As a result, the sensor response of the KH20 was examined to determine whether the data for July 2003 were research quality.

The KH20 measures atmospheric water vapor concentration through the absorption of krypton between two windows. The absorption was then translated into a voltage measurement by the sensor. The window on the source tube of the KH20 is prone to scaling that is invisible to the eye caused by disassociation of atmospheric constituents by the ultraviolet radiation. The rate of scaling is a function of the atmospheric humidity and, in high humidity environments, scaling can occur within a few hours. This scaling attenuates the signal and can shift the calibration curve. The effects of scaling can be reversed by wiping the windows with a moist swab. Brotzge (2000) noted that although the scaling on the windows was not directly correlated with inaccurate measurements, it could lead to much greater variability (high-frequency noise) in the collected observations. If the noise becomes indistinguishable from the variance, the observations cannot be trusted. Using this information, time series of the 5-minute average KH20 Krypton voltage and the natural logarithm of the Krypton voltage were plotted for WASH (Fig. 3.8), NRMN (Fig. 3.9), and MARE (Fig. 3.10).

Examination of the Krypton voltages and Mesonet QA database quickly revealed that due to several consecutive cloudy days between 5 June and 19 August 2003, the slave battery for the WASH Super Site fully discharged (Fig. 3.8). As a result, data from WASH were not archived and could not be utilized for this study. The data from the NRMN KH20 yielded a significant reduction in voltage from previous years just prior to JU2003 and failed approximately six months after JU2003 (Fig. 3.9). In addition, several hours of NRMN KH20 data at the beginning of JU2003 were characterized by negative krypton voltages, which are outside the accepted range for the sensor (Mauder and Foken 2004). The MARE KH20 experienced a steady decline in voltage after installation in 1999 (Fig. 3.10). During JU2003, the MARE KH20 voltages never exceeded 50 mV. Network-wide, nearly all sensors failed by 2005. Voltage time

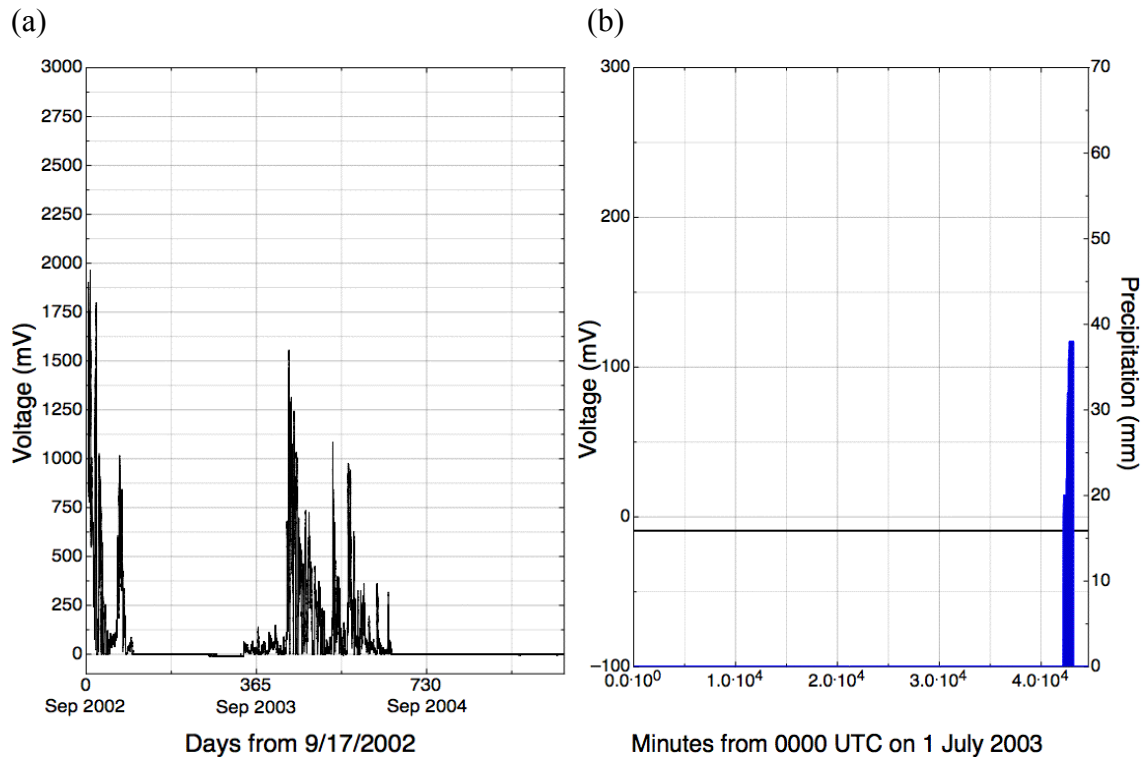


Figure 3.8. Average Krypton voltage (mV; black) and precipitation (mm; blue) at WASH from (a) 17 September 2002 through 5 July 2005, and (b) 1-31 July 2003.

series were also compared with site visit logs to determine what, if any, impact window cleaning had on sensor performance. As with Brotzge (2000), no differences were observed. The reduction in voltages were so great by June 2003, it was determined that data from the KH20s during JU2003 were not research quality. Because the remaining components of the surface energy balance were research quality, latent heat fluxes were estimated as the residual of the surface energy balance. It should be noted that by calculating latent heat flux as the residual of the surface energy balance, the measurement errors in the remaining components are compounded in the estimate of latent heat flux. In addition, the moisture correction cannot be applied to the sensible heat flux values.

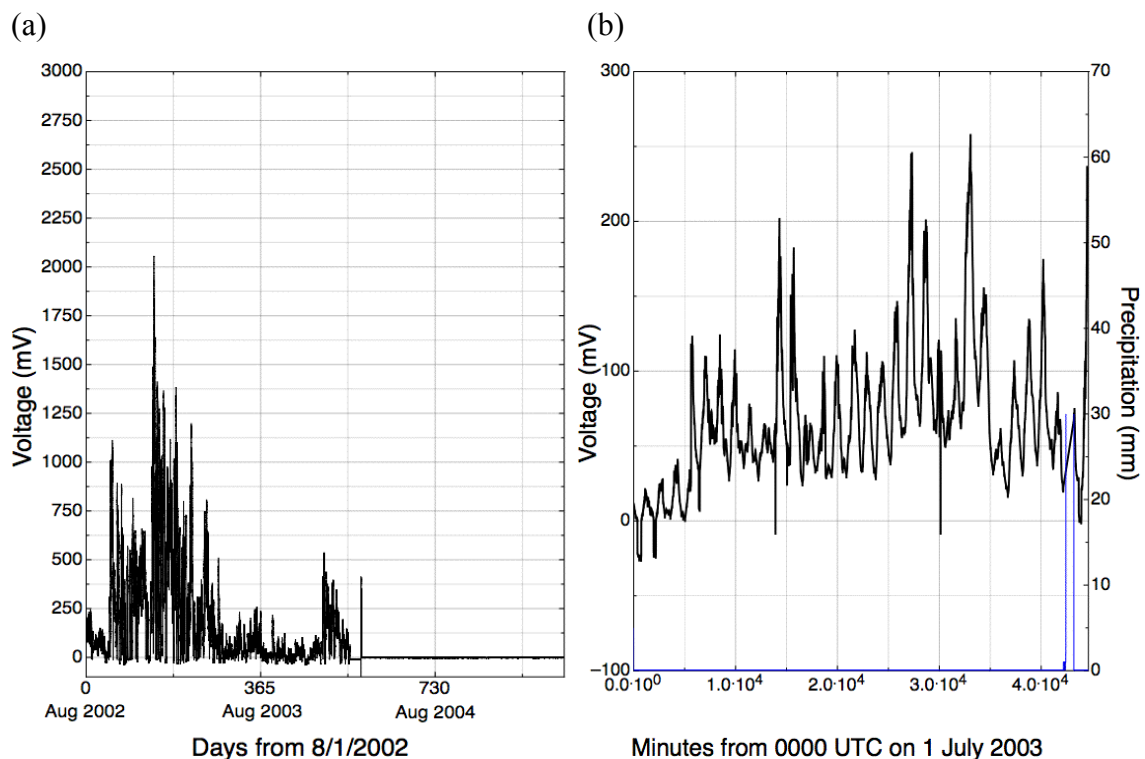


Figure 3.9. Average Krypton voltage (mV; black) and precipitation (mm; blue) at NRMN from (a) 1 August 2002 through 26 April 2005, and (b) 1-31 July 2003.

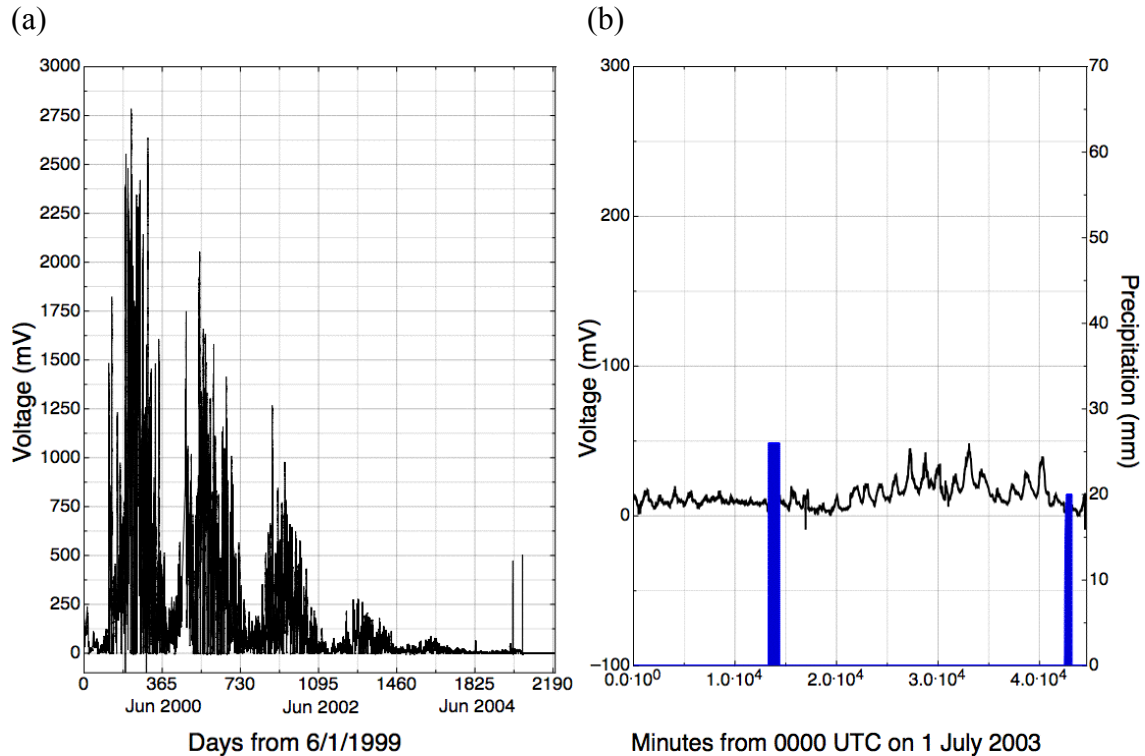


Figure 3.10. Average Krypton voltage (mV; black) and precipitation (mm; blue) at MARE from (a) 1 June 1999 through 31 May 2005, and (b) 1-31 July 2003.

Sensible Heat Fluxes

Prior studies that utilized the OASIS Super Site data and Mesonet documentation noted that the sampling rate of the eddy correlation system was 8 Hz (Brotzge 2000; Sridhar et al. 2002). However, issues with the datalogger restricted the sampling rate to 6 Hz for the period of interest, resulting in 1800 observations per 5-minute sample period (P. K. Hall, Jr., personal communication); the datalogger issue has since been addressed and the current sampling frequency for the CSAT3s at NRMN and WASH is 8 Hz.

The CSAT3 sonic anemometer cannot accurately measure the winds when the transducers are wet without rain protection wicks. Thus, initial efforts to develop automated QA tests began with inspection of all periods of active precipitation. Brotzge

(2000) performed a similar automated test by flagging all eddy correlation data on days with any measured precipitation. While this approach was the simplest way to filter potentially bad observations, it was quickly discovered that this technique also discarded many research quality observations. To avoid the exclusion of research quality data, the periods of active precipitation were documented via graphical inspection of precipitation, net radiation, and sensible heat flux time series (Fig. 3.11). The quality assurance flags for each datum during active precipitation were: 2 = warning, 3 = sensor failure. Sensor failure was defined as the lack of a sensor response, or consecutive observations of sensible heat flux with values of 0.00 W m^{-2} (Fig. 3.11b).

While documenting periods of active precipitation, it was found that periods of questionable data and sensor failure occurred in the absence of precipitation. The datalogger-derived values of sensible heat flux assume a constant air density of 1.2 kg m^{-3} . To account for natural variations in air density, the corrected sensible heat fluxes at OASIS Super Sites include the calculation of the air density via the equation of state with observed values of air temperature and pressure. While documenting active precipitation periods, isolated spikes in corrected sensible heat flux with magnitudes greater than 1000 W m^{-2} were noted. However, coincident spikes in the logger-derived values (Fig. 3.12a) were not noted. Air temperature and pressure data were analyzed and excluded as causes of the spikes. Upon inspection of the data files, it was discovered that covariance values measured by the sonic anemometer with very small magnitudes were expressed in scientific notation, while the ingest software did not support scientific notation. Thus, covariance values listed as $4\text{E-}6$ were ingested as 4.0 instead of

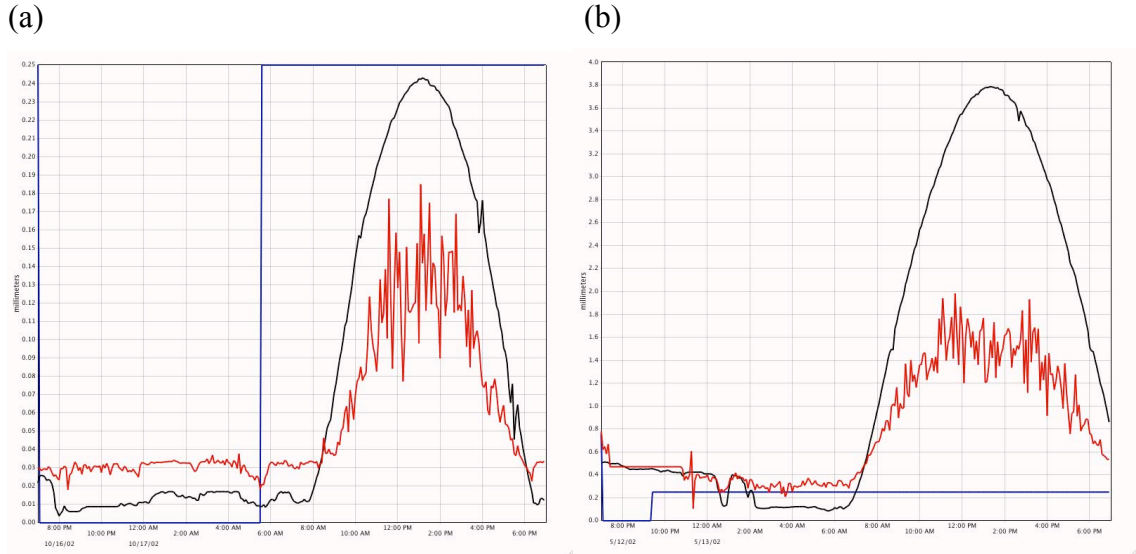


Figure 3.11. Times series of net radiation (W m^{-2} ; black), density-corrected sensible heat flux (W m^{-2} ; red), and precipitation (mm; blue) at MARE on (a) 17 October 2002 and (b) 13 May 2002.

0.000004. As a result, the calculated values of corrected sensible heat flux were one to two orders of magnitude larger than typical peak daytime values. Once the ingest software was modified to allow for scientific notation, the data were reprocessed and corrected.

Conditions favorable for the condensation of water vapor near the surface include clear skies, high relative humidity, and low wind speed. To determine whether sensor failure during periods without precipitation was the result of condensation on the sonic transducers, relative humidity and wind speed data were analyzed. Figure 3.12b illustrates a case of water vapor condensing on the transducers of the sonic anemometer. The relative humidity was greater than or equal to 95% for approximately six hours prior to and during the period of sensor failure. In addition, the wind speeds during this period were less than 2.5 m s^{-1} (not shown). To verify that sensor failure was the result of condensation, surface observations from the Ardmore Municipal Airport (KADM;

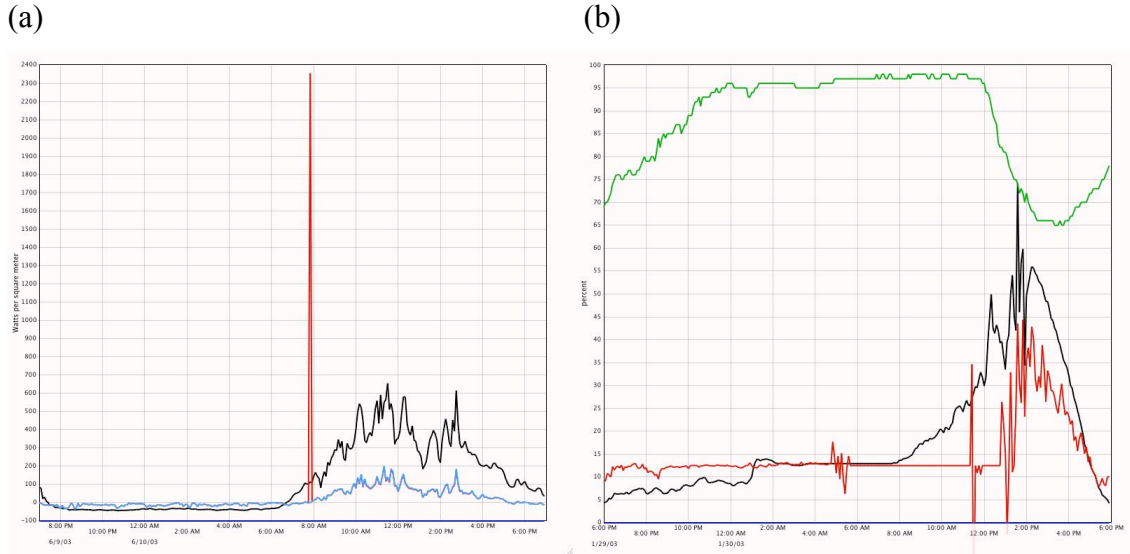


Figure 3.12. Time series plots of net radiation (W m^{-2} ; black), logger-derived sensible heat flux (W m^{-2} ; light blue), density-corrected sensible heat flux (W m^{-2} ; red), precipitation (mm; blue), and relative humidity (%; green) at (a) the Idabel Super Site on 10 June 2003 and (b) Burneyville Super Site on 30 January 2003.

Ardmore, OK), approximately 48 km from Burneyville, were examined. KADM, as well as other surrounding surface observation stations, reported relative humidity values near 100%, overcast cloud cover, and either fog or haze for several hours before and during the period of interest. After investigation of similar occurrences, it was recommended that all periods with relative humidity values greater than 97% and wind speed values less than 2.5 m s^{-1} be flagged by automated routines. Because these conditions do not guarantee sensor failure, inspection of these occurrences by QA meteorologists is necessary to ensure data are flagged correctly.

The sensible heat flux values were also inspected for high amplitude spikes or large changes between consecutive observations. It was found that intermittent clouds on precipitation-free days during the warm season could produce changes up to 250 W m^{-2} between consecutive 5-minute observations. As such, implementation of an

automated QA step test was nearly impossible. Thus, it was determined that visual inspection was the most appropriate manner to evaluate whether large step changes were erroneous because most spikes and large step changes not related to cloud cover would also have failed a precipitation or relative humidity test.

After the subjective manual QA was applied to the sensible heat flux data, the number of high frequency variables missing (NMMISS; Monroe 2007) from the 5-minute mean values was used to identify suspect observations not evident during visible inspection and explain peculiar patterns observed in the data. All 5-minute observations missing more than 300 high frequency values were flagged as suspect data, independent of the manual QA.

Remaining Components of the Surface Energy Balance

The radiative and ground heat flux measurements were not nearly as sensitive to moisture and precipitation as the turbulent fluxes. These observations were visually inspected and subjected to automated range tests described by Brotzge (2000). Because soil moisture measurements are included in the calculation of ground heat fluxes, the automated and manual QA performed by Mesonet QA meteorologists served as a preliminary filter for ground heat fluxes. Due to the co-location of the CNR1 with the NR-LITE used at standard OASIS sites, net radiation values measured by the two sensors were compared to manually detect spurious values. In addition, the downward shortwave radiation from the CNR1 was compared with the co-located measurements of solar radiation from the Li-Cor LI200S pyranometer, a core Mesonet variable. Finally,

the skin temperature values measured by the Apogee IRT were used to calculate upward longwave radiation and compared with the values from the CNR1.

3.3. OKLAHOMA CITY MORPHOLOGY

Burian et al. (2005) analyzed a three-dimensional building dataset, digital orthophotos, detailed land use/land cover information, a digital elevation model, and roads to derive urban morphological characteristics for a 27-km² area of OKC using a GIS. Most of the calculated parameters were similar to those for other cities. Methods of calculation, urban morphological parameters according to land use type, and more

Table 3-3. Urban morphological parameters calculated by Burian et al. (2005) for a 27-km² area of Oklahoma City, Oklahoma.

Land Use Class	Area (km ²)	Plan-area weighted mean building height (m)	Standard deviation of building height (m)	Plan area fraction	Height-to-Width Ratio
Residential	8.71	5.3	2.1	0.08	0.07
Single-family	7.58	4.5	1.8	0.07	0.06
Multi-family	1.13	8.1	6.2	0.14	0.10
Commercial & Services	6.26	9.6	7.3	0.16	0.08
Non-high-rise	6.14	6.8	3.0	0.15	0.07
High-rise	0.12	40.1	25.2	0.71	1.46
Industrial	4.46	6.7	3.8	0.10	0.03
Transportation, Communication, Utility	2.06	4.2	0.9	0.00	0.01
Other Urban or Built-up	5.48	11.6	5.7	0.11	0.05
Vegetated	2.28	4.2	2.2	0.03	0.01
Built-up	3.20	11.7	11.7	0.18	0.08

detailed discussion can be found in Burian et al. (2005). Urban parameters important to this study are listed in Table 3-3.

4. MODELING SYSTEMS

Of the different types of boundaries in atmospheric models, the lower boundary, the land surface, is the one with the most physical significance (Pielke 2002). As a result, varying characteristics of this boundary significantly impact the properties of the overlying PBL. Primarily, the PBL is modified by the land surface through the exchange of water and energy at the land surface-atmosphere interface. In addition, modifications to the PBL by the land surface further impact mesoscale and synoptic scale processes. Thus, because of the critical importance of the land surface in mesoscale atmospheric systems, the interactions between the land surface and the atmosphere must be represented as accurately as possible (Pielke 2002).

4.1. HIGH-RESOLUTION LAND DATA ASSIMILATION SYSTEM (HRLDAS)

The National Center for Atmospheric Research (NCAR) developed the uncoupled High-Resolution Land Data Assimilation System (HRLDAS; Chen et al. 2007), to initialize the land surface states of the Weather Research and Forecasting (WRF) coupled modeling system. The HRLDAS is executed in an uncoupled mode on the same parent and nested grids as the WRF model, ensuring that the coupled WRF model and uncoupled HRLDAS model share the same LSM, land use data, soil texture data, terrain height, vegetation properties, and LSM parameters (Chen et al. 2007). This allows the HRLDAS soil states (soil moisture and soil temperature) to be directly ingested into the coupled WRF model without spatial interpolation.

The foundation of the HRLDAS is the Noah LSM, a soil-vegetation-atmosphere transfer model initially developed at Oregon State University (Pan and Mahrt 1987). Since then, it has been continuously modified by the National Centers for Environmental Prediction (NCEP) and collaborators for use in the NCEP's regional and global prediction models and data assimilation systems (Chen et al. 1996, 1997; Betts et al. 1997; Koren et al. 1999; Ek et al. 2003). The Noah LSM utilizes an implicit surface-layer parameterization scheme based on MOST. Its treatment of canopy resistance depends on soil moisture, solar insolation, water vapor pressure deficit, and air temperature (Chen et al. 1996). In addition, the Noah LSM calculates the thermal conductivity of soil as a function of soil moisture, porosity, quartz content, and dry density (Peters-Lidard et al. 1998). The Noah LSM has four soil layers of thicknesses of 10, 30, 60, and 100 cm, variable rooting depth according to vegetation, and constant total column depth of 200 cm. Details on the physics of the Noah LSM are documented in Appendix A.

4.2. THE WEATHER RESEARCH AND FORECASTING MODEL VERSION 3

The Weather Research and Forecasting (WRF) model (Skamarock et al. 2008) is a modern mesoscale NWP model with two dynamical cores designed to serve both operational forecasting and atmospheric research. The collaborative partners that developed the WRF model include the NCAR, NCEP, Forecast Systems Laboratory, Air Force Weather Agency, Naval Research Laboratory, University of Oklahoma, and Federal Aviation Administration.

The Advanced Research WRF (ARW) model is a fully compressible, non-hydrostatic model that utilizes the terrain-following η -coordinate (Skamarock et al. 2008). The ARW model utilizes a staggered Arakawa-C grid and allows one-way, two-way, and moving nesting. In addition, the ARW model allows users to choose various sub-grid scale parameterization schemes in seven categories: microphysics, cumulus convection, atmospheric radiation, land surface, surface layer, PBL, and turbulent mixing. This study used the WRF model version 3.4.1 with the ARW dynamical core.

4.2.1. Microphysics Schemes in the ARW Model

The microphysics schemes include explicitly resolved water vapor, cloud, and precipitation processes. The WRF Single Moment 6-class (WSM6; Dudhia 1989; Hong et al. 1998, 2004; Dudhia et al. 2008) mixed-phase scheme was used as the microphysics option, as mixed-phased schemes (i.e., interaction of ice and water particles) should be used for grid sizes less than 10 km (Skamarock et al. 2008).

4.2.2. Cumulus Convection Schemes in the ARW Model

The cumulus convection schemes account for the sub-grid scale effects of convective and shallow clouds. They are designed to represent the vertical fluxes due to unresolved updrafts and downdrafts and compensating motion outside of the clouds. When grid sizes are less than 5 km, convective eddies are resolvable and no cumulus convection scheme is needed (Skamarock et al. 2008). This study used the Kain-Fritsch scheme for domains with grid spacings larger than 5 km, due to its thorough testing within the Eta model (Kain 2004).

4.2.3. Atmospheric Radiation Schemes in the ARW Model

The atmospheric radiation schemes represent atmospheric heating due to radiative flux divergence and surface downward longwave and shortwave radiation for the LSM. Longwave radiation includes infrared radiation absorbed and emitted by gases and surfaces. Upward longwave radiation flux from the ground is determined by the surface emissivity, which depends on the land use type and skin (ground) temperature. Shortwave radiation includes visible and surrounding wavelengths that make up the solar spectrum. Thus, the only source of shortwave radiation is the sun. However, processes include absorption, reflection, and scattering in the atmosphere and at surfaces. For shortwave radiation, the upward flux is the reflection due to surface albedo. Within the atmosphere, the radiation responds to model-predicted cloud and water vapor distributions, specified carbon dioxide, ozone, and trace gas concentrations. Atmospheric radiation schemes provide potential temperature tendencies. This study used the Rapid Radiative Transfer Model (RRTM; Mlawer et al. 1997) for longwave radiation and the Dudhia (1989) shortwave radiation scheme. The RRTM and Dudhia schemes have been extensively applied in high-resolution urban WRF studies (Lin et al. 2008; Miao et al. 2009; Grossman-Clarke et al. 2010; Chen et al. 2011a; Hu et al. 2013; Loridan et al. 2013) and allow for a more consistent comparison to prior results for other cities.

4.2.4. Surface Layer Schemes in the ARW Model

The surface layer schemes calculate friction velocities and exchange coefficients that enable the calculation of surface sensible and latent heat fluxes by the land surface

scheme and surface stress in the PBL scheme. Over water surfaces, the surface fluxes and diagnostic fields are computed directly in the surface layer scheme. The schemes provide no tendencies, only the stability-dependent information about the surface layer for the land surface and PBL schemes. Each surface layer scheme is linked to a particular PBL scheme. The MM5 and Eta surface layer schemes were used because they are linked to the two PBL schemes investigated in this study.

The MM5 surface layer scheme uses MOST with stability functions from Paulson (1970), Dyer and Hicks (1970), and Webb (1970) to compute surface exchange coefficients for heat, moisture, and momentum. A convective velocity following Beljaars (1994) is used to enhance surface fluxes of heat and moisture. The four stability regimes follow Zhang and Anthes (1982) and are defined in terms of the bulk Richardson number (Jiménez et al. 2012). For water surfaces, the Beljaars (1994) formulation for convective velocity is replaced by one proportional to the vertical thermal gradient to help in weak-wind situations. Charnock's formula (Charnock 1955) relates roughness length to friction velocity. No thermal roughness length parameterization is included in the MM5 scheme. This surface layer scheme must be used with the Medium Range Forecast (MRF) or Yonsei University (YSU) PBL schemes.

The Eta surface layer scheme (Janjic 1996, 2002) is also based on MOST with stability functions from Paulson (1970) and Holtslag and de Bruin (1988). The Eta surface layer scheme includes parameterizations of a viscous sub-layer. Over water surfaces, the viscous sub-layer is parameterized explicitly according to Janjic (1994).

Over land, the effects of the viscous sub-layer are taken into account through variable roughness heights for temperature and humidity as proposed by Zilitinkevich (1995) where C_{zil} , an empirical coefficient, is set to 0.1 based on field measurements over grassland (Chen et al. 1997). The Beljaars (1994) correction is applied to avoid singularities in cases of an unstable surface layer and vanishing wind speed. The Eta surface layer scheme must be run in conjunction with the Mellor-Yamada-Janjic (MYJ) PBL scheme.

4.2.5. Land Surface Schemes in the ARW Model

The land surface schemes use information from the surface layer, atmospheric radiation, microphysics, and cumulus convection schemes, and information about the land surface state to compute heat and moisture fluxes over land and sea ice. The heat and moisture fluxes then serve as the lower boundary conditions for the PBL schemes. The land surface scheme options that represent soil and vegetation processes with varying complexity. In addition to heat and moisture fluxes, the land surface schemes update the skin temperature, soil temperature profile, soil moisture profile, and snow cover. None of the schemes permit interactions between neighboring grid points. This study used the Noah LSM (Section 4.1; Appendix A) as it is the only land surface scheme that can be coupled with the Single-layer Urban Canopy Model (Section 4.2.7).

4.2.6. Planetary Boundary Layer Schemes in the ARW Model

The PBL scheme uses the surface fluxes calculated by the LSMs and surface layer schemes to represent the sub-grid scale turbulent vertical fluxes of heat, moisture, and momentum within the PBL and the entire atmospheric column. How these vertical

fluxes are represented is referred to as the turbulence closure problem. Two approaches are typically followed, local and non-local closure schemes. Local closure relates the unknown turbulence quantities at a given point in space to known quantities of the flow at the same point (Garratt 1992). This usually involves a flux-gradient term that relates turbulent transfer and molecular diffusion. Non-local closure relates unknown turbulence quantities over a region of space.

When the PBL scheme is activated, explicit vertical diffusion is deactivated under the assumption that the PBL scheme handles this process. The PBL schemes determine the vertical profiles of the temperature, moisture, and horizontal momentum fluxes within the mixed and stable layers, then providing atmospheric tendencies of temperature, moisture, and horizontal momentum in the entire atmospheric column. Most PBL schemes consider dry mixing, but can include saturation effects in the vertical stability that determines the mixing. The schemes are one-dimensional and assume scale separation between sub-grid eddies and resolved eddies. This study used the YSU and MYJ PBL schemes because they are the most widely used schemes applied in urban areas in conjunction with the Single-layer Urban Canopy Model (Lin et al. 2008; Miao et al. 2009; Grossman-Clarke et al. 2010; Flagg and Taylor 2011; Chen et al. 2011b; Hu et al. 2013; Loridan et al. 2013). Two PBL schemes were used to contrast the impact of varying urban parameters with varying the PBL scheme.

The YSU PBL scheme (Hong et al. 2006) is the next generation of the Medium-Range Forecast (MRF) scheme. It is a first-order non-local turbulence closure scheme that incorporates a counter-gradient term that corrects the local gradients of heat and

moisture and incorporates the contribution of large-scale eddies to the total flux in the mixed boundary layer (Hong and Pan 1996). The top of the PBL is defined using a critical bulk Richardson number of zero. The YSU scheme includes explicit treatment of the entrainment layer at the top of the PBL by introducing an entrainment flux term at the inversion layer (Noh et al. 2003; Hong et al. 2006). Above the mixed layer, a local diffusion approach is applied to account for free atmospheric diffusion.

The Mellor-Yamada-Janjić (MYJ) PBL scheme (Janjić 1990, 1996, 2001) is a local turbulence closure scheme. It uses the 1.5-order (level 2.5) turbulence closure model of Mellor and Yamada (1982) and determines eddy diffusion coefficients from prognostically calculated TKE. The MYJ PBL scheme imposes an upper limit on the master length scale, which is a function of the TKE and the buoyancy and shear of the flow. The PBL height is the height at which the TKE reaches a prescribed lower bound.

4.2.7. Single-Layer Urban Canopy Model

A single-layer urban canopy model (SLUCM) may be coupled with the Noah LSM within both the HRLDAS and ARW models using a tile approach (Chen et al. 2011b). Each urban grid box is assigned a fraction of urban surface (urban fraction; f_{urb}) and a fraction of vegetated surface (grassland). Each scheme runs separately and the output fluxes are weighted according to the fraction of the grid cell considered urbanized,

$$Q_{GRID} = Q_{SLUCM} \times f_{urb} + Q_{Noah} \times (1 - f_{urb}), \quad (4.1)$$

where Q_{GRID} is the grid-average value of an outgoing flux, and Q_{SLUCM} and Q_{Noah} refer to the scheme's modeled fluxes (Loridan et al. 2010).

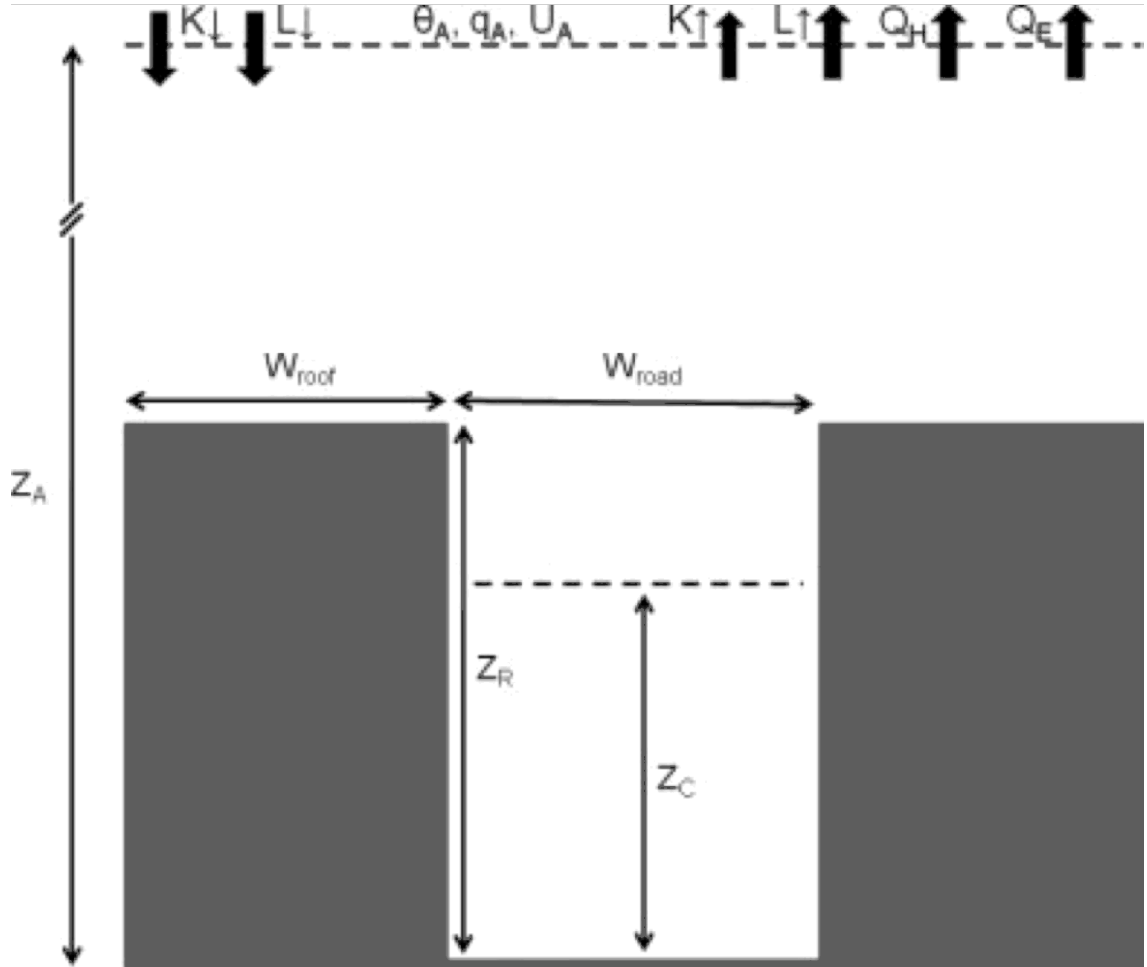


Figure 4.1. Schematic of the two-dimensional canyon used in the SLUCM (Loridan et al. 2010).

The SLUCM is based on 2-dimensional street canyons of infinite length (Kusaka et al. 2001; Kusaka and Kimura 2004a; Chen et al. 2006), defined by mean average values of building height (Z_R), street width (W_{road}), and roof width (W_{roof}) (Fig. 4.1; Loridan et al. 2010). From these defined dimensions, several urban parameters are derived [e.g., normalized canyon height (Z_{norm}), attenuation coefficient in the wind profile (a), roughness lengths for heat and momentum of roof surfaces and the canyon space (Z_{0R} , Z_{0HR} , Z_{0C} , Z_{0HC})]. The portion of canyon surfaces covered by walls, roads, and roofs are normalized by the total width ($W_{roof} + W_{road}$) to provide F_{walls} , F_{roof} , and

F_{road} fractions and determine the contribution each surface type has on the fluxes from the SLUCM

$$Z_{norm} = \frac{Z_R}{W_{roof} + W_{road}}, \quad (4.2)$$

$$F_{walls} = 2Z_{norm} = \frac{2Z_R}{W_{roof} + W_{road}}, \quad (4.3)$$

$$F_{roof} = \frac{W_{roof}}{W_{roof} + W_{road}}, \quad (4.4)$$

$$F_{road} = \frac{W_{road}}{W_{roof} + W_{road}}, \quad (4.5)$$

$$Q_{SLUCM} = F_{roof} Q_{roof} + F_{walls} Q_{walls} + F_{road} Q_{road}. \quad (4.6)$$

Shortwave Radiation Fluxes

The shortwave radiation treatment of the SLUCM includes the effects of shadows on the street canyon. The normalized shadow l_{shadow} on the road is defined as

$$l_{shadow} = \begin{cases} Z_{norm} \tan \theta_z \sin \theta_n & (l_{shadow} < l_{road}) \\ l_{road} & (l_{shadow} > l_{road}) \end{cases}, \quad (4.7)$$

where θ_z is the solar zenith angle and θ_n is the difference between the solar azimuth angle and canyon orientation. The net shortwave radiation absorbed by the roof, wall and road are calculated from

$$S_{roof} = S_D (1 - \alpha_{roof}) + S_Q (1 - \alpha_{roof}), \quad (4.8)$$

$$S_{wall,1} = S_D \frac{l_{shadow}}{2Z_{norm}} (1 - \alpha_{wall}) + S_Q \Phi_{wall \rightarrow sky} (1 - \alpha_{wall}), \quad (4.9)$$

$$\begin{aligned} S_{wall,2} = S_D \frac{l_{road} - l_{shadow}}{l_{road}} \alpha_{road} \Phi_{wall \rightarrow road} (1 - \alpha_{wall}) \\ + S_Q \Phi_{road \rightarrow sky} \alpha_{road} \Phi_{wall \rightarrow road} (1 - \alpha_{wall}) \\ + S_D \frac{l_{shadow}}{2Z_{norm}} \alpha_{wall} \Phi_{wall \rightarrow wall} (1 - \alpha_{wall}) \\ + S_Q \Phi_{wall \rightarrow sky} \alpha_{wall} \Phi_{wall \rightarrow wall} (1 - \alpha_{wall}) \end{aligned}, \quad (4.10)$$

$$S_{road,1} = S_D \frac{l_{road} - l_{shadow}}{l_{road}} (1 - \alpha_{road}) + S_Q F_{road \rightarrow sky} (1 - \alpha_{road}), \quad (4.11)$$

$$S_{road,2} = S_D \frac{l_{shadow}}{2Z_{norm}} \alpha_{wall} \Phi_{road \rightarrow wall} (1 - \alpha_{road}) + S_Q \Phi_{wall \rightarrow sky} \alpha_{wall} \Phi_{road \rightarrow wall} (1 - \alpha_{road}) \quad (4.12)$$

The shortwave radiation is positive when directed towards the surface. S_D and S_Q are direct and diffuse shortwave radiation received by a horizontal surface, respectively. The subscripts 1 and 2 refer to the absorption of direct and reflected radiation, respectively. α_{roof} , α_{wall} , and α_{road} are albedo of the roof, wall, and road surfaces. The view factors required to represent the trapping of radiation inside an infinitely long two-dimensional canyon depend on F_{road} , F_{walls} , and Z_{norm} .

$$\Phi_{wall \rightarrow sky} = \frac{2}{N} \sum_{k=1}^N \left\{ \frac{1}{4} \left(1 + \frac{Z_{norm} - \frac{d_z}{2} - kd_z}{\sqrt{\left(Z_{norm} - \frac{d_z}{2} - kd_z \right)^2 + F_{road}^2}} \right) \right\}, \quad (4.13)$$

$$\Phi_{road \rightarrow sky} = 1 - \left(\frac{F_{walls}}{F_{road}} \right) \Phi_{wall \rightarrow sky}, \quad (4.14)$$

$$\Phi_{wall \rightarrow road} = \Phi_{wall \rightarrow sky}, \quad (4.15)$$

$$\Phi_{wall \rightarrow wall} = 1 - (\Phi_{wall \rightarrow sky} + \Phi_{wall \rightarrow road}), \quad (4.16)$$

$$d_z = \frac{Z_{norm}}{N+1} \quad N: \text{iteration limit } (N=100). \quad (4.17)$$

Diffuse shortwave and downward longwave radiation are assumed to be emitted from the entire sky.

Longwave Radiation Fluxes

The net longwave radiation fluxes absorbed by the roof, wall, and ground (road) surfaces are calculated from

$$L_{roof} = \varepsilon_{roof} (L \downarrow - \sigma T_{roof}^4), \quad (4.17)$$

$$L_{wall,1} = \varepsilon_{wall} \left(\begin{array}{l} L \downarrow \Phi_{wall \rightarrow sky} + \varepsilon_{road} \sigma T_{road}^4 F_{wall \rightarrow road} \\ + \varepsilon_{wall} \sigma T_{wall}^4 \Phi_{wall \rightarrow wall} - \sigma T_{wall}^4 \end{array} \right), \quad (4.18)$$

$$L_{wall,2} = \varepsilon_{wall} \left[\begin{array}{l} (1 - \varepsilon_{road}) L \downarrow \Phi_{road \rightarrow sky} \Phi_{wall \rightarrow road} \\ + (1 - \varepsilon_{road}) \varepsilon_{wall} \sigma T_{wall}^4 \Phi_{road \rightarrow wall} \Phi_{wall \rightarrow road} \\ + (1 - \varepsilon_{wall}) L \downarrow \Phi_{wall \rightarrow sky} \Phi_{wall \rightarrow wall} \\ + (1 - \varepsilon_{wall}) \varepsilon_{road} \sigma T_{road}^4 \Phi_{wall \rightarrow road} \Phi_{wall \rightarrow wall} \\ + \varepsilon_{wall} (1 - \varepsilon_{wall}) \sigma T_{wall}^4 \Phi_{road \rightarrow wall} \Phi_{wall \rightarrow wall} \end{array} \right], \quad (4.19)$$

$$L_{road,1} = \varepsilon_{road} \left[L \downarrow \Phi_{road \rightarrow sky} + \varepsilon_{wall} \sigma T_{wall}^4 \Phi_{road \rightarrow wall} - \sigma T_{road}^4 \right], \quad (4.20)$$

$$L_{road,2} = \varepsilon_{road} \left[\begin{array}{l} (1 - \varepsilon_{wall}) L \downarrow \Phi_{wall \rightarrow sky} \Phi_{road \rightarrow wall} \\ + (1 - \varepsilon_{wall}) \varepsilon_{road} \sigma T_{road}^4 \Phi_{wall \rightarrow road} \Phi_{road \rightarrow wall} \\ + \varepsilon_{wall} (1 - \varepsilon_{wall}) \sigma T_{wall}^4 \Phi_{wall \rightarrow wall} \Phi_{road \rightarrow wall} \end{array} \right]. \quad (4.21)$$

$L \downarrow$ is the downward atmospheric longwave radiation. T_{roof} , T_{wall} , and T_{road} are the surface temperatures of the roof, wall, and road, respectively. The subscripts 1 and 2 refer to the absorption of direct and reflected radiation.

Turbulent Heat Fluxes

Bulk transfer equations are used to model the sensible heat fluxes (H_{roof}) and latent heat fluxes (LE_{roof}) above roof surfaces in the SLUCM

$$H_{roof} = -\rho c_p C_{roof} U_A (T_A - T_{roof}), \quad (4.22)$$

$$LE_{roof} = -\rho L_v C_{roof} U_A \beta_{roof} (q_A - q_{roof}), \quad (4.23)$$

where the subscript A refers to the atmospheric forcing of temperature (T), specific humidity (q), and wind (U), ρ is the density of air, c_p is the specific heat, L_v is the latent heat of vaporization, and β_{roof} is the minimum soil moisture availability of the roof.

MOST is applied to determine the turbulent exchange coefficients above the roof and canyon space and are identical to those calculated by the surface layer scheme

(Section 4.2.4). The canyon roughness length for momentum (Z_{0C}) and zero-plane displacement height (Z_D) are parameterized as functions of canyon geometry

$$Z_{0C} = Z_R \left(1 - \frac{Z_D}{Z_R}\right) \exp \left\{ - \left[0.5 \beta_m \frac{C_D}{k^2} \left(1 - \frac{Z_D}{Z_R}\right) \left(\frac{Z_{norm}}{W_{roof} + W_{road}} \right) \right]^{-0.5} \right\}, \quad (4.24)$$

$$Z_D = Z_R \left[1 + \alpha_m^{-F_{roof}} (F_{roof} - 1) \right], \quad (4.25)$$

where $C_D = 1.2$ for the drag coefficient (Grimmond and Oke 1999c) and $\beta_m = 1.0$ and $\alpha_m = 4.43$ for empirical constants (MacDonald et al. 1998).

The sensible heat fluxes from wall and road surfaces are derived from Jurges' formula (Kusaka et al. 2001)

$$H_{walls} = C_{wall} (T_{wall} - T_{canopy}), \quad (4.26)$$

$$H_{road} = C_{road} (T_{road} - T_{canopy}), \quad (4.27)$$

$$C_{wall} = C_{road} = \begin{cases} 7.51 U_{canopy}^{0.78} & (U_{canopy} \geq 5 \text{ ms}^{-1}) \\ 6.15 + 4.18 U_{canopy} & (U_{canopy} < 5 \text{ ms}^{-1}) \end{cases}, \quad (4.28)$$

where H_{walls} and H_{road} are the sensible heat fluxes from the wall and road, respectively. C_{wall} and C_{road} are the wall and road exchange coefficients for heat, respectively. T_{wall} and T_{road} are the surface temperatures at the wall and road, respectively. T_{canopy} is the urban canopy air temperature. U_{canopy} is the wind speed within the canyon.

The latent heat fluxes from wall (LE_{walls}) and road (LE_{road}) surfaces are calculated as

$$LE_{walls} = -\rho L_v C_{wall} U_A \beta_{wall} (q_A - q_{wall}), \quad (4.29)$$

$$LE_{road} = -\rho L_v C_{road} U_A \beta_{road} (q_A - q_{road}), \quad (4.30)$$

where C_{wall} and C_{road} are defined in Equation 4.28. β_{wall} and β_{road} are the minimum soil moisture availabilities of the wall and road surfaces, respectively.

The roof, wall, and road surface temperatures are derived as temperatures that balance the SEBs on the individual canyon surfaces through their effects on the heat fluxes. The one-dimensional energy conservation equation is solved to calculate the roof, wall, and road interior temperatures for the layers. The boundary condition is zero heat flux (used in current study) or constant temperature in the bottom layer. The ground heat flux ($G_{Z,S}$) and interior temperature ($T_{Z,S}$) at depth Z to the S surface are calculated by

$$G_{Z,S} = -k_S \frac{\partial T_{Z,S}}{\partial z}, \quad (4.31)$$

$$\frac{\partial T_{Z,S}}{\partial t} = -\frac{1}{\rho_S c_S} \frac{\partial G_{Z,S}}{\partial z}, \quad (4.32)$$

where k_S is the thermal conductivity and $\rho_S c_S$ is the volumetric heat capacity that are specific to the surface S . The subscript S refers to the roof, wall, or road surface. Equation 4.6 is then used to calculate the SLUCM heat fluxes.

Wind Speed Within the Canopy

The mean wind speed within the urban canopy (U_{canopy}) at height $Z_C = 0.7Z_R$ is used as a reference to calculate the turbulent fluxes from the wall and road surfaces. Because the SLUCM does not compute the wind profile down to the street level, a logarithmic profile is assumed from the height of the first model level (Z_A) to the top of the buildings (Z_R). An exponential profile is assumed from Z_R to Z_C . The wind speed at roof level (U_{roof}) and U_{canopy} are calculated as

$$U_{canopy} = U_{roof} e^{-a\left(1-\frac{Z_C}{Z_R}\right)}, \quad (4.33)$$

$$U_{roof} = U_A \frac{\ln\left(\frac{Z_R - Z_D}{Z_{0C}}\right)}{\ln\left(\frac{Z_A - Z_D}{Z_{0C}}\right)}, \quad (4.34)$$

$$a = \frac{kZ_R}{l_m \ln\left(\frac{Z_R - Z_D}{Z_{0C}}\right)}, \quad (4.35)$$

$$l_m = k(Z_R - Z_D), \quad (4.36)$$

where U_A is the wind speed at the height of the first model level, a is an attenuation coefficient (Inoue 1963) and l_m is the mixing length.

4.3. ATMOSPHERIC DATA

The ability of a LSM to accurately represent land surface-atmosphere interactions depends not only on the model physics, but also on the atmospheric forcing data ingested by the model (typically provided by an atmospheric model). This project uses data from the North American Regional Reanalysis (NARR; Mesinger et al. 2006) for initial and lateral boundary conditions for the WRF model, and near-surface atmospheric data for the HRLDAS model. The NCEP NARR is a long-term (1979-present) atmospheric and land surface dataset for North America (Mesinger et al. 2006). The NARR system includes: 32-km grid spacing, 45 vertical layers, NCEP's mesoscale Eta forecast model and the Eta Data Assimilation System (EDAS; Rogers et al. 2001), the Noah LSM, and the assimilation of observed precipitation. Due to the project emphasis on the surface energy balance, downward shortwave radiation data from Phase 2 of the North American Land Data Assimilation System (NLDAS-2; Xia et al. 2012) were used for the HRLDAS model. When compared with observations from the Oklahoma Mesonet, the NARR data display high bias in downward shortwave radiation

during the daytime (Monroe 2007). The NLDAS-2 uses a ratio-based algorithm to correct the downward shortwave radiation from the NARR towards a 5-year (1996 – 2000) GOES retrieved solar radiation (Pinker et al. 2003; Cosgrove and Alonge 2008).

5. URBAN-RURAL COMPARISON OF OBSERVATIONS

The magnitude of urban-atmosphere interactions is often estimated by comparing data from an urban area with observations from the surrounding rural area (Oke 1987). The surface data collected during JU2003 were utilized to quantify the overall effects of the urban canopy on the urban heat island.

To minimize the impacts of varying cloud cover between observation sites and observe the maximum urban-atmosphere interactions, 10 days during JU2003 characterized by strong radiative forcing and weak wind shear were chosen for the urban-rural comparison (3, 10, 11, 14, 15, 16, 17, 19, 23, and 24 July 2003). For each of the 10 days, solar insolation was near theoretical values.

5.1. AIR TEMPERATURE

Data from the 32 PNNL HOBO temperature data loggers and 6 Oklahoma Mesonet sites surrounding the OKC metropolitan area (Fig. 5.1; ELRE, GUTH, KING, MINC, NRMN, and SPEN) were block averaged to hourly values. The Mesonet hourly values were then averaged across all six sites to create a mean diurnal cycle of rural air temperatures (Basara et al. 2008). Similarly, the HOBO hourly values were averaged across all 32 HOBO sites to create a mean diurnal cycle of urban air temperatures. The mean diurnal cycle of the UHI intensity (ΔT_{u-r}) was also calculated.

The mean diurnal cycles of urban air temperatures, rural air temperatures, and ΔT_{u-r} are illustrated in Figure 5.2. Consistent with other studies (Wanner and Hertig 1984; Ackerman 1985; Kim and Baik 2005; Basara et al. 2008), the UHI intensity was strongest during the overnight hours and was negative (i.e., urban cool island) during

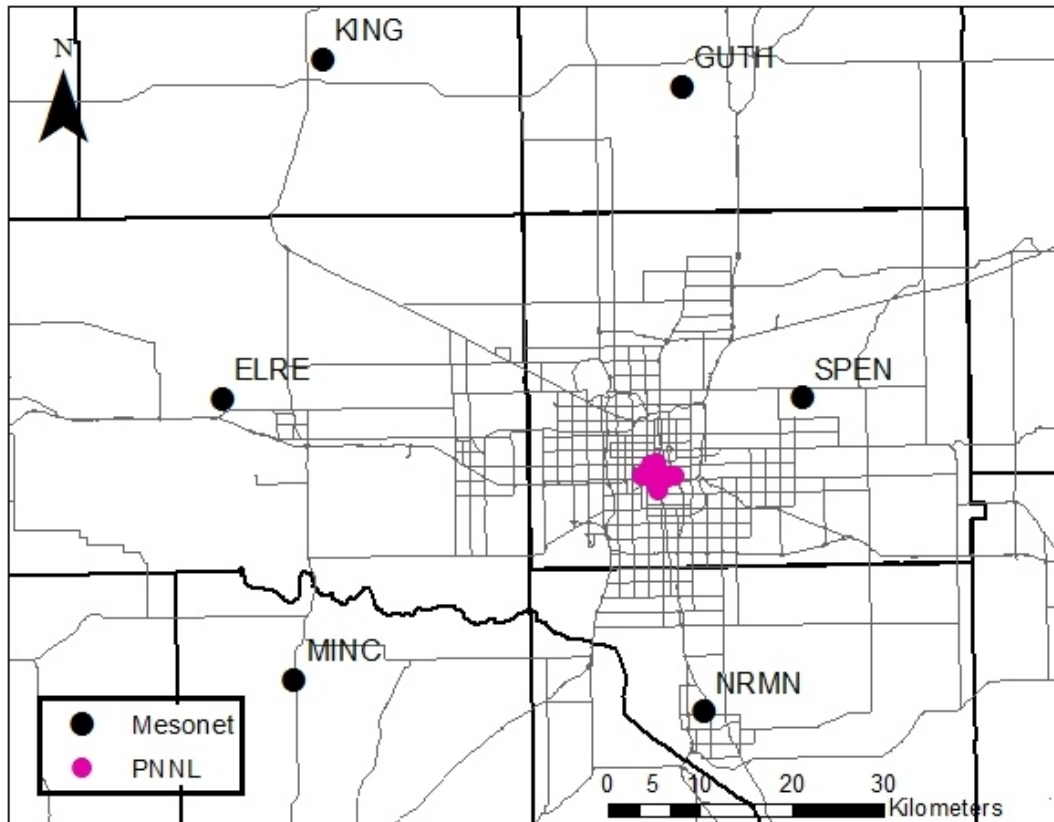


Figure 5.1. Locations of the HOBO temperature data loggers deployed by Pacific Northwest National Laboratory (PNNL) and the surrounding Oklahoma Mesonet sites during Joint Urban 2003.

the daytime hours. During the nighttime hours, ΔT_{u-r} values peaked at 1.5 K, with the maximum UHI intensity occurring between 0300 and 0500 UTC (1 to 3 hours after sunset). Conversely, during the daytime the values of ΔT_{u-r} were negative and the urban areas were 1.2 K cooler than rural locations. The rural temperature values warmed faster than the urban values following sunrise and cooled faster after sunset. Basara et al. (2008) provided the following as possible reasons for the differences in urban and rural heating/cooling rates: greater turbulent mixing in the rural locations following sunrise coupled with shadowing of urban sites, greater heat storage in the urban areas following sunset, and greater spatial variability of temperatures measured at the rural Mesonet

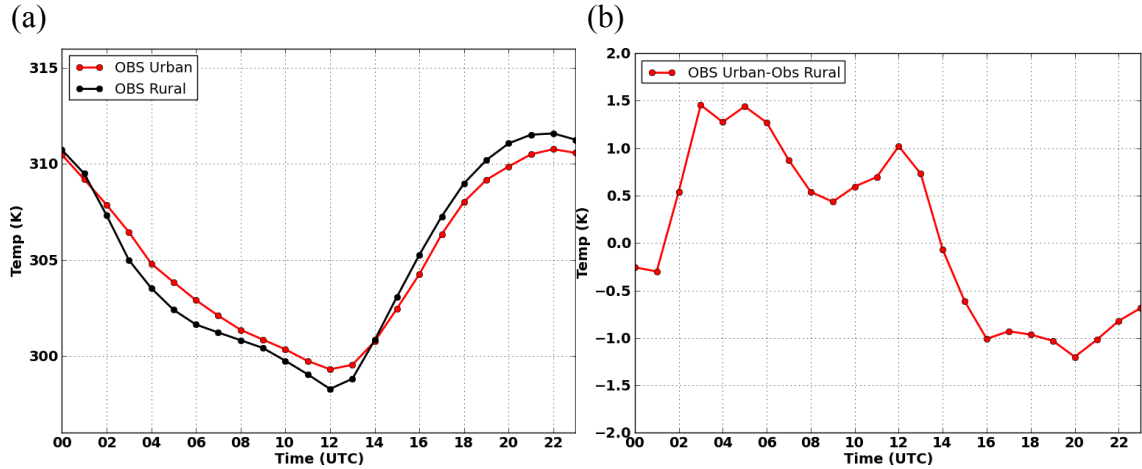


Figure 5.2. The mean diurnal cycles of (a) urban air temperatures (red) and rural air temperatures (black) and (b) temperature differences between urban and rural locations from 10 days with solar insolation near theoretical values during July 2003.

sites. The possible role of urban Q_E in moderating daytime urban temperatures is investigated in Section 5.2 as the ATDD Concrete and Gravel energy balance sites were located along the east-west transect of the HOBO sites.

5.2. COMPONENTS OF THE SURFACE ENERGY BALANCE

Data from the Mesonet Super Sites (5-min averages), ASU site (5-min and 1-min averages), and ATDD sites (30-min averages) were block averaged to hourly values to reduce the highly variable nature of the flux measurements and ensure consistency across the JU2003 dataset. Mean diurnal cycles were created for the following variables: K_{\downarrow} , K_{\uparrow} , L_{\downarrow} , L_{\uparrow} , Q^* , Q_G , Q_H , and Q_E . Components of the SEB not directly measured (Q_E at NRMN and MARE; Q_G at ATDD Gravel, IU TMA, TMB, and WH) were estimated as the residuals of the SEB equations, when possible. It should be noted that the residual approach allowed any anthropogenic heat flux and the measurement

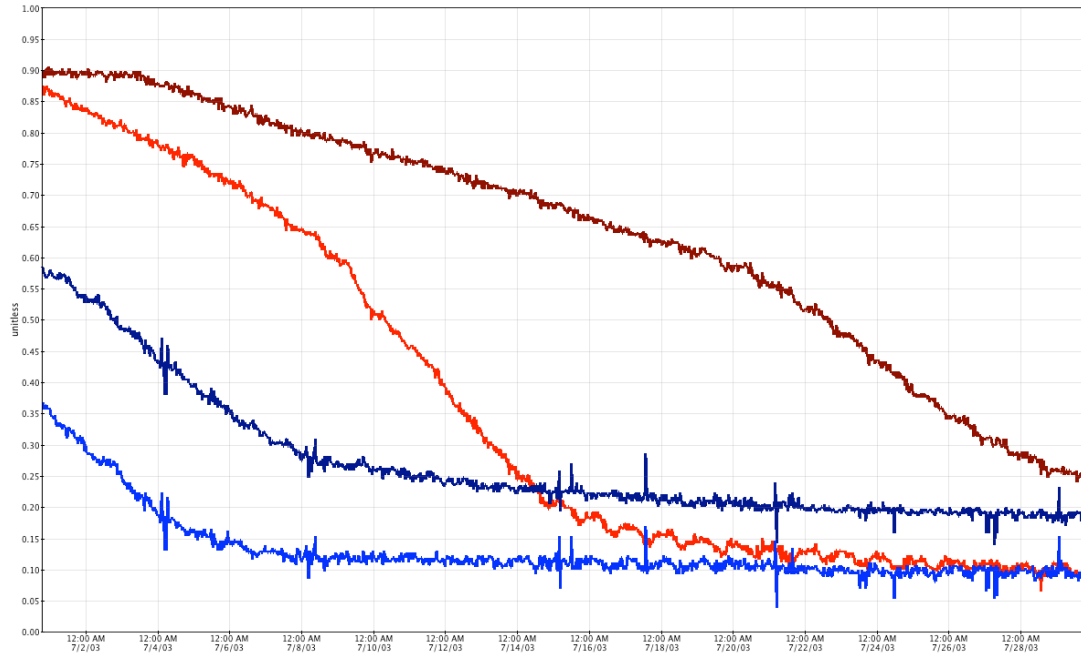


Figure 5.3. Time series of fractional water index at 25 cm at NRMN (light blue), 60 cm at NRMN (dark blue), 25 cm at MARE (red), and 60 cm at MARE (dark red) for 1-30 July 2003.

errors in the other terms of the SEB equation to accumulate in the estimated term. Thus, the residual terms were interpreted as upper limits to the variables estimated.

Prior to JU2003, Oklahoma experienced below-average temperatures and above-average rainfall; June 2003 was 8th coolest and 25th wettest June in Oklahoma's 112-year climate record (McManus 2003a). An unseasonably strong cold front produced over 7.5 cm of rain at MARE on 25-26 June (McManus 2003b). As a result, the soil conditions at the two rural reference sites for the urban-rural comparison, NRMN and MARE, were significantly different; the soil moisture values at MARE were higher than at NRMN (Fig. 5.3).

July 2003 yielded below-average rainfall and above-average temperatures and was the fourth driest July on record (McManus 2003b). Thus, the soil profiles at both

the NRMN and MARE sites dried through the period and, by 20 July 2003, the 25-cm fractional water index at MARE was within 0.05 of the 25-cm fractional water index at NRMN. However, it was not until 29 July that the 60-cm fractional water indices at NRMN and MARE were within 0.05 of each other. Because MARE was anomalously moist compared to the other locations of the study due to the isolated precipitation event, NRMN was selected as the rural reference site. The components of the SEB at the ASU, IU (GR, BH, TMA, TMB, and WH), and ATDD (Gravel and Concrete) sites were all compared with the NRMN site data.

Figure 5.4 displays the mean diurnal cycles of K_{\downarrow} (a) and K_{\uparrow} (b), as well as the urban-rural differences with NRMN as the rural reference site (c, d). Except for during sunrise and sunset at the ASU and ATDD Concrete site, K_{\downarrow} at both the urban and rural sites are within the approximate range of instrument error (± 5 to 10%) and variation between instrument manufacturers. After inspection of each daily diurnal cycle for the ASU site (not shown), it was determined that the -52 W m^{-2} spike in K_{\downarrow} at 1300 UTC (Fig. 5.4c) was due to a shadow from a 17-meter tree approximately 29 m to the east of the ASU tower. At very low sun angles, just after sunrise, the shadow of the tree was cast over the pyranometer. The ATDD Concrete site displayed 60 W m^{-2} decreases in K_{\downarrow} at sunrise and 80 to 100 W m^{-2} decreases in K_{\downarrow} at sunset due to building shadows.

The effect of the tree shadow was also evident in the mean diurnal cycle of K_{\uparrow} one hour later at 1400 UTC (Fig. 5.4b, d). The delay in timing of the tree shadow in K_{\uparrow} was likely due to the horizontal distance between the sensors. In addition, values of K_{\uparrow} at the ASU site were 10 to 34 W m^{-2} greater than K_{\uparrow} observed at NRMN during the

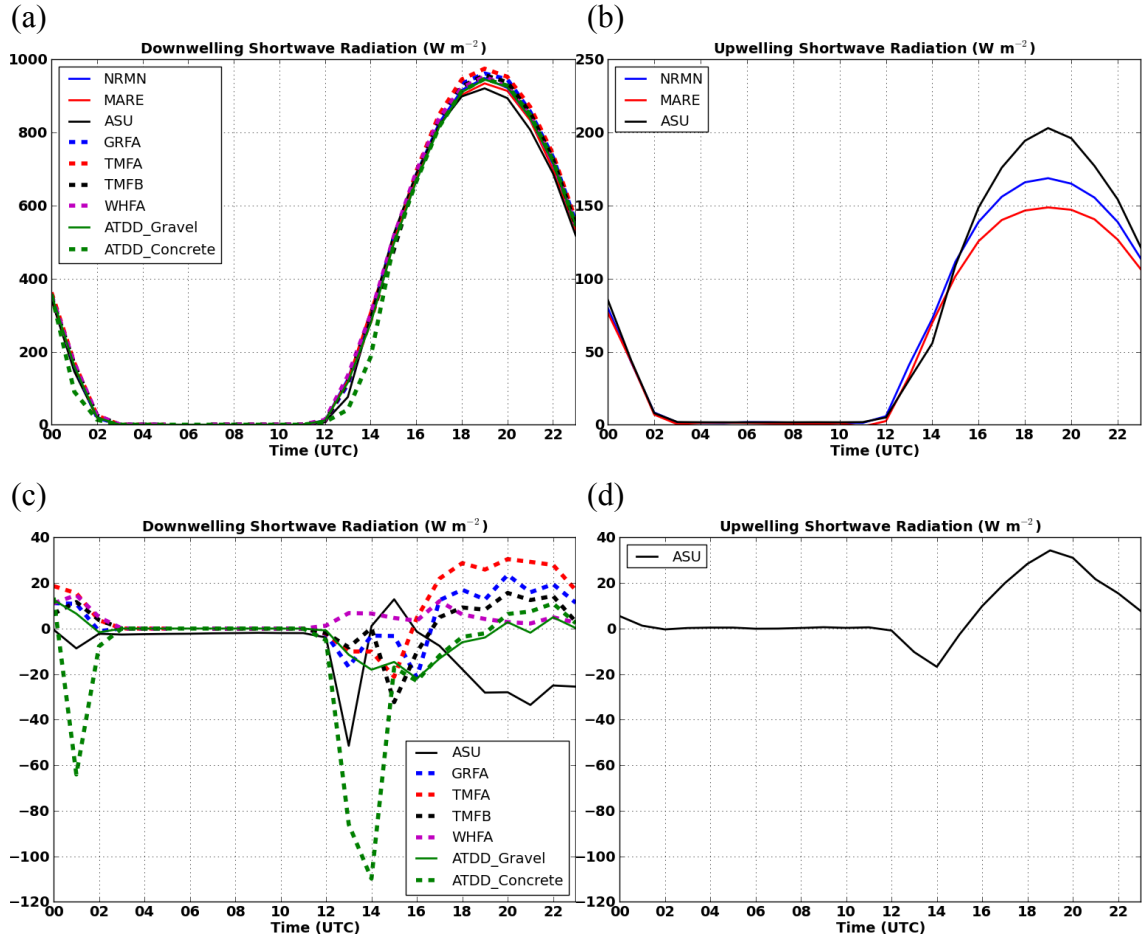


Figure 5.4. The mean diurnal cycles of (a) downwelling shortwave radiation and (b) upwelling shortwave radiation at the NRMN, MARE, ASU, IU BH, IU GR, IU TMA, IU TMB, IU WH, ATDD Gravel, and ATDD Concrete sites from 10 days with solar insolation near theoretical values during July 2003. The respective differences between urban (ASU, ATDD, IU) and rural (NRMN) mean diurnal cycles of (c) downwelling shortwave radiation and (d) upwelling shortwave radiation.

daytime, due to the higher albedo as a result of drier soils downwind of OKC's CBD.

The increased values of $K\uparrow$ contradicted to the results of Aida (1982) and Christen and Vogt (2004), which concluded that $K\uparrow$ is less in urban areas than in rural areas due to radiation trapping in urban canyons and the decreased albedo of construction materials commonly found in urban areas. However, the ASU site was located in an open grassy field northwest of the CBD. As a result, the construction materials of the urban canopy

were not within the optical path of the pyranometer and radiation trapping was minimal. Thus, the dry soil conditions dominated the diurnal trend of K_{\uparrow} at the ASU site. Conversely, values of K_{\uparrow} at the MARE site were 10 to 20 $W\ m^{-2}$ less than that at NRMN during daytime hours due to the lower albedo as a result of the wetter soils from the significant rainfall received prior to JU2003. The coefficients of determination (R^2) and slopes of the best-fit lines are presented in Table 5-1. The scatterplots associated with the information in Table 5-1 can be found in Appendix B.

The mean diurnal cycles of L_{\downarrow} and L_{\uparrow} are illustrated in Figure 5.5. L_{\downarrow} was only available for the two rural sites. Values of L_{\downarrow} observed at NRMN were 5 $W\ m^{-2}$ less than that at MARE during nighttime hours and 10 to 18 $W\ m^{-2}$ less during daytime hours. The increased L_{\downarrow} at MARE was supported by increased atmospheric moisture due to recent

Table 5-1. The coefficients of determination (R^2) and slopes of the best-fit lines for the components of the surface energy balance at the ASU, ATDD, and IU sites relative to NRMN from 10 days with solar insolation near theoretical values during July 2003.

	ASU		IU GR		IU BH		IU TMA		IU TMB		IU WH		ATDD Gravel		ATDD Concrete	
	R^2	Slope	R^2	Slope	R^2	Slope	R^2	Slope	R^2	Slope	R^2	Slope	R^2	Slope	R^2	Slope
K_{\downarrow}	0.998	0.981	0.999	1.009	—	—	0.999	1.030	0.999	1.006	0.999	1.005	0.999	0.994	0.992	1.008
Q^*	0.992	0.897	0.993	0.842	—	—	0.996	1.015	0.998	0.995	0.996	0.977	0.996	0.874	0.990	0.905
Q_H	0.939	0.883	0.843	0.865	0.730	0.866	0.678	0.793	0.773	0.795	0.754	0.763	0.915	0.72	0.793	0.657
Q_E	0.860	0.281	0.704	0.711	0.706	0.930	0.411	0.718	0.683	0.746	0.743	0.731	0.339	0.068	0.069	0.032
Q_G	0.839	0.887	0.530	0.248	—	—	0.585	1.892	0.727	1.824	0.773	1.854	—	—	0.320	1.087

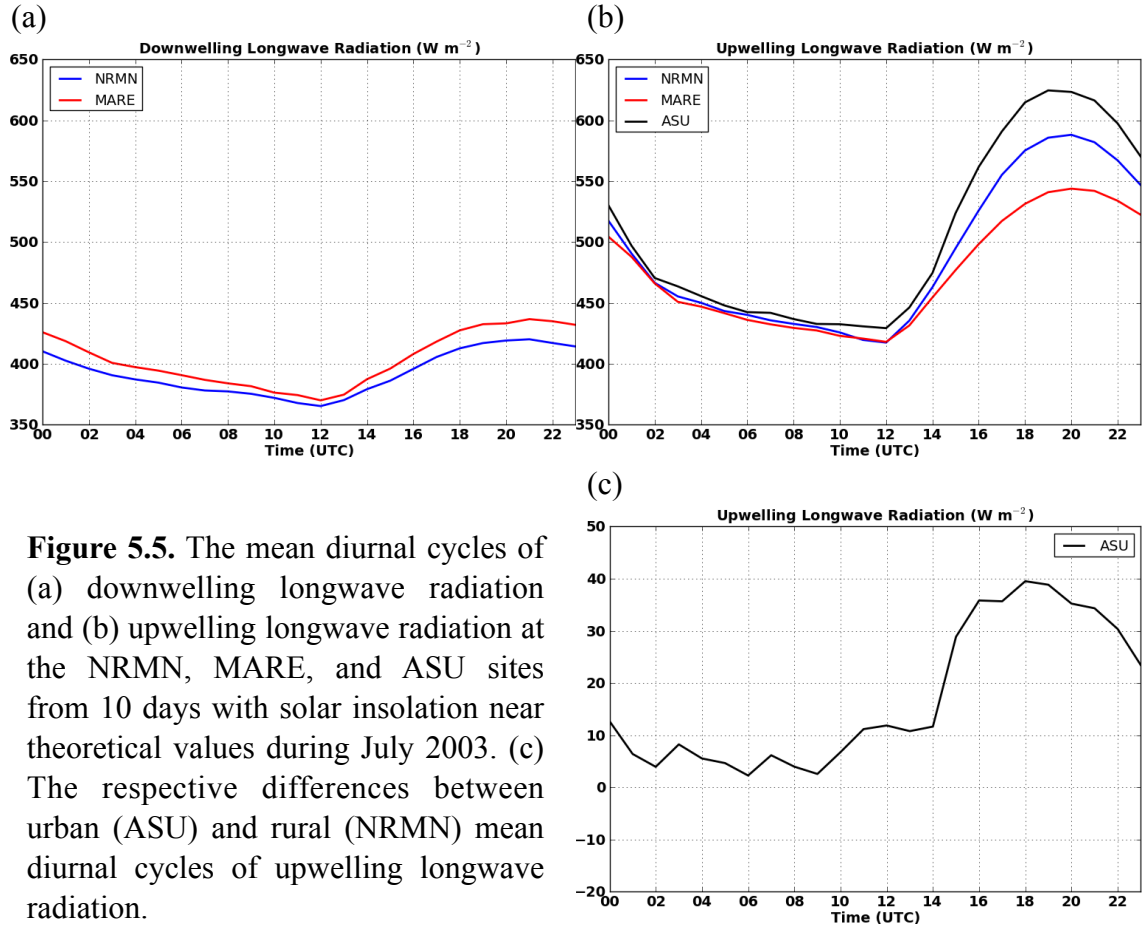


Figure 5.5. The mean diurnal cycles of (a) downwelling longwave radiation and (b) upwelling longwave radiation at the NRMN, MARE, and ASU sites from 10 days with solar insolation near theoretical values during July 2003. (c) The respective differences between urban (ASU) and rural (NRMN) mean diurnal cycles of upwelling longwave radiation.

heavy rainfall.

The values of L_{\uparrow} observed at the ASU site were greater than those observed at the NRMN site during all hours of the day (Fig. 5.5b, c). However, the largest urban-rural differences occurred during the daytime hours, during which values of L_{\uparrow} at the ASU site were 10 to 40 $W m^{-2}$ greater than L_{\uparrow} observed at the NRMN site and were the result of increased surface temperatures due to relatively dry soil conditions. The increased L_{\uparrow} also resulted in air temperatures at the ASU site that increased more quickly after sunrise compared to the IU sites (not shown). Values of L_{\uparrow} at the MARE site were 20 to 45 $W m^{-2}$ less than those at the NRMN site. The increased soil moisture

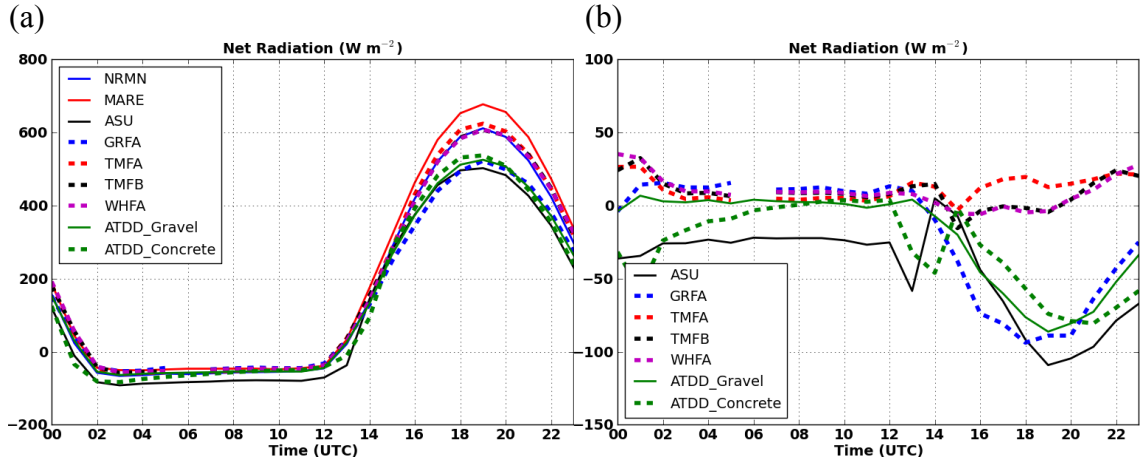


Figure 5.6. (a) The mean diurnal cycles of net radiation at the NRMN, MARE, ASU, IU BH, IU GR, IU TMA, IU TMB, IU WH, ATDD Gravel, and ATDD Concrete sites from 10 days with solar insolation near theoretical values during July 2003. (b) The respective differences between urban (ASU, ATDD, IU) and rural (NRMN) mean diurnal cycles of net radiation.

at the MARE site (1) increased the soil heat capacity and (2) reduced the heating rate and temperature of the land surface, effectively reducing $L\uparrow$.

The mean diurnal cycles of Q^* are displayed in Figure 5.6a, b. For values of Q^* , IU TMA, TMB, and WH are within the range of instrument error of NRMN for all hours of the day. The vertical distance between TMA and TMB influenced values of Q^* during daytime hours more than the horizontal distance between TMB and WH (~ 0.5 km; Fig. 5.6b). The TMA net radiometer, mounted ~ 43 m higher than the TMB radiometer, measured larger values of Q^* during the daytime than the TMB net radiometer, consistent with observations of $K\downarrow$. The mean peak values of Q^* at ASU, IU GR, ATDD Gravel, and ATDD Concrete were approximately 75 to 100 $W m^{-2}$ less than those observed at NRMN and IU TMA, TMB, and WH (Fig. 5.6a, b). Daytime trends of Q^* measured at the ASU site were primarily due to the combination of increased values of $K\uparrow$ and $L\uparrow$, which resulted from decreased albedo and increased surface temperatures

due to dry soil conditions relative to NRMN. The effects of the tree shadow for ASU and building shadows for ATDD Concrete noted in the discussion of K_{\downarrow} are also evident in the mean diurnal cycles of Q^* . Values of Q^* observed at the ASU site during the nighttime hours were approximately 25 W m^{-2} less than values observed at all other SEB sites due to the increased L_{\uparrow} . Conversely, Q^* observed at the MARE site was greater than that observed at NRMN during the daytime hours. The decreased K_{\uparrow} and

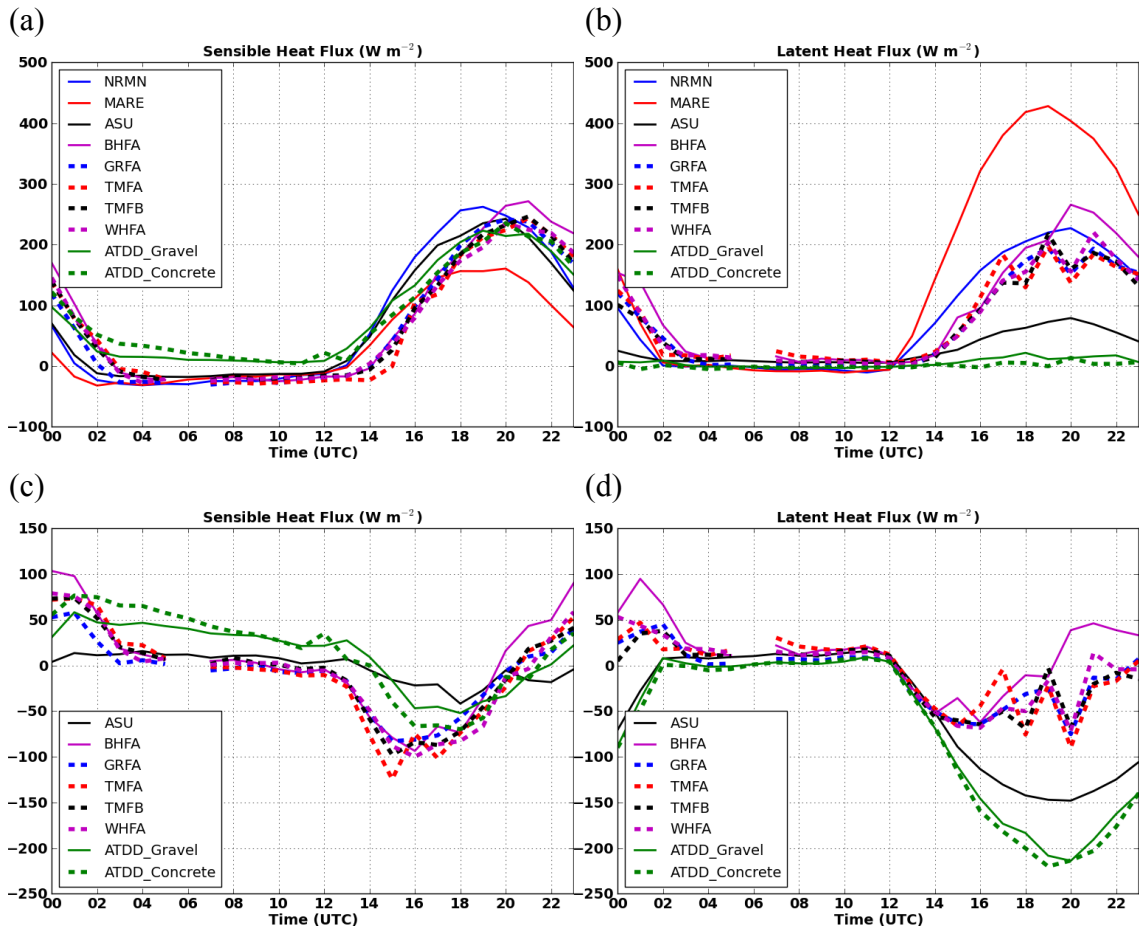


Figure 5.7. The mean diurnal cycles of (a) sensible heat flux and (b) latent heat flux at the NRMN, MARE, ASU, IU BH, IU GR, IU TMA, IU TMB, IU WH, ATDD Gravel, and ATDD Concrete sites from 10 days with solar insolation near theoretical values during July 2003. The respective differences between urban (ASU, ATDD, IU) and rural (NRMN) mean diurnal cycles of (c) sensible heat flux and (d) latent heat flux.

$L\uparrow$, and increased $L\downarrow$, which resulted from the significant rainfall difference between NRMN and MARE, were the primary contributing factors.

Figure 5.7 displays the mean diurnal cycles of Q_H (a) and Q_E (b), as well as the urban-rural differences with NRMN as the rural reference site (c, d). All sites over grass maintained negative values of Q_H during the nighttime hours. The urban Q_H diurnal cycles lagged the rural diurnal cycles such that urban Q_H peaked 1 to 2 hours later than rural Q_H . With exception of the ASU site, urban Q_H values remained positive approximately one hour later than rural values, which may be important in the growth of the UHI (Oke 1987). The ATDD Gravel and Concrete sites maintained positive Q_H throughout the night (25 to 50 $W m^{-2}$). Despite the differences in surface cover at the sites (grass, gravel, concrete), the peak daytime values of Q_H were surprisingly consistent across the urban sites. The curve of Q_H at MARE yielded an amplitude approximately 100 $W m^{-2}$ less than NRMN due to the significant rainfall received prior to JU2003.

Q_E measured at the urban sites exhibited a similar one-hour lag as Q_H . As with Q_H , the amplitude of the diurnal cycle observed at most of the urban sites was similar in magnitude to that observed at the NRMN site (Fig. 5.7). However, the peak values of Q_E observed at the ASU site and the ATDD sites were approximately 150 $W m^{-2}$ and 220 $W m^{-2}$ less than those observed at the NRMN site, respectively. As a result, it is unlikely that Q_E in the CBD played a significant role on the development of the urban cool island during the day. On the other hand, peak values of Q_E observed at the MARE site were more than 200 $W m^{-2}$ greater than values observed at NRMN.

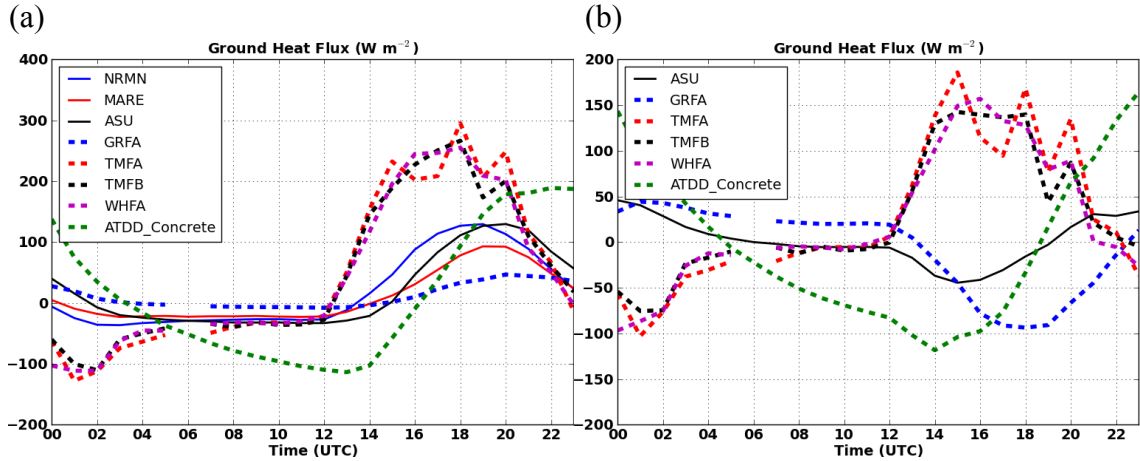


Figure 5.8. (a) The mean diurnal cycles of ground heat flux at the NRMN, MARE, ASU, IU BH, IU GR, IU TMA, IU TMB, IU WH, ATDD Gravel, and ATDD Concrete sites from 10 days with solar insolation near theoretical values during July 2003. (b) The respective differences between urban (ASU, ATDD, IU) and rural (NRMN) mean diurnal cycles of storage heat flux.

Two methods were used to estimate Q_G , measurement via soil heat flux plates (NRMN, MARE, ASU, IU GR, ATDD Concrete) and residual of the SEB (Q_{Gres} ; IU TMA, TMB, WH) and the diurnal trends in Q_G depended heavily on the method of estimation. During the nighttime hours, values of Q_{Gres} reached minimum values of approximately $-100 W m^{-2}$ near sunset when stored heat was released as $L\uparrow$, Q_H , and Q_E and then decayed throughout the night (Christen and Vogt 2004). The differences in daytime values of Q_{Gres} between sites (IU TMA, TMB, WH) reflected trends in Q_E , which were discussed in the preceding paragraphs. Relative to the Q_G measured with soil heat flux plates, the mean diurnal cycles of Q_{Gres} were characterized by a much more pronounced temporal hysteresis (Fig. 5.8), where peak values of Q_{Gres} were reached one to two hours before peak values of Q_G were observed. The largest differences between the residual and measured variables occurred at times of highest

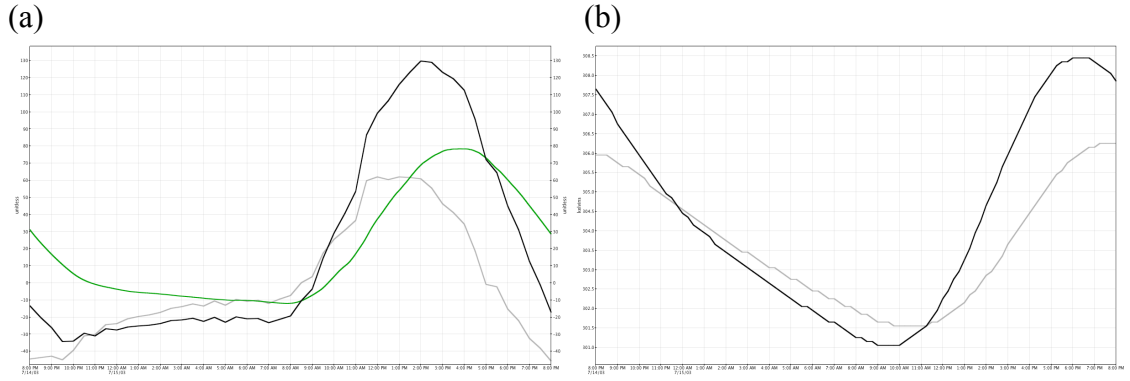


Figure 5.9. The diurnal cycles of (a) the conductive heat flux at a fixed depth (green), energy stored in the layer above the heat flux plates (grey), and the surface storage heat flux (black); and (b) soil temperatures under sod at 5 cm (black) and 10 cm (grey) at the NRMN site from 14 July 2003.

energy input, which Weber (2006) attributed to systematic underestimation of one of the measured turbulent fluxes.

Measurements of Q_G obtained with soil heat flux plates exhibited significant site-to-site variability. Except for a one-hour time lag, the diurnal cycle of values of Q_G observed at NRMN and ASU were similar. Surprisingly, the ASU curve peaked one hour later than the NRMN curve. As mentioned in Section 2.2.1, measurements of Q_G are calculated from the measured conductive heat flux at a fixed depth and the storage term.

Based on values observed at the NRMN site, it can be assumed that the diurnal cycle of Q_G measured at the ASU site heavily depended on the conductive heat flux, typically measured 6.5 cm below ground level (Fig. 5.9a), which results in significant errors in Q_G (Mayocchi and Bristow 1995). An explanation for a strong dependence of Q_G on the conductive heat flux includes underestimation of the specific heat of the soil in the sampling of bulk density and/or soil water content by mass. On the other hand,

incorrect installation of the soil temperature sensors (e.g., installed at an angle) could result in the measurement being taken at a deeper depth than intended, delaying and reducing the amplitude of the diurnal cycle, as illustrated by the diurnal cycles of soil temperature at 5 cm and 10 cm at the NRMN site in Figure 5.9b.

The diurnal cycle of Q_G observed at the IU GR site exhibited a similar time lag as the ASU site, with a daytime peak approximately 75 W m^{-2} less than the NRMN site. The diurnal cycle of Q_G at the ATDD Concrete site lagged the ASU and IU GR sites by 1 to 2 hours. These results contradict those of Doll et al. (1985), who placed soil temperature probes in concrete by drilling holes, placing the sensors at the recording levels, and then backfilling fill concrete. Doll et al. (1985) found Q_G values measured in soil lagged Q_G measured in concrete. When accounting for the Q_G in the concrete layer as well as the soil below concrete, Q_G for soil peaked approximately two hours earlier than for concrete (Doll et al. 1985). Due to a lack of metadata regarding how Q_G was measured for the concrete surface, the only conclusion drawn is that Q_G measured at the site was only based on the conductive heat flux.

Finally, the peak values of Q_G observed at the MARE site were approximately 50 W m^{-2} less than the NRMN peak values, with the MARE curve peaking later than the NRMN curve as a result of the slow heating of the soil due to evapotranspiration supported by the moist soils.

5.3. PARTITIONING OF AVAILABLE ENERGY

In addition to comparing the diurnal cycles of individual components of the SEB across all sites, the partitioning of available energy into Q_H , Q_E , and ΔQ_S at each site

Table 5-2. Mean daily values of net radiation, sensible heat flux, latent heat flux, storage heat flux, normalized sensible heat flux, normalized latent heat flux, normalized storage heat flux, and Bowen ratio ($\beta = Q_H/Q_E$) calculated over daytime observations from 10 days with solar insolation near theoretical values during July 2003.

Site	Q^*	Q_H	Q_E	Q_G	Q_H/Q^*	Q_E/Q^*	Q_G/Q^*	β
NRMN	414.17	177.58	164.78	72.30	0.43	0.40	0.17	1.08
MARE	464.40	105.83	312.04	46.57	0.23	0.67	0.10	0.34
ASU	350.93	161.90	50.17	70.81	0.46	0.14	0.20	3.23
IU GR	358.70	152.74	132.50	27.15	0.43	0.37	0.08	1.15
IU BH	—	168.32	165.37	—	—	—	—	1.02
IU TMA	430.05	145.22	132.42	150.14	0.34	0.31	0.35	1.10
IU TMB	421.17	150.18	127.63	143.82	0.36	0.30	0.34	1.18
IU WH	421.63	148.39	136.45	136.79	0.35	0.32	0.32	1.09
Gravel	365.17	161.17	11.54	—	0.44	0.03	—	13.97
Concrete	389.90	168.20	4.18	108.33	0.43	0.01	0.28	40.24

was investigated. Table 5-2 presents mean fluxes and mean normalized fluxes calculated over daytime observations from 10 days with solar insolation near theoretical values. Daytime observations were defined by values of Q^* greater than 100 W m^{-2} to avoid stable or near-neutral boundary layer conditions typical at sunrise (Hernandez-Ramirez et al. 2009).

For the ASU site, 46% of the available energy was partitioned into Q_H , 14% into Q_E , and 20% into Q_G . These results are consistent with the range of values published for Q_H and Q_E for sites located within the urban core (Grimmond et al. 2004a; Christen and Vogt 2004; Offerle et al. 2006a). For the IU GR site, Q_H accounted for 43%, Q_E accounted for 37%, and Q_G accounted for 8% of available energy. For the IU TMA, TMB and WH, available energy was nearly equally partitioned across Q_H , Q_E , and Q_G ,

approximately 35%, 31%, and 34%, respectively. These values are consistent with energy partitioning in suburban neighborhoods of other metropolitan areas (Grimmond et al. 2004a; Christen and Vogt 2004; Offerle et al. 2006a). For the ATDD sites, Q_H accounted for 43 to 44% of available energy, slightly lower than estimates for urban core sites where Q_H typically accounts for 50 to 95% of available energy (Grimmond et al. 2004a; Christen and Vogt 2004; Offerle et al. 2006a; Loridan and Grimmond 2012). Q_E only accounted for 1 to 3% of available energy at the ATDD sites. Q_G accounted for 28% of available energy for the ATDD Concrete site. The MARE site was the only site consistent with rural areas, where Q_H accounted for only 23% of available energy, and Q_G for 10%. Because Q_E was determined as the residual of the SEB, Q_E accounted for 67% of the available energy.

The normalized heat fluxes at the three sites that measured each component of the SEB allowed for a crude estimate of SEB closure. Closure at the ASU, IU GR, and ATDD Concrete sites was 81%, 87%, and 72%, respectively. Sporadic data outages during the field experiment contributed to the lack of closure at the ASU and IU GR sites. The atypical timing of the diurnal cycle of Q_G at the ATDD Concrete site likely played a significant role in the lack of closure at the site.

6. MODEL EXPERIMENTS

6.1. EXPERIMENT DESIGN

The case investigated in the current study was 0000 UTC 14 July 2003 to 0000 UTC 16 July 2003. This case was chosen because it includes two consecutive days analyzed in Chapter 5 where few, if any, clouds were present and the low-level jet was relatively weak (Fast et al. 2005; Hu et al. 2013).

Validating grid-average model results with instantaneous point-scale observations is a recurring problem. Averaging point-scale observations in time partially

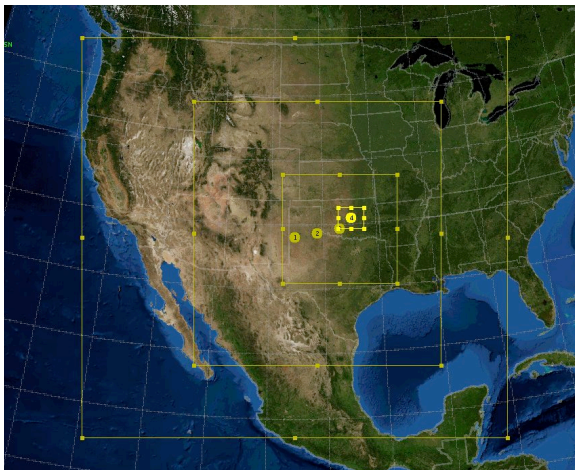


Figure 6.1. Locations of domains employed in the WRF and HRLDAS models.

remedies this problem by increasing the source area or field of view of the instrument. Time averaging allows point measurements to involve a spatial average. Due to the heterogeneous nature of urban areas and the relatively small number of SEB sites during

JU2003, the observed data were block-averaged to hourly values and used primarily to investigate the importance of four urban canopy parameters relative to the variability of the observations.

6.1.1. Model Domain Specifications

Version 3.4.1 of the HRLDAS and WRF models utilized four domains with one-way nesting, 40 vertical levels, and grid spacings of 27 km, 9 km, 3 km, and 1 km (Fig. 6.1). The innermost domain was centered over OKC. The physics options used were

outlined in Chapter 4. The initial atmospheric and all lateral boundary conditions for the WRF model were provided from the NARR data. The initial land surface states for the WRF model are outlined in Section 6.1.3. The NARR data provided the atmospheric data and initial conditions for the HRLDAS model.

The urban land use categories were derived from the National Land Cover Data 2001 (NLCD 2014). The four urban land use types (Developed, Open Space; Developed, Low Intensity; Developed, Medium Intensity; and Developed, High Intensity) were aggregated into three categories: low-intensity residential (LIR), high-intensity residential (HIR), and industrial/commercial (I/C). Outside of urban areas, the USGS land-use and soil texture data were used.

6.1.2. Urban Canopy Parameters

In version 3.4.1 of the WRF model, the SLUCM looks up approximately 30 input parameters for the thermal properties of the surfaces, dimensions of canyon geometry, and internal building temperatures (Loridan et al. 2010; Wang et al. 2011) from a table with three different urban classes (LIR, HIR, and I/C). Some studies either use the default values or do not specify whether urban canopy parameter values were modified (Holt and Pullen 2007; Lin et al. 2008; Miao et al. 2009; Tewari et al. 2010; Zhang et al. 2011; Hu et al. 2013). Users should adapt the values based on the city of interest (Grossman-Clarke et al. 2010; Flagg and Taylor 2011; Carter et al. 2012; Kim et al. 2013).

The performance of the SLUCM depends, in part, on the accuracy of the input parameters (Wang et al. 2011). Due to the high level of uncertainty in the specification

of urban canopy parameter values, two studies have implemented complex methods to thoroughly determine the sensitivity of the offline SLUCM to urban parameter values. Loridan et al. (2010) used the Multiobjective Shuffled Complex Evolution Metropolis (MOSCEM) algorithm (Vrugt et al. 2003) to examine the sensitivity of the components of the SEB in the offline SLUCM to variations in the SLUCM and Noah LSM parameters. Wang et al. (2011) used an advanced Monte Carlo simulation tool, subset simulation (Au and Beck 2001), to conduct an analysis of the sensitivity of heat fluxes and surface temperatures to changes in individual urban canopy parameters in the offline SLUCM. These two studies revealed a strong sensitivity to roof parameters and weak sensitivity to road parameters (Loridan et al. 2010; Wang et al. 2011). The two studies disagreed on the importance of roof, building, and road emissivities. Wang et al. (2011) found that emissivity of roof, building, and road surfaces had minimal impacts while Loridan et al. (2010) found the roof emissivity increased Q_H . Urban fraction was the only urban parameter to impact Q_E , as it is handled entirely by the Noah LSM (Loridan et al. 2010).

Some studies have investigated the sensitivity of a small number of urban parameters using the fully coupled WRF-Noah-SLUCM. For example, Lin et al. (2008) examined the impact of variations of Q_F on the PBL height and surface air temperature. They also examined the impacts of heat capacity, thermal conductivity, albedo, and roughness length of the roof, building wall, and ground surfaces. Similarly, Miao et al. (2009) conducted four tests by increasing and decreasing building heights and Q_F .

The current study is unique in that it examines the sensitivity to parameter changes in both coupled (WRF-Noah-SLUCM) and uncoupled (HRLDAS-Noah-SLUCM) modes. The findings of Loridan et al. (2010) and Wang et al. (2011) were used to narrow down the list of urban canopy parameters to investigate. Table 6-1 and Appendix C list the parameter values used in the coupled and uncoupled SLUCM

Table 6-1. Urban canopy parameter values selected for Oklahoma City sensitivity analysis for low-intensity residential (LIR), high-intensity residential (HIR), and industrial/commercial (I/C) land use categories. Bold numbers indicate values used in the Control model prediction.

Parameter	LIR	HIR	I/C	Reference
Building height (Z_R)	4.5	8.1	8.4	Burian et al. (2005)
	5.0	7.5	10.0	Default
Standard deviation of building height (σ_z)	1.8	6.2	8.9	Burian et al. (2005)
	1.0	3.0	4.0	Default
Roof width (W_{roof})	8.7	13.4	23.7	
	11.7	17.4	30.7	Burian et al. (2005)
	14.7	21.4	37.7	
Thermal conductivity of roof (k_{roof})	0.05	0.05	0.05	Roberts et al. (2006)
	0.74	0.74	0.74	ASHRAE (2009)
	1.40	1.40	1.40	Roberts et al. (2006)
Surface albedo of roof (α_{roof})	0.05	0.05	0.05	Loridan et al. (2010)
	0.20	0.20	0.20	Default
	0.40	0.40	0.40	Loridan et al. (2010)
Road width (W_{road})	7.50	7.50	7.50	Scott (2006)
Urban fraction (f_{urb})	0.50	0.90	0.95	Default
	0.40	0.50	0.60	

predictions for the sensitivity analysis, as well as parameter values that were changed from their default values due to additional data sources specific to OKC. Building height (Z_R) and standard deviation of building height (σ_z) were taken directly from the values derived by Burian et al. (2005) for Single-family (single house lots) and Multifamily (multiple-unit structures) land use categories of the Association of Central Oklahoma Governments, respectively. The I/C values for SLUCM were derived by combining the Commercial and Services; Industrial; Transportation, Communication, and Utility, and the Built-up sub-category of the Other Urban or Built-up land use types. Roof width (W_{roof}) was derived from Building Plan Area of Burian et al. (2005) assuming buildings were square shaped. Had distance between buildings from Burian et al. (2005) been used to prescribe road width (W_{road}) in the SLUCM, W_{road} would have varied between 75 and 182 m. Instead, Scott (2006) was used to convert the average number of lanes for over 55,000 road segments in the OKC metropolitan area to W_{road} using the standard lane width of 3.6 m used by the U.S. Interstate Highway System (FHWA 2013). It should be noted that Q_F was neglected in the current study.

Each urban canopy parameter was changed one at a time for both the WRF and HRLDAS model predictions. Initially, seven model runs were conducted for each PBL scheme. The control set of parameter values (control run) are presented in bold in Table 6-1. The naming convention for the parameter deviations relative to the control run are explained in Table 6-2. The Z_R , σ_z , and f_{urb} variations were run with the YSU PBL scheme only.

Table 6-2. Descriptions of the parameter variations for each HRLDAS and WRF model predictions.

Model Run	Description
arook_up	α_{roof} set to 0.40 for all urban categories (LIR, HIR, I/C)
arook_down	α_{roof} set to 0.05 for all urban categories (LIR, HIR, I/C)
krook_up	k_{roof} set to 1.4 for all urban categories (LIR, HIR, I/C)
krook_down	k_{roof} set to 0.05 for all urban categories (LIR, HIR, I/C)
Wrook_up	W_{roof} set to 14.7 (LIR), 21.4 (HIR), and 37.7 (I/C)
Wrook_down	W_{roof} set to 8.7 (LIR), 13.4 (HIR), and 23.7 (I/C)
defZR	Z_R set to the default values of 5.0 (LIR), 7.5 (HIR), and 10.0 (I/C)
defZR_SigmaZ	Z_R set to the default values of 5.0 (LIR), 7.5 (HIR), and 10.0 (I/C) σ_z set to the default values of 1.0 (LIR), 3.0 (HIR), and 4.0 (I/C)
defSigmaZ	σ_z set to the default values of 1.0 (LIR), 3.0 (HIR), and 4.0 (I/C)
furb	f_{urb} set to 0.40 (LIR), 0.50 (HIR), and 0.60 (I/C)

6.1.3. Land Surface Initialization

The reliability of a LSM is limited by the accuracy of the forcing data and initial conditions (Rodell et al. 2005; de Goncalves et al. 2006). In addition, each LSM has a unique land surface equilibrium that is determined primarily by the model physics (Cosgrove et al. 2003; Rodell et al 2005). If the initial conditions deviate from the land surface equilibrium, the model must adjust to the forcing fields until they reach an equilibrium state (i.e., model spin-up). Consequently, if the model spin-up process is not executed properly, the initial conditions may produce errors whereby the land surface state drifts toward the model equilibrium. For example, Chen and Dudhia (2001) discovered that a 10% change in initial soil moisture resulted in a 30-W m⁻² variation in surface fluxes while a change of 0.1 in the initial soil moisture caused a change of approximately 200 W m⁻². Further, the influence of initial soil moisture on the surface

heat fluxes was carried over into the 24- to 48-hour simulation period (Chen and Dudhia 2001).

In the case where long-term forcing datasets are not available, a common method to spin up the LSM is to recursively simulate a single year (Chen et al. 1997; Schlosser et al. 2000; Cosgrove et al. 2003; Rodell et al. 2005; de Goncalves et al. 2006). As such, spin-up is considered complete when the land surface states cease to vary significantly from one year to the next. However, one year is rarely representative of climatological conditions. As a result, meteorological anomalies can accumulate in the land surface states and the land surface can equilibrate to an unnatural state (Schlosser et al. 2000; Rodell et al. 2005).

Cosgrove et al. (2003) determined that rough equilibrium could be reached within 1 to 2 years and fine scale equilibrium within 5.5 years with the Noah LSM. This estimate is consistent with the 16 months of spin-up time required to reach rough equilibrium for sandy clay loam soils noted by Chen et al. (2007). Given the multiple years of the NARR forcing data available (1979-2003) prior to the period of interest, the current study opted for the more conservative approach and used a 5-year spin-up time using the HRLDAS model. All four domains for the control run were initialized with the NARR data on 1 June 1998. The Noah LSM was run within the HRLDAS using the NARR data and NLDAS-2 solar radiation data through 31 July 2003. A restart file was saved for 5 February 2003 and used to allow each variation in urban parameter (Table 6-2) to spin up for four months. The HRLDAS model output for 0000 UTC for 14 July 2003 replaced the NARR surface states in the WRF input files (i.e., wrfinput_d0x)

generated by the real.exe program for each domain. This process ensured that any trends seen in the HRLDAS and WRF model output were not the result of land surface drift toward model equilibrium.

6.2. LAND SURFACE SPIN-UP

To determine the importance of land surface spin-up relative to changes in urban canopy parameters, the WRF model was run with varying land surface spin-up lengths. The spin-up model predictions using the HRLDAS model were one and two years in length using the control set of urban canopy parameters. The WRF model was then run with the initial conditions produced by the 1- and 2-year spin-up runs. An additional WRF model prediction was conducted simply using the NARR data for the initial conditions without any spin-up using the HRLDAS model, which will be referred to as the cold start.

The metric used to determine whether the land surface states reached equilibrium was the percent difference where the 5-year simulation was used as the “control” simulation, given by

$$\text{Percent Difference} = 100 \frac{\text{Value}_X - \text{Value}_5}{0.5(\text{Value}_X + \text{Value}_5)}, \quad (6.1)$$

where Value_X is the model output value for the variable of interest after X months of spin-up time and Value_5 is the model output value after five years of spin-up time. Thus, positive values of percent difference indicate that the initial conditions were too wet (warm), while negative values indicate that the initial conditions were too dry (cool) relative to the control. Two specific values of percent difference were used as thresholds

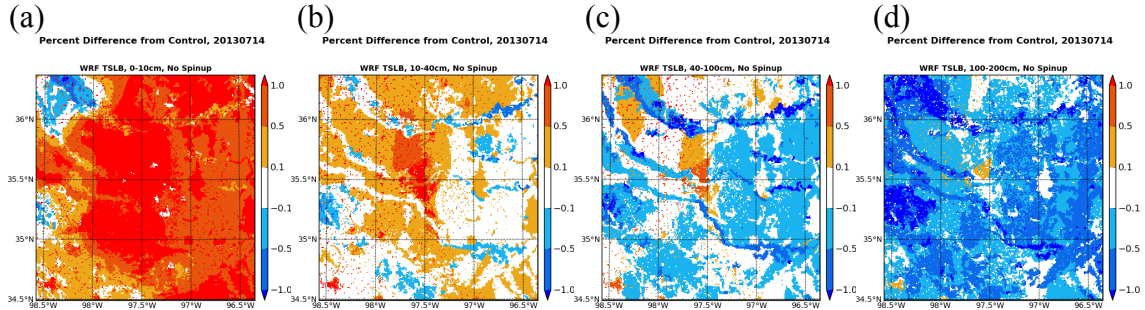


Figure 6.2. Percent difference values of soil temperature (a) 0-10 cm, (b) 10-40 cm, (c) 40-100 cm, and (d) 100-200 cm soil temperature after no land surface spin-up relative to the control run.

to quantify whether the values of percent difference had reached equilibrium: 1% and 0.1%. The 1% difference represents rough equilibrium, or the level where the LSM ceases to exhibit model output changes on a practical scale and represents the error in many observation systems (Cosgrove et al. 2003). The 0.1% difference represents fine scale equilibrium as required by the Simplified Simple Biosphere (SSiB) modeling group (Yang et al. 1995; Cosgrove et al. 2003).

6.2.1. Spin-Up Results

Figure 6.2 illustrates the percent difference in initial soil temperatures used by the WRF model with NARR data for the initial conditions (i.e., cold start) and the control initial conditions that had a 5-year spin-up. The white shading represents the grid cells that are within $\pm 0.1\%$ difference of the control run initial conditions. For the 0-10 cm and 10-40 cm soil layers, significant portions of the domain exceeded the $+0.1\%$ and $+1\%$ thresholds, meaning the NARR initial conditions were warmer than the control initial conditions. For the 40-100 cm and 100-200 cm soil layers, the NARR initial soil temperatures were predominantly 0.1 to 1% cooler than the control run's

initial soil temperatures. The 0-10 cm, 10-40 cm, and 40-100 cm soil layers reached fine scale equilibrium after two years of spin-up (now shown). A small number of grid cells in the NW corner of the domain did not reach fine scale equilibrium after two years of spin-up for the 100-200 cm soil layer (not shown).

Soil temperature has less interannual variability and variational inertia than soil moisture (Houser et al. 1999; Cosgrove et al. 2003). As a result, soil moisture required more spin-up time to reach rough equilibrium than soil temperature. Figure 6.3 illustrates the percent difference in initial soil moisture used by the WRF model for a cold start, 1-year spin-up, and 2-year spin-up and the control initial conditions that had a 5-year spin-up. A cold start failed to meet the conditions of rough equilibrium for all

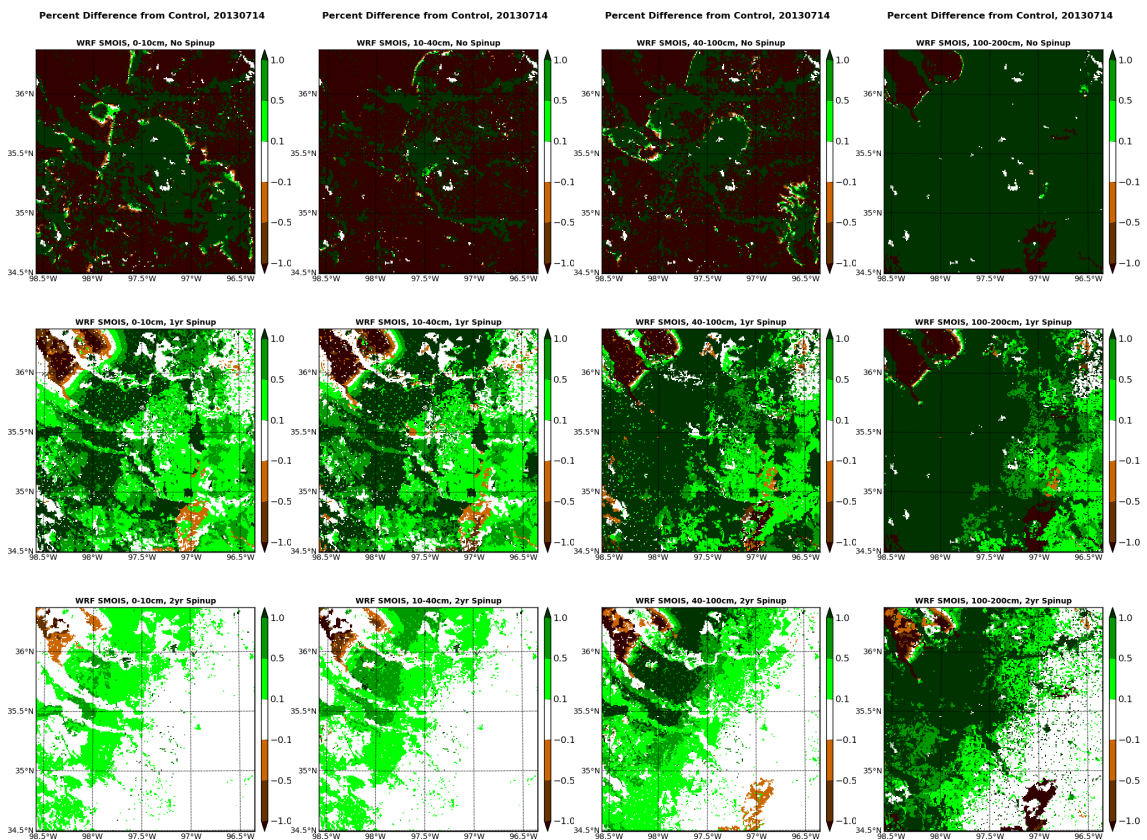


Figure 6.3. Percent difference values of soil temperature for 0-10 cm (column 1), 10-40 cm (column 2), 40-100 cm (column 3), and 100-200 cm (column 4) after a cold start (row 1), 1-year spin-up (row 2), and 2-year spin-up (row 3) relative to the control run.

soil layers. As the depth and thickness of the soil layers increased, more grid cells were outside the $\pm 0.1\%$ range of fine scale equilibrium and the $\pm 1\%$ range of rough equilibrium. For the 100-200 cm soil layer, the root depths of only the forest (deciduous broadleaf, deciduous needleleaf, evergreen broadleaf, and evergreen needleleaf) land use categories extend into the layer, leaving gravitational drainage as the primary method of drying the soil layer during spin-up. Similarly, the 100-200 cm soil layer requires infiltration from upper layers to eliminate dry anomalies in the initial conditions, resulting in longer spin-up times. In comparison, the root depths of 12 land use categories extend into the 40-100 cm soil layer.

Figure 6.4 illustrates the impact of insufficient spin-up of the land surface states for a LIR grid cell on components of the SEB. The initial NARR soil moisture states for the grid cell were significantly higher than those allowed one or more years of spin up. For Q^* and Q_G , the impact of a cold start was of the same order of magnitude as varying the urban canopy parameters. However, for Q_E (Q_H), the predicted fluxes were nearly 200 W m^{-2} greater (less) than predicted fluxes after just one year of spin-up. Initializing with wet urban soil moisture conditions can lead to reduced maximum daytime temperatures, a stronger urban cool island, and decreased urban wind speeds (Husain et al. 2014). Further, Husain et al. (2014) found that rural soil moisture played an even greater role in determining near surface temperatures and wind speeds for both urban and rural environments. Land surface spin-up should not be neglected for urban modeling studies. While urban grid cells tend to spin up faster than vegetated grid cells, improper initialization of the vegetated grid cells surrounding a city can significantly

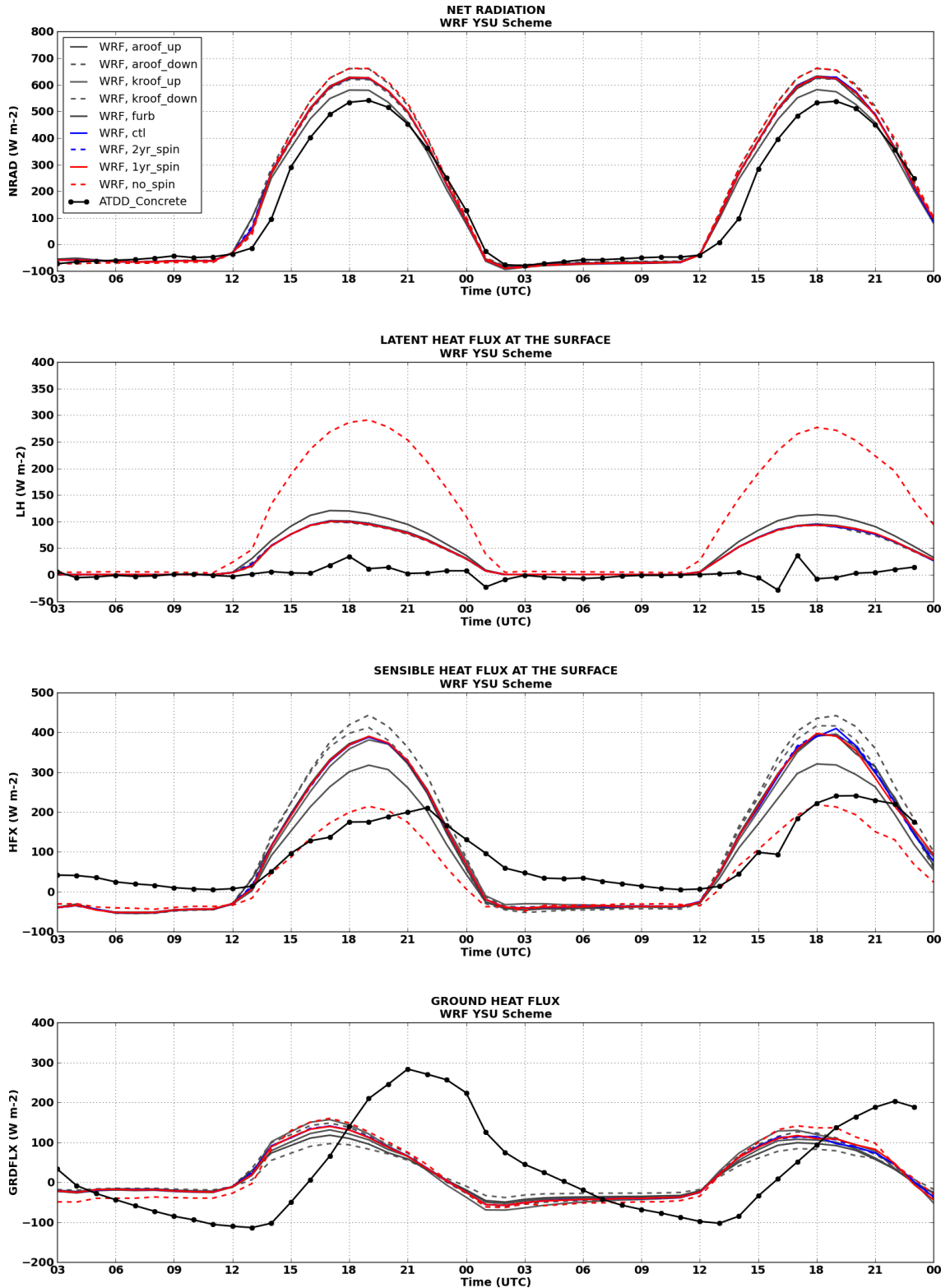


Figure 6.4. Diurnal cycles of net radiation, latent heat fluxes, sensible heat fluxes, and ground heat fluxes predicted by the WRF model using the YSU PBL scheme for 14-15 July 2003. Observational data from the ATDD Concrete site are shown for comparison.

impact predictions of surface layer variables and urban phenomena such as the UHI.

6.3. CASE STUDY: 14-15 JULY 2003

The HRLDAS and WRF model data were extracted for cells that coincided with three or more PNNL HOBO sites, each of the six Mesonet sites surrounding OKC, and each of the ASU, ATDD, and IU sites. Data from the PNNL HOBO sites were averaged to represent the observed mean for that grid cell.

6.3.1. Air Temperature

During two heat-wave events in the central U.S., approximately 65% of all heat-related deaths in 1995 occurred in Chicago (Kunkel et al. 1996) and approximately 80% of all deaths in 1999 occurred in metropolitan areas (Palecki et al. 2001). A significant contributor to the number of deaths during the Chicago heat wave in 1995 was increased nighttime values of apparent temperature (Karl and Knight 1997). In most cities, observations from within the urban core or even surrounding suburban areas are not available. Decisions regarding heat-related warnings and intervention planning are typically dependent upon airport measurements (Basara et al. 2010) and NWP models. Due to the nonlinear interactions between UHIs and heat waves and resulting heat stress for urban residents (Li and Bou-Zeid 2013), it is critical that NWP models (including WRF) capture the influence of urban land use on the 2-m air temperature.

Figures 6.5 and 6.6 illustrate the urban and rural 2-m air temperatures predicted by the WRF model using the MYJ and YSU PBL schemes, respectively. Except for the overnight hours on 15 July (0000 UTC to 1200 UTC), variations in the urban canopy parameters produced an approximately 1-K spread of urban temperatures. The spread of

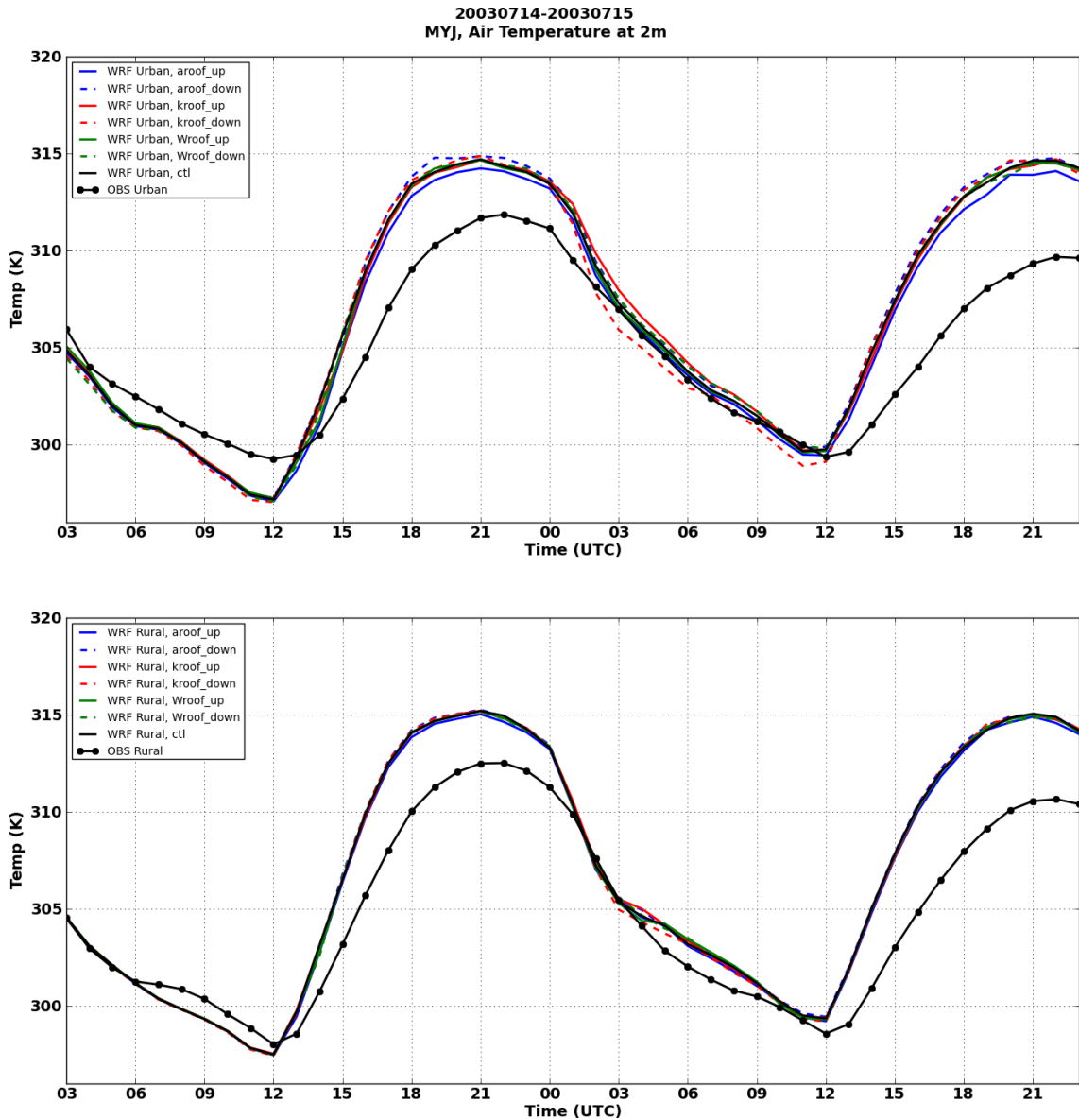


Figure 6.5. Diurnal cycles of mean urban and rural air temperatures at 2 m predicted by the WRF model using the MYJ PBL scheme for 14-15 July 2003. Observational data from the PNNL HOBO and Mesonet sites are shown for comparison.

predicted urban temperatures increased during the overnight hours of 15 July 2003, during which a decreased k_{roof} and increased f_{urb} produced the largest temperature decreases. The decreased k_{roof} reduced the rate of heat transfer through the top roof layer. As a result, a decrease (increase) in k_{roof} resulted in an increased (decreased) amplitude in the diurnal cycle of 2-m air temperatures. After sunset, roof temperatures

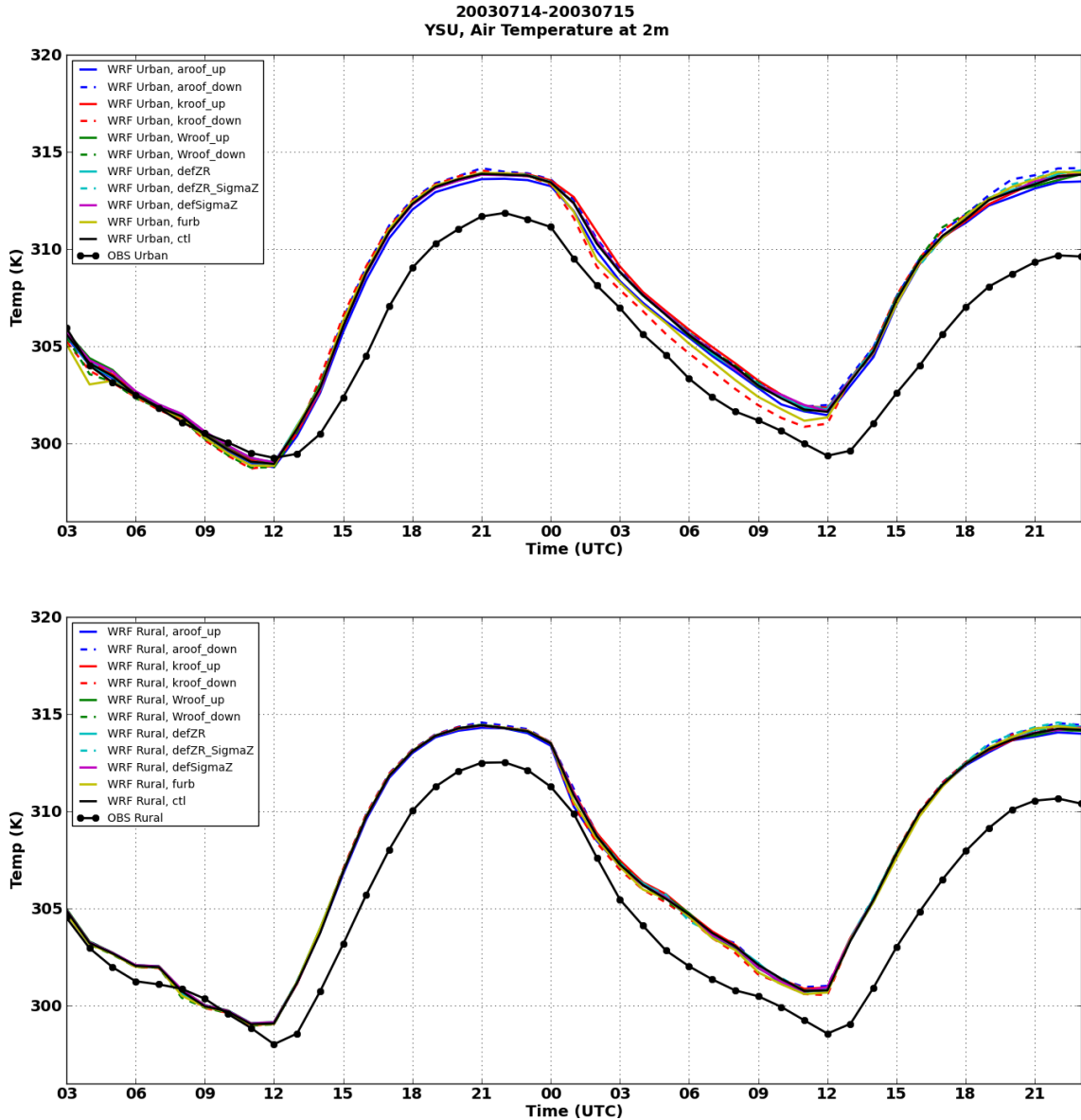


Figure 6.6. Diurnal cycles of mean urban and rural air temperatures at 2 m predicted by the WRF model using the YSU PBL scheme for 14-15 July 2003. Observational data from the PNNL HOBO and Mesonet sites are shown for comparison.

cooled more quickly and contributed to lower nighttime 2-m air temperatures. The decreased f_{urb} decreased the fraction of the grid cell comprised of urban surface and increased the vegetated fraction, resulting in decreased nighttime temperatures. During the daytime hours, the decrease (increase) in α_{roof} increased (decreased) the 2-m air temperatures due to the resulting increase (decrease) in energy available to heat the roof

surface. However, differences in urban air temperatures due to the change in PBL scheme were greater than the temperature changes due to urban parameter variations. The changes in the predicted rural temperatures were attributed to the NRMN grid cell being classified as LIR land use in the NLCD 2001.

The MYJ PBL scheme resulted in a larger amplitude diurnal cycle than the YSU scheme. As a result, nighttime urban air temperatures predicted when using the MYJ scheme compared well with the observed temperatures. However, the daytime predicted temperatures were 2-5 K greater than observed. Meanwhile the temperatures predicted when using the YSU scheme were consistently higher than the observed temperatures for all hours.

After the initial analysis of the sensitivity of the 2-m air temperature to variations in the α_{roof} , k_{roof} , and W_{roof} , additional model predictions were conducted using only the YSU PBL scheme. The additional urban canopy parameters included decreasing the f_{urb} (discussed above), using the default values for σ_z , using the default values for Z_R , and using the default values for both σ_z and Z_R . Varying Z_R and σ_z did not significantly impact the 2-m air temperatures.

Figure 6.7 displays the predicted ΔT_{u-r} for each parameter variation and both PBL schemes. The ΔT_{u-r} predicted with both PBL schemes, regardless of the parameter variations, was consistent with the ΔT_{u-r} observed, but only because both the predicted urban and rural temperatures at 2 m exhibited the same trends. The diurnal cycle of ΔT_{u-r} predicted by the WRF model peaked 1 to 2 hours earlier than the observed ΔT_{u-r} due to rapid rural cooling at sunset.

To better understand the lack of response of predicted 2-m temperatures to variations in urban parameters, the method of calculating the diagnostic 2-m temperature within the WRF model was examined. The 2-meter temperature field (T_{2m}) does not affect model-level fields, but is diagnosed from model-level fields and land surface fields (Jiménez et al. 2012; Li and Bou-Zeid 2014),

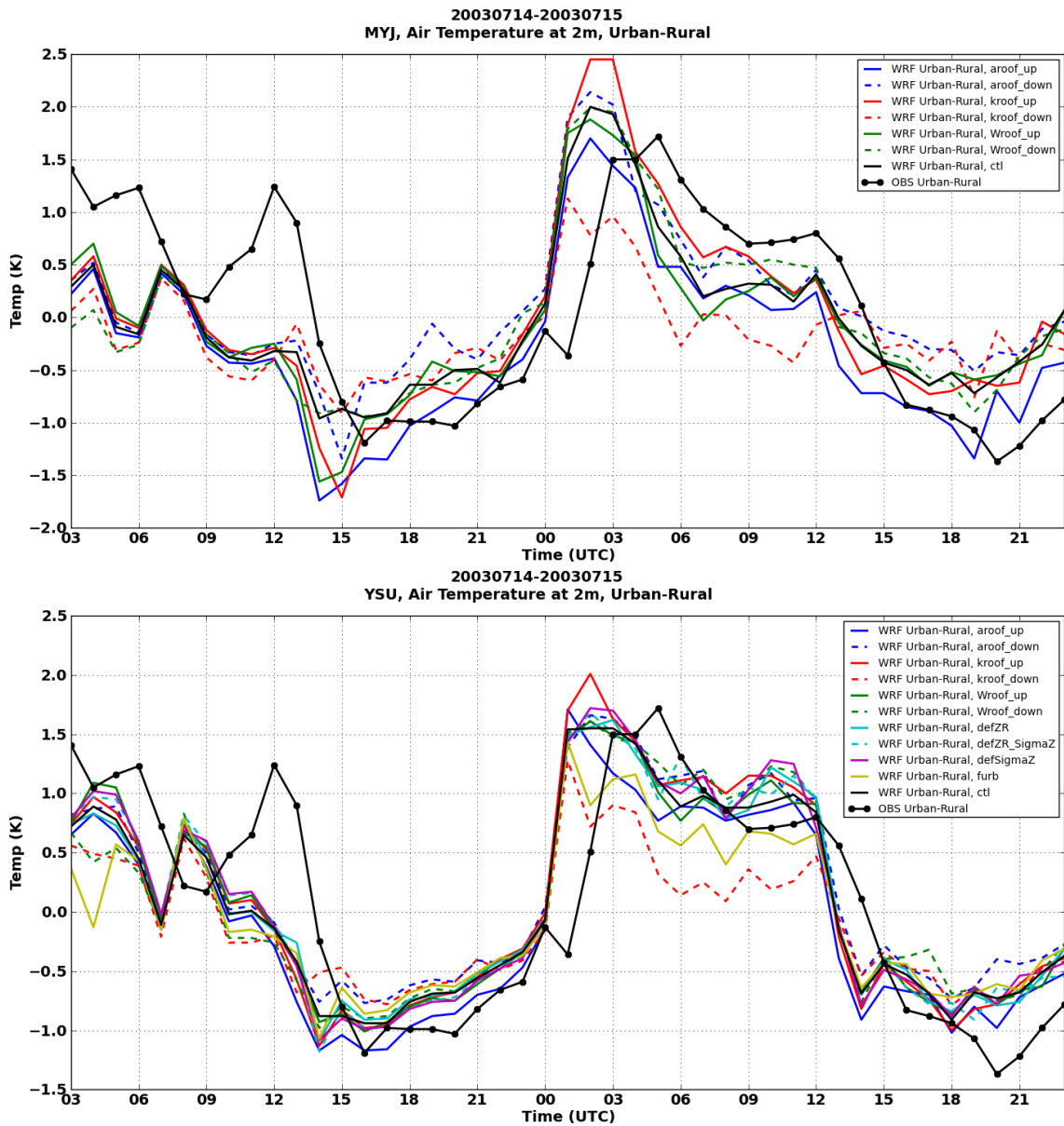


Figure 6.7. Diurnal cycles of mean UHI intensity at 2 m predicted by the WRF model using the MYJ and YSU PBL schemes for 14-15 July 2003. Observational data from the PNNL HOBO and Mesonet sites are shown for comparison.

$$T_{2m} = T_{skin} - \frac{Q_H}{\rho C_{H2} U_2}, \quad (6.2)$$

where T_{skin} is the land surface or skin temperature, Q_H is the sensible heat flux at the surface, ρ is the density of air, C_{H2} is the exchange coefficient at two meters, and U_2 is the wind speed at 2 m.

For urban grid cells when the SLUCM is not used, 2-m air temperature is calculated according to Equation 6.2 using a look-up table for the roughness length specified for urban land use to calculate C_{H2} . When the SLUCM is used, the urban grid cells are divided into impervious and vegetated parts. The vegetated portion of the grid cell is assumed to be grassland. The assigned fractions of the urban and vegetated parts are based on the f_{urb} specified for each urban land use category in the urban parameter table. The Noah LSM is called to calculate the T_{skin} for the vegetated fraction. Then the SLUCM is called to calculate the T_{skin} for the impervious fraction. The T_{skin} for the entire grid cell is calculated as a weighted mean of the impervious and vegetated surface temperatures

$$T_{skin} = T_{skin(SLUCM)} \times f_{urb} + T_{skin(Noah)} \times (1 - f_{urb}). \quad (6.3)$$

The surface temperature for the impervious portion of the grid is calculated as a diagnostic variable by the SLUCM following

$$T_{skin(SLUCM)} = T_A + \frac{H_{SLUCM}}{\rho C_H U_A}, \quad (6.4)$$

where T_A is the air temperature at the lowest model level and H_{SLUCM}

$$H_{SLUCM} = H_{roof} F_{roof} + F_{walls} H_{walls} + F_{road} H_{road}, \quad (6.5)$$

is the area-weighted mean of sensible heat fluxes from the roof (H_{roof}), wall (H_{walls}), and road (H_{road}). The equation for 2-m air temperature then becomes

$$T_{2m} = T_{skin} - \frac{H_{SLUCM} \times f_{urb} + H_{Noah} \times (1 - f_{urb})}{\rho C_{H2} U_2}. \quad (6.6)$$

Due to the contribution of H_{SLUCM} in Equations 6.4 and 6.6, the sensitivity of sensible heat fluxes, and other components of the SEB, to variations in urban canopy parameters were examined next.

6.3.2. Components of the Surface Energy Balance

Figures 6.8 and 6.9 illustrate the Q^* , Q_E , Q_H , and Q_G predicted by the WRF model using the MYJ and YSU PBL schemes, respectively, for the grid cell containing the ATDD Concrete site. All components of the SEB responded similarly to changes in the urban parameters, regardless of the PBL scheme used. Examination of cloud fraction and downwelling shortwave radiation (not shown) revealed minor differences in predicted cloud cover associated with a boundary moving southeast across the domain, evident between 1300 and 1600 UTC on 14 July 2003 in all components of the SEB. Aside from differences in early morning clouds, the magnitudes of the fluxes with each PBL scheme were typically within 40 W m⁻². Due to the consistency in response to variations in urban parameters for each grid cell examined, the discussion forward will primarily focus on the YSU results. The MYJ figures complimentary to those presented here, can be found in Appendix D.

Table 6-3 summarizes the mean peak daytime and nighttime differences in components of the SEB between each model run varying urban parameters and the

control run. The land use for the grid cells containing the ATDD Concrete and ATDD Gravel sites were LIR and I/C, respectively (Figure. 6.10). The higher f_{urb} associated with I/C land use (0.95) resulted in much larger predicted variations in Q^* , Q_H , and Q_G than predicted variations for LIR land use ($f_{urb} = 0.5$) relative to the control run. Consistent across all grid cells examined (Figures 6.11-6.13; Table 6-3), α_{roof} was the only urban canopy parameter that significantly impacted Q^* as it defined the percentage of S_{\downarrow} reflected by the roof surface. A decrease (increase) in α_{roof} resulted in an increase (decrease) in S_{\uparrow} and decrease (increase) in Q^* .

The predicted daytime values of Q_E for the grid cell containing the ATDD Gravel site (I/C) were 100 to 150 $W\ m^{-2}$ less than the predicted Q_E values for the LIR grid cells (Figs. 6.9-6.10). Consistent with Loridan et al. (2010), the only urban parameter to significantly impact Q_E was f_{urb} . Q_E was only sensitive to f_{urb} because the SLUCM predicted values of Q_E equal to 0 $W\ m^{-2}$ for the entire forecast period. The f_{urb} simply increased the percentage of Q_E predicted by the Noah LSM that contributed to the calculation. All other parameter variations impacted Q_E by less than 10 $W\ m^{-2}$.

The urban parameter variations that most significantly impacted Q_H were increased α_{roof} , decreased α_{roof} , and decreased k_{roof} . As stated previously, due to the higher associated f_{urb} , the Q_H for the grid cell with I/C land use (ATDD Gravel; Fig. 6.10) varied more with parameter changes than Q_H for the LIR grid cells (Figs. 6.9, 6.11-6.13; Table 6-3). The α_{roof} impacted Q_H by altering the amount of energy (Q^*) available to heat the roof surface and increased Q_H over the roof. The decrease (increase) in k_{roof} decreased (increased) the transfer of heat through the roof layer and

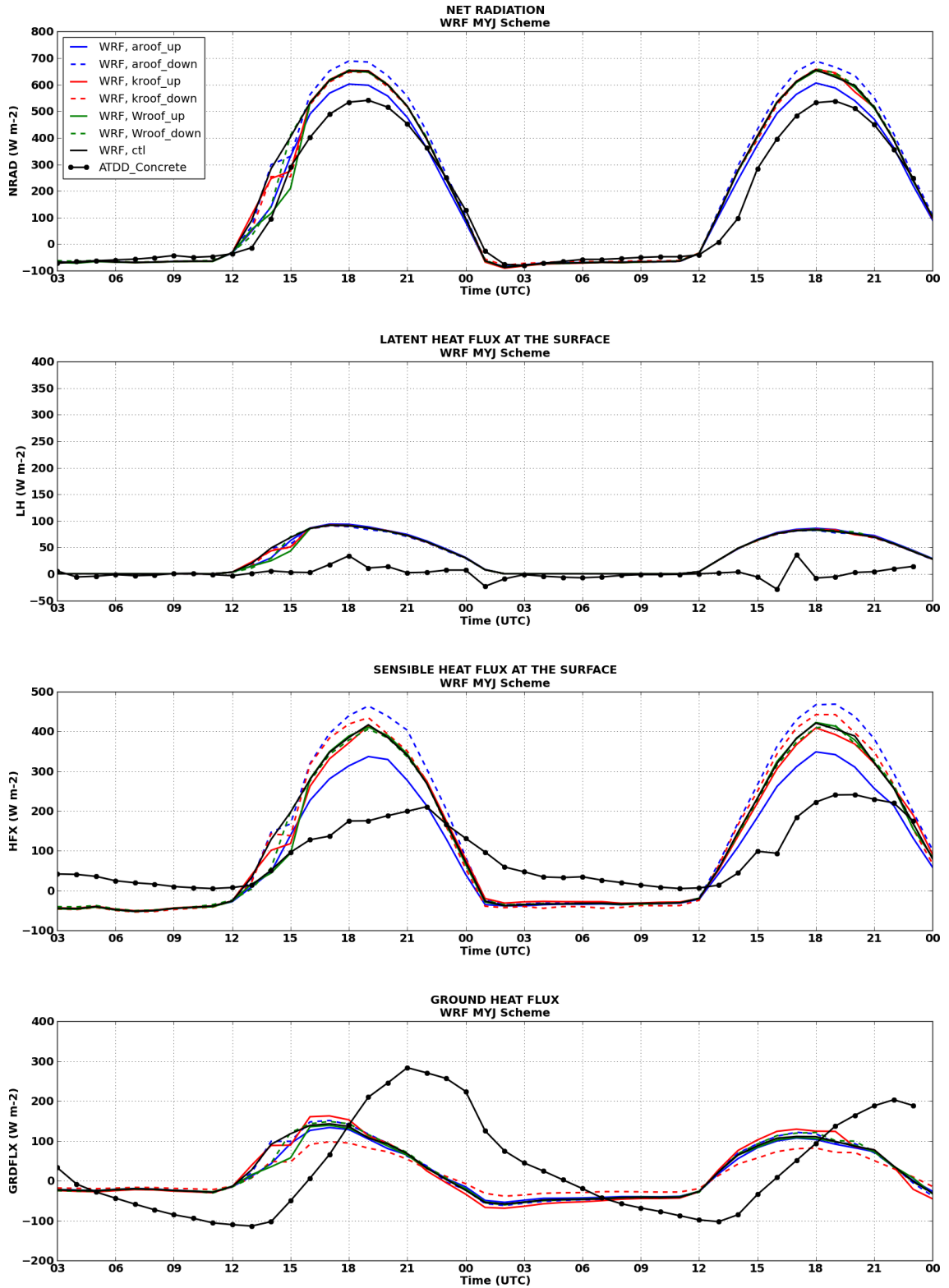


Figure 6.8. Diurnal cycles of net radiation, latent heat fluxes, sensible heat fluxes, and ground heat fluxes predicted by the WRF model using the MYJ PBL scheme for 14-15 July 2003. Observational data from the ATDD Concrete site are shown for comparison.

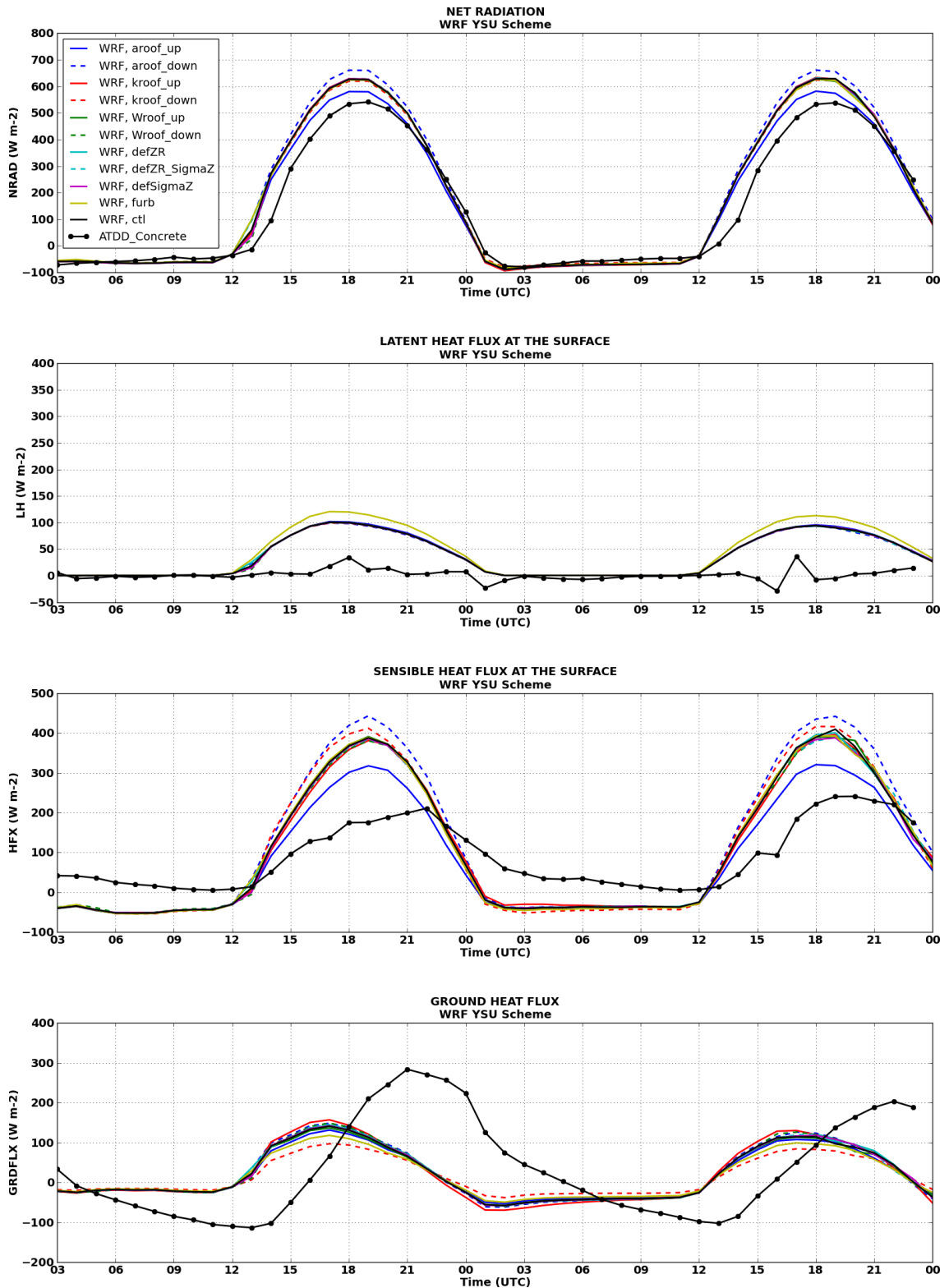


Figure 6.9. Diurnal cycles of net radiation, latent heat fluxes, sensible heat fluxes, and ground heat fluxes predicted by the WRF model using the YSU PBL scheme for 14-15 July 2003. Observational data from the ATDD Concrete site are shown for comparison.

resulted in higher (lower) roof surface temperatures and Q_H .

The urban canopy parameters that impacted Q_G the most were decreased k_{roof} , decreased f_{urb} , and increased k_{roof} . Q_G is directly proportional to k_{roof} , as it controls the

Table 6-3. Mean peak daytime (nighttime) differences in heat fluxes ($W\ m^{-2}$) between model runs varying urban parameters and the control run.

		$\alpha_{roof}\ \uparrow$	$\alpha_{roof}\ \downarrow$	$k_{roof}\ \uparrow$	$k_{roof}\ \downarrow$	$f_{urb}\ \downarrow$
Q^*	LIR	-51.5	37.5	3.5 (-5.8)	-7.8 (7.6)	—
	I/C	-135.9	99.3	7.0 (-7.8)	-15.1 (10.7)	—
Q_E	LIR	7.9	-6.2	—	—	24.9
	HRLDAS	—	—	—	—	—
		—	—	—	—	—
	I/C	—	—	—	—	78.2
Q_H	HRLDAS	—	—	—	—	35.5
	LIR	-82.7	55.7	-14.6 (9.4)	32.8 (-14.4)	6.2 (-10.0)
	HRLDAS	—	—	—	—	—
		—	—	—	—	—
I/C	-130.0	88.8	-38.4 (24.0)	78.1 (-35.6)	8.7 (-35.1)	
Q_G	HRLDAS	-107.1	80.9	-34.7 (26.9)	79.5 (-47.0)	55.6 (-32.1)
	LIR	-11.8 (6.8)	10.5 (-5.7)	18.1 (-12.0)	-40.2 (21.2)	-20.3 (11.0)
	HRLDAS	—	—	—	—	—
		—	—	—	—	—
I/C	-25.1 (16.8)	21.2 (-13.8)	45.2 (-32.3)	-100.4 (51.2)	-63.9 (34.7)	
HRLDAS	-19.7 (16.8)	14.3 (-10.9)	46.2 (-35.9)	-101.4 (68.0)	-62.7 (49.3)	

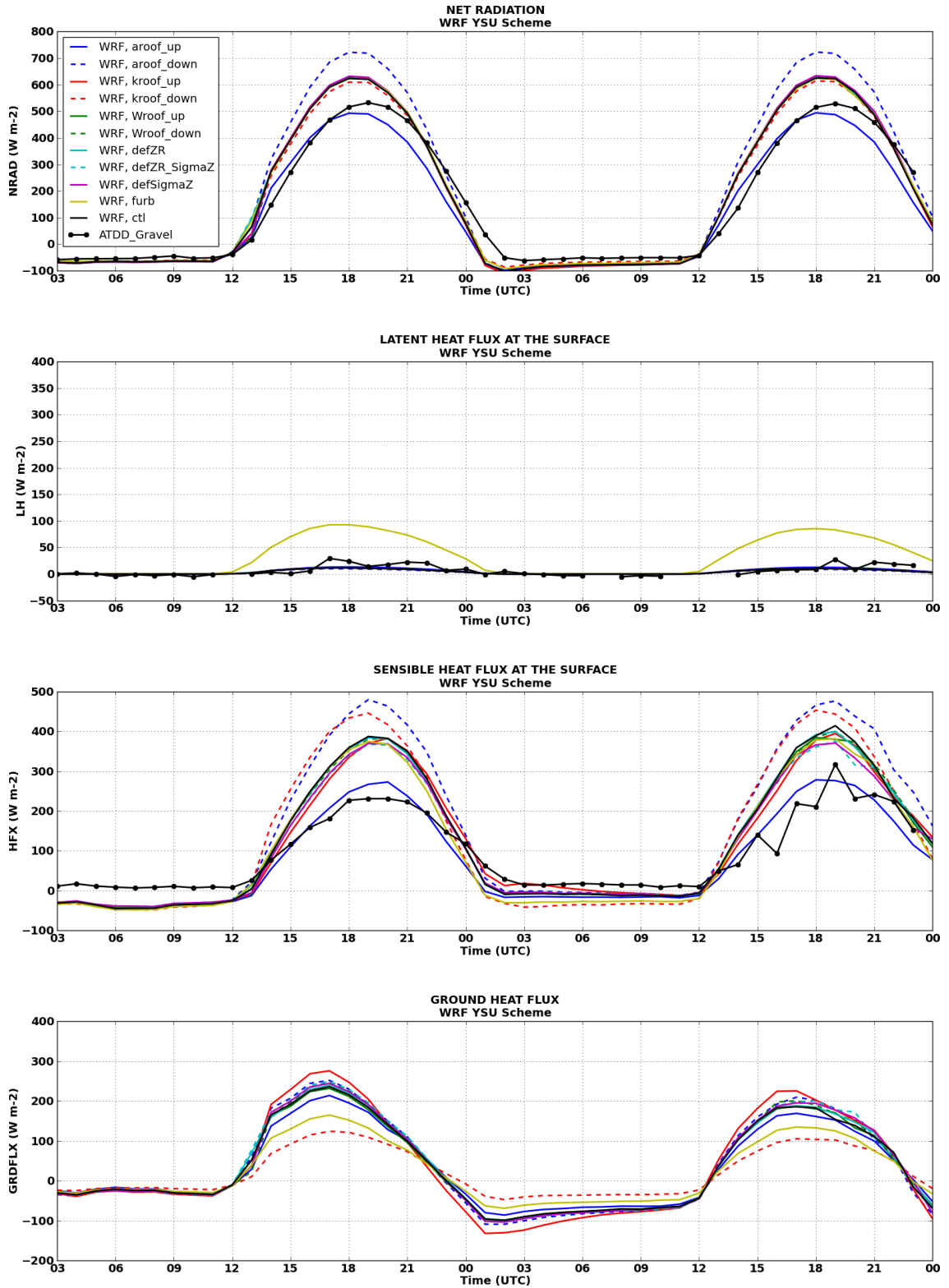


Figure 6.10. Diurnal cycles of net radiation, latent heat fluxes, sensible heat fluxes, and ground heat fluxes predicted by the WRF model using the YSU PBL scheme for 14-15 July 2003. Observational data from the ATDD Gravel site are shown for comparison.

transfer of heat through the roof layer. An increase (decrease) in k_{roof} resulted in an increased (decreased) amplitude of the diurnal cycle of Q_G . During the day, the increased (decreased) k_{roof} increased (decreased) the transfer of heat into the roof layer compared to the control run (Figs. 6.9-6.13; Table 6-3). At night, the transfer of heat toward the surface of the roof layer was increased (decreased). The values of Q_G predicted by the SLUCM were higher than those predicted by the Noah LSM. The decrease in f_{urb} decreased the SLUCM contribution to the grid cell Q_G .

Compared to the observations from the SEB sites, predicted values of Q^* were either 50 to 100 $W m^{-2}$ greater than the observed values (ASU, ATDD Concrete, ATDD Gravel, IU GR), or compared favorably with observations (IU TMA, IU TMB, IU WH, NRMN). Values of Q_E observed at the ATDD Concrete site were significantly less than those predicted by the WRF model because the site location was the most urbanized site while the land cover for the grid cell containing that site was LIR. Except for the ATDD Gravel site, the LIR grid cells predicted Q_E values that were significantly lower than observed values, likely due to site proximity to suburban neighborhoods with lawn irrigation. Even at the ATDD sites, observed Q_H values were 100 to 150 $W m^{-2}$ less than the predicted values. However, observed Q_H values remained positive overnight at the two ATDD sites, while the WRF model failed to maintain positive Q_H during nighttime hours. Positive Q_H values at night are considered a significant contributor to the development of the UHI (Yap and Oke 1974; Kalanda et al. 1980; Oke 1988; Grimmond and Oke 1995; Grimmond et al. 2004a; Offerle et al. 2006b). Finally, the diurnal cycle of Q_G predicted by the WRF model consistently peaked earlier than the

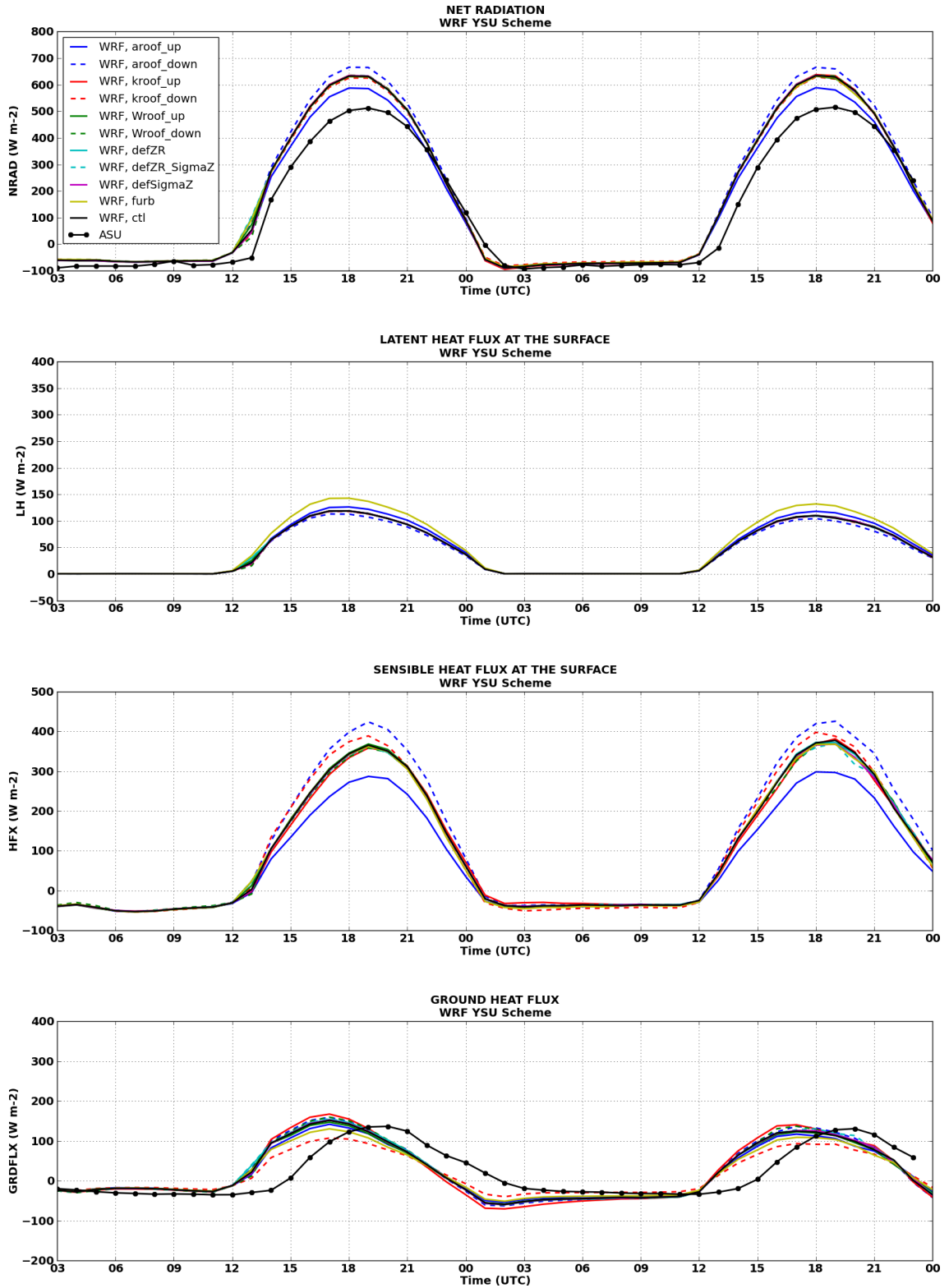


Figure 6.11. Diurnal cycles of net radiation, latent heat fluxes, sensible heat fluxes, and ground heat fluxes predicted by the WRF model using the YSU PBL scheme for 14-15 July 2003. Observational data from the ASU site are shown for comparison.

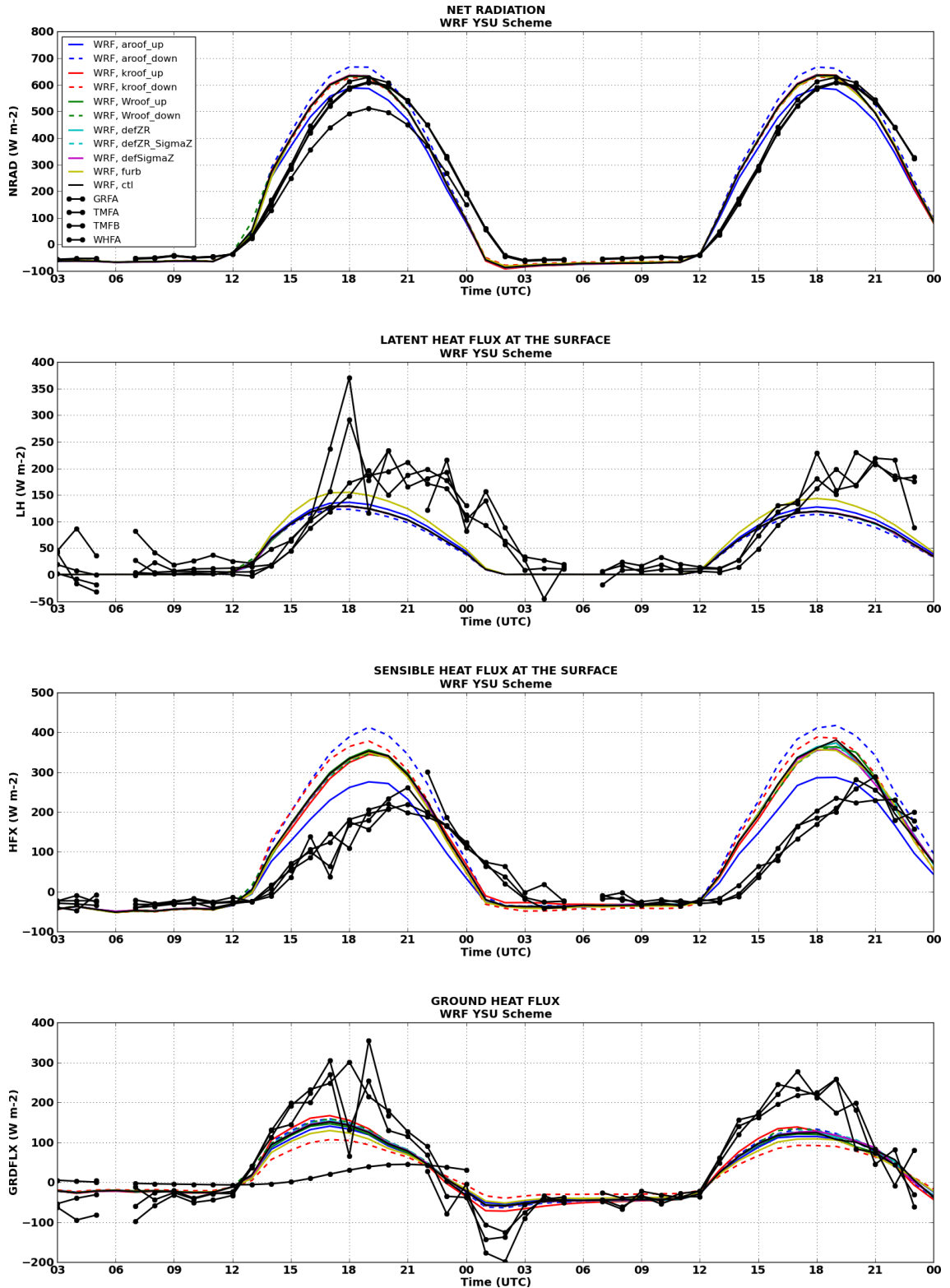


Figure 6.12. Diurnal cycles of net radiation, latent heat fluxes, sensible heat fluxes, and ground heat fluxes predicted by the WRF model using the YSU PBL scheme for 14-15 July 2003. Observational data from the IU GR, TMA, TMB, and WH sites are shown for comparison.

observed diurnal cycle.

In addition to comparing the influence of the PBL schemes on the relative importance of urban canopy parameters, the current study also looked at the impact of running the Noah-SLUCM within the HRLDAS in an uncoupled mode (Table 6-3). The assumption was that the fluxes would be more responsive to changes in the urban canopy parameters without the feedback mechanisms in coupled systems (Best et al. 2006). It was not possible to calculate a Q^* from the HRLDAS input and output data as the calculated emissivity was not included in the HRLDAS output files. Initially, values of predicted Q_E from the HRLDAS model for all urban land use categories were on the order of $2 \times 10^{-5} \text{ W m}^{-2}$ for all time steps. The non-urban grid cells were unaffected. After a series of tests and close examination of the HRLDAS source code, an error was detected in the code that couples the Noah LSM with the SLUCM. The vegetated Q_E from the Noah LSM was converted from units of W m^{-2} to $\text{kg m}^{-2} \text{ s}^{-1}$. The vegetated Q_E was then used to calculate the grid cell Q_E in W m^{-2} . Figures 6.14-6.17 illustrate the heat fluxes predicted by the HRLDAS model. A units correction was applied to the grid cell Q_E values because, as was the case with the WRF model, the Q_E values predicted by the SLUCM were 0 W m^{-2} . Values of Q_E predicted by the HRLDAS model for all urban land use types were 50 to 75 W m^{-2} less than values of Q_E predicted by the WRF model for all parameter variations. Values of Q_H predicted by the HRLDAS model for LIR grid cells were approximately 25 to 75 W m^{-2} greater than values of Q_H predicted by the WRF model for all parameter variations and PBL schemes. Q_H values predicted by the HRLDAS model for the I/C grid cell were slightly less than Q_H predicted by the WRF

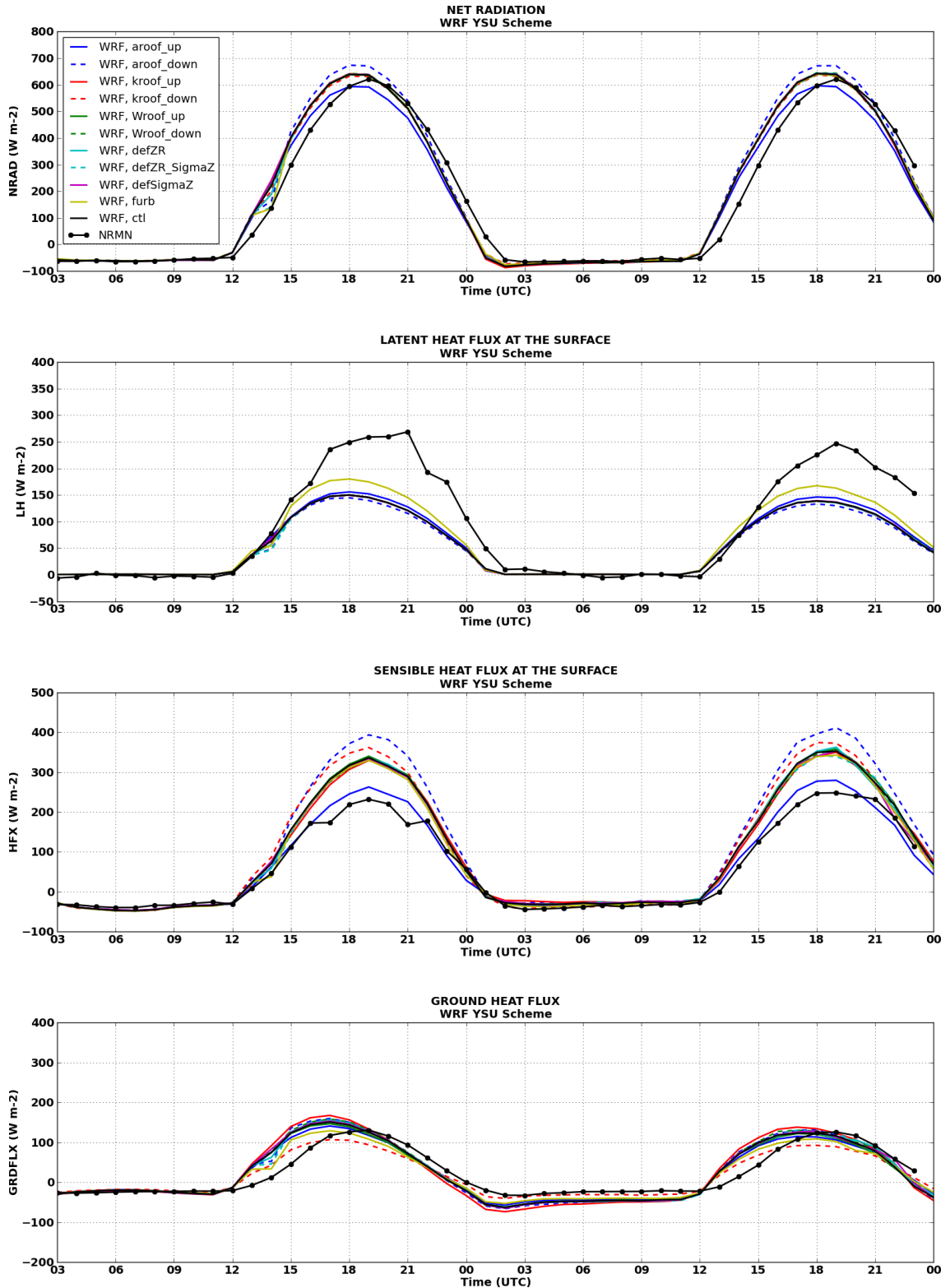


Figure 6.13. Diurnal cycles of net radiation, latent heat fluxes, sensible heat fluxes, and ground heat fluxes predicted by the WRF model using the YSU PBL scheme for 14-15 July 2003. Observational data from the NRMN site are shown for comparison.

model for all parameter variations. Values of Q_G predicted by the HRLDAS model were approximately 25 W m^{-2} greater than those predicted by the WRF model. The responses of the fluxes to changes in the urban canopy parameters were nearly the same when Noah-SLUCM was run in an uncoupled mode with the HRLDAS compared to coupled

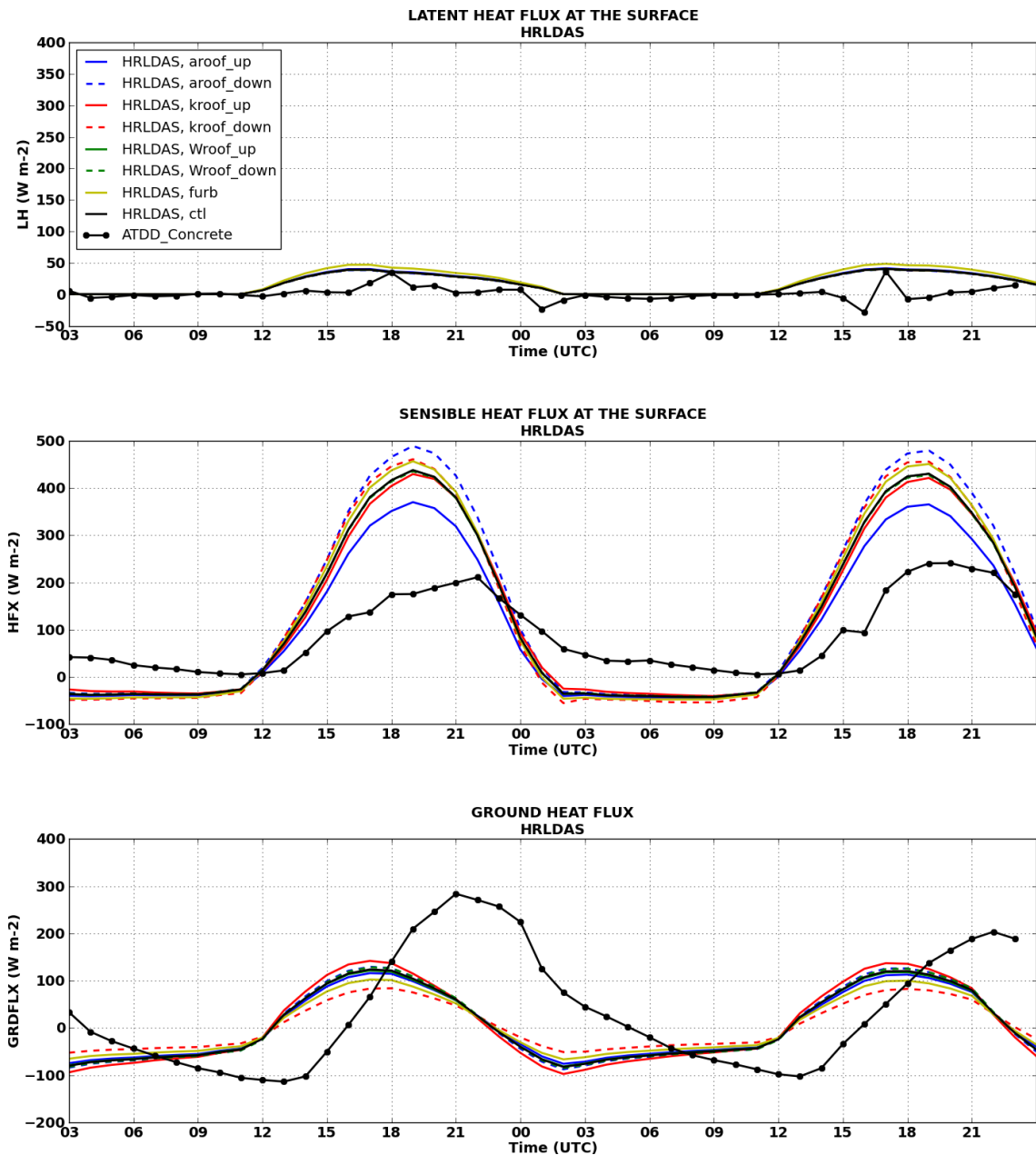


Figure 6.14. Diurnal cycles of latent heat fluxes, sensible heat fluxes, and ground heat fluxes predicted by the HRLDAS model for 14-15 July 2003. Observational data from the ATDD Concrete site are shown for comparison.

mode with the WRF model. Notable exceptions were the sensitivities of Q_E and Q_H to f_{urb} (Table 6-3). Values of Q_E predicted by the HRLDAS were less sensitive to the f_{urb} than Q_E predicted by the WRF model. For I/C land use (ATDD Gravel), the decrease in f_{urb} from 0.95 to 0.6 resulted in peak Q_E values of 50 W m^{-2} predicted by the HRLDAS

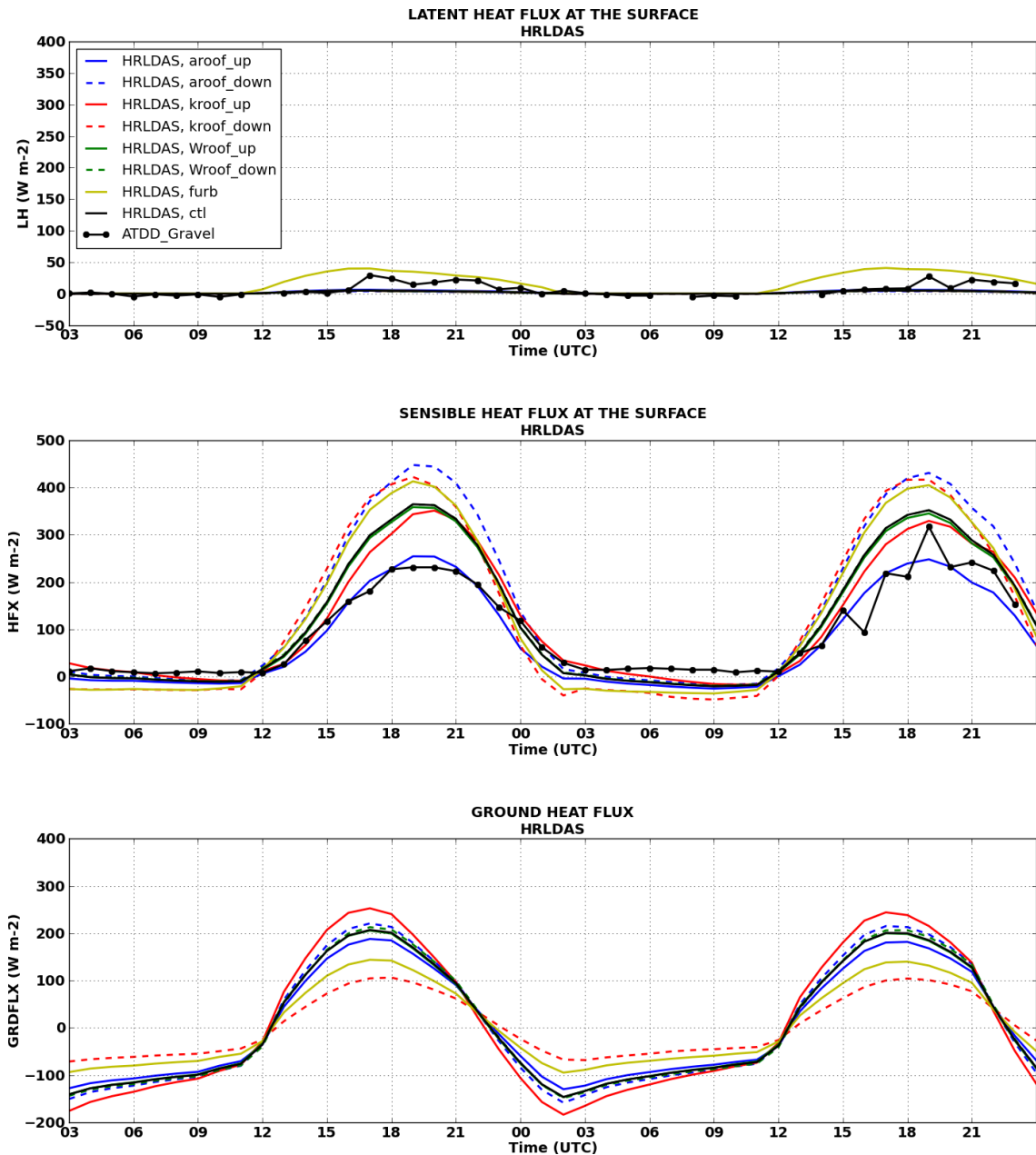


Figure 6.15. Diurnal cycles of latent heat fluxes, sensible heat fluxes, and ground heat fluxes predicted by the HRLDAS model for 14-15 July 2003. Observational data from the ATDD Gravel site are shown for comparison.

and 100 W m^{-2} predicted by the WRF model. Changes in the W_{roof} , Z_R , and σ_z did not significantly impact the components of the SEB in both uncoupled land and coupled land-atmospheric systems. The lack of response of 2-m air temperatures to changes in

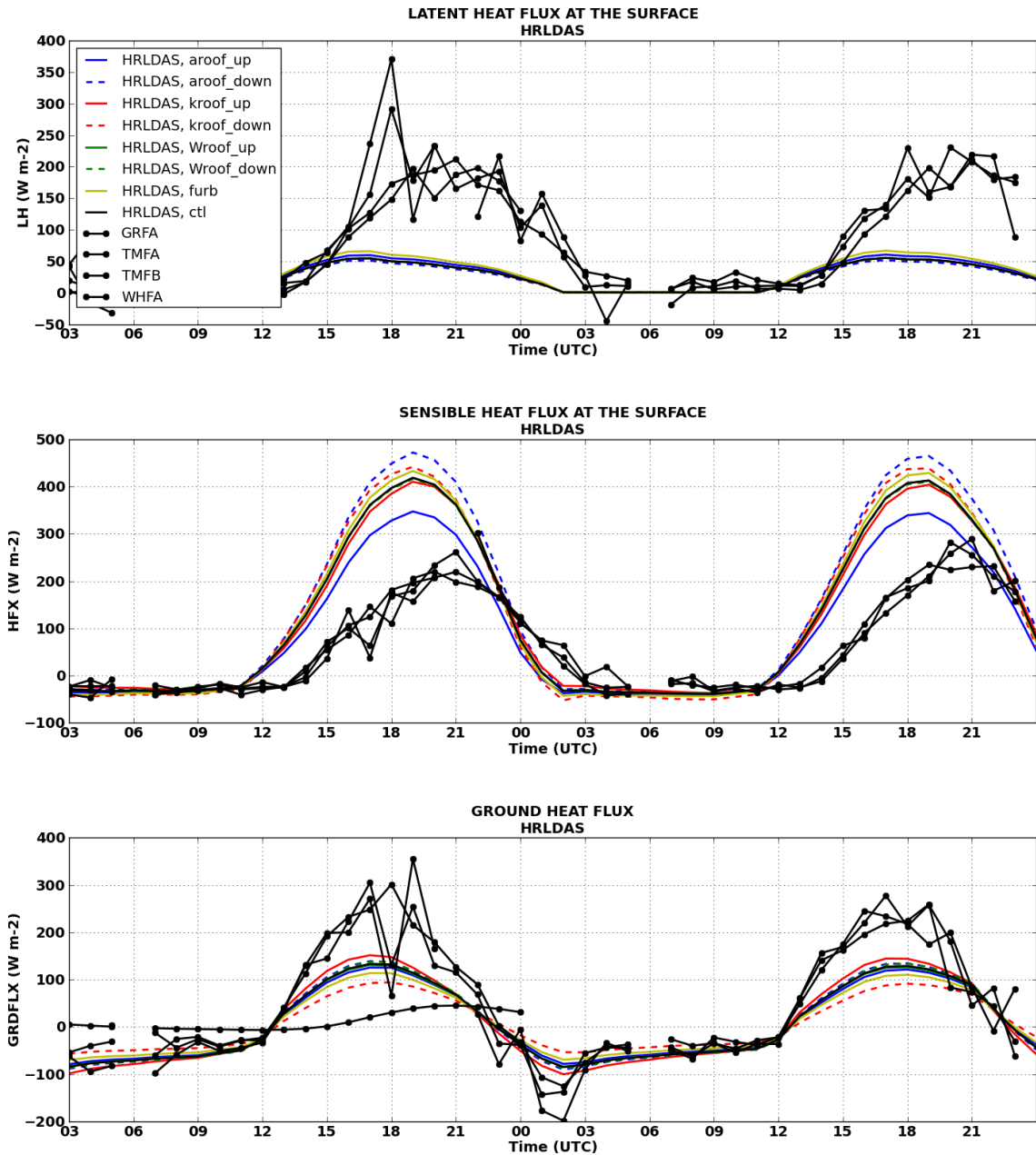


Figure 6.16. Diurnal cycles of latent heat fluxes, sensible heat fluxes, and ground heat fluxes predicted by the HRLDAS model for 14-15 July 2003. Observational data from the IU GR, TMA, TMB, and WH sites are shown for comparison.

urban parameters was not due to a lack of response in Q_H . As a result, the sensitivity of T_{skin} to changes in urban canopy parameters was investigated.

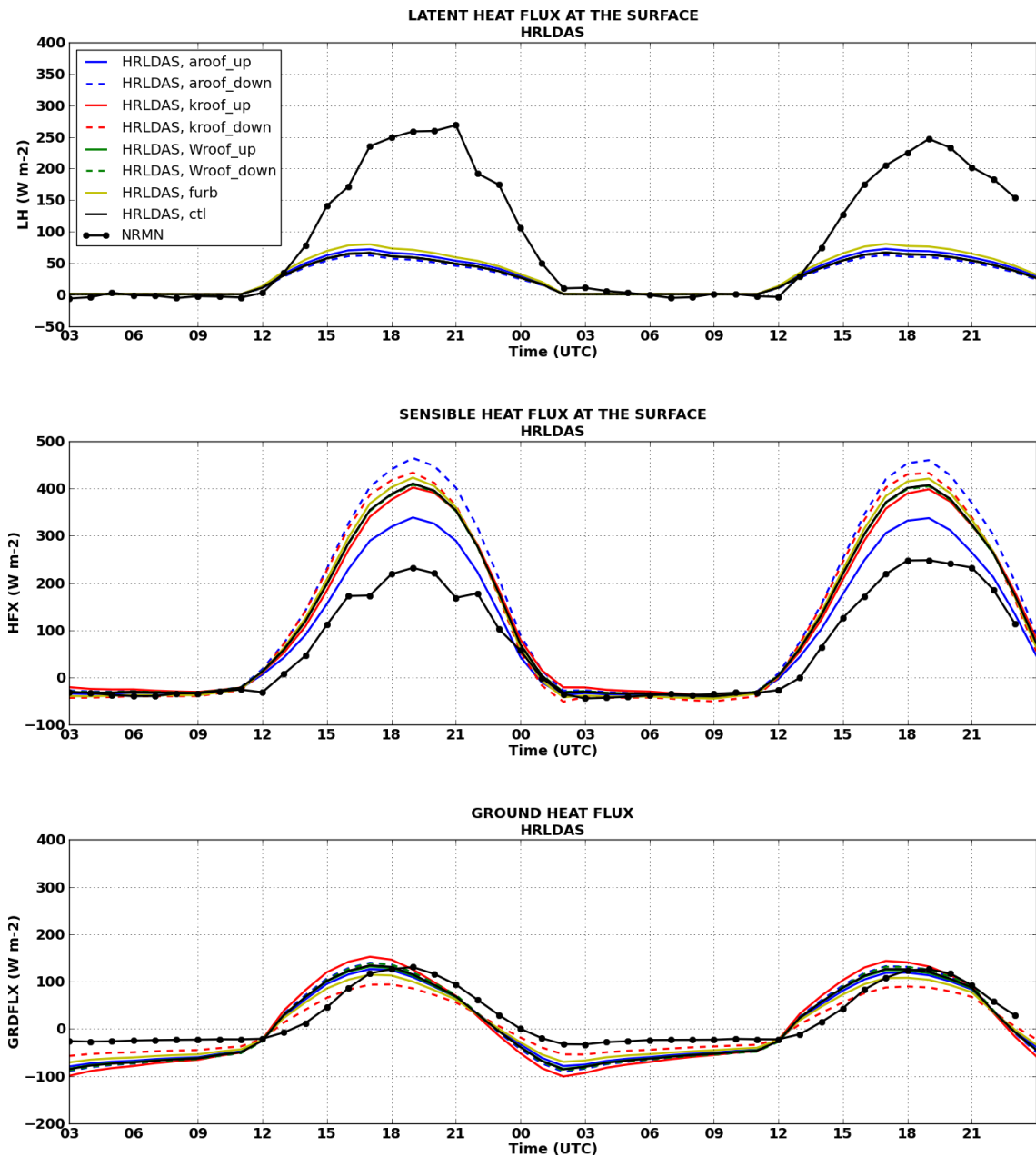


Figure 6.17. Diurnal cycles of latent heat fluxes, sensible heat fluxes, and ground heat fluxes predicted by the HRLDAS model for 14-15 July 2003. Observational data from the NRMN site are shown for comparison.

6.3.3. Skin Temperature

Figure 6.18 shows urban T_{skin} predicted by the WRF model using the MYJ and YSU PBL schemes. In contrast to 2-m air temperature, changes in urban canopy parameters produced changes in predicted T_{skin} during both daytime and nighttime hours. T_{skin} was most sensitive during the daytime to increases (decreases) in α_{roof} , and predicted 1-2 K decreases (increases) in T_{skin} , as it altered the amount of energy available for heating the roof surface. The decrease in k_{roof} increased predicted T_{skin} by 1 K during the daytime due to the reduced transfer of heat through the roof layer. k_{roof} was most impactful during the night, resulting in a 2 K decrease in T_{skin} . After sunset, the decreased k_{roof} resulted in more rapid cooling of the roof surface and reduced transfer of heat toward the surface of the roof layer. In contrast, when the k_{roof} was increased, nighttime values of T_{skin} increased due to the increased transfer of heat from within the roof layer toward the surface.

While the sensitivity of T_{skin} was greater than the sensitivity of 2-m temperature to changes in urban canopy parameters, it was surprising that large changes in Q_H (up to 120 W m^{-2}) resulted in modest changes in T_{skin} (1-2 K). Recalling how the WRF model calculates $T_{skin(SLUCM)}$, Equation 6.4 is only correct if the C_H uses roughness lengths for the impervious surfaces (Li and Bou-Zeid 2014). In version 3.4.1 of the WRF model, the C_H used for the urban grid cell was calculated using the roughness lengths of the vegetated grassland surface as opposed to roughness lengths appropriate for urban land use. This inconsistency in roughness lengths does not capture the bulk influence of the

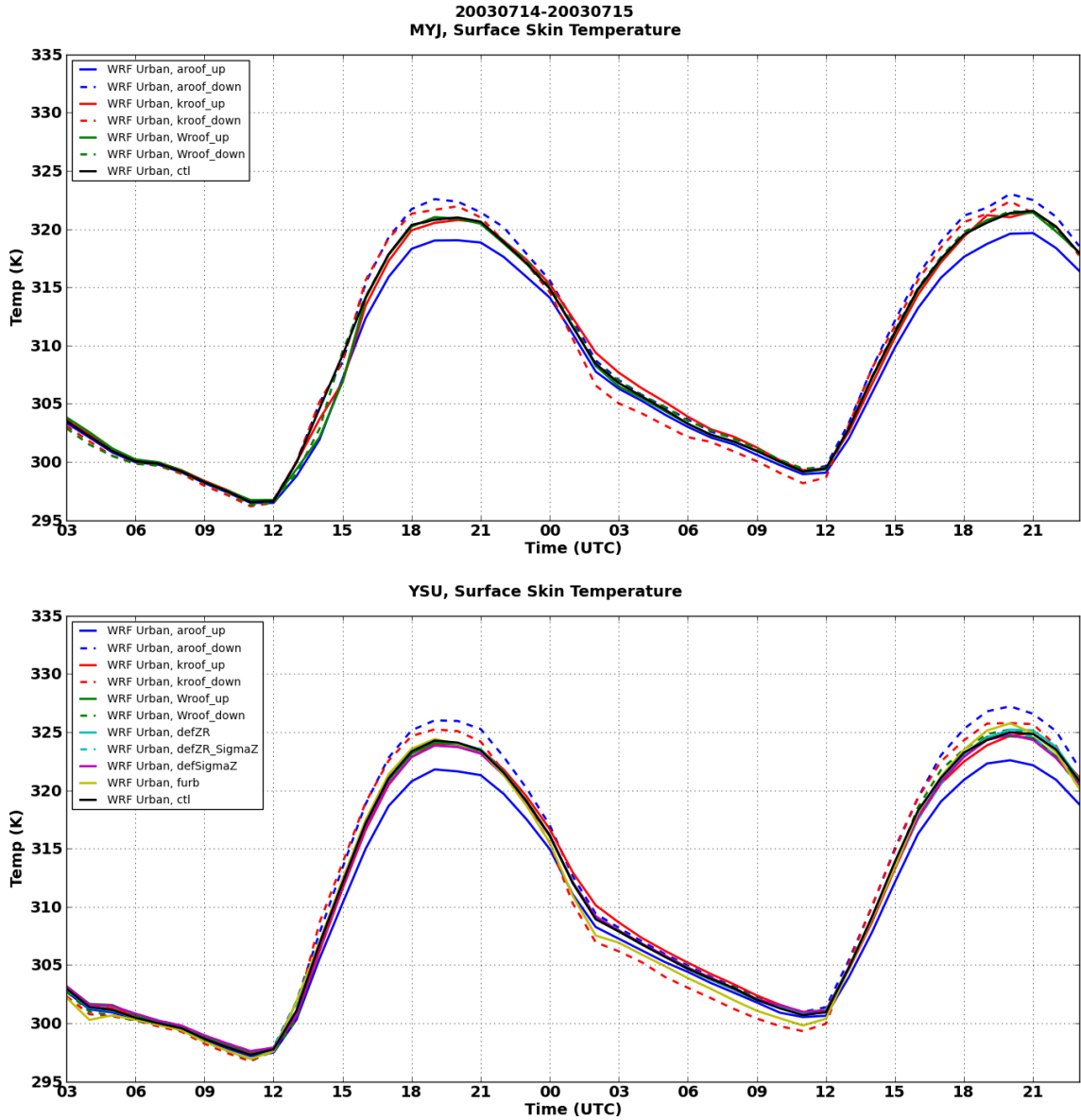


Figure 6.18. Diurnal cycles of mean urban skin temperatures predicted by the WRF model using the MYJ and YSU PBL schemes for 14-15 July 2003.

impervious fraction and causes the reduced sensitivity of 2-m air temperature to changes in urban canopy parameters.

Li and Bou-Zeid (2014) presented an alternate method to calculate $T_{skin(SLUCM)}$

$$T_{skin(SLUCM)} = T_{roof} \times F_{roof} + T_{canyon} \times (1 - F_{roof}), \quad (6.7)$$

where F_{roof} was defined in Equation 4.4. T_{roof} and T_{canyon} are the temperatures of the roof and canyon, respectively, which are prognostic variables calculated by the SLUCM. This method is similar to the “complete urban surface temperature” proposed by Voogt and Oke (1997), except the wall and road temperatures are incorporated through the T_{canyon} . A new 2-m air temperature can be calculated by substituting the $T_{skin(SLUCM)}$ used to calculate T_{skin} in Equation 6.6 with that in Equation 6.7. The default calculation of 2-m air temperature (using C_{H2} for grassland at 2 m) is adequate because 2-m air temperatures are less sensitive to C_{H2} than the skin temperature and it is not truly representative of the air temperature at 2 m given the complexity of the urban surface (Li and Bou-Zeid 2014).

Figure 6.19 illustrates the T_{skin} and 2-m air temperatures for urban grid cells as a result of implementing Equation 6.7 in the SLUCM. The method for calculating $T_{skin(SLUCM)}$ resulted in a 1-3 K increase in T_{skin} during the day for all parameter variations compared to the original method. Except for decreased T_{skin} at night when the k_{roof} was decreased, the nighttime spread of predicted T_{skin} with variations in urban parameters did not change with the use Equation 6.7. Seemingly negligible variations in predicted T_{skin} relative to the control run (< 1 K) were noted during the daytime with variations in W_{roof} and f_{urb} .

Daytime values of 2-m air temperature were warmer due to warmer values of T_{skin} calculated using Equation 6.7. Nighttime values of 2-m air temperature were consistent with trends in T_{skin} and the original calculation of 2-m air temperatures. Decreased k_{roof} was the only urban parameter to which nighttime 2-m air temperatures

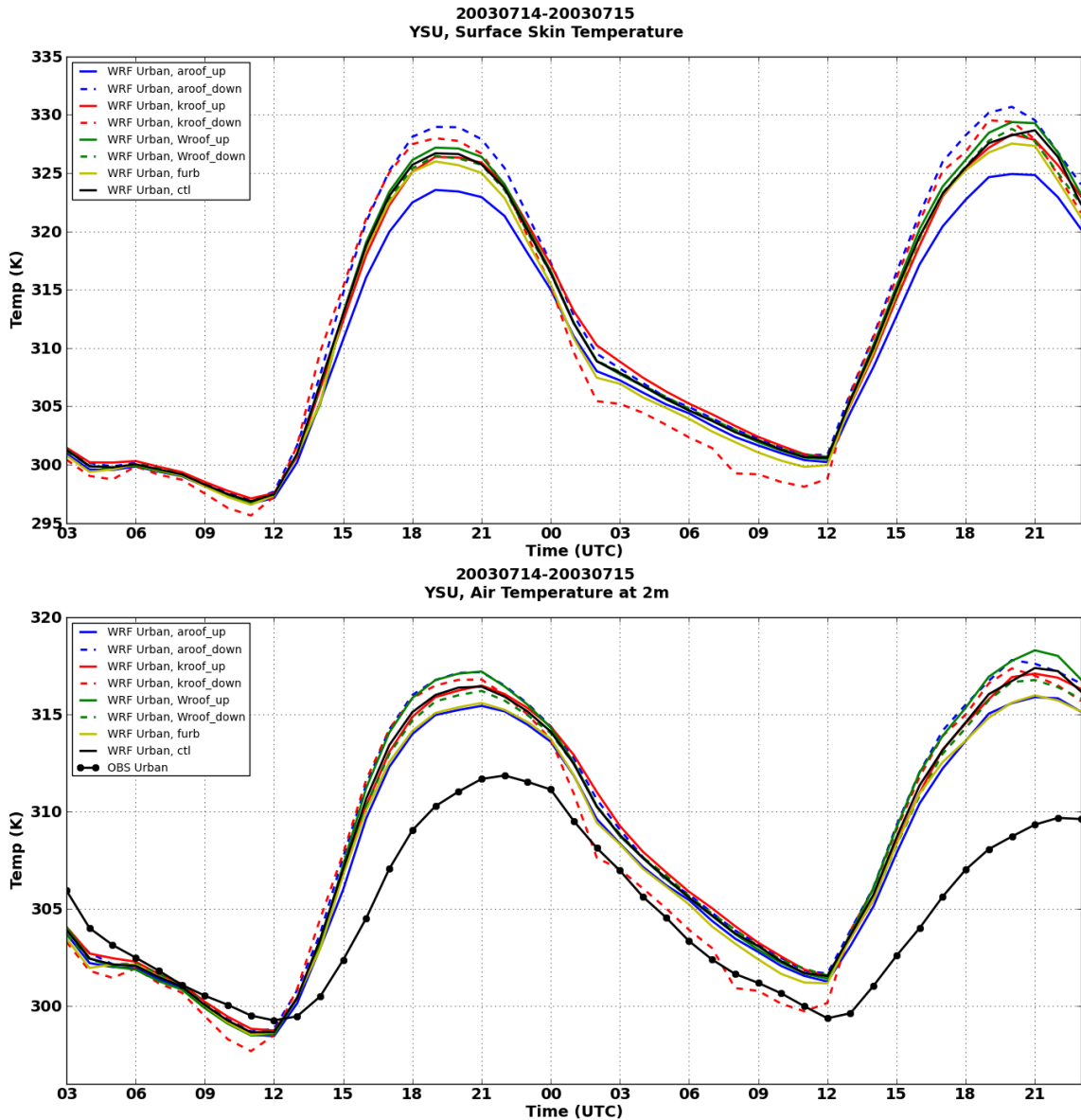


Figure 6.19. Diurnals cycle of mean urban skin temperatures and air temperatures at 2 m predicted by the WRF model using the YSU PBL scheme for 14-15 July 2003. Observational data from the PNNL HOBO and Mesonet sites are shown for comparison.

were sensitive. Despite none of the components of the SEB being sensitive to the W_{roof} , when combined with the new formulation for $T_{skin(SLUCM)}$, the 2-m air temperatures were most sensitive to increased W_{roof} and decreased α_{roof} during the daytime and decreased k_{roof} at all hours of the day. The increased sensitivity of 2-m air temperature to W_{roof} was

due to W_{roof} being used directly in the calculation of $T_{skin(SLUCM)}$ combined with the lack of response of Q_H to W_{roof} . Because 2-m air temperature is a function of the difference between T_{skin} and Q_H , a slight sensitivity of T_{skin} to W_{roof} and a lack of sensitivity of Q_H to W_{roof} produced a 2-m air temperature sensitive to W_{roof} . The increased sensitivity of 2-m air temperatures to f_{urb} was similar to that of W_{roof} .

Implementing Equation 6.7 in the SLUCM increased the sensitivity of 2-m air temperatures to urban canopy parameters, especially during the daytime. However, its implementation also increased the disparity between observed and predicted daytime temperatures. Due to the sensitivity of 2-m air temperature to the method of calculating T_{skin} , additional cases and approaches to calculate T_{skin} should be investigated.

6.4. SUMMARY

Model runs were conducted using the HRLDAS and the WRF model to study the sensitivity of 2-m air temperatures and components of the SEB to urban canopy parameters for the SLUCM. The 2-m air temperatures during the day were not sensitive to changes in urban canopy parameters, regardless of the PBL scheme used in the WRF model. Predicted nighttime temperatures decreased in response to a decrease in k_{roof} .

The components of the SEB were more sensitive to urban canopy parameters than 2-m air temperatures. Changes in the Q^* due to changes in α_{roof} were accompanied by compensating changes in Q_H due to increased roof surface heating. Similarly, changes in Q_H due to changes in k_{roof} were accompanied by compensating changes in Q_G . The f_{urb} was the only urban parameter to significantly impact Q_E because Q_E predicted by the SLUCM was 0 W m⁻² for the entire period. The f_{urb} simply determined

what percentage of Q_E predicted by the Noah LSM contributed to the grid cell value. The fluxes predicted for grid cells classified as I/C land use experienced larger responses to changes to α_{roof} , k_{roof} , and f_{urb} than those predicted for LIR grid cells. When run in the uncoupled mode, the responses of the fluxes to changes in the urban canopy parameters were nearly the same as when run in the coupled mode. The exception was Q_E , where the response of Q_E to f_{urb} in uncoupled model was less than the response in coupled mode.

Upon examination of T_{skin} predicted by the WRF model, it was determined that the diagnostic T_{skin} calculated by the SLUCM used the roughness length for grassland instead of a value appropriate for urban land cover. A different method was used to calculate the T_{skin} within the SLUCM. The results revealed higher values of T_{skin} , especially during the day, and increased sensitivity to the urban parameters. When the new values of T_{skin} were used to calculate the diagnostic 2-m temperature, W_{roof} emerged as an additional urban parameter to which 2-m temperature was sensitive. Due to the sensitivity of 2-m temperature to the T_{skin} , additional cases and methods to calculate T_{skin} need to be examined.

7. SUMMARY AND CONCLUSIONS

7.1. FINAL REMARKS

The most documented urban-induced weather phenomenon is the UHI effect whereby air temperature in the urban canopy is warmer compared to the rural surroundings. Changes in the surface energy and radiation balances contribute the development of the UHI. Between 28 June and 31 July 2003, a vast array of instrument systems collected high-resolution observations of meteorological variables in and around Oklahoma City during JU2003. The data collected from the field measurements, combined with data collected from existing atmospheric observing systems in central Oklahoma presented a unique opportunity to investigate the UHI of OKC.

As NWP models continue to evolve toward finer grid spacing, it becomes increasingly important to properly represent urban influences in land surface, surface layer, and PBL schemes. Recent efforts to “urbanize” NWP and climate models resulted in the development of a number urban canopy models of varying complexity. Validation of such models is inconsistent in regards to validating before or after coupling to an atmospheric model and what type of observations (near surface variables or energy fluxes) are used.

The first objective of this study was to quantify the spatial and temporal variability of the SEB within and surrounding OKC. Near-surface air temperatures within the urban core and in the surrounding rural areas revealed a 1.5 K UHI 1 to 3 hours after sunset and a 1.2 K urban cool island during the daytime for OKC. Energy fluxes observed over a range of surface conditions (concrete, gravel, grass, grass near

neighborhoods with irrigated lawns) were analyzed for spatial and temporal trends. Observing sites closer to the urban core released 40% of available energy through sensible heat fluxes and 25% through ground heat fluxes. Urban core sites also released more longwave radiation due to increased surface temperatures as a result of drier soil conditions. Suburban sites equally released energy through sensible, latent, and ground heat fluxes. The partitioning of energy at rural sites was highly influenced by soil moisture conditions prior to the field experiment. Heavy rainfall prior to JU2003 resulted in over half of the available energy partitioned into latent heat fluxes at one rural site.

The second objective of this study was to quantify the differences in the components of the SEB between uncoupled (land) and coupled (land-atmosphere) predictions. A comparison of SEB components from uncoupled and coupled predictions revealed slightly larger fluxes predicted by the uncoupled system. The exception was latent heat fluxes, in which values predicted by the uncoupled system were approximately half as large as the values predicted by the coupled system.

The final goal of this study was to assess the sensitivity of uncoupled and coupled predictions using an urban canopy model to determine the critical urban canopy parameters for OKC. Predicted values of air temperature, skin temperature, and energy fluxes were examined to determine which urban canopy parameters were critical to defining the urban morphology of OKC. The urban canopy model was most sensitive to the albedo of the roof, thermal conductivity of the roof, and urban fraction of the grid cell. Changes in net radiation due to a change in roof albedo were offset by changes in

sensible heat fluxes. Similarly, changes in ground heat fluxes due to a change in the thermal conductivity of the roof were offset by changes in the sensible heat fluxes. Changes in latent heat fluxes due to urban fraction were accompanied by offsetting changes in the sensible heat fluxes. It was also discovered that not spinning up the land surface states prior to running the coupled land-atmospheric model were capable of producing energy flux variations much larger than the urban canopy parameters.

Despite the urban parameters changing energy fluxes in excess of 100 W m^{-2} , the diagnostic 2-m air temperatures were not significantly impacted. The lack of sensitivity of 2-m air temperatures to urban canopy parameters, particularly in the daytime, was due to the method used to calculate the skin temperature of the impervious fraction of the grid cell. Implementation of a new method to calculate the skin temperature revealed that the sensitivity of 2-m air temperatures to changes in urban parameters were strongly tied to the method in which skin temperature was calculated.

7.2. FUTURE WORK

The National Research Council (2012) identified the urban boundary layer as “the most understudied and undersampled layer in the urban atmosphere” due to difficulty of access. Unmanned aircraft systems (UAS) are capable of collecting meteorological data to characterize the evolution of temperature, humidity, and winds within the boundary layer, as well as estimate the turbulent sensible, latent, and momentum fluxes, longwave and shortwave radiation, and skin temperature (Knuth et al. 2013). Provided they are safely integrated into the national airspace over the next several years, UAS could serve a new method to collect data to characterize both the

urban and surrounding rural boundary layer and surface characteristics without installing several large towers across a metropolitan area.

Grimmond et al. (2010) found that urban energy balance models have the least capability to model latent heat fluxes. Given that humid heat waves have a stronger impact on human health (Guirguis et al. 2014), future research in urban canopy model development should focus on improving the modeling of latent heat fluxes through better integration of urban vegetation. While a tile approach works for cities where irrigation is not a significant source of moisture, it does not allow direct interaction of built and vegetated surfaces or the capability to account for external water sources such as street cleaning.

Future research should also focus on creating urban canopy parameter datasets. The lack of information on some urban canopy parameters has resulted in tuning the parameter to minimize differences between predicted and observed variables. The National Urban Database with Access Portal's gridded urban parameter datasets for 44 cities was included in the recent release of the WRF model version 3.5 for use with both the single-layer and multi-layer urban canopy models. However, limitations exist with respect to urban fraction.

A significant need exists for two-way interactions between urban meteorologists and end user communities (e.g., emergency managers, public utilities, and urban planners) to better understand user information needs and steer the direction of urban meteorological research. Coordination with state programs experienced in extension, education, and outreach at the local level, such as Land Grant and Sea Grant Extension

or OK-First, could help identify user groups and initiate and facilitate ongoing dialogue. To sustain this effort in the long term and ensure research is socially relevant to end users will require an interdisciplinary team of both physical and social scientists that speak the same language.

REFERENCES

- Ackerman, B., 1985: Temporal march of the Chicago heat island. *J. Climate Appl. Meteor.*, **24**, 547-554.
- , 1987: Climatology of Chicago area urban-rural differences in humidity. *J. Climate Appl. Meteor.*, **26**, 427-430.
- Aida, M., 1982: Urban albedo as a function of the urban structure – a model experiment. *Bound.-Layer Meteor.*, **23**, 405-413.
- , and M. Yaji, 1979: Observations of downward atmospheric radiation in the Tokyo area. *Bound.-Layer Meteor.*, **16**, 453-465.
- , and K. Gotoh, 1982: Urban albedo as a function of the urban structure – a two-dimensional numerical simulation. *Bound.-Layer Meteor.*, **23**, 415-424.
- Allwine, K. J., and J. E. Flaherty, 2006: Joint Urban 2003: Study overview and instrument locations. PNNL Tech. Rep. PNNL-15967, 92 pp.
- , J. H. Shinn, G. E. Streit, K. L. Clawson, and M. Brown, 2002: Overview of URBAN 2000: A multiscale field study of dispersion through an urban environment. *Bull. Amer. Meteor. Soc.*, **83**, 521-536.
- Arnfield, A. J., 1982: An approach to the estimation of the surface radiative properties and radiation budgets of cities. *Phys. Geogr.*, **3**, 97–122.
- , 1988: Validation of an estimation model for urban surface albedo. *Phys. Geog.*, **9**, 361-372.
- , 2003: Two decades of urban climate research: A review of turbulence, exchange of energy and water, and the urban heat island. *Int. J. Climatol.*, **23**, 1-26.
- , and C. S. B. Grimmond, 1998: An urban canyon energy budget model and its application to urban storage heat flux modeling. *Energy and Buildings*, **27**, 61-68.
- ASHRAE, 2009: Material properties. *2009 ASHRAE Handbook: Fundamentals*. American Society of Heating, Refrigerating and Air-Conditioning Engineers, 26.1–26.22.
- Atkinson, B. W., 2003: Numerical modeling of urban heat-island intensity. *Bound.-Layer Meteor.*, **109**, 285-310.
- Au, S. K., and J. L. Beck, 2001: Estimation of small failure probabilities in high dimensions by subset simulation. *Probab. Eng. Mech.*, **16**, 263-277.

- Baker, L. A., A. J. Brazel, N. Selover, C. Martin, N. McIntyre, R. S. Steiner, A. Nelson, and L. Musacchio, 2002: Urbanization and warming of Phoenix (Arizona, USA): Impacts, feedbacks and mitigation. *Urban Ecosyst.*, **6**, 183-203.
- Barlow, J. F., and S. E. Belcher, 2002: A wind tunnel model for quantifying fluxes in the urban boundary layer. *Bound.-Layer Meteor.*, **104**, 131-150.
- , I. N. Harman, and S. E. Belcher, 2004: Scalar fluxes from urban street canyons. Part I: Laboratory simulation. *Bound.-Layer Meteor.*, **113**, 369-385.
- Basara, J. B., 2001: The value of point-scale measurements of soil moisture in planetary boundary layer simulations. Ph. D. dissertation, School of Meteorology, University of Oklahoma.
- , and K. C. Crawford, 2002: Linear relationships between root-zone soil moisture and atmospheric processes in the planetary boundary layer. *J. Geophys. Res.*, **107**, 10, 1-18.
- , P. K. Hall Jr., A. J. Schroeder, B. G. Illston, and K. L. Nemunaitis, 2008: Diurnal cycle of the Oklahoma City urban heat island. *J. Geophys. Res.*, **113**, D20109, doi:10.1029/2008JD010311.
- , H. G. Basara, B. G. Illston, and K. C. Crawford, 2010: The impact of the urban heat island during an intense heat wave in Oklahoma City. *Adv. Meteor.*, **2010**, doi:10.1155/2010/230365.
- , and Coauthors, 2011: The Oklahoma City Micronet. *Meteor. Appl.*, **18**, 252-261.
- Beljaars, A. C. M., 1994: The parameterization of surface fluxes in large-scale models under free convection. *Quart. J. Roy. Meteor. Soc.*, **121**, 255-270.
- Bergstrom, R. W., and J. T. Peterson, 1977: Comparison of predicted and observed solar radiation in an urban area. *J. Appl. Meteor.*, **16**, 1107-1115.
- Best, M. J., 1998: A model to predict surface temperatures. *Bound.-Layer Meteor.*, **88**, 279-306.
- , 2005: Representing urban areas within operational numerical weather prediction models. *Bound.-Layer Meteor.*, **114**, 91-109.
- Betts, A. K., F. Chen, K. Mitchell, and Z. Janjic, 1997: Assessment of the land surface and boundary layer models in two operational versions of the NCEP Eta model using FIFE data. *Mon. Wea. Rev.*, **125**, 2896-2916.

- Betts, R., and M. J. Best, 2004: Changes in urban temperature and humidity due to radiative forcing, landscape effects and local heat sources. BETWIXT Tech. Briefing Note 6, Version 1, 14 pp.
- Bornstein, R. D., 1968: Observations of the urban heat island effect in New York City. *J. Appl. Meteor.*, **7**, 575-582.
- , 1975: The two-dimensional URBMET urban boundary layer model. *J. Appl. Meteor.*, **14**, 1459-1477.
- , and D. S. Johnson, 1977: Urban-rural wind velocity differences. *Atmos. Environ.*, **11**, 597-604.
- Bowne, N. E., and J. T. Ball, 1970: Observational comparison of rural and urban boundary layer turbulence. *J. Appl. Meteor.*, **9**, 862-873.
- Brazel, S. W., and R. C. Balling, Jr., 1986: Temporal analysis of long-term atmospheric moisture levels in Phoenix, Arizona. *J. Climate Appl. Meteor.*, **25**, 112-117.
- Brazel, A. J., H. J. Verville, and R. Lougeay, 1992: Spatial-temporal controls on cooling degree hours: An energy demand parameter. *Theor. Appl. Climatol.*, **47**, 81-92.
- , N. Selover, R. Vose, and G. Heisler, 2000: The tale of two climates – Baltimore and Phoenix urban LTER sites. *Clim. Res.*, **15**, 123-135.
- Brest, C. L., 1987: Seasonal albedo of an urban/rural landscape from satellite observations. *J. Climate Appl. Meteor.*, **26**, 1169-1187.
- Brock, F. V., K. C. Crawford, R. L. Elliott, G. W. Cuperus, S. J. Stadler, H. L. Johnson, and M. D. Eilts, 1995: The Oklahoma Mesonet: A technical overview. *J. Atmos. Oceanic Tech.*, **12**, 5-19.
- Brook, R. R., 1972: The measurement of turbulence in a city environment. *J. Appl. Meteor.*, **11**, 443-450.
- Brotzge, J. A., 2000: Closure of the surface energy budget. Ph.D. dissertation, School of Meteorology, University of Oklahoma, 208 pp.
- , and K. C. Crawford, 2003: Examination of the surface energy budget: A comparison of eddy correlation and Bowen ratio measurement systems. *J. Hydrometeor.*, **4**, 2, 160-178.
- , and S. J. Richardson, 2003: Spatial and temporal correlation among Oklahoma Mesonet and OASIS surface-layer measurements. *J. Appl. Meteor.*, **42**, 5-19.

- , S. J. Richardson, K. C. Crawford, T. W. Horst, F. V. Brock, K. S. Humes, Z. Sorbjan, and R. L. Elliot, 1999: The Oklahoma Atmospheric Surface-layer Instrumentation System (OASIS) Project. *13th Symp. on Boundary Layer and Turbulence*, Dallas, TX, Amer. Meteor. Soc., 612-615.
- Brown, M. J., 2000: Urban parameterizations for mesoscale meteorological models. *Mesoscale Atmospheric Dispersion*, Z. Boybeyi, Ed., WIT Press, 193-255.
- , and M. Williams, 1998: An urban canopy parameterization for mesoscale meteorological models. Preprints, *2nd Symp. on Urban Environment*, Albuquerque, NM, Amer. Meteor. Soc., 144-147.
- Brühl, Chr., and W. Zdunkowski, 1983: An approximate calculation method for parallel and diffuse solar irradiances on inclined surfaces in the presence of obstructing mountains or buildings. *Arch. Met. Geograph. Biocl.*, **32**, 111-129.
- Burian, S. J., W. S. Han, and M. J. Brown, 2005: Morphological analyses using 3D building databases: Oklahoma City, Oklahoma. Los Alamos National Laboratory Tech. Memo LA-UR-05-1821, 63 pp.
- Ca, V. T., T. Asaeda, and Y. Ashie, 1999: Development of a numerical model for the evaluation of the urban thermal environment. *J. Wind Eng. Ind. Aerod.*, **81**, 181-196.
- Camuffo, D. and A. Bernardi, 1982: An observational study of heat fluxes and their relationships with net radiation. *Bound.-Layer Meteor.*, **23**, 359-368.
- Carter, M., J. M. Shepherd, S. Burian, and I. Jeyachandran, 2012: Integration of lidar data into a coupled mesoscale-land surface model: A theoretical assessment of sensitivity of urban-coastal mesoscale circulation to urban canopy parameters. *J. Atmos. Oceanic Tech.*, **29**, 328-346.
- Castro, I. P., H. Cheng, and R. Reynolds, 2006: Turbulence over urban-type roughness: Deductions from wind-tunnel measurements. *Bound.-Layer Meteor.*, **118**, 109-131.
- Cayan, D. R., and A. V. Douglas, 1984: Urban influences on surface temperatures in the southwestern United States during recent decades. *J. Climate Appl. Meteor.*, **23**, 1520-1530.
- Chandler, T. J., 1965: *The Climate of London*. Hutchinson, London, 292 pp.
- Changnon, S. A., Jr. (ed.), 1981. METROMEX: A review and summary. Meteor. Monogr., No. 40, 181 pp.

- , 1992: Inadvertent weather modification in urban areas: Lessons for global climate change. *Bull. Amer. Meteor. Soc.*, **73**, 619-752.
- , and R. G. Semonin, 1978: Chicago Area Program: A major new atmospheric effort. *Bull. Amer. Meteor. Soc.*, **59**, 153-160.
- , F. A. Huff, and R. G. Semonin, 1971: METROMEX: An investigation of inadvertent weather modification. *Bull. Amer. Meteor. Soc.*, **52**, 958-967.
- , E. Uthe, J. M. Hales, R. R. Braham, and A. H. Auer, 1976: METROMEX update. *Bull. Amer. Meteor. Soc.*, **57**, 304-308.
- Charnock, H., 1955: Wind stress on a water surface. *Quart. J. Roy. Meteor. Soc.*, **81**, 639-640.
- Chen, F., and J. Dudhia, 2001: Coupling an advanced land surface-hydrology model with the Penn State-NCAR MM5 modeling system. Part I: Model implementation and sensitivity. *Mon. Wea. Rev.*, **129**, 569-585.
- , and Coauthors, 1996: Modeling of land-surface evaporation by four schemes and comparison with FIFE observations. *J. Geophys. Res.*, **101**, 7251-7268.
- , Z. Janjic, and K. Mitchell, 1997: Impact of atmospheric surface-layer parameterizations in the new land-surface scheme of the NCEP mesoscale Eta model. *Boundary-Layer Meteor.*, **85**, 391-421.
- , M. Tewari, H. Kusaka, and T. T. Warner, 2006: Current status of urban modeling in the community Weather Research and Forecast (WRF) model. Preprints, *6th Symp. on Urban Environment*, Atlanta, GA, Amer. Meteor. Soc., J1.4.
- , and Coauthors, 2007: Description and evaluation of the characteristics of the NCAR High-Resolution Land Data Assimilation System. *J. Appl. Meteor. Climatol.*, **46**, 694-713.
- , S. Miao, M. Tewari, J.-W. Bao, and H. Kusaka, 2011a: A numerical study of interactions between surface forcing and sea breeze circulations and their effects on stagnation in the greater Houston area. *J. Geophys. Res.*, **116**, D12105, doi: 10.1029/2010JD015533.
- , and Coauthors, 2011b: The integrated WRF/urban modelling system: Development, evaluation, and applications to urban environmental problems. *Int. J. Climatol.*, **31**, 273-288.
- Chen, T. H., and Coauthors, 1997: Cabauw experimental results from the Project for Intercomparison of Land-Surface Parameterization Schemes (PILPS). *J.*

- Climate*, **10**, 1194-1215.
- Cheng, H., and I. P. Castro, 2002: Near wall flow over urban-like roughness. *Bound.-Layer Meteor.*, **104**, 229-259.
- Ching, J. K. S., 1985: Urban-scale variations of turbulence parameters and fluxes. *Bound.-Layer Meteor.*, **33**, 335-361.
- , and Coauthors, 2009: National Urban Database and Access Portal Tool. *Bull. Amer. Meteor. Soc.*, **90**, 8, 1157-1179.
- , J. F. Clarke, and J. M. Godowitch, 1983: Modulation of heat flux by different scales of advection in an urban environment. *Bound.-Layer Meteor.*, **25**, 171-191.
- Christen, A., and R. Vogt, 2004: Energy and radiation balance of a central European city. *Int. J. Climatol.*, **24**, 1395-1421.
- Clarke, J. F., 1969: A meteorological analysis of carbon dioxide concentrations measured at a rural location. *Atmos. Environ.*, **3**, 375-383.
- Clawson, K. L., and Coauthors, 2005: Joint Urban 2003 (JU03) SF6 atmospheric tracer field tests. NOAA Tech. Memo OAR ARL-254, 216 pp.
- Cleugh, H. A., and T. R. Oke, 1986: Suburban-rural energy balance comparisons in summer for Vancouver, B.C. *Bound.-Layer Meteor.*, **36**, 351-369.
- Coccal, O., and S. E. Belcher, 2004: A canopy model of mean winds through urban areas. *Quart. J. Roy. Meteor. Soc.*, **130**, 1349-1372.
- , T. G. Thomas, I. P. Castro, and S. E. Belcher, 2006: Mean flow and turbulence statistics over groups of urban-like cubicle obstacles. *Bound.-Layer Meteor.*, **121**, 491-519.
- Comrie, A. C., 2000: Mapping a wind-modified urban heat island in Tucson, Arizona (with comments on integrating research and undergraduate learning). *Bull. Amer. Meteor. Soc.*, **81**, 2417-2431.
- Cosby, B. J., G. M. Hornberger, R. B. Clapp, and T. R. Ginn, 1984: A statistical exploration of the relationships of soil moisture characteristics to the physical properties of soils. *Water Resour. Res.*, **20**, 682-690.
- Cosgrove, B. A., and C. J. Alonge, 2008: Application of NARR-based NLDAS ensemble simulations to continental-scale drought monitoring. Preprints, *22nd Conf. On Hydrology*, New Orleans, LA, Amer. Meteor. Soc., 5.3.

- , and Coauthors, 2003: Land surface model spin-up behavior in the North American Land Data Assimilation System (NLDAS). *J. Geophys. Res.*, **108**(D22), 8845, doi:10.1029/2002JD003316.
- Cowling, E. B., and C. Furiness, 2004: The state of the Southern Oxidants Study (SOS): Policy-relevant findings in ozone and PM_{2.5} pollution research 1994-2003. SOS Tech. Report SOS-3: 1994-2003, 223 pp.
- , W. L. Chameides, C. S. Kiang, F. C. Fehsenfeld, and J. F. Meagher, 1998: Introduction to special section: Southern Oxidants Study Nashville/Middle Tennessee Ozone Study. *J. Geophys. Res.*, **103**, 22 209-22 212.
- Cros, B., and Coauthors, 2004: The ESCOMPTE program: An overview. *Atmos. Res.*, **69**, 241-279.
- Cuenca, R. H., M. Ek, and L. Mahrt, 1996: Impact of soil water property parameterization on atmospheric boundary-layer simulation. *J. Geophys. Res.*, **101**, 7269-7277.
- Dabberdt, W. F., and Coauthors, 2000: Forecast issues in the urban zone: Report of the 10th Prospectus Development Team of the U.S. Weather Research Program. *Bull. Amer. Meteor. Soc.*, **81**, 2047-2064.
- de Goncalves, L. G. G., W. J. Shuttleworth, E. J. Burke, P. Houser, D. L. Toll, M. Rodell, and K. Arsenault, 2006: Toward a South American Land Data Assimilation System: Aspects of land surface model spin-up using the Simplified Simple Biosphere. *J. Geophys. Res.*, **111**, D17110, doi: 10.1029/2005JD006297.
- Delage, Y., and P. A. Taylor, 1970: Numerical studies of heat island circulations. *Bound.-Layer Meteor.*, **1**, 201-226.
- Dickinson, A., Henderson-Sellers, and P. J. Kennedy, 1993: Biosphere-Atmosphere Transfer Scheme (BATS) Version 1e as coupled to the NCAR Community Climate Model. NCAR Tech. Note NCAR/TN-387+STR, 72 pp.
- Doll, D., J. K. S. Ching, and J. Kaneshiro, 1985: Parameterization of subsurface heating for soil and concrete using net radiation data. *Bound.-Layer Meteor.*, **32**, 351-372.
- Doran, J. C., and Coauthors, 1998: The IMADA-AVER boundary layer experiment in the Mexico City area. *Bull. Amer. Meteor. Soc.*, **79**, 2497-2508.
- , J. D. Fast, and J. Horel, 2002: The VTMX 2000 campaign. *Bull. Amer. Meteor. Soc.*, **83**, 537-551.

- Draxler, R. R., 1986: Simulated and observed influence of the nocturnal urban heat island on the local wind field. *J. Climate Appl. Meteor.*, **25**, 1125-1133.
- Duckworth, F. S., and J. S. Sandberg, 1954: The effect of cities upon horizontal and vertical temperature gradients. *Bull. Amer. Meteor. Soc.*, **35**, 198-207.
- Dudhia, J., 1989: Numerical study of convection observed during the winter monsoon experiment using a mesoscale two-dimensional model. *J. Atmos. Sci.*, **46**, 3077–3107.
- , S.-Y. Hong, and K.-S. Lim, 2008: A new method for representing mixed-phase particle fall speeds in bulk microphysics parameterizations. *J. Meteor. Soc. Japan*, **86A**, 33-44.
- Dugas, W. A., L. J. Fritschen, L. W. Gay, A. A. Held, and A. D. Matthias, 1991: Bowen ratio, eddy correlation, and portable chamber measurements of sensible and latent heat flux over irrigated spring wheat. *Agric. Forest Meteor.*, **56**, 1-20.
- Dugway Proving Ground, 2003: Data submission procedures for Joint Urban 2003 database/website. Dugway Proving Ground Tech. Note 03-90-2, Meteorology Division, 8 pp.
- Dupont, E., L. Menut, B. Carissimo, J. Pelon, and P. Flamant, 1999: Comparison between the atmospheric boundary layer in Paris and its rural suburbs during the ECLAP experiment. *Atmos. Environ.*, **33**, 979-994.
- Dupont, S., T. L. Otte, and J. K. S. Ching, 2004: Simulation of meteorological fields within and above urban and rural canopies with a mesoscale model (MM5). *Bound.-Layer Meteor.*, **113**, 111-158.
- , P. G. Mestayer, E. Guilloteau, E. Berthier, and H. Andrieu, 2006: Parameterization of the urban water budget with the Submesoscale Soil Model. *J. Appl. Meteor. Climatol.*, **45**, 624-648.
- Dyer, A. J., and B. B. Hicks, 1970: Flux-gradient relationships in the constant flux layer. *Quart. J. Roy. Meteor. Soc.*, **96**, 715-721.
- Ek, M. B., 2005: Interactions of the land-surface with the atmospheric boundary layer. Ph. D. Thesis, Wageningen University, Wageningen, Gelderland, The Netherlands, 210 pp.
- , K. E. Mitchell, Y. Lin, P. Grunmann, E. Rogers, G. Gayno, and V. Koren, 2003: Implementation of the upgraded Noah land-surface model in the NCEP operational mesoscale Eta model. *J. Geophys. Res.*, **108**(D22), 8851, doi: 10.1029/2002JD003296.

- Eliasson, I., and B. Holmer, 1990: Urban heat island circulation in Göteborg, Sweden. *Theor. Appl. Climatol.*, **42**, 187-196.
- , B. Offerle, C. S. B. Grimmond, and S. Lindqvist, 2006: Wind fields and turbulence statistics in an urban street canyon. *Atmos. Environ.*, **40**, 1-16.
- Epperson, D. L., J. M. Davis, P. Bloomfield, T. R. Karl, A. L. McNab, and K. P. Gallo, 1995: Estimating the urban bias of surface shelter temperatures using upper-air and satellite data. Part II: Estimation of the urban bias. *J. Appl. Meteor.*, **34**, 358-370.
- Estournel, C., R. Vehil, D. Guedalia, J. Fontan, and A. Druilhet, 1983: Observations and modeling of downward radiative fluxes (solar and infrared) in urban/rural areas. *J. Climate Appl. Meteor.*, **22**, 134-142.
- Fan, H., and D. J. Sailor, 2005: Modeling the impacts of anthropogenic heating on the urban climate of Philadelphia: A comparison of the implementations in two PBL schemes. *Atmos. Environ.*, **39**, 73-84.
- Fast, J. D., J. C. Doran, W. J. Shaw, R. L. Coulter, and T. J. Martin, 2000: The evolution of the boundary layer and its effect on air chemistry in the Phoenix area. *J. Geophys. Res.*, **105**, 22 833-22 848.
- , J. C. Torcolini, and R. Redman, 2005: Pseudovertical temperature profiles and the urban heat island measured by a temperature datalogger network in Phoenix, Arizona. *J. Appl. Meteor.*, **44**, 3-13.
- Fiebrich, C. A., J. E. Martinez, J. A. Brotzge, and J. B. Basara, 2003: The Oklahoma Mesonet's skin temperature network. *J. Atmos. Oceanic Tech.*, **20**, 1496-1504.
- FCDMC, cited 2007: FCDMC ALERT System Interactive Product Catalog. [<http://156.42.96.39/alert/APC.pdf>.]
- FHWA, cited 2013: Mitigation Strategies for Design Exceptions - July 2007. [http://safety.fhwa.dot.gov/geometric/pubs/mitigationstrategies/chapter3/3_lanewidth.htm.]
- Flagg, D. D., and P. A. Taylor, 2011: Sensitivity of mesoscale model urban boundary layer meteorology to the scale of urban representation. *Atmos. Chem. Phys.*, **11**, 2951-2972.
- Forster, P. M. de F., and S. Solomon, 2003: Observations of a “weekend effect” in diurnal temperature range. *Proc. Natl. Acad. Sci. U.S.A.*, **100**, 11 225-11 230.
- Fritschen, L. J., E. T. Kanemasu, D. Nie, E. A. Smith, J. B. Stewart, S. B. Verma, and

- M. L. Wesely, 1992: Comparisons of surface flux measurement systems used in FIFE 1989. *J. Geophys. Res.*, **97**(D17), 18 697-18 713.
- Garratt, J. R., 1992: *The Atmospheric Boundary Layer*. Cambridge University Press, 316 pp.
- Graham, I. R., 1968: An analysis of turbulence statistics at Fort Wayne, Indiana. *J. Appl. Meteor.*, **7**, 90-93.
- Greenland, D., and L. W. Swift, Jr., 1991: Climate variability and ecosystem response: Opportunities for the LTER network. *Bull. Ecol. Soc. Am.*, **72**, 118-126.
- Grimmond, C. S. B., 1988: An evaporation-interception model for urban areas. Ph. D. Dissertation, The University of British Columbia, Vancouver, B.C., 206 pp.
- , 2006: Progress in measuring and observing the urban atmosphere. *Theor. Appl. Climatol.*, **84**, 3-22.
- , and T. R. Oke, 1995: Comparison of heat fluxes from summertime observations in the suburbs of four North American cities. *J. Appl. Meteor.*, **34**, 873-889.
- , and T. R. Oke, 1999a: Evapotranspiration rates in urban areas. *IAHS Publ.*, **259**, 235-243.
- , and T. R. Oke, 1999b: Heat storage in urban areas: Local-scale observations and evaluation of a simple model. *J. Appl. Meteor.*, **38**, 922-940.
- , and T. R. Oke, 1999c: Aerodynamic properties of urban areas derived from analysis of surface form. *J. Appl. Meteorol.*, **38**, 1262-1292.
- , and T. R. Oke, 2002: Turbulent heat fluxes in urban areas: Observations and a local-scale urban meteorological parameterization scheme (LUMPS). *J. Appl. Meteor.*, **41**, 792-810.
- , H. A. Cleugh, and T. R. Oke, 1991: An objective urban heat storage model and its comparison with other schemes. *Atmos. Environ.*, **25B**, 311-326.
- , T. S. King, M. Roth, and T. R. Oke, 1998: Aerodynamic roughness of urban areas derived from wind observations. *Bound.-Layer Meteor.*, **89**, 1-24.
- , J. A. Salmond, T. R. Oke, B. Offerle, and A. Lemonsu, 2004a: Flux and turbulence measurements at a densely built-up site in Marseille: Heat, mass (water and carbon dioxide), and momentum. *J. Geophys. Res.*, **109**, D24101, doi:10.1029/2004JD004936.
- , H.-B. Su, B. Offerle, B. Crawford, S. Scott, S. Zhong, and C. Clements, 2004b:

- Variability of sensible heat fluxes in a suburban area of Oklahoma City. Preprints, *Symp. on Planning, Nowcasting, and Forecasting in the Urban Zone*, Seattle, WA, Amer. Meteor. Soc, J7.2.
- , and Coauthors, 2009: Urban Surface Energy Balance Models: Model characteristics and methodology for a comparison study. *Meteorological and Air Quality Models for Urban Areas*, A. Baklanov et al., Eds., Springer-Verlag, 97-124.
- , and Coauthors, 2010: The International Urban Energy Balance Models Comparison Project: First results from Phase 1. *J. Appl. Meteor. Climatol.*, **49**, 1268-1292.
- , and Coauthors, 2011: Initial results from Phase 2 of the international urban energy balance model comparison. *Intl. J. Climatol.*, **31**, 244-272.
- Grossman-Clarke, S., J. A. Zehnder, T. Loridan, and C. S. Grimmond, 2010: Contribution of land use changes to near-surface air temperatures during recent summer extreme heat events in the Phoenix metropolitan area. *J. Appl. Meteor. Climatol.*, **49**, 1649-1664.
- Guirguis, K., A. Gershunov, A. Tardy, and R. Basu, 2014: The impact of recent heat waves on human health in California. *J. Appl. Meteor. Climatol.*, **53**, 3-19.
- Hage, K. D., 1975: Urban-rural humidity differences. *J. Appl. Meteor.*, **14**, 1277-1283.
- Halvorson, S. F., D. P. Storwold, E. M. Vernon, 2006: Joint Urban 2003 database/web design. Preprints, *6th Symp. on Urban Environment*, Atlanta, GA, Amer. Meteor. Soc., 5.9a.
- Hanks, R. J., and G. L. Ashcroft, 1986: *Applied Soil Physics*. Springer-Verlag, 159 pp.
- Hawkins, T. W., A. J. Brazel, W. L. Stefanov, W. Bigler, and E. M. Safell, 2004: The role of rural variability in urban heat island determination for Phoenix, Arizona. *J. Appl. Meteor.*, **43**, 476-486.
- Hernandez-Ramirez, G., J. L. Hatfield, J. H. Prueger, and T. J. Sauer, 2009: Energy balance and turbulent flux partitioning in a corn-soybean rotation in the Midwestern US. *Theor. Appl. Climatol.*, **100**, 79-92.
- Hilberg, S. D., 1978: Diurnal temperature and moisture cycles. Summary of METROMEX, Vol. 2: Causes of precipitation anomalies. Ill. State Water Survey Bull. 63, 25-42.

- Hildebrand, P. H., and B. Ackerman, 1984: Urban effects on the convective boundary layer. *J. Atmos. Sci.*, **41**, 76-91.
- Holt, T., and J. Pullen, 2007: Urban canopy modeling in the New York City metropolitan area: A comparison and validation of single- and multilayer parameterizations. *Mon. Wea. Rev.*, **135**, 1906-1930.
- Holtslag, A. A. M., and H. A. R. de Bruin, 1988: Applied modeling of the nighttime surface energy balance over land. *J. Appl. Meteor.*, **27**, 689-704.
- Hong, S.-Y., and H.-L. Pan, 1996: Nonlocal boundary layer vertical diffusion in a medium-range forecast model. *Mon. Wea. Rev.*, **124**, 2322-2339.
- , H.-M. H. Juang, and Q. Zhao, 1998: Implementation of prognostic cloud scheme for a regional spectral model. *Mon. Wea. Rev.*, **126**, 2621–2639.
- , J. Dudhia, and S.-H. Chen, 2004: A revised approach to ice microphysical processes for the bulk parameterization of clouds and precipitation. *Mon. Wea. Rev.*, **132**, 103-120.
- , Y. Noh, and J. Dudhia, 2006: A new vertical diffusion package with an explicit treatment of entrainment processes. *Mon. Wea. Rev.*, **134**, 2318-2341.
- Houser, P. R., R. Yang, M. Bosilovich, A. Molod, and S. Nebuda, 1999: Spin-up time scales of the Off-line Land Surface GEOS Assimilation (OLGA) System. Preprints, *14th Conf. on Hydrology*, Dallas, TX, Amer. Meteor. Soc., 281-282.
- Hu, X.-M., P. M. Klein, M. Xue, J. K. Lundquist, and F. Zhang, 2013: Impact of low-level jets on the nocturnal urban heat island intensity in Oklahoma City. *J. Appl. Meteor. Climatol.*, **52**, 1779-1802.
- Husain, S. Z., S. Bélair, and S. Leroyer, 2014: Influence of soil moisture on urban microclimate and surface-layer meteorology in Oklahoma City. *J. Appl. Meteor. Climatol.*, **53**, 83-98.
- Inoue, E., 1963: On the turbulent structure of airflow within crop canopies. *J. Meteor. Soc. Japan*, **41**, 317–326.
- Jackson, P. S., 1978: Wind structure near a city centre. *Bound.-Layer Meteor.*, **15**, 323-340.
- Jacquemin, B., and J. Noilhan, 1990: Sensitivity study and validation of a land surface parameterization using the HAPEX-MOBILHY data set. *Bound.-Layer Meteor.*, **52**, 93-134.

- Janjić, Z. I., 1990: The step-mountain coordinate: Physical package. *Mon. Wea. Rev.*, **118**, 1429-1443.
- , 1994: The step-mountain eta coordinate model: Further developments of the convection, viscous sublayer and turbulence closure schemes. *Mon. Wea. Rev.*, **122**, 927-945.
- , 1996: The surface layer in the NCEP Eta Model. Preprints, *11th Conf. on Numerical Weather Prediction*, Norfolk, VA, Amer. Meteor. Soc., 354-355.
- , 2001: Nonsingular implementation of the Mellor-Yamada Level 2.5 Scheme in the NCEP Meso model. NCEP Office Note, No. 437, 61 pp.
- Jiménez, P. A., J. Dudhia, J. F. González-Rouco, J. Navarro, J. P. Montávez, and E. García-Bustamante, 2012: A revised scheme for the WRF surface layer formulation. *Mon. Wea. Rev.*, **140**, 898-918.
- Jin, M., R. E. Dickinson, and D.-L. Zhang, 2005: The footprint of urban areas on global climate as characterized by MODIS. *J. Climate*, **18**, 1551-1565.
- , J. M. Shepherd, and C. Peters-Lidard, 2007: Development of a parameterization for simulating the urban temperature hazard using satellite observations in climate model. *Nat. Hazards*, **43**, 257-271.
- Johansen, O., 1975: Thermal conductivity of soils. Ph.D. thesis, University of Trondheim, 236 pp. [Available from Universitetsbiblioteket i Trondheim, Høgskoleringen 1, 7034 Trondheim, Norway.]
- Johnson, G. T., T. R. Oke, T. J. Lyons, D. G. Steyn, I. D. Watson, and J. A. Voogt, 1991: Simulation of surface urban heat islands, Part 1: Theory and tests against field data. *Bound.-Layer Meteor.*, **56**, 275-294.
- Kain, J. S., 2004: The Kain-Fritsch convective parameterization: An update. *J. Appl. Meteor.*, **43**, 170-181.
- Kalanda, B. D., T. R. Oke, and D. L. Spittlehouse, 1980: Suburban energy balance estimates for Vancouver, B.C., using the Bowen Ratio-Energy Balance approach. *J. Appl. Meteor.*, **19**, 791-802.
- Kanda, M., T. Kawai, M. Kanega, R. Moriwaki, K. Narita, and A. Hagishima, 2005a: A simple energy balance model for regular building arrays. *Bound.-Layer Meteor.*, **116**, 423-443.
- , T. Kawai, and K. Nakagawa, 2005b: A simple theoretical radiation scheme for regular building arrays. *Bound.-Layer Meteor.*, **114**, 71-90.

- Karl, T. R., and R. W. Knight, 1997: The 1995 Chicago heat wave: how likely is a recurrence?" *Bull. Amer. Meteor. Soc.*, **78**, 1107–1119.
- Kastner-Klein, P., and M. W. Rotach, 2004: Mean flow and turbulence characteristics in an urban roughness sublayer. *Bound.-Layer Meteor.*, **111**, 55-84.
- , R. Berkowicz, and R. Britter, 2004: The influence of street architecture on flow and dispersion in street canyons. *Meteorol. Atmos. Phys.*, **87**, 121-131.
- Kawai, T., and M. Kanda, 2010: Urban energy balance obtained from the Comprehensive Outdoor Scale Model Experiment. Part I: Basic features of the surface energy balance. *J. Appl. Meteor. Climatol.*, **49**, 1341-1359.
- Kim, Y., K. Sartelet, J.-C. Raut, and P. Chazette, 2013: Evaluation of the Weather Research and Forecast/Urban model over greater Paris. *Bound.-Layer Meteor.*, **149**, 105-132.
- Kim, Y.-H., and J.-J. Baik, 2005: Spatial and temporal structure of the urban heat island in Seoul. *J. Appl. Meteor.*, **44**, 591-605.
- Klysik, K., 1996: Spatial and seasonal distribution of anthropogenic heat emissions in Łódź, Poland. *Atmos. Environ.*, **30**, 3397-3404.
- Knuth, S. L., J. J. Cassano, J. A. Maslanik, P. D. Herrmann, P. A. Kernebone, R. I. Crocker, and N. J. Logan, 2013: Unmanned aircraft system measurements of the atmospheric boundary layer over Terra Nova Bay, Antarctica. *Earth Sys. Sci. Data*, **5**, 57-69.
- Kondo, H., Y. Genchi, Y. Kikegawa, Y. Ohashi, H. Yoshikado, and H. Komiyama, 2005: Development of a multi-layer urban canopy model for the analysis of energy consumption in a big city: Structure of the urban canopy model and its basic performance. *Bound.-Layer Meteor.*, **116**, 395-421.
- Koren, V., J. Schaake, K. Mitchell, Q. Duan, F. Chen, and J. Baker, 1999: A parameterization of snowpack and frozen ground intended for NCEP weather and climate models. *J. Geophys. Res.*, **104**, 19 569-19 585.
- Kunkel, K. E., S. A. Changnon, B. C. Reinke, and R. W. Arritt, 1996: The July 1995 heat wave in the midwest: a climatic perspective and critical weather factors. *Bull. Amer. Meteor. Soc.*, **77**, 1507–1518.
- Kusaka, H., and F. Kimura, 2004a: Coupling a single-layer urban canopy model with a simple atmospheric model: Impact on urban heat island simulation for an idealized case. *J. Meteor. Soc. Japan*, **82**, 67-80.

- , and F. Kimura, 2004b: Thermal effects of urban canyon structure on the nocturnal heat island: Numerical experiment using a mesoscale model coupled with an urban canopy model. *J. Appl. Meteor.*, **43**, 1899-1910.
- , H. Kondo, Y. Kikegawa, and F. Kimura, 2001: A simple single-layer urban canopy model for atmospheric models: Comparison with multi-layer and slab models. *Bound.-Layer Meteor.*, **101**, 329-358.
- Landsberg, H. E., 1970: Micrometeorological temperature differentiation through urbanization. Urban Climate, WMO Tech. Note, No. 108, 129-136.
- , 1981: *The Urban Climate*. Academic Press, 275 pp.
- , and T. N. Maisel, 1972: Micrometeorological observations in an area of urban growth. *Bound.-Layer Meteor.*, **2**, 365-370.
- Lee, X., W. Massman, and B. Law, 2004: Handbook of Micrometeorology. Kluwer Academic Publishers, 250 pp.
- Lemonsu, A., C. S. B. Grimmond, and V. Masson, 2004: Modeling the surface energy balance of the core of an old Mediterranean city: Marseille. *J. Appl. Meteor.*, **43**, 312-327.
- , S. Belair, and J. Mailhot, 2009: The new Canadian urban modelling system: Evaluation for two cases from the Joint Urban 2003 Oklahoma City Experiment. *Bound.-Layer Meteor.*, **133**, 47-70.
- Li, D., and E. Bou-Zeid, 2013: Synergistic interactions between urban heat islands and heat Waves: the impact in cities is larger than the sum of its parts. *J. Appl. Meteor. Climatol.*, **52**, 2051-2064.
- , 2014: Quality and sensitivity of high-resolution numerical simulation of urban heat islands. *Environ. Res. Letters*, In review.
- Lien, F.-S., and E. Yee, 2005: Numerical modelling of the turbulent flow developing within and over a 3-D building array, Part III: A distributed drag force approach, its implementation and application. *Bound.-Layer Meteor.*, **114**, 287-313.
- , E. Yee, and J. D. Wilson, 2005: Numerical modelling of the turbulent flow developing within and over a 3-D building array, Part II: A mathematical foundation for a distributed drag force approach. *Bound.-Layer Meteor.*, **114**, 245-285.

- Lin, C.-Y., F. Chen, J.C. Huang, W.-C. Chen, Y.-A. Liou, W.-N. Chen, and S.-C. Liu, 2008: Urban heat island effect and its impact on boundary layer development and land-sea circulation over northern Taiwan. *Atmos. Environ.*, **42**, 5635-5649.
- Liu, Y., F. Chen, T. Warner, and J. Basara, 2006: Verification of a mesoscale data-assimilation and forecasting system for the Oklahoma City area during the Joint Urban 2003 field project. *J. Appl. Meteor. Climatol.*, **45**, 912-929.
- Lloyd, C. R., and Coauthors, 1997: A comparison of surface fluxes at the HAPEX-Sahel fallow bush sites. *J. Hydrol.*, **188-189**, 1-4, 400-425.
- Loridan, T., and C. S. B. Grimmond, 2012: Characterization of energy flux partitioning in urban environments: Links with surface seasonal properties. *J. Appl. Meteor. Climatol.*, **51**, 219-241.
- , C. S. B. Grimmond, S. Grossman-Clarke, F. Chen, M. Tewari, K. Manning, A. Martilli, H. Kusaka, and M. Best, 2010: Trade-offs and responsiveness of the single-layer urban canopy parameterization in WRF: An offline evaluation using the MOSCEM optimization algorithm and field observations. *Q. J. R. Meteor. Soc.*, **136**, 997-1019.
- , F. Lindberg, O. Jorba, S. Kotthaus, S. Grossman-Clarke, and C. S. B. Grimmond, 2013: High resolution simulation of the variability of surface energy balance fluxes across Central London with Urban Zones for Energy partitioning. *Bound.-Layer Meteor.*, **147**, 493-523.
- Lowry, W. P., 1974: Project METROMEX: Its history, status, and future. *Bull. Amer. Meteor. Soc.*, **55**, 2, 87-88.
- , 1977: Empirical estimation of urban effects on climate: A problem analysis. *J. Appl. Meteor.*, **16**, 129-135.
- MacDonald, R. W., 2000: Modelling the mean velocity profile in the urban canopy layer. *Bound.-Layer Meteor.*, **97**, 25-45.
- , R. F. Griffiths, D. J. Hall, 1998. An improved method for estimation of surface roughness of obstacle arrays. *Atmos. Environ.*, **32**, 1857-1864.
- Mailhot, J., and Coauthors, 1998: The Montreal-96 Experiment on Regional Mixing and Ozone (MERMOS): An overview and some preliminary results. *Bull. Amer. Meteor. Soc.*, **79**, 433-442.
- Manley, G., 1958: On the frequency of snowfall in metropolitan England. *Quart. J. Roy. Meteor. Soc.*, **84**, 70-72.

- Martilli, A., 2007: Current research and future challenges in urban mesoscale modelling. *Int. J. Climatol.*, **27**, 1909-1918.
- , A. Clappier, and M. W. Rotach, 2002: An urban surface exchange parameterisation for mesoscale models. *Bound.-Layer Meteor.*, **104**, 261-304.
- Maruyama, T., 1999: Surface and inlet boundary conditions for the simulation of turbulent boundary layer over complex rough surfaces. *J. Wind Eng. Ind. Aerod.*, **81**, 311-322.
- Masson, V., 2000: A physically-based scheme for the urban energy budget in atmospheric models. *Bound-Layer Meteor.*, **94**, 357-397.
- , 2006: Urban surface modeling and the meso-scale impact of cities. *Theor. Appl. Climatol.*, **84**, 35-45.
- , C. S. B. Grimmond, and T. R. Oke, 2002: Evaluation of the Town Energy Balance (TEB) scheme with direct measurements from dry districts in two cities. *J. Appl. Meteor.*, **41**, 1011-1026.
- , and Coauthors, 2004: The Canopy and Aerosol Particles in Toulouse Urban Layer (CAPITOU) experiments: first results. Preprints, *5th Conf. on Urban Environment*, Vancouver, Canada, Amer. Meteor. Soc., 1.2.
- Mauder M., and T. Foken, 2004: Documentation and instruction manual of the eddy covariance software package TK2. Abteilung Mikrometeorologie, Universität Bayreuth Arbeitsergebnisse 26, 44 pp. [Available online at <http://www.bitoeck.uni-bayreuth.de/mm/>.]
- McManus, G. D., 2003a: June 2003. Oklahoma Monthly Climate Summary, Oklahoma Climatological Survey, 18 pp. [Available from Oklahoma Climatological Survey, University of Oklahoma, 120 David L. Boren Blvd, Suite 2900, Norman, OK 73072.]
- McManus, G. D., 2003b: July 2003. Oklahoma Monthly Climate Summary, Oklahoma Climatological Survey, 16 pp. [Available from Oklahoma Climatological Survey, University of Oklahoma, 120 David L. Boren Blvd, Suite 2900, Norman, OK 73072.]
- McNeil, D. D., and J. W. Shuttleworth, 1975: Comparative measurements of the energy fluxes over a pine forest. *Bound.-Layer Meteor.*, **9**, 3, 297-313.
- McPherson, R. A., and Coauthors, 2007: Statewide monitoring of the mesoscale environment: A technical update on the Oklahoma Mesonet. *J. Atmos. Oceanic Tech.*, **24**, 301-321.

- Mellor, G. L., and T. Yamada, 1982: Development of a turbulence closure model for geophysical fluid problems. *Rev. Geophys. Space. Phys.*, **20**, 851-875.
- Menut, L., and Coauthors, 2000: Measurements and modeling of atmospheric pollution over the Paris area: An overview of the ESQUIF Project. *Annales Geophysicae*, **18**, 1467-1481.
- Mesinger, F., and Coauthors, 2006: North American Regional Reanalysis. *Bull. Amer. Meteor. Soc.*, **87**, 343-360.
- Mestayer, P. G., and Coauthors, 2005: The urban boundary layer campaign in Marseille (UBL/CLU-ESCOMPTE): Set-up and first results. *Bound.-Layer Meteor.*, **114**, 315-365.
- Miao, S., F. Chen, M. A. LeMone, M. Tewari, Q. Li, and Y. Wang, 2009: An observational and modeling study of characteristics of urban heat island and boundary layer structures in Beijing. *J. Appl. Meteor. Climatol.*, **48**, 484-501.
- Mlawer, E. J., S. J. Taubman, P. D. Brown, M. J. Iacono, and S. A. Clough, 1997: Radiative transfer for inhomogeneous atmosphere: RRTM, a validated correlated-k model for the long-wave. *J. Geophys. Res.*, **102** (D14), 16663–16682.
- Monin, A. S. and A. M. Obukhov, 1954: Dimensionless characteristics of turbulence in the surface layer. *Tr. Geofis. Inst. Akad. Nauk SSSR*, **24**, 163-87.
- Monroe, J. W., 2007: Evaluating NARR surface reanalysis variables and NLDAS using Oklahoma Mesonet observations. M.S. thesis, University of Oklahoma, 109 pp.
- Moriwaki, R., and M. Kanda, 2004: Seasonal and diurnal fluxes of radiation, heat, water vapor, and carbon dioxide over a suburban area. *J. Appl. Meteor.*, **43**, 1700-1710.
- National Research Council, 2010: *When weather matters: Science and services to meet critical societal needs*. Washington, DC: The National Academies Press.
- , 2012: *Urban meteorology: Forecasting, monitoring, and meeting users' needs*. Washington, DC: The National Academies Press.
- NLCD, cited 2014: Multi-Resolution Land Characteristics Consortium (MRLC). [Available online at <http://www.epa.gov/mrlc/definitions.html>.]
- Noh, Y., W. G. Cheon, S.-Y. Hong, and S. Raasch, 2003: Improvement of the K-profile model for the planetary boundary layer based on large eddy simulation data. *Bound.-Layer Meteor.*, **107**, 401-427.

- Noilhan, J., and S. Planton, 1989: A simple parameterization of land surface processes for meteorological models. *Mon. Wea. Rev.*, **123**, 3344-3357.
- Nunez, M., and T. R. Oke, 1977: The energy balance of an urban canyon. *J. Appl. Meteor.*, **16**, 11-19.
- , I. Eliasson, and J. Lindgren, 2000: Spatial variations of incoming longwave radiation in Göteborg, Sweden. *Theor. Appl. Climatol.*, **67**, 181-192.
- Offerle, B., C. S. B. Grimmond, and T. R. Oke, 2003: Parameterization of net all-wave radiation for urban areas. *J. Appl. Meteor.*, **42**, 1157-1173.
- , C. S. B. Grimmond, and K. Fortuniak, 2005: Heat storage and anthropogenic heat flux in relation to the energy balance of a central European city centre. *Int. J. Climatol.*, **25**, 1405-1419.
- , C. S. B. Grimmond, K. Fortuniak, and W. Pawlak, 2006a: Intraurban differences of surface energy fluxes in a central European city. *J. Appl. Meteor. Climatol.*, **45**, 125-136.
- , C. S. B. Grimmond, K. Fortuniak, K. Klysiak, and T. R. Oke, 2006b: Temporal variations in heat fluxes over a central European city centre. *Theor. Appl. Climatol.*, **84**, 103-115.
- Oikawa, S., and Y. Meng, 1995: Turbulence characteristics and organized motion in a suburban roughness sublayer. *Bound.-Layer Meteor.*, **74**, 289-312.
- Oke, T. R., 1973: City size and the urban heat island. *Atmos. Environ.*, **7**, 769-779.
- , 1979: Advectively-assisted evapotranspiration from irrigated urban vegetation. *Bound.-Layer Meteor.*, **17**, 167-173.
- , 1987: *Boundary Layer Climates*. 2d ed. Routledge, 435 pp.
- , 1988: The urban energy balance. *Prog. Phys. Geogr.*, **12**, 471-508.
- , 2004: Initial guidance to obtain representative meteorological observations at urban sites. Instruments and Methods of Observation Programme, IOM Rep. 81, World Meteorological Organization Tech. Document 1250, 51 pp.
- , and C. East, 1971: The urban boundary layer in Montreal. *Bound.-Layer Meteor.*, **1**, 411-437.
- , and R. F. Fuggle, 1972: Comparison of urban/rural counter and net radiation at night. *Bound.-Layer Meteor.*, **2**, 290-308.

- , and J. H. McCaughey, 1983: Suburban-rural energy balance comparisons for Vancouver, B.C.: An extreme case? *Bound.-Layer Meteor.*, **26**, 337-354.
- , and H. A. Cleugh, 1987: Urban heat storage derived as energy balance residuals. *Bound.-Layer Meteor.*, **39**, 233-245.
- , B. D. Kalanda, and D. G. Steyn, 1981: Parameterisation of heat storage in urban areas. *Urban Ecol.*, **5**, 45-54.
- , G. T. Johnson, D. G. Steyn, and I. D. Watson, 1991: Simulation of surface urban heat islands under ‘ideal’ conditions at night. Part 2: Diagnosis of causation. *Bound.-Layer Meteor.*, **56**, 339-358.
- Oleson, K. W., G. B. Bonan, J. Feddema, M. Vertenstein, and C. S. B. Grimmond, 2008: An urban parameterization for a global climate model. Part I: Formulation and evaluation for two cities. *J. Appl. Meteor. Climatol.*, **47**, 1038-1060.
- Osmond, P., 2004: Rooftop “greening” as an option for microclimatic amelioration in a high-density building complex. Preprints, *5th Conf. on Urban Environment*, Vancouver, BC, Canada, Amer. Meteor. Soc., 4.2.
- Otte, T. L., A. Lacser, S. Dupont, and J. K. S. Ching, 2004: Implementation of an urban canopy parameterization in a mesoscale meteorological model. *J. Appl. Meteor.*, **43**, 1648-1665.
- Palecki, M. A., S. A. Changnon, and K. E. Kunkel, 2001: The nature and impacts of the July 1999 heat wave in the midwestern United States: learning from the lessons of 1995. *Bull. Amer. Meteor. Soc.*, **82**, 1353– 1367.
- Pan, H.-L., and L. Mahrt, 1987: Interaction between soil hydrology and boundary layer development. *Bound.-Layer Meteor.*, **38**, 185-202.
- Paulson, C. A., 1970: The mathematical representation of wind speed and temperature profiles in the unstable atmospheric surface layer. *J. Appl. Meteor.*, **9**, 857-861.
- Pearlmutter, D., P. Berliner, and E. Shaviv, 2005: Evaluation of urban surface energy fluxes using an open-air scale model. *J. Appl. Meteor.*, **44**, 532-545.
- Peters-Lidard, C. D., M. S. Zion, and E. F. Wood, 1997: A soil-vegetation-atmosphere transfer scheme for modeling spatially variable water and energy balance processes. *J. Geophys. Res.*, **102**, 4303-4324.
- , E. Blackburn, X. Liang, and E. F. Wood, 1998: The effect of soil thermal conductivity parameterization on surface energy fluxes and temperatures. *J. Atmos. Sci.*, **55**, 1209-1224.

- Peterson, J. T., 1969: The climate of cities: A survey of recent literature. National Air Pollution Control Administration, Publication No. AP-59, U.S. Government Printing Office, Washington, D.C., 48 pp.
- , and T. L. Stoffel, 1980: Analysis of urban-rural solar radiation data from St. Louis, Missouri. *J. Appl. Meteor.*, **19**, 275-283.
- Peterson, T. C., 2003: Assessment of urban versus rural in situ surface temperatures in the contiguous United States: No difference found. *J. Climate*, **16**, 2941-2959.
- Pielke, R. A., 2002: *Mesoscale Meteorological Modeling*. 2d ed. Academic Press, 676 pp.
- Pigeon, G., A. Lemonsu, V. Masson, and P. Durand, 2003: Sea-town interactions over Marseille – Part II: Consequences on atmospheric structure near the surface. Preprints, *5th Int. Conf. on Urban Climate*, Lodz, Poland, Int. Assoc. Urban Climate, 3.4.
- Pinker, R. T., and Coauthors, 2003: Surface radiation budgets in support of the GEWEX Continental Scale International Project (GCIP) and the GEWEX Americas Prediction Project (GAPP), including the North American Land Data Assimilation System (NLDAS) Project. *J. Geophys. Res.*, **108**(D22), 8844, doi: 10.1029/2002JD003301.
- Rafailidis, S., 1997: Influence of building areal density and roof shape on the wind characteristics above a town. *Bound.-Layer Meteor.*, **85**, 255-271.
- Raupach, M. R., 1994: Simplified expressions for vegetation roughness length and zero-plane displacement as functions of canopy height and area index. *Bound.-Layer Meteor.*, **71**, 211-216.
- Roberts, S. M., T. R. Oke, C. S. B. Grimmond, and J. A. Voogt, 2006: Comparison of four methods to estimate urban heat storage. *J. Appl. Meteor. Climatol.*, **45**, 1766-1781.
- Rodell, M., P. R. Houser, A. A. Berg, and J. S. Famiglietti, 2005: Evaluation of 10 methods for initializing a land surface model. *J. Hydrometeorol.*, **6**, 146-155.
- Rogers, E., T. L. Black, D. G. Deaven, G. J. DiMego, Q. Zhao, M. Baldwin, N. W. Junker, and Y. Lin, 1996: Changes to the operational “Early” Eta analysis/forecast system at the National Centers for Environmental Prediction. *Wea. Forecasting*, **11**, 391-413.
- Rotach, M. W., 1993a: Turbulence close to a rough urban surface. Part I: Reynolds stress. *Bound.-Layer Meteor.*, **65**, 1-28.

- , 1993b: Turbulence close to a rough urban surface. Part II: Variances and gradients. *Bound.-Layer Meteor.*, **66**, 75-92.
- , and Coauthors, 2005: BUBBLE – an urban boundary layer meteorology project. *Theor. Appl. Climatol.*, **81**, 231-261.
- Roth, M., 2000: Review of atmospheric turbulence over cities. *Quart. J. Roy. Meteor. Soc.*, **126**, 941-990.
- , and T. R. Oke, 1994: Comparison of modelled and "measured" heat storage in suburban terrain. *Beiträge zur Physik der Atmosphäre*, **67**, 149-156.
- , and T. R. Oke, 1995: Relative efficiencies of turbulent transfer of heat, mass, and momentum over a patchy urban surface. *J. Atmos. Sci.*, **52**, 1863-1874.
- , T. R. Oke, and W. Emery, 1989a: Satellite-derived urban heat islands from three coastal cities and the utility of such data in urban climatology. *Int. J. Remote Sens.*, **10**, 1699-1720.
- , T. R. Oke, and D. G. Steyn, 1989b: Velocity and temperature spectra and cospectra in an unstable suburban atmosphere. *Bound.-Layer Meteor.*, **47**, 309-320.
- Sailor, D. J., and H. Fan, 2002: Modeling the diurnal variability of effective albedo for cities. *Atmos. Environ.*, **36**, 713-725.
- , and L. Lu, 2004: A top-down methodology for developing diurnal and seasonal anthropogenic heating profiles for urban areas. *Atmos. Environ.*, **38**, 2737-2748.
- Salamanca, F., and A. Martilli, 2010: A new building energy model coupled with an urban canopy parameterization for urban climate simulations—Part II. Validation with one dimension off-line simulations. *Theor. Appl. Climatol.*, **99**, 345-356.
- , A. Krpo, A. Martilli, and A. Clappier, 2010: A new building energy model coupled with an urban canopy parameterization for urban climate simulations—Part I. Formulation, verification, and sensitivity analysis of the model. *Theor. Appl. Climatol.*, **99**, 331-344.
- , A. Martilli, M. Tewari, and F. Chen, 2011: A study of the urban boundary layer using different urban parameterizations and high-resolution urban canopy parameters with WRF. *J. Appl. Meteor. Climatol.*, **50**, 1107-1128.
- Schlosser, C. A., and Coauthors, 2000: Simulations of a boreal grassland hydrology at Valdai, Russia: PILPS phase 2(d). *Mon. Wea. Rev.*, **128**, 301-321.

- Schmid, H. P., H. A. Cleugh, C. S. B. Grimmond, and T. R. Oke, 1991: Spatial variability of energy fluxes in suburban terrain. *Bound.-Layer Meteor.*, **54**, 249-276.
- Schroeder, A. J., J. B. Basara, and B. G. Illston, 2010: Challenges associated with classifying urban meteorological stations: The Oklahoma City Micronet example. *The Open Atmos. Sci. J.*, **4**, 88-100.
- Scott, J. W., Jr., 2006: USGS *Vector Road Dataset for Oklahoma County, OK, and Vicinity*, Version 2.0. U.S. Geological Survey. Retrieved from <http://www.usgs.gov/> [April 4, 2013].
- Shafer, M. A., C. A. Fiebrich, D. S. Arndt, S. E. Fredrickson, and T. W. Hughes, 2000: Quality assurance procedures in the Oklahoma Mesonet. *J. Atmos. Oceanic Tech.*, **17**, 474-494.
- Shahgedanova, M., T. P. Burt, and T. D. Davies, 1997: Some aspects of the three-dimensional heat island in Moscow. *Int. J. Climatol.*, **17**, 1451-1465.
- Shea, D. M., and A. H. Auer, 1978: Thermodynamic properties and aerosol patterns in the plume downwind of St. Louis. *J. Appl. Meteor.*, **17**, 689-698.
- Shreffler, J. H., 1979a: Urban-rural differences in tower-measured winds, St. Louis. *J. Appl. Meteor.*, **18**, 829-835.
- , 1979b: Heat island convergence in St. Louis during calm periods. *J. Appl. Meteor.*, **18**, 1512-1520.
- Shuttleworth, J. W., and Coauthors, 1984: Eddy correlation measurements of energy partition for Amazonian forest. *Quart. J. Roy. Meteor. Soc.*, **110**, 466, 1143-1162.
- Sisterson, D. L., and B. A. Dirks, 1978: Structure of the daytime urban moisture field. *Atmos. Environ.*, **12**, 1943-1949.
- Skamarock, W. C., J. B. Klemp, J. Dudhia, D. O. Gill, D. M. Barker, M. G. Duda, X.-Y. Huang, W. Wang, and J. G. Powers, 2008: A description of the Advanced Research WRF Version 3. NCAR Tech Note-475+STR, 113 pp.
- Sorbjan, Z., and M. Uliasz, 1982: Some numerical urban boundary-layer studies. *Bound.-Layer Meteor.*, **22**, 481-502.
- Sprigg, W. A., and W. E. Reifsnyder, 1972: Solar radiation attenuation through the lowest 100 meters of an urban atmosphere. *J. Geophys. Res.*, **77**(33), 6499-6507.
- Spronken-Smith, R. A., T. R. Oke, and W. P. Lowry, 2000: Advection and the surface

- energy balance across an irrigated urban park. *Int. J. Climatol.*, **20**, 1033-1047.
- Sridhar, V., R. L. Elliot, F. Chen, and J. A. Brotzge, 2002: Validation of the NOAA-OSU land surface model using surface flux measurements in Oklahoma. *J. Geophys. Res.*, **107**(D20), 4418, doi:10.1029/2001JD001306.
- Stannard, D. I., J. H. Blanford, W. P. Kustas, W. D. Nichols, S. A. Amer, T. J. Schmugge, and M. A. Weltz, 1994: Interpretation of surface flux measurements in heterogeneous terrain during the Monsoon '90 experiment. *Water Resour. Res.*, **30**, 1227-1240.
- Stewart, I. D., and T. R. Oke, 2012: Local climate zones for urban temperature studies. *Bull. Amer. Meteor. Soc.*, **93**, 12, 1879-1900.
- Steyn, D. G., 1982: Turbulence in an unstable surface layer over suburban terrain. *Bound.-Layer Meteor.*, **22**, 183-191.
- , J. W. Bottenheim, and R. B. Thomson, 1997: Overview of tropospheric ozone in the Lower Fraser Valley, and the Pacific '93 field study. *Atmos. Env.*, **31**, 2025-2035.
- Stull, R. B., 1988: *An Introduction to Boundary Layer Meteorology*. Kluwer Academic Publishers, 670 pp.
- Suckling, P. W., 1980: The energy balance microclimate of a suburban lawn. *J. Appl. Meteor.*, **19**, 606-608.
- Taha, H., 1999: Modifying a mesoscale meteorological model to better incorporate urban heat storage: A bulk-parameterization approach. *J. Appl. Meteor.*, **38**, 466-473.
- Tanner, C. B., 1960: Energy balance approach to evapotranspiration from crops. *Soil. Sci. Soc. Amer. Proc.*, **24**, 1-9.
- , E. Swiatek, and J. P. Greene, 1993: Density fluctuations and use of the Krypton hygrometer in surface flux measurements. *Irrigation and Drainage Systems*, 945-950.
- Tapper, N. J., 1990: Urban influences on boundary layer temperature and humidity: results from Christchurch, New Zealand. *Atmos. Environ.*, **24**, 19-27.
- Tewari, M., H. Kusaka, F. Chen, W. J. Coirier, S. Kim, A. A. Wyszogrodzki, and T. T. Warner, 2010: Impact of coupling a microscale computational fluid dynamics model with a mesoscale model on urban scale contaminant transport and dispersion. *Atmos. Res.*, **96**, 656-664.

- Thom, A. S., 1972: Momentum, mass and heat exchange of vegetation. *Quart. J. Roy. Meteor. Soc.*, **98**, 124-134.
- , J. B. Stewart, H. R. Oliver, and J. H. C. Gash, 1975: Comparison of aerodynamic and energy budget estimates of fluxes over a pine forest. *Quart. J. Roy. Meteor. Soc.*, **101**, 93-105.
- Twine, T. E., and Coauthors, 2000: Correcting eddy-covariance flux underestimates over a grassland. *Agr. Forest Meteor.*, **103**, 3, 279-300.
- Uehara, K., S. Wakamatsu, and R. Ooka, 2003: Studies on critical Reynolds number indices for wind-tunnel experiments on flow within urban areas. *Bound.-Layer Meteor.*, **107**, 353-370.
- United Nations, cited 2010: World urbanization prospects, The 2007 Revision Population Database. [Available online at [http://esa.un.org/unup/.](http://esa.un.org/unup/)]
- Uno, I., S. Wakamatsu, H. Ueda, and A. Nakamura, 1988: An observational study of the structure of the nocturnal urban boundary layer. *Bound.-Layer Meteor.*, **45**, 59-82.
- , H. Ueda, and S. Wakamatsu, 1989: Numerical modeling of the nocturnal urban boundary layer. *Bound.-Layer Meteor.*, **49**, 77-98.
- Unwin, D. J., 1980: The synoptic climatology of Birmingham's heat island, 1965–1974. *Weather*, **35**, 43-50.
- Urano, A., T. Ichinose, and K. Hanaki, 1999: Thermal environment simulation for three dimensional replacement of urban activity. *J. Wind Eng. Ind. Aerod.*, **81**, 197-210.
- Voogt, J. A., and T. R. Oke, 1997: Complete urban surface temperatures. *J. Appl. Meteor.*, **36**, 1117-1132.
- , and C. S. B. Grimmond, 2000: Modeling surface sensible heat flux using surface radiative temperatures in a simple urban area. *J. Appl. Meteor.*, **39**, 1679-1699.
- , and Coauthors, 2007: The Environmental Prediction in Canadian Cities (EPiCC) Network. *Proc. 7th Symp. of the Urban Environment*, San Diego, CA, Amer. Meteor. Soc., P1.16.
- Vrugt, J. A., H. V. Gupta, L. A. Bastidas, W. Bouten, and S. Sorooshian, 2003: Effective and efficient algorithm for multiobjective optimization of hydrological models. *Water Resour. Res.*, **39**(12), doi:10.1029/2002WR001746.

- Vukovich, F. M., and J. W. Dunn, 1978: A theoretical study of the St. Louis heat island: Some parameter variations. *J. Appl. Meteor.*, **17**, 1585-1594.
- , J. W. Dunn III, and B. W. Crissman, 1976: A theoretical study of the St. Louis heat island: The wind and temperature distribution. *J. Appl. Meteor.*, **15**, 417-440.
- , W. J. King, J. W. Dunn III, and J. J. B. Worth, 1979: Observations and simulations of the diurnal variation of the urban heat island circulation and associated variations of the ozone distribution: A case study. *J. Appl. Meteor.*, **18**, 836-854.
- Wang, Z.-H., E. Bou-Zeid, and J. A. Smith, 2011a: A spatially-analytical scheme for surface temperatures and conductive heat fluxes in urban canopy models. *Bound.-Layer Meteorol.*, **138**, 171-193.
- , E. Bou-Zeid, S. K. Au, and J. A. Smith, 2011: Analyzing the sensitivity of WRF's single-layer urban canopy model to parameter uncertainty using advanced Monte Carlo simulation. *J. Appl. Meteor. Climatol.*, **50**, 1795-1814.
- Wanner, H., and J.-A. Hertig, 1984: Studies of urban climates and air pollution in Switzerland. *J. Climate Appl. Meteor.*, **23**, 1614-1625.
- Watson, I., and G. Johnson, 1987: Graphical estimation of sky view-factors in urban environments. *J. Climatol.*, **7**, 193-197.
- Watson, T. B., J. Heiser, P. Kalb, R. N. Dietz, R. Wilke, R. Wieser, and G. Vignato, 2006: The New York City Urban Dispersion Program March 2005 Field Study: Tracer methods and results. Tech. Rep. BNL-75592-2006, Brookhaven National Laboratory, Environmental Sciences Department, 44 pp.
- Webb, E. K., 1970: Profile relationships: The log-linear range and extension to strong stability. *Quart. J. Roy. Meteor. Soc.*, **96**, 67-90.
- , G. I. Pearman, and R. Leuning, 1980: Correction of flux measurements for density effects due to heat and water vapour transfer. *Quart. J. Roy. Meteor. Soc.*, **106**, 85-100.
- Weber, S., 2006: Comparison of in-situ measured ground heat fluxes within a heterogeneous urban ballast layer. *Theor. Appl. Climatol.*, **83**, 169-179.
- Wesely, M. L., and R. C. Lipschutz, 1976: An experimental study of the effects of aerosols and diffuse and direct solar radiation received during the summer near Chicago. *Atmos. Environ.*, **10**, 981-987.
- White, J. M., F. D. Eaton, and A. H. Auer, Jr., 1978: The net radiation budget of the St.

- Louis metropolitan area. *J. Appl. Meteor.*, **17**, 593-599.
- Whiteman, C. D., J. M. Hubbe, and W. J. Shaw, 2000: Evaluation of an inexpensive temperature data logger for meteorological applications. *J. Atmos. Oceanic Tech.*, **17**, 77-81.
- Wilson, K., and Coauthors, 2002: Energy balance closure at FLUXNET sites. *Agric. For. Meteor.*, **113**, 223-243.
- Wong, K. K., and R. A. Dirks, 1978: Mesoscale perturbations on airflow in the urban mixing layer. *J. Appl. Meteor.*, **17**, 677-688.
- Xia, Y., M. Ek, H. Wei, and J. Meng, 2012: Comparative analysis of relationships between NLDAS-2 forcings and model outputs. *Hydrol. Process.*, **26**, 467-474.
- Yang, Z.-L., R. E. Dickinson, A. Henderson-Sellers, and A. J. Pittman, 1995: Preliminary study of spin-up processes in land surface models with the first stage data of Project for Intercomparison of Land Surface Parameterization Schemes Phase 1(a). *J. Geophys. Res.*, **100**(D8), 16 553-16 578.
- Yap, D., and T. R. Oke, 1974: Sensible heat fluxes over an urban area—Vancouver, B.C., *J. Appl. Meteor.*, **13**, 880-890.
- Yersel, M., and R. Goble, 1986: Roughness effects on urban turbulence parameters. *Bound.-Layer Meteor.*, **37**, 271-284.
- Zhang, D.-L., and R. A. Anthes, 1982: A high-resolution model of the planetary boundary layer—sensitivity tests and comparisons with SESAME-79 data. *J. Appl. Meteor.*, **21**, 1594-1609.
- , Y.-X. Shou, R. R. Dickerson, and F. Chen, 2011: Impact of upstream urbanization on the urban heat island effects along the Washington-Baltimore corridor. *J. Appl. Meteor. Climatol.*, **50**, 2012-2029.
- Zilitinkevich, S. S., 1995: Non-local turbulent transport: pollution dispersion aspects of coherent structure of convective flows. *Air Pollution III*, Vol. I, *Air Pollution Theory and Simulation*, H. Power, N. Moussiopoulos and C.A. Brebbia. Eds., Computational Mechanics Publications, 53-60.

A. APPENDIX: PROGNOSTIC EQUATIONS FOR THE NOAH LSM

A.1. SOIL MOISTURE

The prognostic equation for volumetric soil moisture content (Θ ; dimensionless) in the Noah LSM is the diffusive form of Richard's equation

$$\frac{\partial \Theta}{\partial t} = \frac{\partial}{\partial z} \left(D_{\Theta} \frac{\partial \Theta}{\partial z} \right) + \frac{\partial D = K_{\Theta}}{\partial z} + F_{\Theta} \quad (\text{A.1})$$

where the soil water diffusivity (D_{Θ} ; $\text{m}^2 \text{s}^{-1}$) and hydraulic conductivity (K_{Θ} ; m s^{-1}) are functions of Θ (Hanks and Ashcroft 1986). F_{Θ} represents the sources and sinks for soil water, such as precipitation, evaporation, and runoff. The hydraulic conductivity and soil water diffusivity are given by

$$K_{\Theta} = K_{\Theta_s} \left(\frac{\Theta}{\Theta_s} \right)^{2b+3} \quad (\text{A.2})$$

$$D_{\Theta} = \left(\frac{bK_{\Theta_s} \Psi_s}{\Theta_s} \right) \left(\frac{\Theta}{\Theta_s} \right)^{b+2} \quad (\text{A.3})$$

where K_{Θ_s} is the saturation hydraulic conductivity, Θ_s is the saturation volumetric soil moisture content, b is an empirically-derived constant, and $\Psi_s(\text{m})$ is the saturation soil moisture potential, all of which are dependent on soil texture (Ek 2005). Because hydraulic conductivity and soil water diffusivity are non-linear functions of soil moisture, particularly when the soil is dry, they can change rapidly by several orders of magnitude with small variations in soil moisture (Chen and Dudhia 2001). As a result, the partitioning of available energy into latent and sensible heat fluxes is significantly impacted by the soil moisture parameterization (Cuenca et al. 1996). The layer-integrated form of (A.1) is

$$\Delta z_i \frac{\partial \Theta}{\partial t} = \left(D_\Theta \frac{\partial \Theta}{\partial z} + K_\Theta \right)_{z_{i+1}} - \left(D_\Theta \frac{\partial \Theta}{\partial z} + K_\Theta \right)_{z_i} \quad (\text{A.4})$$

where Δz_i is the thickness of the i th soil layer. At the bottom of the soil model, the hydraulic diffusivity is assumed to be zero. As a result, the soil water flux is only due to gravitational drainage or subsurface runoff.

A.2. SOIL TEMPERATURE

Soil heat transfer is controlled by the diffusion equation for soil temperature

$$C_T \frac{\partial T}{\partial t} = \frac{\partial}{\partial z} \left(K_T \frac{\partial T}{\partial z} \right) \quad (\text{A.5})$$

where C_T ($\text{J m}^{-3} \text{K}^{-1}$) is the volumetric heat capacity and K_T ($\text{W m}^{-1} \text{K}^{-1}$) is the soil thermal conductivity, which are functions of volumetric soil moisture content (Pan and Mahrt 1987). The layer-integrated form of (A.5) for the i th soil layer is

$$\Delta z_i C_{T_i} \frac{\partial T_i}{\partial t} = \left(K_T \frac{\partial T}{\partial z} \right)_{z_{i+1}} - \left(K_T \frac{\partial T}{\partial z} \right)_{z_i} \quad (\text{A.6})$$

Volumetric heat capacity is calculated as

$$C_T = \Theta C_{water} + (1 - \Theta_s) C_{soil} + (\Theta_s - \Theta) C_{air} \quad (\text{A.7})$$

where the saturation soil moisture content (Θ_s) varies with soil texture (Cosby et al. 1984). The volumetric heat capacities are $C_{water} = 4.2 \times 10^6 \text{ J m}^{-3} \text{K}^{-1}$, $C_{soil} = 1.26 \times 10^6 \text{ J m}^{-3} \text{K}^{-1}$, and $C_{air} = 1004 \text{ J m}^{-3} \text{K}^{-1}$.

Soil thermal conductivity is computed according to the Johansen (1975) method as a function of soil saturation, porosity, quartz content, and dry density, as well as the phase of water:

$$K_T = K_e (K_{sat} - K_{dry}) + K_{dry} \quad (\text{A.8})$$

where K_e is the Kersten number, a function of the degree of saturation and phase of the water, K_{sat} is the saturated thermal conductivity, and K_{dry} is the dry thermal conductivity (Peters-Lidard et al. 1998). In the presence of a vegetation layer, the soil thermal conductivity under vegetation (K_{T_0}) is reduced from the bare soil value by an exponential function of green vegetation fraction (Peters-Lidard et al. 1997):

$$K_T = K_{T_0} e^{(-\beta_{veg}\sigma_f)} \quad (\text{A.9})$$

where σ_f is the green vegetation fraction and $\beta_{veg} = 2.0$ is an empirical constant (Ek et al. 2003).

A.3. CANOPY WATER

The water budget for the intercepted canopy water (W_c) is

$$\frac{\partial W_c}{\partial t} = \sigma_f P - D - E_c \quad (\text{A.10})$$

where P is the total precipitation, D is the excess precipitation that drips off the canopy and reaches the ground, and E_c is canopy water evaporation.

A.4. THE SURFACE ENERGY BALANCE

The surface energy balance is evaluated as

$$(1 - \alpha)S \downarrow + L \downarrow - \varepsilon \sigma T_s^4 = H + L_v E_p + G \quad (\text{A.11})$$

where α is the surface albedo, $S \downarrow$ is the downwelling shortwave radiation, $L \downarrow$ is the downwelling longwave radiation, ε is the surface emissivity, $\sigma = 5.67 \times 10^{-8} \text{ W m}^{-2} \text{ K}^{-4}$ is the Stefan-Boltzmann constant, T_s is the surface skin temperature, H is the sensible heat flux, $L_v = 2.5 \times 10^6 \text{ J kg}^{-1}$ is the latent heat, E_p is the potential evaporation, and G is the ground heat flux.

A.4.1. Sensible Heat Flux

Sensible heat flux uses a saturated surface temperature appropriate for the potential evaporation and is defined as

$$\begin{aligned} H &= \rho c_p C_h U (\theta_s - \theta_a) \\ &= \rho c_p C_h U [(\theta_s - T_a) - (\theta_a - T_a)] \end{aligned} \quad (\text{A.12})$$

where ρ is the air density, c_p is the specific heat, C_h is the exchange coefficient for heat, and U , T_a , and θ_a are the wind speed, air temperature, and potential temperature (Ek 2005). To calculate potential evaporation, sensible heat flux is computed using values from the previous model time step and is updated later.

A.4.2. Ground Heat Flux

Ground heat flux is calculated as

$$G = -K_T \frac{\partial T_{s_1}}{\partial z} \quad (\text{A.13})$$

where K_T is the soil thermal conductivity and $\partial T_{s_1} / \partial z$ is the soil temperature gradient in the upper soil layer. In finite difference form, (A.13) is

$$G = -K_T \frac{T_s - T_{s_1}}{\Delta z} \quad (\text{A.14})$$

where T_s is the surface temperature, T_{s_1} is the temperature of the upper soil layer, and Δz is the mid-point of the upper soil layer (Ek 2005). As with sensible heat flux, the ground heat flux is calculated with values from the previous model time step and is updated later in order to calculate potential evaporation.

A.4.3. Linearized Surface Energy Balance

Upwelling longwave radiation, σT_s^4 , is linearized as

$$\sigma T_s^4 \approx \sigma T_a^4 \left[1 + 4 \left(\frac{T_s - T_a}{T_a} \right) \right] \quad (\text{A.15})$$

Further, F_n is defined as

$$F_n = (1 - \alpha)S \downarrow + L \downarrow - \epsilon \sigma T_a^4 - G \quad (\text{A.16})$$

and substituted into (A.11) with (A.15) and (A.12) to obtain

$$F_n - 4\sigma T_a^4 \left(\frac{T_s - T_a}{T_a} \right) = \rho c_p C_h U [(T_s - T_a) - (\theta_a - T_a)] + L_v E_p \quad (\text{A.17})$$

where it is assumed that $\theta_s = T_s$ (Ek 2005).

A.4.4. Potential Evaporation

Potential evaporation (E_p) is calculated by a Penman-based energy balance approach that includes a stability-dependent aerodynamic resistance (Mahrt and Ek 1984),

$$\begin{aligned} L_v E_p &= \rho c_p C_q U (q_{s,sat} - q_a) \\ &= \rho c_p C_h U \left[\frac{dq_s}{dT} (T_s - T_a) + (q_{a,sat} - q_a) \right] \end{aligned} \quad (\text{A.18})$$

where $q_{s,sat}$ is the surface saturation specific humidity, $q_{a,sat}$ is the atmospheric saturation specific humidity, q_a is the atmospheric specific humidity, and it is assumed that the exchange coefficients for heat (C_h) and moisture (C_q) are equal. To remove surface skin temperature from the expression for potential evaporation, (A.18) must be solved for $T_s = T_a$,

$$T_s - T_a = \left[\frac{L_v E_p}{\rho L_v C_h U} - (q_{a,sat} - q_a) \right] \left(\frac{dq_s}{dT} \right)^{-1} \quad (\text{A.19})$$

By substituting (A.19) into (A.17) and rearranging, the equation for potential evaporation becomes

$$L_v E_p = \rho c_p C_h U \left\{ \frac{\Delta \left[\frac{F_n}{\rho c_p C_h U} + (\theta_a - T_a) \right] + A(r+1)}{\Delta + r + 1} \right\} \quad (\text{A.20})$$

where

$$\begin{aligned} \Delta &= \frac{dq_s}{dT} \frac{L_v}{c_p} \\ A &= \frac{L_v}{c_p} (q_{a,sat} - q_a) \\ r &= \frac{4\sigma T_a^4 R_d}{p_s c_p C_h U} \end{aligned}$$

For cases when $\theta_s \neq T_s$, (A.20) assumes the general form

$$L_v E_p = \rho c_p C_h U \left\{ \frac{\Delta \left[\frac{F_n}{\rho c_p C_h U} + (\theta_a - T_a) \right] + A(r+1) + (A - \Delta T_a) \delta_\theta}{\Delta + r + 1 + \delta_\theta} \right\} \quad (\text{A.21})$$

where

$$\begin{aligned} \delta_\theta &= \left[\left(\frac{p_{00}}{p_s} \right)^\kappa - 1 \right] \\ p_{00} &= 1000 \text{ HPa} \\ \kappa &= \frac{R_d}{c_p} \end{aligned}$$

p_s is surface pressure, and R_d is the dry gas constant (Ek 2005).

A.5. SURFACE EVAPOTRANSPIRATION

The total evaporation (E) is the sum of the direct evaporation from the top shallow soil layer (E_{dir}), evaporation of precipitation intercepted by the canopy (E_c), and transpiration via the canopy and roots (E_t),

$$E = E_{dir} + E_c + E_t \quad (\text{A.22})$$

A.5.1. Direct Soil Evaporation

The direct evaporation from the top shallow soil layer is expressed as

$$E_{dir} = (1 - \sigma_f) \beta E_p \quad (\text{A.23})$$
$$\beta = \left(\frac{\Theta_1 - \Theta_w}{\Theta_{fc} - \Theta_w} \right)^2$$

where Θ_1 is the volumetric water content of the top soil layer, Θ_{fc} is the field capacity, Θ_w is the wilting point, and σ_f is the green vegetation fraction, which is critical for the partitioning total evaporation between direct evaporation and canopy transpiration (Chen and Dudhia 2001).

A.5.2. Canopy Evaporation

The wet canopy evaporation (E_c) is calculated by

$$E_c = \sigma_f E_p \left(\frac{W_c}{S} \right)^n \quad (\text{A.24})$$

where W_c is the intercepted canopy water content, S is the saturated canopy water content, and $n = 0.5$ (Pan and Mahrt 1987). Canopy water content increases by precipitation and dewfall. Once saturated, additional water is assumed to fall to the ground surface.

A.5.3. Canopy Transpiration and Canopy Resistance

Canopy transpiration is determined by

$$E_t = \sigma_f k_v E_p \left[1 - \left(\frac{W_c}{S} \right)^n \right] \quad (\text{A.25})$$

where k_v is a plant coefficient related to the canopy resistance (R_c) by

$$k_v = \frac{(r + 1 + \Delta + \delta_\theta)}{(r + 1 + \delta_\theta)(1 + R_c C_h U) + \Delta} \quad (\text{A.26})$$

The canopy resistance accounts for the reduction in transpiration due to plant stomatal control and is commonly expressed as a function of solar radiation (R_{c_s}), specific humidity deficit (R_{c_q}), air temperature (R_{c_T}), and soil moisture (R_{soil}). Canopy resistance follows the formulation of Jacquemin and Noilhan (1990):

$$R_c = \frac{R_{c_{\min}}}{\text{LAI} R_{c_s} R_{c_T} R_{c_q} R_{soil}} \quad (\text{A.27})$$

where ($R_{c_{\min}}$) is the minimum canopy resistance and $\text{LAI} = 4$ is the leaf area index (Ek et al. 2003). The solar radiation function is expressed as

$$R_{c_s} = \frac{\frac{R_{c_{\min}}}{R_{c_{\max}}} + \frac{a_{s_1} S \downarrow a_{s_2}}{\text{LAI}}}{1 + \frac{a_{s_1} S \downarrow a_{s_2}}{\text{LAI}}} \quad (\text{A.28})$$

where a_{s_1} and a_{s_2} are coefficients. $R_{c_{\max}}$ is the cuticular resistance of the leaves as in Dickinson et al. (1993). The specific humidity deficit function is

$$R_{c_q} = \frac{1}{1 + a_{q_1} (q_{a,sat} - q_a)} \quad (\text{A.29})$$

where a_{q_1} is a coefficient, $q_{a,sat}$ is the saturation specific humidity, and q_a is the atmospheric specific humidity. The temperature function is calculated by

$$R_{c_r} = 1 - a_{T_1} (T_{ref} - T_a)^2 \quad (\text{A.30})$$

where a_{T_1} is a coefficient, $T_{ref} = 298$ K is a reference temperature (Noilhan and Planton 1989), and T_a is the air temperature. The soil moisture availability function is

$$R_{soil} = \sum_{i=1}^n \frac{(\Theta_i - \Theta_w) \Delta z_i}{(\Theta_{fc} - \Theta_w) \Delta z} \quad (\text{A.31})$$

where n is the number of soil layers, Θ_w is the wilting point, Θ_{fc} is the field capacity, Δz_i is the thickness of the i th soil layer, and Δz is the thickness of the entire soil column.

A.6. SURFACE EXCHANGE COEFFICIENTS

The surface exchange coefficient for heat and moisture (C_h) depends on atmospheric stability in terms of near-surface bulk Richardson number (Ri_b) of the form

$$Ri_b = \frac{g (\theta_{v_a} - \theta_{v_s}) z}{\theta_{v_a} U^2} \quad (\text{A.32})$$

where g is the acceleration due to gravity, z is the height of the atmospheric observations, θ_{v_a} is the virtual potential temperature of the atmosphere, and θ_{v_s} is the virtual potential temperature at the surface. Following Louis (1979) and Louis et al. (1982), the surface exchange coefficient for heat and moisture is

$$C_h = \left(\frac{k^2}{R} \right) \frac{F_h}{\ln(z/z_{0_m}) \ln(z/z_{0_h})} \quad (\text{A.33})$$

where k is the von Karman constant, R , estimated as 1.0, is the ratio of drag coefficients for momentum and heat in the neutral limit, z is the atmospheric reference height, z_{0_m}

and z_{0_h} are the roughness lengths for momentum and heat, respectively (Ek 2005).

For unstable conditions ($Ri_b < 0$),

$$F_h = 1 - \frac{15 Ri_b}{1 + 75 k^2 \left[\ln(z/z_{0_m}) \right]^{-1} \left[\ln(z/z_{0_h}) \right]^{-1} \left[Ri_b(z/z_{0_m}) \right]^{1/2}} \quad (\text{A.34})$$

For stable conditions ($Ri_b > 0$),

$$F_h = \frac{1}{1 + 10 Ri_b (1 + 8 Ri_b)} \quad (\text{A.35})$$

A.7. SURFACE TEMPERATURE

To determine the surface skin temperature (T_s), the actual evaporation (A.22), instead of potential evaporation, is used in the surface energy balance (A.11). It should be noted that the actual evaporation can be expressed as $E = \beta E_p$ where β is a factor that absorbs all influences that reduce the potential evaporation to the actual evaporation. Thus, the surface energy balance becomes

$$(1 - \alpha) S \downarrow + L \downarrow - \varepsilon \sigma T_s^4 = H + \beta L_v E_p + G \quad (\text{A.36})$$

Using (A.12) and (A.15), the surface energy balance is rewritten as

$$(1 - \alpha) S \downarrow + L \downarrow - 4 \sigma T_a^4 \left(\frac{T_s - T_a}{T_a} \right) = \rho c_p C_h U \left[(\theta_s - T_a) - (\theta_a - T_a) \right] + \beta L_v E_p + G \quad (\text{A.37})$$

Using the definition of ground heat flux from (A.14) and r from (A.20), surface skin temperature can be solved for as

$$T_s = \frac{\Delta z \rho c_p C_h U \left[T_a (r + 1) + (\theta_a - T_a) \right] + \Delta z \left[(1 - \alpha) S \downarrow + L \downarrow - \sigma T_a^4 - \beta L_v E_p \right] + K_T T_{s1}}{\Delta z \rho c_p C_h U (r + 1) + K_T} \quad (\text{A.38})$$

For the case when $\theta_s \neq \theta_a$, (A.38) becomes

$$T_s = \frac{\Delta z \rho c_p C_h U [T_a(r+1) + (\theta_a - T_a)] + \Delta z [(1 - \alpha) S \downarrow + L \downarrow - \sigma T_a^4 - \beta L_v E_p] + K_T T_{s_1}}{\Delta z \rho c_p C_h U (r + 1 + \delta_\theta) + K_T} \quad (\text{A.39})$$

After updating the soil moisture content, soil temperature, and surface skin temperature, the ground and sensible heat fluxes are updated.

B. APPENDIX: SURFACE ENERGY BALANCE COMPONENTS

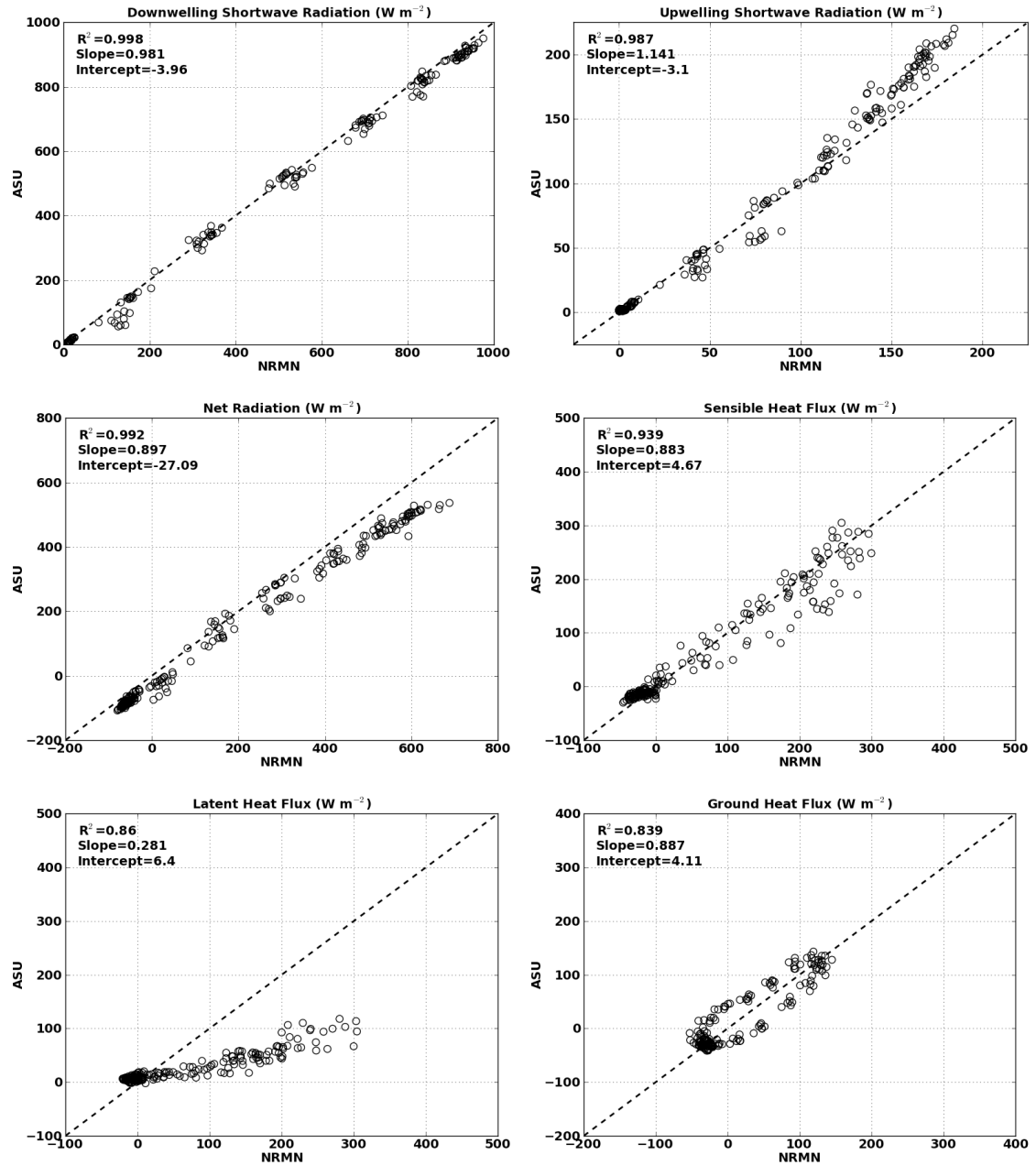


Figure B.1. Scatter plots of downwelling shortwave radiation, upwelling longwave radiation, net radiation, sensible heat fluxes, latent heat fluxes, and ground heat fluxes for the ASU vs. NRMN sites from 10 days with solar insolation near theoretical values during July 2003.

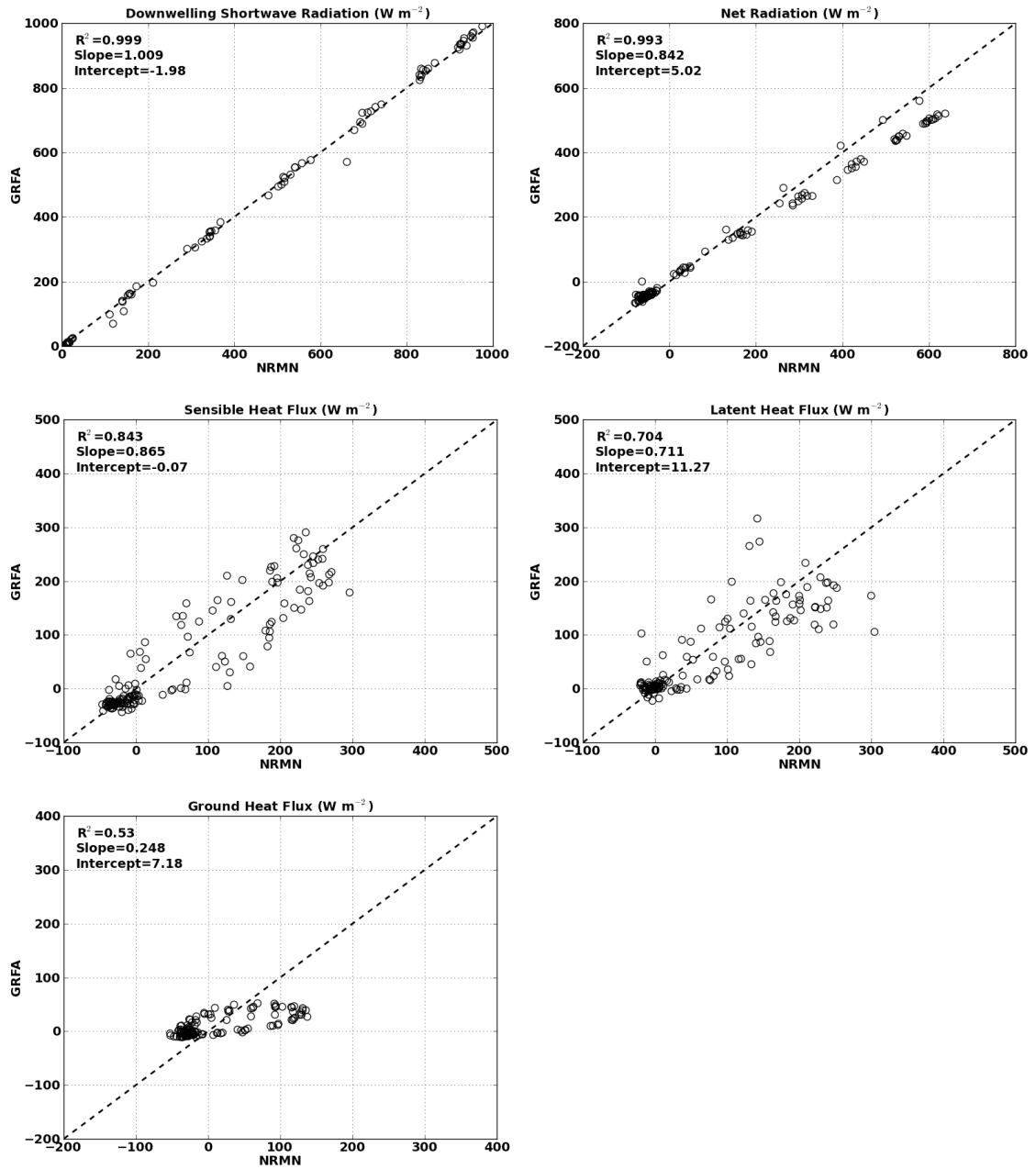


Figure B.2. Scatter plots of downwelling shortwave radiation, net radiation, sensible heat fluxes, latent heat fluxes, and ground heat fluxes for the IU GR vs. NRMN sites from 10 days with solar insolation near theoretical values during July 2003.

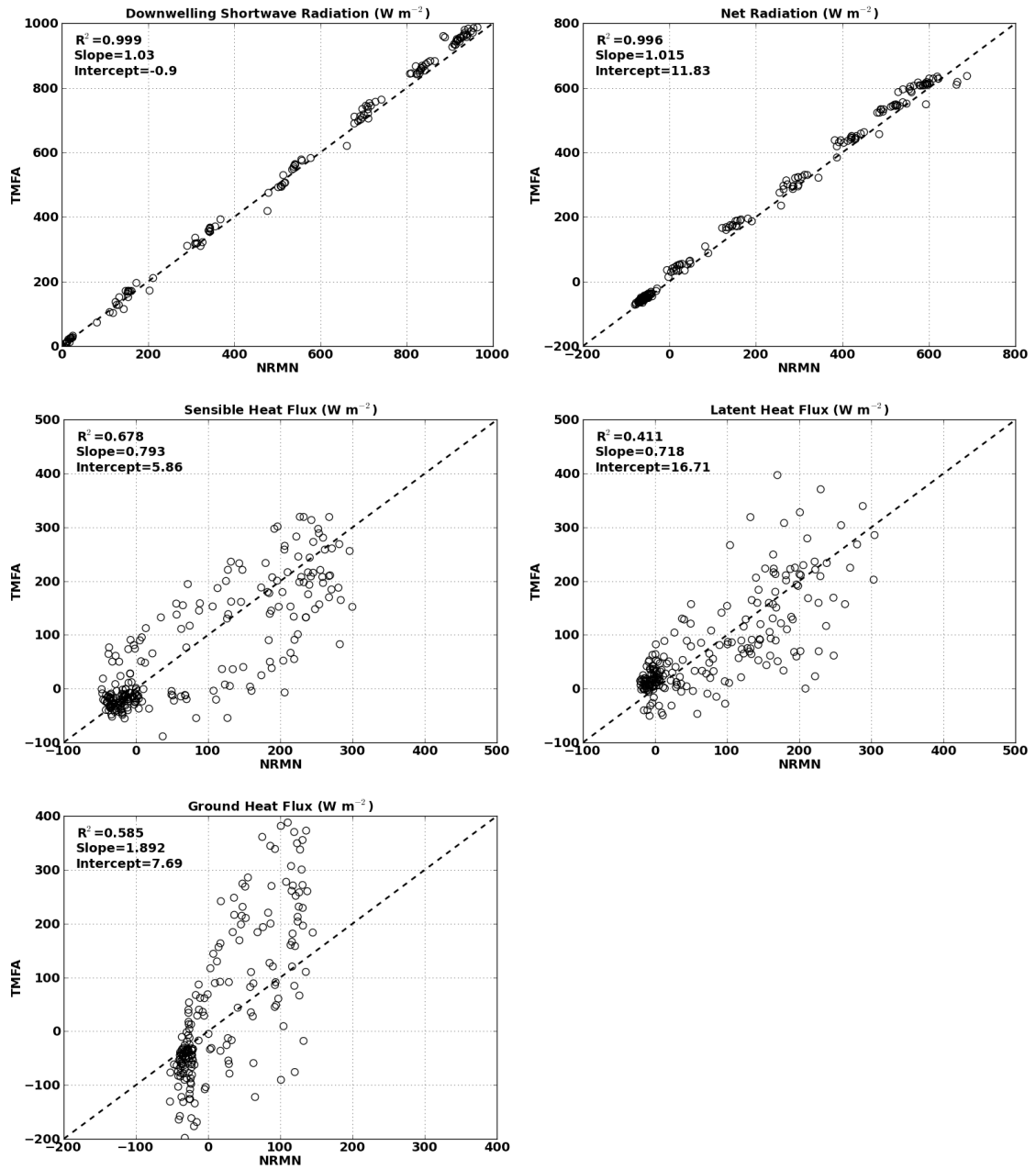


Figure B.3. Scatter plots of downwelling shortwave radiation, net radiation, sensible heat fluxes, latent heat fluxes, and ground heat fluxes for the IU TMA vs. NRMN sites from 10 days with solar insolation near theoretical values during July 2003.

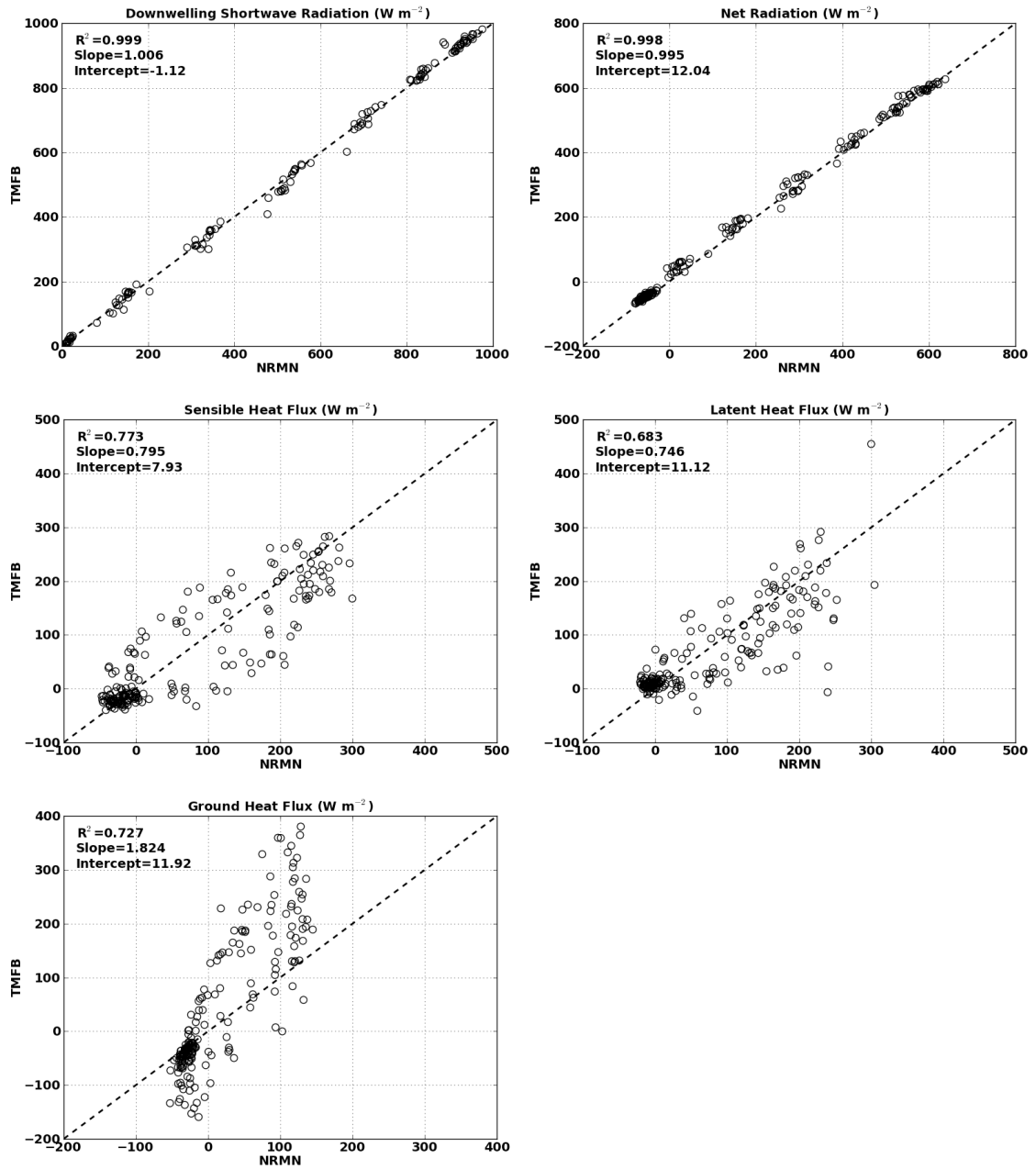


Figure B.4. Scatter plots of downwelling shortwave radiation, net radiation, sensible heat fluxes, latent heat fluxes, and ground heat fluxes for the IU TMB vs. NRMN sites from 10 days with solar insolation near theoretical values during July 2003.

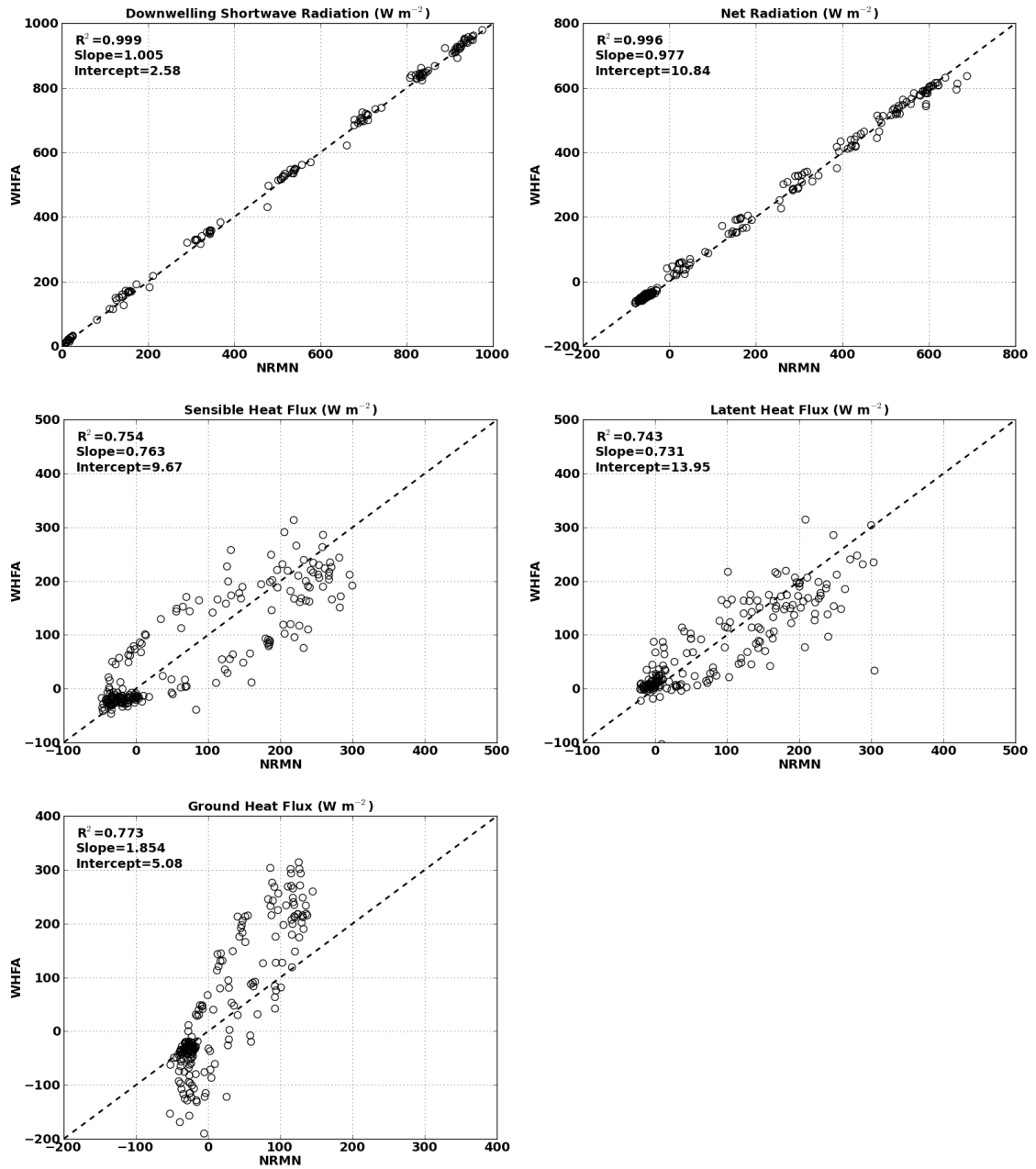


Figure B.5. Scatter plots of downwelling shortwave radiation, net radiation, sensible heat fluxes, latent heat fluxes, and ground heat fluxes for the IU WH vs. NRMN sites from 10 days with solar insolation near theoretical values during July 2003.

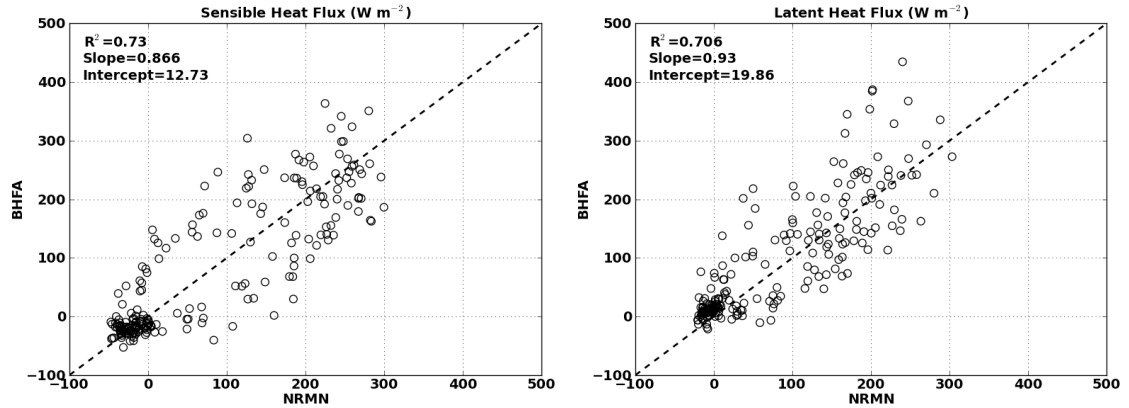


Figure B.6. Scatter plots of sensible heat fluxes and latent heat fluxes for the IU BH vs. NRMN sites from 10 days with solar insolation near theoretical values during July 2003.

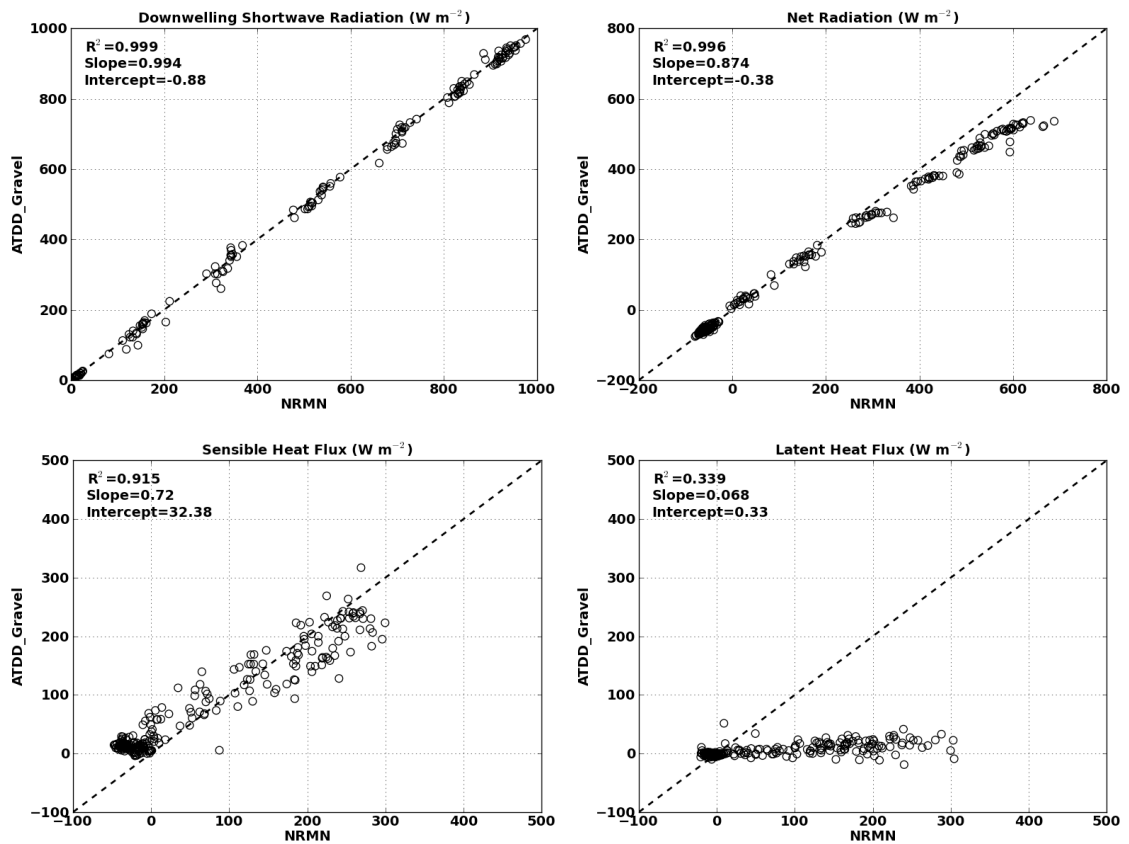


Figure B.7. Scatter plots of downwelling shortwave radiation, net radiation, sensible heat fluxes, and latent heat fluxes for the ATDD Gravel vs. NRMN sites from 10 days with solar insolation near theoretical values during July 2003.

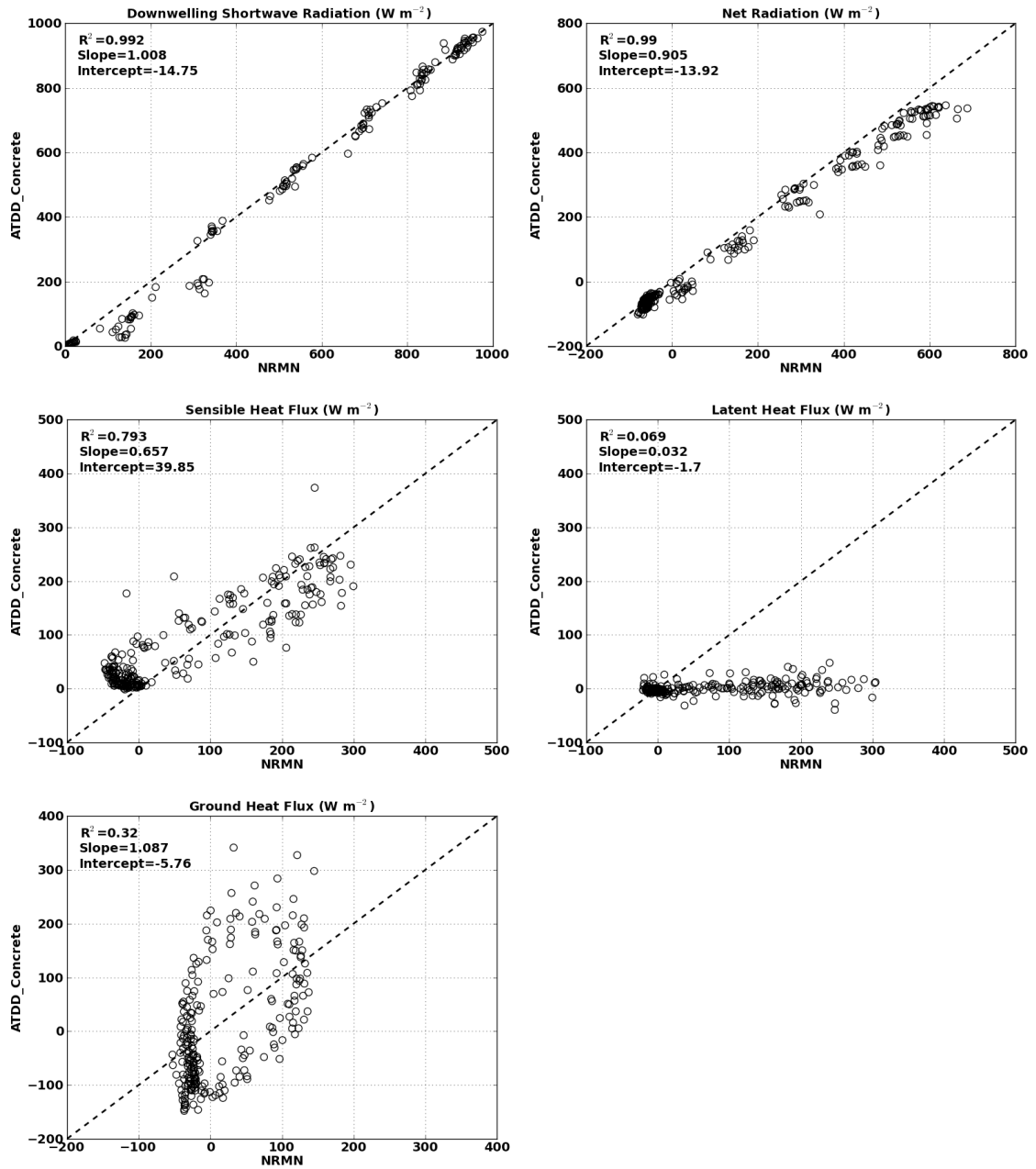


Figure B.8. Scatter plots of downwelling shortwave radiation, net radiation, sensible heat fluxes, latent heat fluxes, and ground heat fluxes for the ATDD Concrete vs. NRMN sites from 10 days with solar insolation near theoretical values during July 2003.

C. APPENDIX: URBPARAM.TBL

The parameters in this table may vary greatly from city to city.
The default values are probably not appropriate for any given city.
Users should adapt these values based on the city they are working
with.

Urban Parameters depending on Urban type
USGS

Number of urban categories: 3

Where there are multiple columns of values, the values refer, in
order, to: 1) Commercial, 2) High intensity residential, and 3) Low
intensity residential: I.e.:

Index: 1 2 3
Type: Commercial, Hi-dens Res, Low-dens Res
#

ZR: Roof level (building height) [m]
(sf_urban_physics=1)

ZR: 8.4, 8.1, 4.5
#ZR: 10.0, 7.5, 5.0 #defZR and defZR_SigmaZ

SIGMA_ZED: Standard Deviation of roof height [m]
(sf_urban_physics=1)

SIGMA_ZED: 8.9, 6.2, 1.8
#SIGMA_ZED: 4.0, 3.0, 1.0 #def_SigmaZ and defZR_SigmaZ

ROOF_WIDTH: Roof (i.e., building) width [m]
(sf_urban_physics=1)

ROOF_WIDTH: 30.7, 17.4, 11.7
#ROOF_WIDTH: 37.7, 21.4, 14.7 #Wroof_up
#ROOF_WIDTH: 23.7, 13.4, 8.7 #Wroof_down

ROAD_WIDTH: road width [m]
(sf_urban_physics=1)
#

ROAD_WIDTH: 7.5, 7.5, 7.5

```

#
# AH: Anthropogenic heat [ W m{-2} ]
#   (sf_urban_physics=1)
#

AH: 0.0, 0.0, 0.0

#
# FRC_URB: Fraction of the urban landscape which does not have natural
#   vegetation. [ Fraction ]
#   (sf_urban_physics=1,2,3)
#

FRC_URB: 0.95, 0.9, 0.5
#FRC_URB: 0.6, 0.5, 0.4 #furb

#
# CAPR: Heat capacity of roof [ J m{-3} K{-1} ]
#   (sf_urban_physics=1,2,3)
#

CAPR: 1.0E6, 1.0E6, 1.0E6,

#
# CAPB: Heat capacity of building wall [ J m{-3} K{-1} ]
#   (sf_urban_physics=1,2,3)
#

CAPB: 1.0E6, 1.0E6, 1.0E6,

#
# CAPG: Heat capacity of ground (road) [ J m{-3} K{-1} ]
#   (sf_urban_physics=1,2,3)
#

CAPG: 1.4E6, 1.4E6, 1.4E6,

#
# AKSR: Thermal conductivity of roof [ J m{-1} s{-1} K{-1} ]
#   (sf_urban_physics=1,2,3)
#

AKSR: 0.74, 0.74, 0.74,
#AKSR: 1.4, 1.4, 1.4, #kroof_up
#AKSR: 0.05, 0.05, 0.05, #kroof_down

#
# AKSB: Thermal conductivity of building wall [ J m{-1} s{-1} K{-1} ]
#   (sf_urban_physics=1,2,3)

```

```

#
AKSB: 0.67, 0.67, 0.67,

#
# AKSG: Thermal conductivity of ground (road) [ J m{-1} s{-1} K{-1} ]
#   (sf_urban_physics=1,2,3)
#

AKSG: 0.4004, 0.4004, 0.4004,

#
# ALBR: Surface albedo of roof [ fraction ]
#   (sf_urban_physics=1,2,3)
#

ALBR: 0.20, 0.20, 0.20
#ALBR: 0.40, 0.40, 0.40 #arook_up
#ALBR: 0.05, 0.05, 0.05 #arook_down

#
# ALBB: Surface albedo of building wall [ fraction ]
#   (sf_urban_physics=1,2,3)
#

ALBB: 0.20, 0.20, 0.20

#
# ALBG: Surface albedo of ground (road) [ fraction ]
#   (sf_urban_physics=1,2,3)
#

ALBG: 0.20, 0.20, 0.20

#
# EPSR: Surface emissivity of roof [ - ]
#   (sf_urban_physics=1,2,3)
#

EPSR: 0.90, 0.90, 0.90

#
# EPSB: Surface emissivity of building wall [-]
#   (sf_urban_physics=1,2,3)
#

EPSB: 0.90, 0.90, 0.90

#

```



```

# EPSG: Surface emissivity of ground (road) [ - ]
#   (sf_urban_physics=1,2,3)
#
EPSG: 0.95, 0.95, 0.95

#
# ZOB: Roughness length for momentum, over building wall [ m ]
#   Only active for CH_SCHEME == 1
#   (sf_urban_physics=1)
#
ZOB: 0.0001, 0.0001, 0.0001

#
# ZOG: Roughness length for momentum, over ground (road) [ m ]
#   Only active for CH_SCHEME == 1
#   (sf_urban_physics=1,2,3)
#
ZOG: 0.01, 0.01, 0.01

#
# AKANDA_URBAN: Coefficient modifying the Kanda approach to computing
# surface layer exchange coefficients.
#   (sf_urban_physics=1)
AKANDA_URBAN: 1.29 1.29 1.29

# DDZR: Thickness of each roof layer [ m ]
#   This is currently NOT a function urban type, but a function
#   of the number of layers. Number of layers must be 4, for now.
#   (sf_urban_physics=1)
DDZR: 0.05, 0.05, 0.05, 0.05

#
# DDZB: Thickness of each building wall layer [ m ]
#   This is currently NOT a function urban type, but a function
#   of the number of layers. Number of layers must be 4, for now.
#   (sf_urban_physics=1)
#
DDZB: 0.05, 0.05, 0.05, 0.05

#
# DDZG: Thickness of each ground (road) layer [ m ]
#   This is currently NOT a function urban type, but a function
#   of the number of layers. Number of layers must be 4, for now.

```

```

# (sf_urban_physics=1)
#

DDZG: 0.05, 0.25, 0.50, 0.75

#
# BOUNDR: Lower boundary condition for roof layer temperature [ 1: Zero-
# Flux, 2: T = Constant ]
# (sf_urban_physics=1)
#

BOUNDR: 1

#
# BOUNDB: Lower boundary condition for wall layer temperature [ 1: Zero-Flux,
# 2: T = Constant ]
# (sf_urban_physics=1)
#

BOUNDB: 1

#
# BOUNDG: Lower boundary condition for ground (road) layer temperature [ 1:
# Zero-Flux, 2: T = Constant ]
# (sf_urban_physics=1)
#

BOUNDG: 1

#
# TRLEND: Lower boundary condition for roof temperature [ K ]
# (sf_urban_physics=1,2,3)
#

TRLEND: 293.00, 293.00, 293.00

#
# TBLEND: Lower boundary temperature for building wall temperature [ K ]
# (sf_urban_physics=1,2,3)
#

TBLEND: 293.00, 293.00, 293.00

#
# TGLEND: Lower boundary temperature for ground (road) temperature [ K ]
# (sf_urban_physics=1,2,3)
#

TGLEND: 293.00, 293.00, 293.00

```

```
#
# Ch of Wall and Road [ 1: M-O Similarity Theory, 2: Empirical Form of Narita et
al., 1997 (recommended) ]
#   (sf_urban_physics=1)
#
```

```
CH_SCHEME: 2
```

```
#
# Surface and Layer Temperatures [ 1: 4-layer model, 2: Force-Restore
method ]
#   (sf_urban_physics=1)
#
```

```
TS_SCHEME: 1
```

```
#
# AHOPTION [ 0: No anthropogenic heating, 1: Anthropogenic heating will be
added to sensible heat flux term ]
#   (sf_urban_physics=1)
#
```

```
AHOPTION: 0
```

```
#
# Anthropogenic Heating diurnal profile.
# Multiplication factor applied to AH (as defined in the table above)
# Hourly values ( 24 of them ), starting at 01 hours Local Time.
# For sub-hourly model time steps, value changes on the hour and is
# held constant until the next hour.
#   (sf_urban_physics=1)
#
#
```

```
AHDIUPRF: 0.16 0.13 0.08 0.07 0.08 0.26 0.67 0.99 0.89 0.79 0.74 0.73 0.75
0.76 0.82 0.90 1.00 0.95 0.68 0.61 0.53 0.35 0.21 0.18
```

D. APPENDIX: ENERGY FLUXES WITH MYJ PBL SCHEME

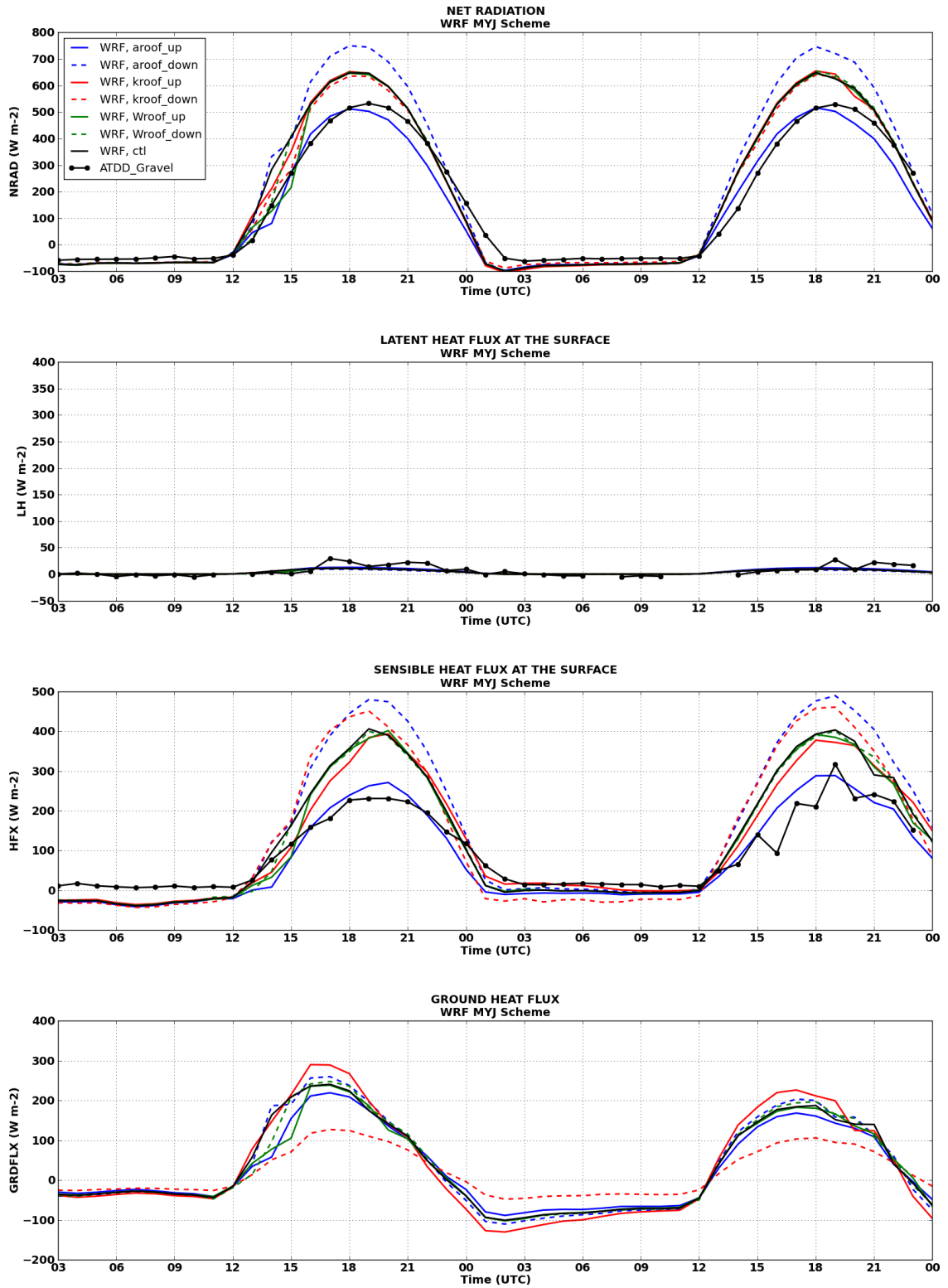


Figure C.1. Diurnal cycles of net radiation, latent heat fluxes, sensible heat fluxes, and ground heat fluxes predicted by the WRF model using the MYJ PBL scheme for 14-15 July 2003. Observational data from the ATDD Gravel site are shown for comparison.

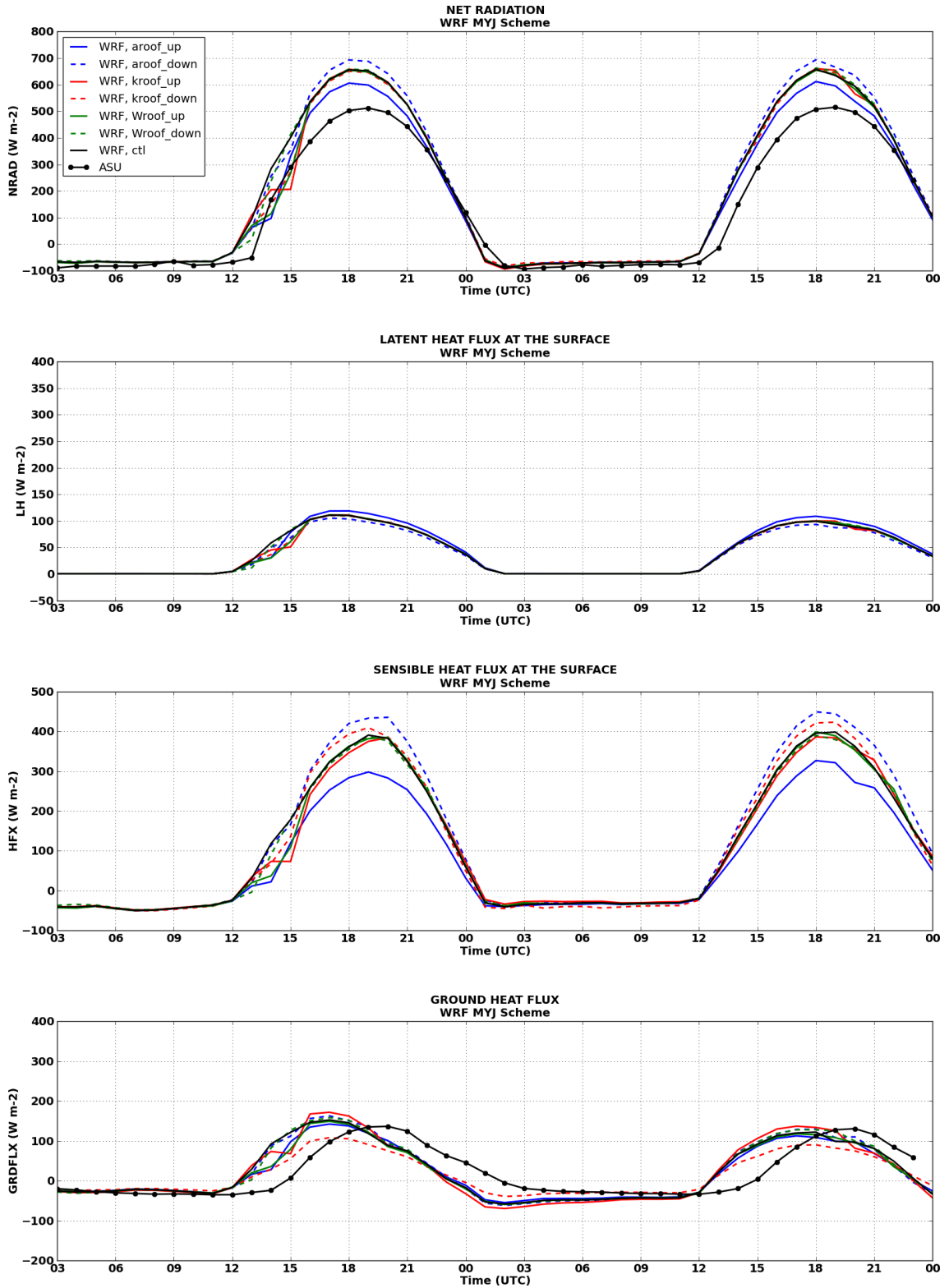


Figure C.2. Diurnal cycles of net radiation, latent heat fluxes, sensible heat fluxes, and ground heat fluxes predicted by the WRF model using the MYJ PBL scheme for 14-15 July 2003. Observational data from the ASU site are shown for comparison.

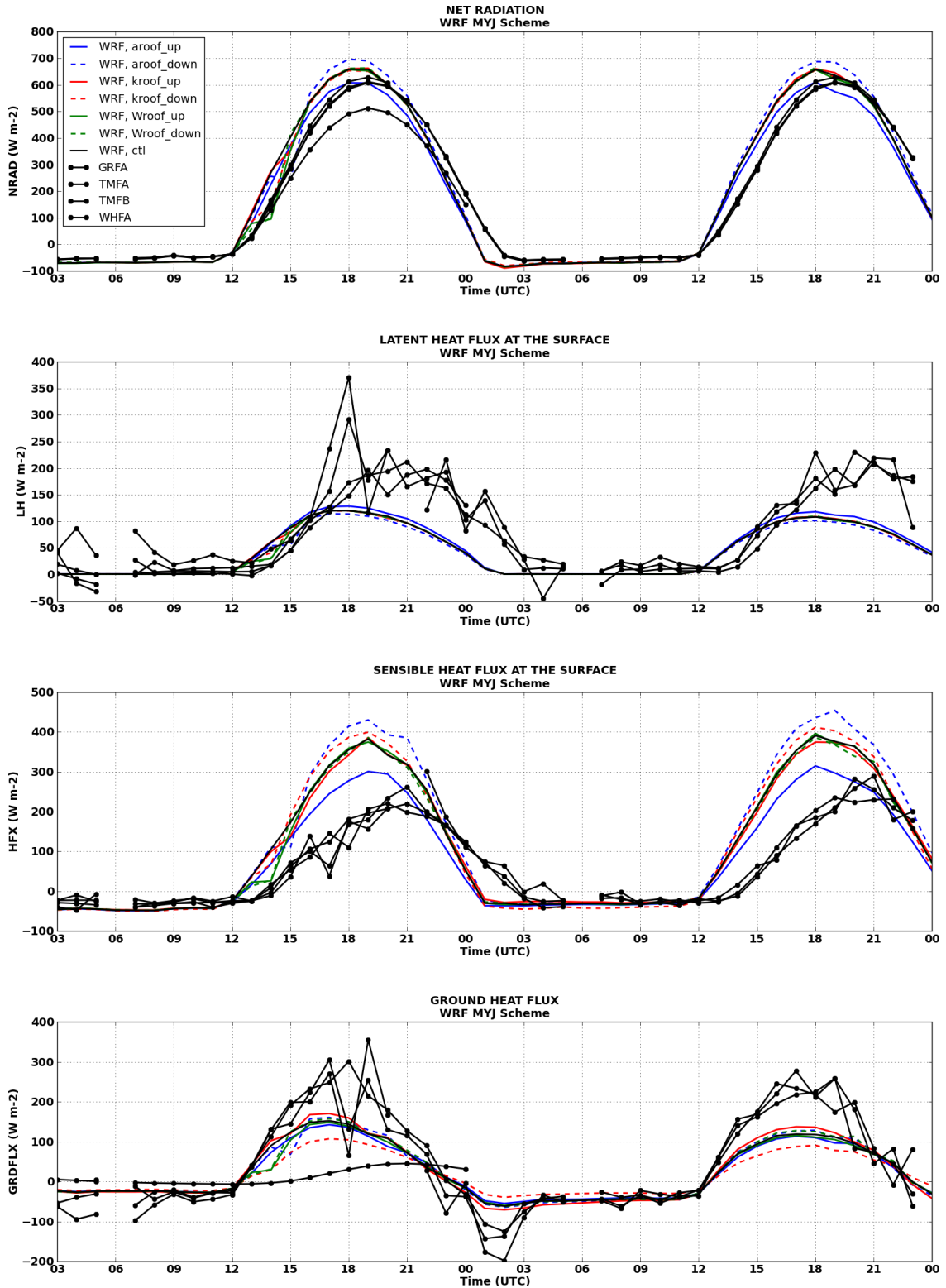


Figure C.3. Diurnal cycles of net radiation, latent heat fluxes, sensible heat fluxes, and ground heat fluxes predicted by the WRF model using the MYJ PBL scheme for 14-15 July 2003. Observational data from the IU GR, TMA, TMB, and WH sites are shown for comparison.

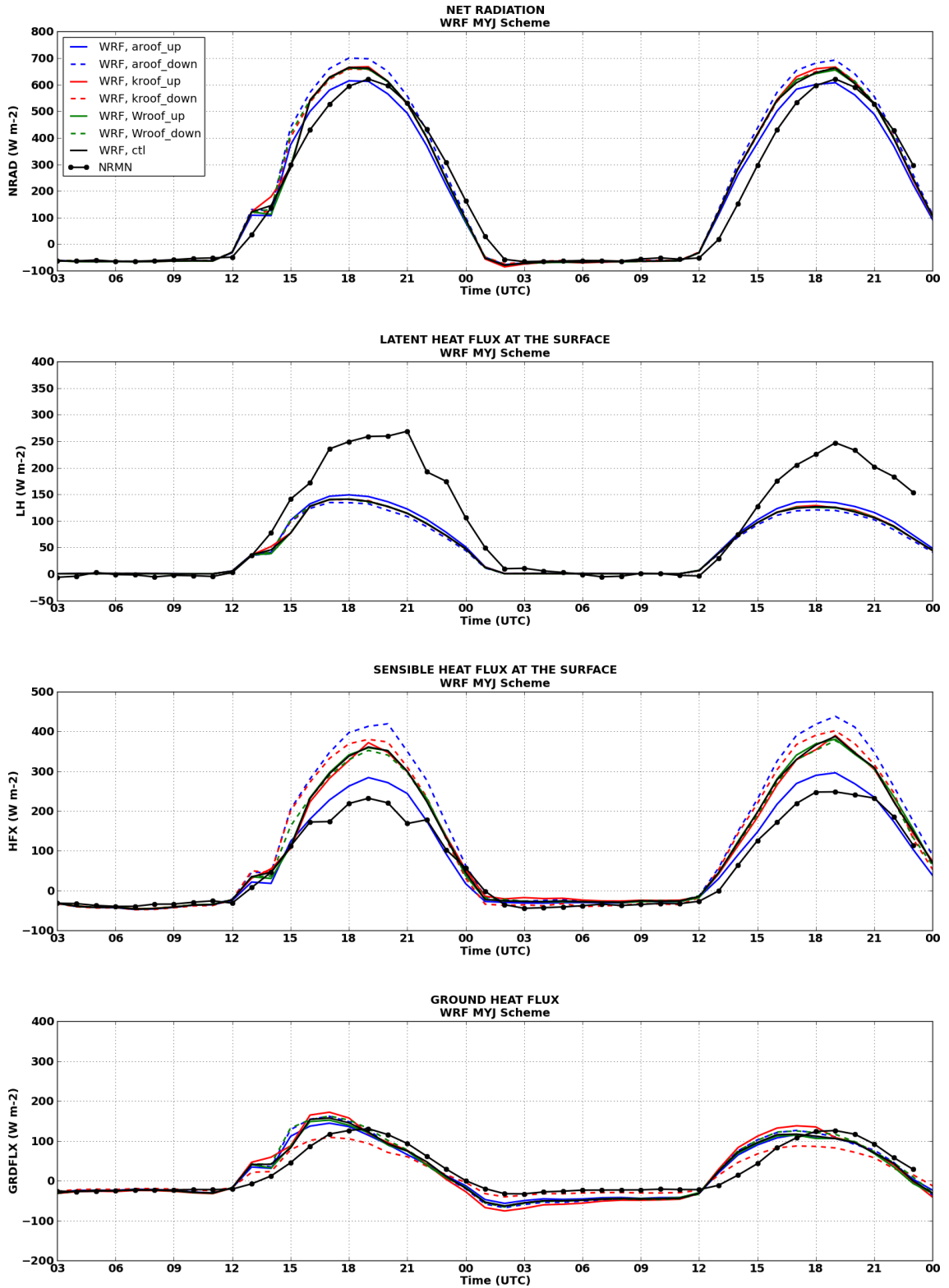


Figure C.4. Diurnal cycles of net radiation, latent heat fluxes, sensible heat fluxes, and ground heat fluxes predicted by the WRF model using the MYJ PBL scheme for 14-15 July 2003. Observational data from the NRMN site are shown for comparison.